Multi-Frequency Acoustics for Deep-Sea Sediment Plume Monitoring

A deep-sea nodule collection application

MSc Offshore and Dredging Engineering
Julian Roderik Manrho

Delft University of Technology

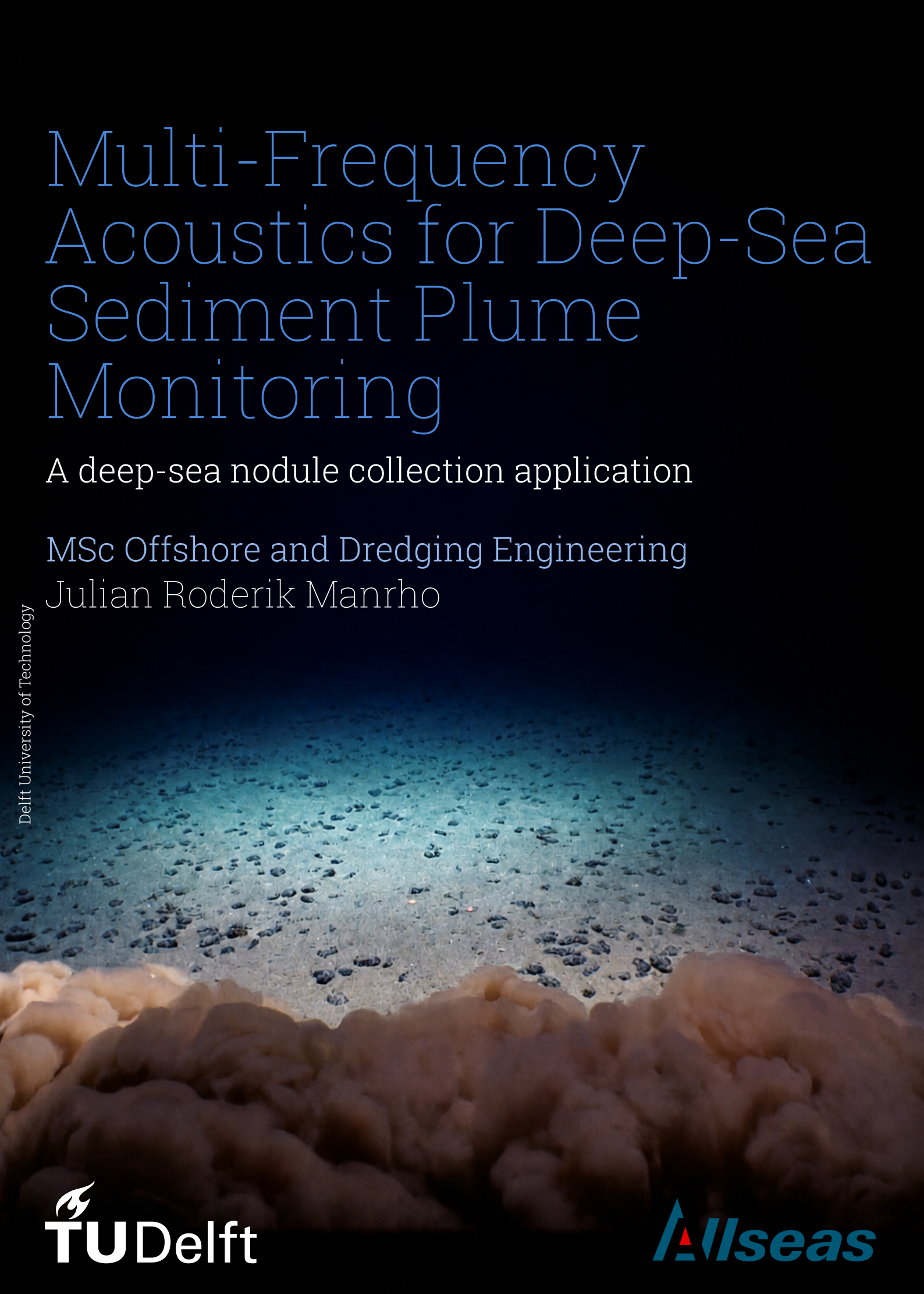

TU Delft

Allseas

Multi-Frequency Acoustics for Deep-Sea Sediment Plume Monitoring

A deep-sea nodule collection application

by

Julian Roderik Manrho

University Supervisor:	Dr. ir. R.L.J. Helmons
Company Supervisor:	Dr. Ir. M. Akritidis,
	Ir. F. van Grunsven
Project Duration:	17 November, 2025 - 27 August, 2026
Faculty:	Maritime and transport technology, Delft

Cover: Image of a disturbed seafloor containing polymetallic nodules in the Pacific Ocean [1] . Modified using AI-assisted tools to extend the vertical extent and correct the aspect ratio.

TU Delft

Allseas

Preface

Among the least explored environments on Earth, the abyssal plains are home to unique ecosystems that have evolved under highly stable conditions over millions of years, making them particularly sensitive to disturbance. Yet beneath these ecosystems lie vast quantities of critical metals that could play a key role in supporting the global energy transition. As interest in deep-sea nodule collection continues to grow, so does the need to understand and minimise its environmental impacts.

One of the primary environmental concerns associated with deep-sea nodule collection is the generation of suspended sediment plumes. These plumes consist of fine sediment particles that can remain suspended in the water column for extended periods and disperse beyond the immediately disturbed area. The interaction of these fine sediment plumes with the surrounding environment may affect benthic ecosystems beyond the directly disturbed area. Reliable monitoring of these plumes is therefore essential for predicting their environmental footprint and forms the basis for future environmental regulations.

This thesis investigates the application of multi-frequency acoustic sensing techniques for monitoring suspended sediment plumes generated during deep-sea nodule collection operations. The performance of various inversion methods and measurement approaches is evaluated in light of the conventional optical sensing technique currently used for suspended sediment monitoring, thereby assessing the uncertainties, capabilities, and potential advantages of acoustic monitoring.

This thesis was originally initiated with the expectation that the commercial inversion software would perform sufficiently well to enable the assessment of the influence of processes such as flocculation, using supporting instruments including the LISST-100x and particle cameras. This would also have enabled the investigation of potential cross-calibration methods between the sensors. However, as demonstrated in the Results section, the current most advanced commercial software proved incapable of producing reliable inversions. Therefore, after the experimental campaign, the scope of this research shifted towards the evaluation of alternative inversion methods for deep-sea sediments in their primary, unflocculated state. As the literature review (Sections 2 and 3) was developed within the original, broader research scope, its more extensive assessment of dynamic plume states, sediment-monitoring techniques, and the environmental and sediment properties governing their applicability and measurement response was retained in the report to preserve the valuable information and insights obtained during the initial research phase.

This research was conducted as part of a collaboration between Delft University of Technology, Allseas, the University of Gothenburg, and the Kristineberg Center in Sweden.

During the preparation of this thesis and the development of the inversion algorithms, generative AI tools were used to assist with image and text editing, formatting alignment, and debugging python errors. All suggestions were reviewed and verified by the author.

Acknowledgements

The completion of this thesis marks the final step of my MSc in Offshore and Dredging Engineering at Delft University of Technology and the end of an inspiring and rewarding chapter of my academic journey.

This study aims to contribute to a better understanding of the complexities involved in measuring the properties of abyssal fine sediment plumes, while supporting the continued advancement of acoustic inversion methods, cross-calibration frameworks, and suspended sediment monitoring for future offshore applications.

Following my academic path in offshore engineering, I am grateful to have had the opportunity to discover and contribute to this incredible developing field. I particularly enjoyed exploring the multifaceted topic of deep-sea mining through workshops, countless open discussions, and the experience gained in experimental research and acoustic inversion modelling.

I would like to express my sincerest gratitude to Rudy Helmons (TU Delft supervisor) for his academic guidance, insightful discussions, and exceptional responsiveness, ensuring that I always felt supported throughout this project. With equal gratitude I would like to thank Frans van Grunsven and Marios Akritidis (Allseas supervisors) for their persistent efforts to the feasibility of this project, their invaluable technical insights, and for making me feel welcome within the Allseas community from day one.

I would also like to thank Prof. Laurenz Thomsen and Vignesh Gokuladas Menon, from the University of Gothenburg, for their invaluable support during the experimental campaign in Sweden. Their expertise, guidance, and willingness to share their knowledge made it possible to simulate deep-sea conditions using thermoregulated laboratory facilities and authentic CCZ deep-sea sediment samples.

I would also like to thank my parents and sister for their unwavering support throughout my academic journey and for always believing in me.

Finally, I would like to thank my wife, Vlada, whose endless encouragement, love, and patience supported me throughout this journey, from taking on everyday responsibilities, to discussing research ideas, reviewing drafts, and always believing in me. This thesis will forever remind me not only of everything I learned along the way, but also of the unforgettable moment among the Swedish fjords when she became my fiancée. She has been my greatest source of strength.

Looking back on this journey, I am reminded that achievements are rarely accomplished alone.

Julian Roderik Manrho
Delft, August 2026

Abstract

Deep-sea nodule collection generates suspended sediment plumes that may affect the surrounding benthic environment. Reliable monitoring of suspended sediment concentration (SSC) and particle size near the plume source is therefore important for plume characterization, modelling, and environmental impact assessment. This study evaluates the applicability of multi-frequency acoustic backscatter measurements for determining SSC and particle size estimates under conditions representative of deep-sea nodule collection plumes.

An experimental campaign was conducted in a recirculation tank using two representative deep-sea box-core sediments, referred to as CCZ sediment and Sediment B. Multi-frequency acoustic backscatter measurements were obtained at 1, 2, 4, and 5 MHz frequencies and were evaluated against gravimetric SSC measurements over an experimental suspended sediment concentration range of $0.16 - 32.4$ g/L. The recirculation tank was designed to generate a relatively homogeneous suspension of unflocculated deep-sea sediment, thereby simulating conditions within a collector vehicle diffuser. Four acoustic inversion methods were evaluated. Methods 1 and 2 applied commercially available bin-based inversion approaches to resolve SSC and particle size over range, whereas Methods 3 and 4 applied profile-averaged inversion approaches implemented in a custom Python workflow.

The commercially available bin-based inversion methods did not provide reliable results for the investigated fine-grained deep-sea sediments. Method 1 substantially overestimated particle size, by factors of 4.1 and 18.2 for the CCZ sediment and Sediment B, respectively, which corresponded to SSC underestimations of approximately 1.2 and 2.0 orders of magnitude. Method 2 did not yield reliable SSC inversions due to its strong sensitivity to small deviations in the prescribed particle-size parameters (D_{50} and σ). In contrast, the profile-averaged Methods 3.1 and 4.4 provided quantifiable SSC estimates for both sediments. The inversion performance was governed primarily by the prescribed median particle diameter (D_{50}), while constraining the particle-size distribution width (σ) provided limited additional benefit. The D_{50}-constrained configurations were therefore selected as the representative cases.

Over the common evaluated SSC range of $0.5 - 18.0$ g/L, Method 3.1 achieved proportional biases of $+36.1\,\%$ and $+1.2\,\%$ for the CCZ sediment and Sediment B, respectively, with corresponding R^2 values of 0.995 and 0.978. Method 4.4 achieved proportional biases of $+9.8\,\%$ and $-15.5\,\%$, with R^2 values of 0.944 and 0.867, respectively. For the CCZ sediment, extending the evaluated range to 32.4 g/L resulted in proportional biases of $+31.1\,\%$ and $+19.2\,\%$ for Methods 3.1 and 4.4, respectively. Across the selected configurations, the proportional bias remained within approximately $\pm 36\,\%$. Particle-size and distribution-width inversions were substantially more sensitive to uncertainties in the acoustic measurements and could not yet be reliably quantified.

For comparison, the optical backscatter sensor (OBS) produced slopes of 0.857 ($R^2 = 0.983$) for Sediment B and 0.546 ($R^2 = 0.884$) for the CCZ sediment. The difference in performance between the sediments demonstrates the dependence of optical measurements on representative sediment-specific calibration. Multi-frequency acoustic backscatter, in contrast, provided range-averaged SSC estimates without requiring sediment-specific calibration, although its effective measurement range significantly decreased with increasing SSC.

Overall, multi-frequency acoustic backscatter shows strong potential for range-averaged SSC monitoring within or close to deep-sea nodule collector diffusers, where particle properties remain relatively stable and theoretical attenuation and scattering models are most applicable. Its ability to provide measurements over a larger representative volume without sediment-specific calibration offers an important advantage over conventional optical point measurements. However, further development is required to improve particle-size inversion and measurement reliability at elevated SSC, followed by validation under representative deep-sea operational conditions.

Contents

Acknowledgements ii

Nomenclature xiii

1 Introduction 1
- 1.1 Background and Relevance . . . 1
  - 1.1.1 Deep-Sea Minerals and Their Extraction . . . 1
  - 1.1.2 The Environmental Impact of Plumes . . . 2
  - 1.1.3 The Need for Real-time Plume Measurements . . . 2
- 1.2 Problem Statement . . . 2
- 1.3 Main Research Question . . . 3
  - 1.3.1 Sub-Questions . . . 3
- 1.4 Scope Definition . . . 3
- 1.5 Thesis Outline . . . 4

2 Deep-sea Sediment Properties and Plume Mechanisms 5
- 2.1 Sediment Composition . . . 5
- 2.2 Aggregation and Settling Mechanisms of Sediment Plumes . . . 5
- 2.3 Sediment Plume Behaviour . . . 6
  - 2.3.1 Spatial Evolution of In-Situ Sediment Plumes . . . 6
  - 2.3.2 Plume Behaviour in Confined Laboratory Test Setups . . . 7

3 Suspended Sediment Measurement Techniques 9
- 3.1 State of the Art in Suspended Sediment Monitoring . . . 9
- 3.2 General Principles of Backscatter-Based Measurements . . . 9
- 3.3 Optical Backscatter Theory . . . 10
  - 3.3.1 Scattering and Attenuation . . . 10
  - 3.3.2 Controls on Optical Backscatter Signal . . . 10
  - 3.3.3 Optical Calibration and Regression Model . . . 11
  - 3.3.4 Sensitivity Regime . . . 12
- 3.4 Acoustic Backscatter Theory . . . 12
  - 3.4.1 Scattering, Attenuation and Geometric Spreading . . . 13
  - 3.4.2 The Forward Formulation . . . 13
  - 3.4.3 The Inversion Problem . . . 14
  - 3.4.4 Single and Multiple Frequency Inversion, and their Limitations . . . 15
- 3.5 Acoustic Inversion Approaches . . . 17
  - 3.5.1 Implicit Bin-based Inversion . . . 17
  - 3.5.2 Explicit Profile-Averaged Inversion . . . 18
  - 3.5.3 Controls on Acoustic Backscatter Response . . . 19
- 3.6 Supporting Instruments for Sediment Characterisation . . . 19
- 3.7 Synthesis of Literature and Research Positioning . . . 20

4 Inversion and Experimental Methods 21
- 4.1 Selected Inversion Methods Under Evaluation . . . 21
- 4.2 Sediment Properties . . . 23
- 4.3 Sediment Particle Size Distribution Parameters . . . 24
- 4.4 Experimental Setup . . . 24
- 4.5 Instruments . . . 26
- 4.6 Experiment Preparation . . . 27
- 4.7 Measurement Procedures . . . 27
- 4.8 Calibration of Optical Sensor . . . 28

4.9 Gravimetric Analysis and Filtering . . . 30
4.10 Acoustic Background Noise Measurements . . . 31
4.11 Data Acquisition Settings . . . 32
4.12 Data Processing and Filtering . . . 33

5 Results and Analysis **36**
5.1 Experimental Conditions . . . 36
5.1.1 Test Matrix . . . 36
5.1.2 Suspension Homogeneity . . . 37
5.1.3 Particle Size Evolution . . . 38
5.2 Evaluation Metrics . . . 39
5.3 Sensor Performance . . . 40
5.3.1 Optical Backscatter Sensor . . . 40
5.3.2 Acoustic Sensor Range . . . 41
5.4 Bin-Based Inversion Methods . . . 42
5.4.1 Method 1 - SSC and Particle Size Inversion . . . 42
5.4.2 Method 2 - Prescribed Particle Size SSC Inversion . . . 44
5.5 Profile-Averaged Inversion Methods . . . 44
5.5.1 Acoustic Parameter Assessment . . . 44
5.5.2 Method 3 - Attenuation α_{sv} and Backscatter s_v Based Inversion . . . 47
5.5.3 Method 4 - Attenuation(α_{sv}) Based Inversion . . . 52
5.6 Summary of Inversion Results . . . 53

6 Discussion **56**
6.1 Influence of Echo Statistics on Acoustic Inversion . . . 56
6.2 Influence of α_{sv} and s_v on Inversion Performance . . . 57
6.3 Experimental Uncertainty . . . 59
6.4 Factors Influencing OBS Measurement Performance . . . 60
6.5 Representativeness of Experimental Setup . . . 61
6.6 Suitability of Multi-Frequency ABS for Deep-sea Nodule Collection . . . 61

7 Conclusions **63**

8 Recommendations **67**
8.1 Improvements to the Experimental Setup . . . 67
8.2 Alternative Experimental Configuration . . . 67
8.3 Optimisation of Acoustic Measurement Settings . . . 68
8.4 Future Research . . . 68

References **70**

A Attenuation and Backscatter Linear Regression Parameters **74**

B Acoustic Measurement Range Regression Parameters **75**

C Method 1 Analysis **76**

D Method 2 Analysis **86**

E Method 3 Analysis **97**

F Method 4 Analysis **119**

G Test Matrix **135**

H ABS Acquisition Information **138**

I Python Workflow **142**

List of Figures

1.1 A close-up of the undisturbed seafloor in the Pacific Ocean containing polymetallic nodules [1]. . . . 1
1.2 Conceptual illustration of the spatio-temporal evolution of a benthic sediment plume produced by a deep-sea nodule vehicle, and its transition into a near-bed turbidity current under ambient hydrodynamic forcing [8]. . . . 1

2.1 Image taken by a floc-view camera, of flocs formed by artificial clay and flocculant [23] . 6
2.2 Image of flocs formed by illite and 0.75 $mg\,g^1$ of flocculant in saltwater [7] 6
2.3 Schematic representation of the spatial development of a sediment plume behind a nodule collecting vehicle, showing the in-diffuser, near-field, transitional, and far-field plume regions. . . . 7

3.1 Example of a laboratory calibration of the AQUAlogger 310TY mounted on a tripod, showing the response of FTU to SSC for laboratory samples at 0.1 m above seabed for sediment composed out of 18.0 % clay , 81.5 % silt, and 0.5 % sand [37]. Calibration is sensor and sediment specific. . . . 12
3.2 OBS sensitivity trend showing three characteristic response regions: (A) linear (B) inflection due to saturation, and (C) signal reduction by dominant grain-shielding effects. SPM (suspended particculate matter) ranges are sediment and sensor specific, and were measured with nephelometer. Adapted from [39] Bunt et al., 1999 [36]. . . . 12
3.3 Composite dataset from three independent studies showing normalized OBS sensitivity, with fixed SSC, as a function of particle diameter D, with the corresponding decreasing trend predicted by Mie scattering theory [26]. . . . 12
3.4 A schematic presentation of an acoustic beam emitted by a transducer; Indicating its range dependencies (Near-field, side-lobes, far-field). [29] . . . 13
3.5 Dependence of the form function on the dimensionless size parameter ka_s for quartz sands of multiple experimental studies. The vertical dashed lines delimit the Rayleigh, transitional and Geometric regimes [42] . . . 16

4.1 Malvern determined volume-based particle size distributions of the two sediment cases: CCZ sediment in red and Sediment B in blue. . . . 23
4.2 LISST determined volume-based particle size distributions of both sediment cases: the CCZ sediment in red and Sediment B in blue. . . . 24
4.3 Schematic representation of the recirculation tank showing (a) the isometric view, (b) the front view, including the acoustic sensor's field of view (dashed light blue lines), and (c) the side view. The main components include the rectangular tank, accumulation funnel, transducer head assembly, deflector plate, and recirculation pump. The tank was filled with salt water to approximately 10 cm below the top edge. . . . 25
4.4 Schematic overview of the recirculation tank with a magnified view of the upper section. Enlarged details show the deflection plate, which redirects the inflow for improved mixture homogenization, and the transducer head assembly containing the four acoustic transducers. . . . 26
4.5 Relative increase in temporal noise in the acoustic beam due to the presence of the optical sensor at two locations: at transducer height and 10 cm below the transducers against the tank wall. . . . 27
4.6 Overview of the sensor measurement procedure for each SSC step . . . 28

4.7 Schematic representation of the optical backscatter sensor calibration setup. The optical backscatter sensor suspended in a beaker, placed on a stirrer plate to maintain a homogenous suspension throughout the calibration process. Schematic generated with assistance of OpenAI ChatGPT and subsequently reviewed and modified for technical accuracy. . . . 29
4.8 OBS calibration curves for Sediment A (CCZ) and Sediment B. Filled circles indicate data included in the fit, while crosses and empty circle symbols indicate excluded data points. The coloured dashed lines mark the transition between the linear and logarithmic fitting regimes. . . . 29
4.9 Schematic of the equipment used during the filtration process. The membrane filters were placed on top of the filter holder, onto which a known sample volume was applied. The vacuum ensured that the water was pulled through the filter, while the sediment was retained on the membrane filter, which was subsequently dried and weighed. Schematic generated with assistance of OpenAI ChatGPT and subsequently reviewed and modified for technical accuracy . . . 30
4.10 Batch of membrane filters placed in an oven for approximately 16 hours to remove residual moisture prior to weighing. . . . 31
4.11 Signal amplitude in volts as a function of range for each frequency. The bounds of the selected interval used to estimate the average background noise level are defined by the blue dashed lines; the red section is the selected region, and the solid green line represents the final background noise. . . . 32
4.12 Quadratically averaged signal amplitude in volts as a function of range for each frequency. The raw profiles are shown in light grey, and the de-spiked and smoothed profiles are shown in black. . . . 34
4.13 OBS measurements plots, representing the measurements at 3 measurement heights, and four measurement times. All measurements at gravimetric SSC= 8.873 g/L 34
4.14 Examples of particle size distributions measured by the LISST-100X, containing large variations in distribution shape and final bin . . . 35

5.1 Gravimetric measurement locations inside the recirculation tank . . . 38
5.2 Maximum deviation from the mean gravimetric concentration across the three sampling heights at the beginning and end of the experiments for CCZ sediment and Sediment B. 38
5.3 Relative and absolute increases in the D_{10}, D_{50}, and D_{90} particle size percentiles between measurement distances of 0.2 m and 0.8 m from the transducer (over 62.5 seconds). Positive values indicate an increase in particle size with distance from the transducer. . . . 39
5.4 Comparison of the OBS-derived SSC with the gravimetrically determined SSC both the CCZ sediment (left) and Sediment B (right). . . . 40
5.5 Relative error of the OBS-derived SSC as a function of the gravimetrically determined SSC. . . . 41
5.6 Maximum valid acoustic measurement range as a function of SSC for the 1, 2, 4, and 5 MHz transducers, shown for both CCZ sediment and Sediment B. Horizontal dashed lines indicate the theoretical near-field limits of each transducer, while solid lines represent exponential approximations of the measured trends. . . . 42
5.7 Multi-frequency SSC inversion results obtained using the 2, 4, and 5 MHz frequencies. 43
5.8 Example regressions for the CCZ sediment at 3.21 g/L. Plot (a) shows the linear regression to the Fluid corrected backscatter (FCB) of which the slope is used to derive the viscous sediment attenuation. Plot (b) shows the linear horizontal average regression to the micro-bubble corrected signal to obtain the volume backscatter coefficient. . . . 45
5.9 Plots (a) and (b) show the viscous sediment attenuation as a function of suspended sediment concentration for the CCZ sediment and Sediment B, respectively. Plots (c) and (d) show the corresponding volume backscatter coefficient as a function of suspended sediment concentration. The dotted lines represent quadratic least-squares fits included as visual guides to the observed trends. . . . 46

5.10 Plots (a) and (b) show viscous sediment attenuation as a function of suspended sediment concentration for the CCZ sediment and Sediment B, respectively. Plots (c) and (d) show the corresponding volume backscatter coefficient as a function of suspended sediment concentration. The shaded region indicates the range in which the frequencies give the most consistent results. All plots are in log-log scale. 47
5.11 Comparison of the inverted SSC against the gravimetric SSC model outputs for the CCZ sediment and Sediment B 48
5.12 Inverted particle-size distribution parameters without constraints for the CCZ sediement (purple) and Sediment B (green). The left panels present the particle-size inversion and the right panels the distribution-width inversion. 49
5.13 Overlay of the total objective-function error and best-fit SSC solution space for the CCZ sediment. The red contours (appearing as dots at this scale) indicate a $2\,\%$ increase relative to the minimum objective-function error, while the white contours indicate a $\pm 2\,\%$ variation in inverted SSC relative to the global minimum. 50
5.14 Influence of particle-size distribution constraints on the Method 3.1 SSC inversion. Case 1 is unconstrained, Case 2 constrains D_{50}, Case 3 constrains σ, and Case 4 constrains both parameters. For the CCZ sediment, regressions are presented over both $0.5 - 18.0$ g/L and the full $0.5 - 32.4$ g/L concentration range. 51
5.15 Comparison of the bi-modal distribution model against the gravimetric SSC for the CCZ sediment and Sediment B 52

6.1 Probability density function of the normalized echo amplitude for the 1, 2, 4, and 5 MHz transducers at measurement ranges of 0.2, 0.4, and 0.6 m. The dashed black line represents the theoretical Rayleigh distribution. 56
6.2 Raw acoustic data in counts over time and range, showing scattering structures associated with larger particles moving through the water column. A larger scale version of this figure can be found in Appendix **??** 57
6.3 Plots (a) and (b) show the ratio of measured to modelled viscous sediment attenuation for the CCZ sediment and Sediment B, respectively, while plots (c) and (d) show the corresponding ratios for the volume backscatter coefficient. 58

C.2 Particle size estimates for the 0.576 g/L CCZ sediment case, using different levels of profile averaging 77
C.3 Particle size estimates for the 0.850 g/L Sediment B measurement obtained using different frequency combinations: the two lowest frequencies (1 and 2 MHz), the three lowest frequencies (1, 2, and 4 MHz), the two middle frequencies (2 and 4 MHz), the two highest frequencies (4 and 5 MHz), the three highest frequencies (2, 4, and 5 MHz), and all four frequencies (1, 2, 4, and 5 MHz). 78
C.4 Particle size estimates for the 0.576 g/L CCZ sediment measurement obtained using different frequency combinations: the two lowest frequencies (1 and 2 MHz), the three lowest frequencies (1, 2, and 4 MHz), the two middle frequencies (2 and 4 MHz), the two highest frequencies (4 and 5 MHz), the three highest frequencies (2, 4, and 5 MHz), and all four frequencies (1, 2, 4, and 5 MHz). 79
C.5 Particle size ratio relative to the LISST and Malvern measured D_{50}, as a function of gravimetric SSC (g/L) 80
C.6 Particle-size inversion of the CCZ sediment through Method 1. Horizontal plot indicates the maximum range set by SNR=5. Vertical lines indicate the maximum and minimum estimated value. 82
C.7 Particle-size inversion of Sediment B through Method 1. Horizontal plot indicates the maximum range set by SNR=5. Vertical lines indicate the maximum and minimum estimated value. 83
C.9 Particle size estimates for the Sediment B measurement using a prescribed relative standard deviation of 3.0 for the lognormal particle size distribution. 85

D.1 Inverted SSC profile for the CCZ sediment at a measured SSC of 1.25 g/L using only the 1 MHz frequency, illustrating the effect of the lowest-frequency selection. 86

D.2 Inverted SSC profiles for the CCZ sediment at gravimetrically measured SSC = 1.250 g/L using different frequency combinations (part 1). 87
D.3 Inverted SSC profiles for the CCZ sediment at gravimetrically measured SSC = 1.250 g/L using different frequency combinations (part 2). 88
D.4 Inverted SSC profiles for Sediment B at gravimetrically measured SSC = 0.850 g/L using different frequency combinations (part 1). 89
D.5 Inverted SSC profiles for Sediment B at gravimetrically measured SSC = 0.85 g/L using different frequency combinations (part 2). 90
D.6 Inverted SSC profiles for Sediment B using the 4 and 5 MHz frequencies for fixed median particle diameters ranging from 3.5 to 6.5 μm. The cases are ordered from the smallest to the largest prescribed particle size. 92
D.7 Inverted SSC profiles for Sediment B using the 4 and 5 MHz frequencies for prescribed relative standard deviations ranging from 0.7 to 0.9. The cases are ordered from the lowest to the highest relative standard deviation. 93
D.8 Multi-frequency inversion of Sediment B settling out starting from approximately 1 g/L for approximately 2 hours, in 6 recordings of 10 minutes 94
D.9 Multi-frequency inversion results for Sediment B settling from an initial concentration of approximately 1 g/L over a period of approximately 2 hours. Six 10-minute inversion windows are shown, illustrating the temporal evolution of the estimated suspended sediment concentration (top) and particle size parameters (bottom). 95
D.10 Time series of the raw acoustic voltage profiles for 1, 2, 4, and 5 MHz frequencies during the 1 g/L Sediment B settling experiment. 96

E.2 Inverted particle-size distribution parameters without constraints. In each subplot, the left panel presents the particle-size inversion and the right panel the distribution-width inversion. Purple curves correspond to the CCZ sediment and green curves to Sediment B. 99
E.4 Inverted particle-size distribution parameters with the particle size constrained. In each subplot, the left panel presents the particle-size inversion and the right panel the distribution-width inversion. Purple curves correspond to the CCZ sediment and green curves to Sediment B. 101
E.6 Inverted particle-size distribution parameters with the distribution width constrained. In each subplot, the left panel presents the particle-size inversion and the right panel the distribution-width inversion. Purple curves correspond to the CCZ sediment and green curves to Sediment B. 103
E.8 Inverted particle-size distribution parameters with both the particle size and distribution width constrained. In each subplot, the left panel presents the particle-size inversion and the right panel the distribution-width inversion. Purple curves correspond to the CCZ sediment and green curves to Sediment B. 105
E.9 Comparison of the ABS-inverted SSC against the reference SSC for the CCZ sediment and Sediment B using the attenuation-based inversion. 106
E.10 ABS-OBS Inverted particle-size distribution parameters with no constraint. In each subplot, the left panel presents the particle-size inversion and the right panel the distribution-width inversion. Purple curves correspond to the CCZ sediment and green curves to Sediment B. 107
E.11 CCZ sediment inversion results using various frequency combinations $0.5 - 32$ g/L . . . 110
E.12 CCZ sediment inversion results using various frequency combinations $0.5 - 32$ g/L . . . 111
E.13 CCZ sediment inversion results using various frequency combinations $0.5 - 18$ g/L . . . 112
E.14 CCZ sediment inversion results using various frequency combinations $0.5 - 18$ g/L . . . 113
E.15 Sediment B inversion results using various frequency combinations $0.5 - 18$ g/L 114
E.16 Sediment B inversion results using various frequency combinations $0.5 - 18$ g/L 115
E.17 Comparison of the bi-modal distribution model against the gravimetric SSC for the CCZ sediment and Sediment B 116

E.18 ABS Inverted particle-size distribution parameters obtained through the bimodal inversion. In each subplot, the left panel presents the particle-size inversion and the right panel the distribution-width inversion. Purple curves correspond to the CCZ sediment and green curves to Sediment B. 117
E.19 Graphical representation of the obtained particle size distribution shapes per SSC step for the CCZ sediment. 117
E.20 Graphical representation of the obtained particle size distribution shapes per SSC step for Sediment B. 118

F.1 Comparison of the Method 4 inversions applied to the CCZ sediment between 0.5-18 g/L, together with the estimated particle diameter and the estimated distribution widths. 120
F.2 Comparison of the Method 4 inversions applied to the CCZ sediment between 0.5-33 g/L, together with the estimated particle diameter and the estimated distribution widths. 122
F.3 Comparison of the Method 4 inversions applied to the Sediment B between 0.5-18 g/L, together with the estimated particle diameter and the estimated distribution widths. . . . 124
F.4 Comparison of the Method 4 inversions applied to the CCZ sediment between 0.5-18 g/L, together with the estimated particle diameter and the estimated distribution widths. 126
F.5 Comparison of the Method 4 inversions applied to the CCZ sediment between 0.5-32 g/L, together with the estimated particle diameter and the estimated distribution widths. 128
F.6 Comparison of the Method 4 inversions applied to the Sediment B between 0.5-18 g/L, together with the estimated particle diameter and the estimated distribution widths. . . . 130

List of Tables

3.1 Estimated particle diameters corresponding to the lower detection limit and peak sensitivity within the Rayleigh scattering regime for commonly used acoustic frequencies. . . 17

4.1 Overview of the inversion methods evaluated in this study. 22
4.2 Summary of the measured and single-mode GMM fitted particle size distribution parameters used for the acoustic modelling. 24
4.3 De-spiking and smoothing parameters applied to the background noise profile 33

5.1 Test matrix summarizing the target concentration, gravimetrically determined reference SSC, and OBS-derived SSC for both sediments. 37
5.2 Performance metrics of the OBS measured SSC relative to the gravimetrically determined SSC 41
5.3 Performance metrics of Method 3 for the CCZ sediment and Sediment B with a bi-modal defined distribution. 52
5.4 Effect of particle-size and distribution-width constraints on the performance of the oblate-spheroidal attenuation model. 53
5.5 Performance metrics of Methods 3 and 4 for the CCZ sediment and Sediment B. Method 3 evaluates different particle size distribution constraints, while Method 4 evaluates the attenuation-based sub-methods for different constraints on D_{50} and σ. Method 4 results are based on the Φ objective function. 55

6.1 Summary of the measured and single-mode Gaussian mixture model (GMM) [30, 68] fitted particle size distribution parameters used for the acoustic modelling. 60

A.1 Linear regression parameters for the relationships between viscous sediment attenuation (α_{sv}) and SSC, and between the volume backscatter coefficient (s_v) and SSC, for the CCZ sediment and Sediment B. The reported parameters comprise of the slope and the coefficient of determination (R^2). All regressions were forced through the origin for consistency with previous studies. 74

B.1 Parameters of the exponential regression used to approximate the maximum valid measurement range. 75

C.1 Minimum and maximum estimated particle radii and corresponding mean median particle diameter obtained with Method 1 using the 1, 2, 4, and 5 MHz frequencies. The overestimation ratios are calculated relative to the Malvern- and LISST-determined median particle diameters. 81

D.1 Sensitivity of the inverted SSC to the prescribed median particle diameter (D_{50}). The measured SSC was 0.85 g/L. The relative error with respect to the reference case ($D_{50} = 4.5$ μm) was calculated as $(SSC_{D_{50}} - SSC_{4.5})/SSC_{4.5} \times 100$. 91
D.2 Sensitivity of the inverted SSC to the prescribed relative standard deviation. The measured SSC was 0.85 g/L. 93

E.1 Performance metrics of Methods 3 and 4 for the CCZ sediment and Sediment B. Method 3 evaluates different particle size distribution constraints, while Method 4 evaluates the attenuation-based sub-methods for different constraints on D_{50} and σ. Method 4 results are based on the Φ objective function. 98
E.2 Performance metrics of Method 3 for the CCZ sediment and Sediment B relative to the OBS derived SSC with particle size constrained 106

E.3 Performance metrics of the selected single-mode inversion method for the CCZ sediment and Sediment B. 109

F.1 Performance metrics of Methods 4.1, 4.2, 4.3, and 4.4 applied to the CCZ sediment over the SSC range of 0.5–18 g/L. 121
F.2 Performance metrics of Methods 4.1, 4.2, 4.3, and 4.4 applied to the CCZ sediment over the SSC range of 0.5–32 g/L. 123
F.3 Performance metrics of Methods 4.1, 4.2, 4.3, and 4.4 applied to Sediment B using a particle-size search range of 1–40 μm. 125
F.4 Performance metrics of Methods 4.1, 4.2, 4.3, and 4.4 applied to the CCZ sediment over the SSC range of 0.5–18 g/L using particle-size constraints based on the LISST and Malvern measurements. 127
F.5 Performance metrics of Methods 4.1, 4.2, 4.3, and 4.4 applied to the CCZ sediment over the SSC range of 0.5–32 g/L using particle-size constraints based on the LISST and Malvern measurements. 129
F.6 Performance metrics for the four inversion models applied to Sediment B using the LISST and Malvern particle size distributions. M4.1 and M4.3 use prescribed particle size distributions, whereas M4.2 and M4.4 estimate the distribution width during the inversion. The slope is obtained from a linear regression forced through the origin. 131
F.7 Performance metrics of Methods 3 and 4 for the CCZ sediment and Sediment B. Method 3 evaluates different particle size distribution constraints, while Method 4 evaluates the attenuation-based sub-methods for different constraints on D_{50} and σ. For Methods 4.1 and 4.3, the prescribed distribution width is identified by its measurement source (LISST or Malvern). Method 4 results are based on the Φ objective function. 132

Nomenclature

Abbreviations

Abbreviation	Definition
ABS	Acoustic Backscatter Sensor
ADCP	Acoustic Doppler Current Profiler
CCZ	Clarion–Clipperton Zone
FCB	Fluid-Corrected Backscatter
FTU	Formazin Turbidity Unit
GMM	Gaussian Mixture Model
ISA	International Seabed Authority
LISST	Laser In-Situ Scattering and Transmissometry
LOI	Loss on Ignition
MARE	Mean Absolute Relative Error
MF-ABS	Multi-Frequency Acoustic Backscatter Sensor
MSCAT	Multiple Scattering
NIR	Near-Infrared
NTU	Nephelometric Turbidity Unit
OBS	Optical Backscatter Sensor
PSD	Particle Size Distribution
PSU	Practical Salinity Unit
RMSE	Root Mean Square Error
ROV	Remotely Operated Vehicle
SNR	Signal-to-Noise Ratio
SPM	Suspended Particulate Matter
SSC	Suspended Sediment Concentration
TOC	Total Organic Carbon

Symbols

Symbol	Definition	Unit
a	Particle radius	μm
a_0	Median particle radius of a particle size distribution	μm
a_s	Representative particle radius	μm
a_t	Transducer radius	m
c	Speed of sound in the fluid	$\mathrm{m\,s^{-1}}$
D_{10}	Particle diameter below which 10% of the particle volume occurs	μm
D_{50}	Median particle diameter	μm
D_{90}	Particle diameter below which 90% of the particle volume occurs	μm
E	Combined attenuation and backscatter objective function	–
f	Acoustic backscatter form function	–
h	Particle aspect ratio / oblateness parameter	–
k	Acoustic wavenumber	$\mathrm{m^{-1}}$
k_s	Sediment backscattering coefficient	$\mathrm{m\,kg^{-1/2}}$
k_t	Acoustic system calibration constant	$\mathrm{V\,m^{3/2}}$
M	Suspended sediment mass concentration	$\mathrm{kg\,m^{-3}}$
$n(a)$	Particle size distribution as a function of particle radius	–
P_0	Acoustic reference pressure	Pa
R	Transducer receive sensitivity	–
r	Distance from the acoustic transducer	m
r_n	Acoustic near-field distance	m
R^2	Coefficient of determination	–
s_v	Volume backscatter coefficient	$\mathrm{m^{-1}}$
T_v	Voltage transfer function	–
V_{rms}	Root-mean-square received acoustic voltage	V
w	Weighting fraction of a particle-size mode	–
α_s	Total sediment-induced acoustic attenuation coefficient	$\mathrm{m^{-1}}$
α_{ss}	Sediment attenuation due to scattering	$\mathrm{m^{-1}}$
α_{sv}	Sediment attenuation due to viscous losses	$\mathrm{m^{-1}}$
α_w	Water-induced acoustic attenuation coefficient	$\mathrm{m^{-1}}$
χ	Normalized total attenuation cross-section	–
χ_{ss}	Normalized scattering attenuation cross-section	–
χ_{sv}	Normalized viscous attenuation cross-section	–
ε	Convergence criterion for iterative inversions	–
λ	Acoustic wavelength	m
ρ_s	Sediment particle density	$\mathrm{kg\,m^{-3}}$
σ	Log-normal particle size distribution width	–
ψ	Acoustic near-field correction factor	–
Φ	Squared-residual attenuation objective function	–
Γ	Absolute-residual attenuation objective function	–

Statistical and Distribution Parameters

Parameter	Definition
Rel. SD	Relative Standard Deviation of the particle size distribution
RMSE	Root Mean Square Error relative to the reference SSC
MARE	Mean Absolute Relative Error relative to the reference SSC
$\sigma_{\log}$	Standard deviation of the residuals in logarithmic space

1 Introduction

1.1. Background and Relevance

1.1.1. Deep-Sea Minerals and Their Extraction

The energy transition from fossil fuels to sustainable energy sources drives an ever-increasing dependency on critical minerals metals like nickel, cobalt, copper and manganese [2], due to their properties form the basis of electrical systems such as batteries and wind turbines [3]. Large areas in the deep sea, such as the Clarion-Clipperton Zone (CCZ; eastern equatorial Pacific [4]) , contain abundant high-grade mineral resources in the form of so called polymetallic nodules; precipitates of manganese oxide and iron oxyhydroxide, generally spheroidal in shape, strewn across the ocean floor [2, 5], Figure 1.1. The extraction of minerals from these deposits is often considered a promising alternative to land-based mining; however, the topic remains controversial due to its potential environmental impact [3].

Current collection methods makes use of a remotely operated, tracked polymetallic nodule collector vehicle (hereinafter referred to as nodule collecting vehicle) equipped with a jet-based lifting system that exploits the Coandă Effect [6]. This system lifts and collects the nodules, thereby also mobilising the top most layer of the seafloor, consisting of fine mineral sediment and organic matter [7]. The fine sediment, however, does not constitute the high-value mineral material contained within the nodules, and the recovered nodules are therefore pre-emptively separated from the sediment-laden water within the nodule collecting prior to further handling. The excess mixture is discharged by the diffuser behind the nodule collecting vehicle close to the seabed [5], thereby generating a hydrodynamically suspended fine-sediment plume and evolving into a turbidity current, as illustrated in Figure 1.2.

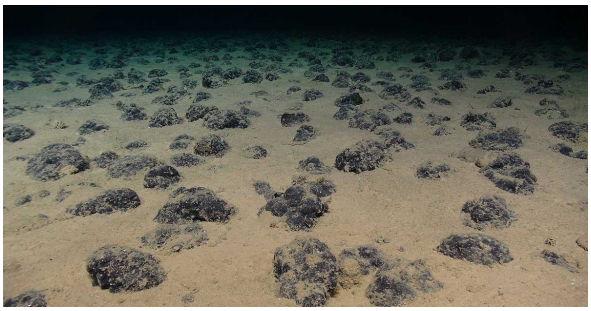

Figure 1.1: A close-up of the undisturbed seafloor in the Pacific Ocean containing polymetallic nodules [1].

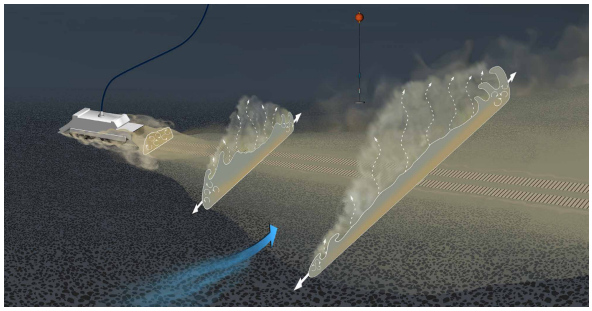

Figure 1.2: Conceptual illustration of the spatio-temporal evolution of a benthic sediment plume produced by a deep-sea nodule vehicle, and its transition into a near-bed turbidity current under ambient hydrodynamic forcing [8].

1.1.2. The Environmental Impact of Plumes

The abyssal plains form a highly stable environment where chemical and physical conditions such as temperature, pH, dissolved ions (of salinity), and hydrodynamic regimes remain near constant year round [6, 9]. Small disturbances pose significant uncertainty and challenges to endemic fauna as nutritional resources are inherently scarce at that depth. High-concentration fine-sediment plumes, such as those generated by nodule collecting discharges, adversely impact benthic habitats [9]; Megafauna consume increased amounts of non-nutritive particles and experience impaired sensory functions, while meiofaunal organisms become buried during the settling process of the suspended particles (also referred to as marine snow), causing suffocation and mortality [9]. In addition, the seafloor becomes covered with a layer of nutritiously poor sediment, leading to nutritional deficiencies [10], and impedes the ability of fauna to attach and anchor themselves to solid substrates which are critical to their survival [6].

While the mechanisms by which sediment plumes can affect the abyssal ecosystems are increasingly recognised, significant uncertainty persists with respect to the magnitude, spatial footprint, and temporal persistence of these effects under operational mining scenarios. Accordingly, improved characterisation and monitoring of sediment plumes are critical to support environmental baseline assessments, impact evaluation, and adaptive management strategies aimed at limiting disturbance to ecologically sensitive regions.

1.1.3. The Need for Real-time Plume Measurements

Anthropogenic sediment plumes may remain suspended for extended periods, with part of the fine-sediment suspension found to propagate over several kilometres beyond the immediate mining area [5, 11, 12]. Accordingly, regulatory frameworks set for plume monitoring, such as those applied in dredging and currently in deep-sea nodule collection [13], increasingly require quantitative and evidence-based environmental assessments. Therefore, continuous high-quality environmental monitoring is increasingly becoming a prerequisite for environmental impact forecasting, baseline threshold establishment, threshold compliance assessment, and adaptive plume management. To support these assessments, numerical models are widely used to describe and predict plume behaviour through sediment dispersion, transport, and deposition processes [10]; providing the spatial and temporal framework to evaluate environmental exposure and forecast potential impacts under varying operational and hydrodynamic conditions.

The reliability of these plume model predictions is, however, strongly dependent on the quality and resolution of the measured monitoring data used for calibration and validation. Accurate measurements of suspended sediment concentration (SSC) and representative particle size are particularly essential, as these parameters along with the presence of organic content directly govern aggregation and settling processes within plume models [7, 14].

In the context of deep-sea nodule collection, the dominant source of plume generation is the diffuser outlet of the collector vehicle. Measurements of SSC and particle size in this near-field region can therefore not only improve plume characterisation of the numerical model, but also enable the mass-load budget estimates of the plume source, a key input for predictive modelling and regulatory assessment.

While motivated by deep-sea mining applications, such integrated backscatter-based measurement frameworks are equally applicable to other sediment-laden flow applications, such as dredging operations and environmental monitoring in comparable fine-grained, high-organic environments.

Deep-sea sediments and their associated plume behaviour are inherently complex; however, multi-frequency acoustic sensors promise robust in-situ plume characterisation capabilities, particularly in combination with optical sensors.

1.2. Problem Statement

Monitoring of sediment plumes generated by deep-sea nodule collection activities has predominantly relied on optical backscatter sensors (OBS) and low-frequency acoustic doppler current profilers (ADCP), deployed both in the near-field on the nodule collection vehicle and in the far-field on ROVs or moored platforms [4, 5, 6, 15]. While these sensors have demonstrated the ability to detect plume presence and broad characteristics, their applicability for detailed plume quantification is limited.

Optical backscatter sensors merely provide point measurements that are prone to saturation at relatively high concentrations, whereas low-frequency ADCP measurements are primarily sensitive to larger flocculated particles and biological scatterers. In addition, both measurement techniques rely on laboratory calibration against well-defined reference sediments, which breaks validity in spatio-temporally variable plumes, such as those behind a nodule collection vehicle. These plumes are prone to continuously varying sediment composition and concentrations, and evolving plume characteristics through aggregation. Especially in deep-sea conditions do such calibration requirements become logistically impractical and introduce significant potential for measurement bias.

Multi-frequency acoustic backscatter sensors (MF-ABS) offer the capability to resolve particle size without pre-emptive calibration requirements, enabling non-intrusive in-situ range-gated measurements and, consequently, suspended sediment concentration inversion. Additionally, theory indicates that higher acoustic frequencies provide increased sensitivity to small particles such as clays and silts, and previous efforts have shown that optical sensors, when used in parallel, can aid in the interpretation of acoustic observations and may even extend the applicable measurement regime by exploiting their complementary response characteristics.

However, the performance and reliability of such multi–high-frequency acoustic approaches, particularly when applied to highly dynamic, aggregation-prone near-field mining plumes, have not yet been systematically studied, validated, or implemented. This knowledge gap currently limits the ability to accurately quantify plume source characteristics and assess environmental impacts under deep-sea nodule mining conditions.

1.3. Main Research Question

How can multi-frequency acoustic backscatter measurements be used to reliably quantify suspended sediment concentration and particle size in deep-sea nodule collection plumes, and how does their performance compare with existing optical measurement techniques?

1.3.1. Sub-Questions

The following sub-questions substantiate the main research question:

1. What sediment properties and plume characteristics are expected in deep-sea nodule collecting operations, and how do they affect acoustic measurements?
2. Which acoustic inversion approaches are available for estimating suspended sediment concentration and particle size, and what are their theoretical capabilities and limitations?
3. What is the achievable accuracy of the investigated inversion methods for inverting suspended sediment concentration for representative deep-sea sediments, and which factors govern their performance?
4. What are the practical capabilities and limitations of optical and multi-frequency acoustic sensors for monitoring suspended sediment concentration and particle size in deep-sea mining plumes?

1.4. Scope Definition

The following scope definition is merely for project proposal purposes and will not be included in the final report.

- Evaluation of multi-frequency acoustic backscatter measurements for quantifying suspended sediment concentration (SSC) and particle size in deep-sea mining diffuser plumes.
- Assessment of the uncertainties, limitations, and practical implementation considerations associated with multi-frequency acoustic monitoring of deep-sea mining plumes.
- Use of the Aqualogger 310TY and assessment of its applicability for calibration, validation, and interpretation.
- Use of gravimetric sampling, LISST and Malvern measurements, and particle size analysis as reference methods for sensor validation.
- Testing of NORI-D and an alternative deap-sea sediment samples at various concentrations

- Assessment of state-of-the-art inversion models found in research and the commercial inversion model through the Aquascat toolkit software
- Development of recommendations for sediment-load characterization and plume monitoring near the diffuser of a deep-sea nodule collector.

Items that are out-of-scope:

- Development of new acoustic scattering, attenuation, or inversion models beyond the evaluation and application of existing methodologies.
- Design and optimization of sensor mounting locations, hardware integration, or deployment systems on a commercial collector vehicle.
- Field validation under operational deep-sea mining conditions.

1.5. Thesis Outline

The thesis is composed of eight sections.

Section 1 (Introduction) introduces the background of deep-sea mining, defines the research problem, presents the research questions, and outlines the scope of the study.

Section 2 (Benthic sediment and plume properties) introduces the composition and properties of abyssal sediments and summarises the mechanisms that govern plume evolution. The aim of this chapter is to provide the physical context required to interpret sensor responses in dynamically evolving environments.

Section 3 (Suspended sediment measurement techniques) introduces the principles of optical and multi-frequency acoustic suspended sediment concentration measurements. It discusses the theoretical basis of acoustic inversion, reviews the principal inversion approaches and their limitations, and identifies the research gap addressed in this thesis.

Section 4 (Experimental Methods) describes the selected inversion methods under evaluation, the laboratory setup, instrumentation, materials, experimental programme, measurement procedures, and data-processing methodology.

Section 5 (Results and Analysis) presents and analyses the experimental and inversion results, including the validation of the experimental assumptions, the performance of the optical backscatter sensor, the acoustic inversion methods.

Section 6 (Discussion) interprets the results in relation to the underlying acoustic assumptions, experimental uncertainties, sensor limitations, and the representativeness of the laboratory experiments for deep-sea mining operations. Finally, the suitability of multi-frequency acoustic backscatter sensing for operational plume monitoring is evaluated.

Section 7 (Conclusion) summarises the main findings by answering the research questions.

Section 8 (Recommendations) provides recommendations for future research, experimental improvements, and further development towards operational deployment.

2

Deep-sea Sediment Properties and Plume Mechanisms

This chapter describes the physical properties of deep-sea sediments and the key mechanisms governing sediment plume behaviour with the aim to provide context required for interpreting optical and acoustic backscatter measurements in later chapters. It outlines sediment composition and grain-size characteristics, followed by aggregation, settling, and plume evolution under varying flow conditions.

2.1. Sediment Composition

Particulate matter found on abyssal plains consist of lithogenic materials such as carbonates, siliceous sediments (e.g. silts, clays and oozes) [16], quartz sands [17], and biogenic material produced by living organisms [11]. The top sediment layer of approximately 10 cm thickness is a semi-liquid layer dominated by the fine silicious material, and is characterised by organic enriched carbon contents, with a total organic content (TOC) of approximately 0.2-0.7 % for the NORI-D and BGR sediment samples in the CCZ [6, 7, 12, 16]. Sediments below the top layer are more heterogeneous and may contain larger fractions of sand, with multimodal distributions being more prominent [18].

The local surface mineral grain sizes vary significantly depending on the location, however clays and silts dominate the total sediment distribution. Box core samples from the GSR (Global seabed resources) license area in the CCZ recorded distribution of 28% (<10 μm), 57% (10-63 μm) and 0.01-17.5% (>63 μm) [11, 17, 19]. Whilst other samples such as the Bluefield box core samples, show bimodal distributions of only silt and clay; containing a 25^{th} and 75^{th} percentile range of 3-4 μm and 26-29 μm respectively [19]. Commonly, approximately 85% of all grains are categorized as fines <63 μm with maximum grain sizes of approximately 128 μm [12].

2.2. Aggregation and Settling Mechanisms of Sediment Plumes

Deep-sea sediment plumes are generated when seabed disturbances resuspend surface sediments and associated organic material into the water column. Once suspended, plume behaviour is governed by the balance between hydrodynamic transport, gravitational settling, and particle aggregation [7, 10]. On abyssal plains, sediments are typically dominated by fine clay-sized particles with small fractions of organic content. Fine clay particles, which are typically plate- shaped, exhibit strong surface charge controlled cohesive behaviour, which promotes aggregation through inter-particle adherence in suspension [7].

In the presence of organic material, the adherence of fine clay particles to larger organic structures leads to flocculation, forming so-called flocs; which are large, fragile, low-density, irregularly shaped aggregates composed of organic matter containing numerous smaller clay particles [19, 20, 21]. The efficiency of flocculation depends on the fraction of clay sediments and organic content, suspended sediment concentration, salinity, and hydrodynamic shear [7, 10].

Elevated salinity levels strengthens physico-chemical bonding between particles, thereby accelerating floc formation. Moderate shear enhances collision frequency and the probability of inter-particle adherence, which promotes floc growth. However, elevated turbulent shear induces violent and frequent inter-particle collisions, which in turn can reversibly break up these structures, a process referred to as floc break-up [10, 11, 22].

The presence of organic material promotes floc growth and leads to a reduction in effective density. For flocculated sediments, effective density decreases with increasing floc size as a result of their porous, fractal structure [23]. This reduction in density is accompanied by a decrease in cohesive strength, rendering larger flocs more susceptible to break-up under hydrodynamic forcing. Figures 2.1 and 2.2 visualize the varying structures of organic materials containing sediment fines.

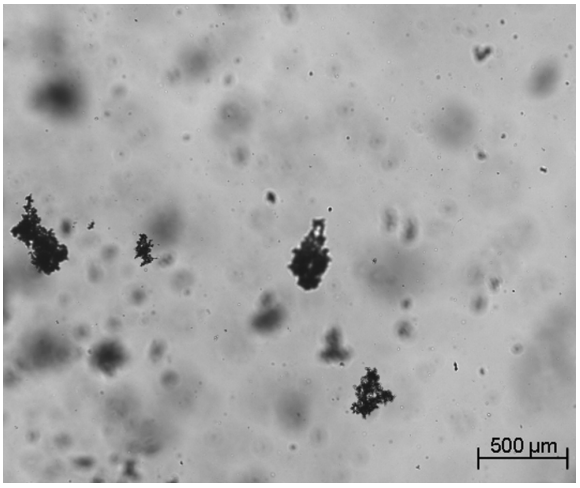

Figure 2.1: Image taken by a floc-view camera, of flocs formed by artificial clay and flocculant [23]

Figure 2.2: Image of flocs formed by illite and 0.75 $mg\,g^1$ of flocculant in saltwater [7]

The balance between flocculation and break-up governs the effective particle size development and, consequently, plume settling velocity. The settling velocity depends on particle mass and hydrodynamic drag, which in turn is controlled by the effective surface area and shape [12]. Particles with low-mass and large surface areas, such as clay particles, exhibit very low settling velocities; the aggregation of these particles into larger flocs increases the mass-to-area ratio and therefore the effective settling velocity despite their reduced density [7, 20]. As a result, flocculation plays a critical role in controlling sediment residence time (time of particle in suspension), vertical plume gradients, and far-field dispersion in deep-sea sediment plumes.

2.3. Sediment Plume Behaviour

Sediment plume behaviour depends on the conditions to which it is exposed. The shear experienced by the plume and its ability to disperse strongly influence its dynamics and characteristics. Therefore, the following two subsections describe the effects of these conditions by identifying and classifying the various behavioural phases and in-situ plume states. This provides a basis for the later assessment of suitable measurement locations and for understanding how plume behaviour can be represented in laboratory experiments.

2.3.1. Spatial Evolution of In-Situ Sediment Plumes

The plume generated behind a nodule collector vehicle is exposed to varying shear and unconfined flow conditions, which influence its behaviour. For the purpose of interpreting the relevant measurement conditions, the following chapter defines four characteristic plume states: In-diffuser flow, near-field plume, transitional plume, and far-field plume. Figure 2.3 provides a two-dimensional representation of the four plume states. However, in practice, plume development also occurs in the lateral direction.

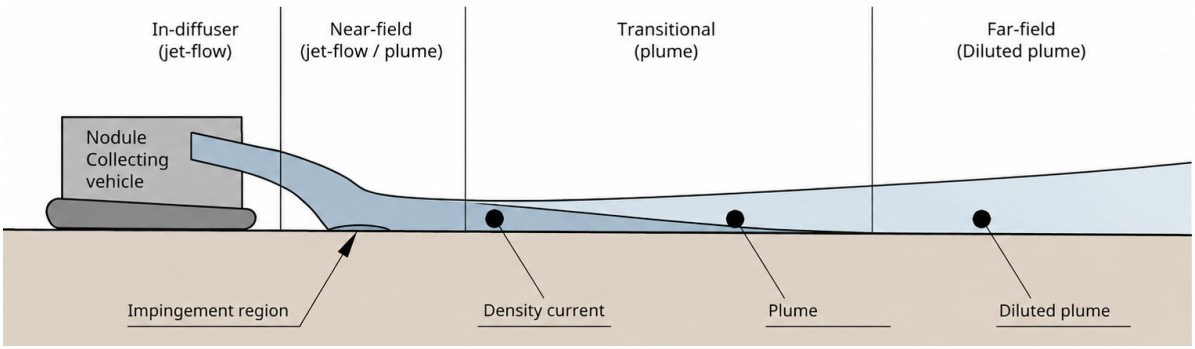

Figure 2.3: Schematic representation of the spatial development of a sediment plume behind a nodule collecting vehicle, showing the in-diffuser, near-field, transitional, and far-field plume regions.

Inside the diffuser, the suspension is dominated by high suspended particle concentrations, shear, and turbulent energy; flocculation has not yet had time to develop, and the particle size distribution can therefore be considered narrow with a large fraction consisting of primary particles. After exiting the collector diffuser the plume is defined as a near-field plume, here the plume transitions to a density current and the interaction of the suspended sediment with the seabed locally condenses the plume (impingement with seabed) increasing the concentrations and shear rates, resulting in rapid flocculation; however, settling remains limited due to elevated turbulent energy, leading to a broadening of the particle size distribution. In the transitional plume, the shear decreases allowing for rapid settling and fallout of aggregated particles. The residual finer particles and aggregates that remain in suspension are in a low energy and low concentration environment, where few particle collisions occur. Consequently, settling and aggregation rates are low, resulting in long particle residence times [10].

Modelling and experimental studies indicate that under conditions typical of nodule collection vehicles (suspended sediment concentrations of approximately 5 g L^{-1} and shear rates of 2–10 s^{-1}), up to 90% of primary particles may aggregate within the first 10 minutes [12]. Separately, under specific mixing conditions of a CCZ sediment mixture, it was found that the median particle size (D_{50}) can increase from 12 μm to 600 μm within 7 minutes, indicating a rapid aggregation process [12, 22]. At a distance of 100 m behind an exploratory (non-commercial) nodule collection vehicle (Apollo II), the suspended sediment concentration (SSC) was 5 mg/L when the vehicle was operating without nodule collection and increased to 20 mg/L during active nodule collection [11].

2.3.2. Plume Behaviour in Confined Laboratory Test Setups

In contrast to in-situ plumes, laboratory fine-sediment plume experiments are often conducted in so-called water column simulators (WCS). These setups simulate aspects of in-situ plume conditions by inducing controlled shear using impellers. However, the relatively constant shear and confined volume limit the spatial development and subsequent dilution of the plume. Under these conditions, the interplay between aggregation and disaggregation (break-up) is well defined and characterised by three distinct phases following plume release: core aggregation, export, and late aggregation [7, 19].

During the core aggregation phase, which occurs immediately after plume formation, high particle concentrations and frequent collisions lead to rapid floc growth and substantial early settling (relatable to in-diffuser and near-field plumes). This is followed by the export phase, during which the largest aggregates formed during core aggregation settle out of the water column (Fallout), resulting in a rapid decrease in suspended sediment concentration and mean particle size (relatable to near-field and transitional plume states). The final late aggregation phase describes the evolution of a diluted plume, in which aggregation continues at low concentrations and at a reduced rate, governed by the scavenging of fine particles by remaining aggregates (Far-field plumes).

Additionally, floc sizes tend to stay at equilibrium with the smallest high-energy eddy [23], and the rate of floc growth and resulting floc size are controlled by sediment concentration and shear rate [24]. This behavioural trend is illustrated in Figure 2.4a.

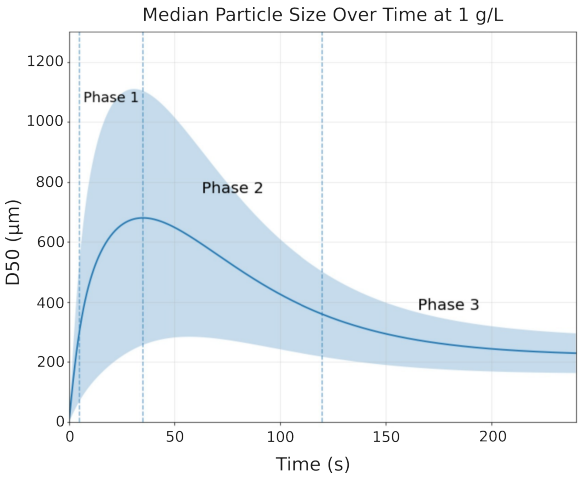

(a) An adaptation of the median particle diameter evolution (considering flocs as particles) over time for a plume at a concentration of 1 $g\,l^{-1}$ and a shear rate of 0.1 s^{-1} [19].

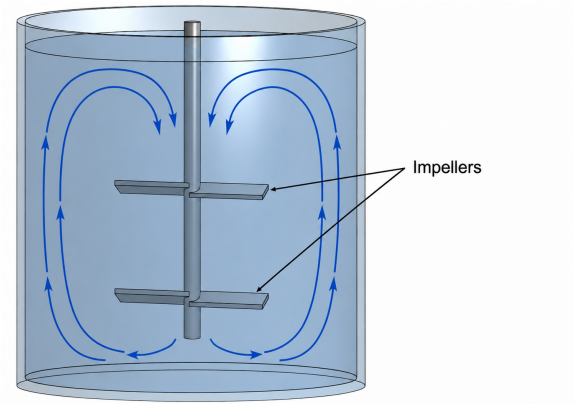

(b) (b) Schematic representation of the recirculating flow generated by the impellers in a water column simulator.

Summary

In-situ plumes are subject to shear and dilution through dispersion, which determine the velocity at which the plume aggregates or disaggregates, and subsequently the settling velocity. This interplay creates definable plume states behind a mining vehicle, namely: In-diffuser flow, near-field plume, transitional plume, and far-field plume. In fine-sediment plume laboratory experiments, aggregation and disaggregation processes are commonly simulated using a water column simulator. However, even under controlled conditions, the plume remains in continuous development as particles aggregate and disaggregate, making it difficult to maintain a consistent floc size. This temporal variability is particularly relevant to the sensor validation discussed in the following sections, as the particle properties influencing sensor response continuously change throughout the experiment.

3

Suspended Sediment Measurement Techniques

This chapter outlines measurements methods for characterizing suspended plumes. Beginning by introducing current state of the art and the operating principle of backscatter sensors, then presents the core theory, calibration requirements, and key limitations of optical and multi-frequency acoustic approaches. Finally, it synthesizes the identified gaps and positions this thesis, motivating the potential value of combining optical and multi-frequency acoustic measurements.

3.1. State of the Art in Suspended Sediment Monitoring

In laboratory environments, techniques such as manual gravimetric analysis, laser in-situ scattering and transmissometry (LISST), high-speed imaging, and laser diffraction can provide particle and suspension characterisation. However, these approaches are often impractical or unreliable for in-situ field applications [25]: Sampling is labour intensive and cumbersome, specially in deep-sea environments; imaging and transmissometry methods are limited to suspended sediment concentrations below approximately 0.75 g/L; and their physical dimensions are often impractical for in-situ measurements.

Therefore, in-situ field monitoring predominantly make use of optical and acoustic backscatter techniques, that have proven to be robust and cost effective [26]. In estuaries, embayments and rivers, dredging companies and marine researchers commonly deploy optical backscatter sensors (OBS), acoustic Doppler current profilers (ADCP), and high frequency acoustic backscatter sensors; where relatively coarse sediments such as sand result in robust inversion performance [27]. Optical sensors offer turbidity point measurements which can be related to suspended sediment concentrations. Acoustic systems offer an advantageous capability to profile non-intrusively, with high spatial and temporal resolution [28, 29].

In deep-sea nodule collecting trials, OBS sensors have been used to measure plume discharge concentrations near the diffuser, while horizontally oriented ADCPs have been deployed to estimate far-field plume height and extent behind the collector vehicle [8]. Both approaches, however, exhibit important limitations. OBS sensors provide only intrusive point measurements, resulting in limited spatial information and reduced capability to resolve for sediment loads; In addition, they are prone to signal saturation at high concentrations [8, 19]. ADCPs, while offering non-intrusive spatial profiling capability, typically operate at a single low frequency, making them predominantly sensitive to larger particles over relatively large sampling volumes with limited resolution. Furthermore, both sensor types require frequent calibration and exhibit strong sensitivity to changes in particle size distribution and composition.

3.2. General Principles of Backscatter-Based Measurements

Backscatter sensors operate in a monostatic/co-located configuration, where the same device emits and receives a signal [30]. Acoustic devices ensonify the medium by emitting and receiving high-

frequency pressure waves through a single piston transducer [30]; and optical devices illuminate the medium with near infra-red light laser diodes and receive signals through photodiodes. In both cases the transmitted wave propagates though the medium, and when the suspended particles are present, light or pressure waves are scattered to the surrounding environment in multiple directions, and a fraction of this energy is backscattered to the sensor. The magnitude of backscattered energy is a single parameter measurement expressed in an electrical output (e.g., voltage), proportional to the backscattered energy. The intensity of the signal depends on the simultaneous physical backscattering and attenuation effects from the suspended particulate matter and the medium. Acoustics additionally suffer from attenuation from geometric spreading effects. These effects are described optics and acoustics in sections 3.3 and 3.4 respectively.

3.3. Optical Backscatter Theory

This section presents the theoretical framework for optical backscatter–based SSC measurements. The governing attenuation and scattering processes are described, followed by the mathematical formulation of the received signal and an assessment of the dominant sediment properties controlling optical attenuation (absorption) and backscattering (e.g. particle size, shape, and refractive index) are discussed. Finally, the commonly applied empirical calibration models used to convert turbidity measurements into SSC are discussed.

3.3.1. Scattering and Attenuation

Optical waves are subject to attenuation which influences the intensity of light backscattered to the sensor and therefore its performance. Attenuation arises from both absorption by the fluid medium and the suspended particles, as well as particle-induced scattering losses. Absorption by the fluid primarily converts optical energy into heat, while particle absorption is governed by near-infrared reflectivity and particle composition. Particle-induced scattering further contributes to attenuation losses, by deflecting photons outside the photodiode acceptance angle, reducing the amount of light captured by the sensor. This mechanism is commonly referred to as out-of-beam loss [26]. Scattering by the clear water is typically negligible and particle-induced scattering dominates the attenuation process.

Mathematically, the various influencing factors that of OBS-signal response can be described by the following formula [31]:

$$F = \frac{3}{2}\frac{VCEQ_b}{\rho D} \tag{3.1}$$

It states that the radiant optical flux from a suspension, F (W), is proportional to the illuminated volume, V (cm^3), the mass concentration of suspended particles, C ($kg\,cm^{-3}$), irradiance, E ($W\,cm^{-2}$), the scattering efficiency, Q_b (-), the inverse of the particle diameter, D (cm), and particle density, ρ ($kg\,cm^{-3}$).

Physically, it defines that the optical backscatter signal is governed by the amount of light scattered back to towards the detector by the particles. The received signal increases with increasing SSC, illuminated volume, and scattering efficiency, while decreases with increasing particle diameter, for a fixed mass concentration.

3.3.2. Controls on Optical Backscatter Signal

The particle mass concentration and particle size are the two dominant factors on optical backscatter response, with associated error magnitudes of O(1000) and O(100), respectively [26]. The scattering efficiency and irradiance are influenced by factors such as particle shape (O(10)), surface roughness, colour, and therefore near-infrared (NIR) reflectivity (O(10)) [32]; as well as suspension composition and flocculation or aggregation effects (O(2)) [26, 33]. The scanning rate, water colour, and ambient light conditions do not play a significant role [33].

Plate-shaped sediments, such as clays, exhibit an elevated ratio of cross-sectional area to volume and therefore display increased reflective efficiency relative to spherical particles [26]. At a 140° scattering angle, such particles scatter approximately 8 times more light. The chemical composition (e.g. salinity) and presence of organic material can further influence the reflective efficiency indirectly, as they promote flocculation processes. As flocs grow, smaller optically efficient primary particles become incorporated into larger, low-density structures, reducing the total cross-sectional area of particles per

unit area and thus the overall reflective efficiency [21, 26, 34]. A previous study found that, for cohesive sediment under equal mass concentration, high- turbulence conditions resulted in 100% increase in backscatter signal relative to low turbulence flows, a behaviour attributed primarily to aggregation and break-up effects [35].

Under natural environmental conditions, plankton may be present and can interfere with calibration relationships derived under controlled laboratory conditions [26, 36]. Plankton generally increases the OBS response relative to suspensions with comparable concentrations of minerogenic particles and therefore over estimates the suspended sediment concentrations. Micro-bubbles however, have shown to have a negligible effect on reflective efficiency for wavelengths between 550 and 1000 nm, [26]; only a small, positive (not quantified) offset was observed in surf-zone measurements (coastal break waters) [36].

3.3.3. Optical Calibration and Regression Model

Optical backscatter sensors measure water turbidity (Tu), which is a relative measure of cloudiness of the water column. Standardized units set by the ISO and EPA include FTU or NTU (Formazin Turbidity Unit and Nepheloid Turbidity Units) [21]. The measure of suspended sediment concentration are commonly obtained through regression-based relationships, which are developed through calibration with reference samples of known concentrations. This method is robust, however it is only valid as long as the sediment properties do not change relative to the calibration conditions. The calibration relationship between Tu and SSC can vary between sensors and across concentration ranges. Previous studies have shown that the Aqualogger 310TY exhibits a monotonically increasing relationship between Tu and SSC up to approximately 40 gL^{-1} for fine sediments of 18.0 % clay , 81.5 % silt, and 0.5 % sand [19, 31, 37], indicating strong potential for high-concentration measurements. For this reason, the response of this sensor is included in this thesis.

At low to moderate concentrations a linear regression model provides a strong fit between optical backscatter response and suspended sediment concentration and therefore OBS sensors are often used in this region. The linear regression fit can be written in the form of:

$$SSC = m * turbidity + C \tag{3.2}$$

Where the slope, m, is mainly a function of the particle size and concentration, and C, is the y-intercept value, representing the clear water sensor signal in the absence of suspended sediment [11, 38].

The region where this fit is valid depends on each sensor. A previous study has shown that the response of the previously mentioned sensor to natural fine sediments (18.0 % clay , 81.5 % silt, and 0.5 % sand) follows an approximately linear increasing trend up to about 4.88 gL^{-1} and for moderate concentrations, the response transitions from a linear to a logarithmically fit, as illustrated by the laboratory calibration of the Aqualogger 310TY shown in Figure 3.1. The exact logarithmic equation can be found in Wang et al. 2020 [37]. At sufficiently high concentrations, beyond the calibrated operating range, grain shielding leads to signal saturation and a reduction in sensor response, as schematically illustrated in Figure 3.2.

The decrease in sensitivity arises from grain shielding, whereby an increasing fraction of effective scattering particles becomes obscured from illumination, leading to an underestimation of SSC. This effect is further intensified in natural sediments due to broad particle size distributions and the presence of weakly reflective particles [21, 36, 39, 40].

The signal experiences saturation in regions (B) and (C) in Figure 3.2. In region (b), the increased concentration reduces the sensitivity such that the sensor response reaches an inflection point and begins to decrease. This introduces ambiguity, as a given signal level may simultaneously correspond to two different sediment concentrations. The sensor sensitivity can be adjusted by changing the gain which increases sensitivity to small variations but shifts the inflection point to lower concentrations [39]. Newer sensors can make use of auto-adjust gain features to increase their sensitivity range.

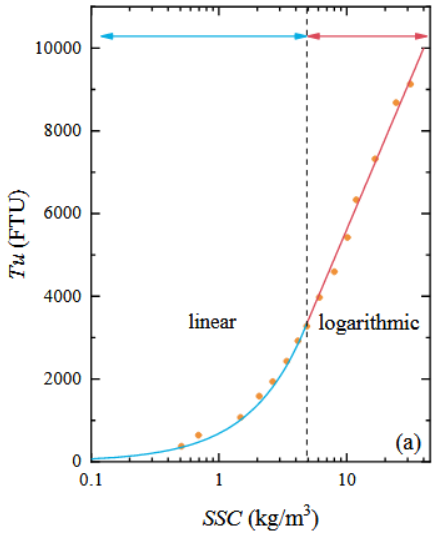

Figure 3.1: Example of a laboratory calibration of the AQUAlogger 310TY mounted on a tripod, showing the response of FTU to SSC for laboratory samples at 0.1 m above seabed for sediment composed out of 18.0 % clay , 81.5 % silt, and 0.5 % sand [37]. Calibration is sensor and sediment specific.

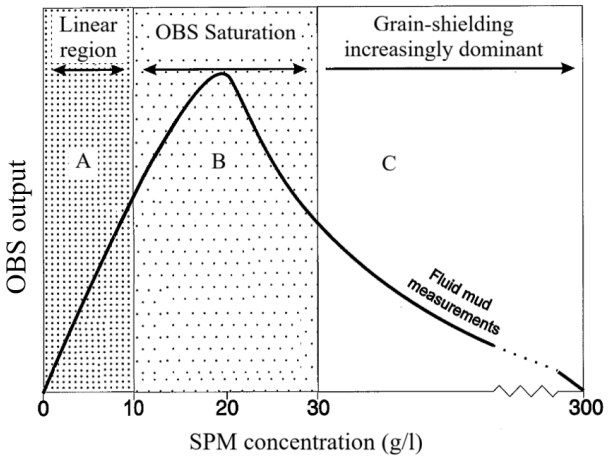

Figure 3.2: OBS sensitivity trend showing three characteristic response regions: (A) linear (B) inflection due to saturation, and (C) signal reduction by dominant grain-shielding effects. SPM (suspended particculate matter) ranges are sediment and sensor specific, and were measured with nephelometer. Adapted from [39] Bunt et al., 1999 [36].

3.3.4. Sensitivity Regime

The applicability of optics to specific sediments is described by the Mie scattering theory, which states that the sensitivity of optical response to sediment is governed by the relation between particle size and wavelength [41]. The theory predicts that signal intensity decreases approximately inversely to particle size [26]. Data from three independent studies are shown in Figure 3.3, illustrating the particle-size sensitivity trend.

With optical sensors operating at wavelengths on the order of nanometres, this implies highest sensitivity to particle sizes in the clay to silt range. This concept overlaps with the acoustic scattering regimes described in Section 3.4.4.

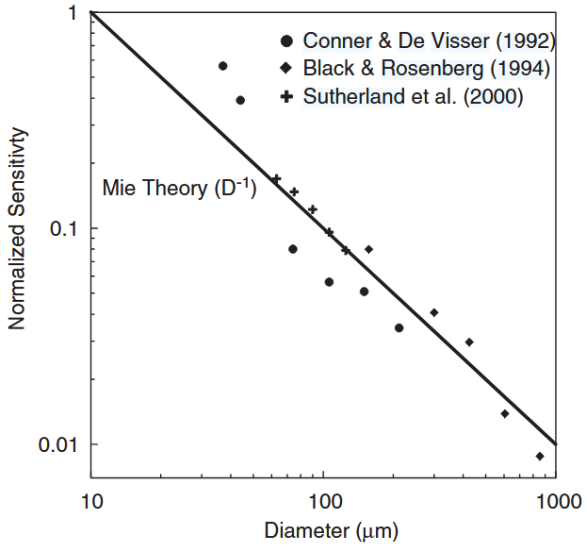

Figure 3.3: Composite dataset from three independent studies showing normalized OBS sensitivity, with fixed SSC, as a function of particle diameter D, with the corresponding decreasing trend predicted by Mie scattering theory [26].

3.4. Acoustic Backscatter Theory

This Section serves to describe the methodology of obtaining suspended sediment concentrations (SSC) from raw acoustic backscatter measurements. It begins with the underlying physical principles of acoustic scattering and attenuation and followed by the mathematical forward formulation of the sensor response. The section then presents the inversion of this formulation and the associated practical considerations required to estimate sediment concentration from measured backscatter signals; referred to as the Inversion problem.

3.4.1. Scattering, Attenuation and Geometric Spreading

As described in Section 3.2, the emitted pressure waves are subject to attenuation, scattering, and additionally to geometric spreading mechanisms.

Geometric Spreading

Geometric spreading arises from the approximately spherical expansion of the acoustic wavefront emitted by the transducer, which causes the acoustic energy to be distributed over an increasingly larger surface area as it develops with range. As a result, the intensity of the received signal decreases with distance from the source. Near the transducer, this behaviour becomes more complex, and therefore a distinction is commonly made between the near-field and far-field region. The distance from the transducer at which this transition between these two regions occur is defined by $r_n = \pi a_t^2 \, \lambda^{-1}$, where, a_t, is the radius of the transceiver, and λ, is the acoustic wavelength [29].

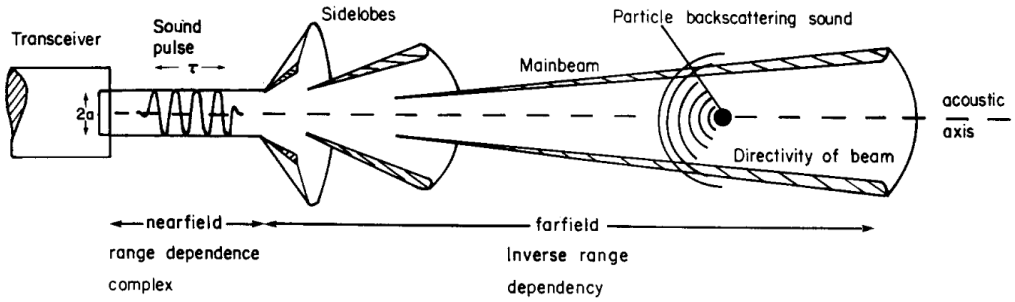

Figure 3.4: A schematic presentation of an acoustic beam emitted by a transducer; Indicating its range dependencies (Near-field, side-lobes, far-field). [29]

Attenuation and Scattering Mechanisms

The attenuation of acoustic waves in a suspension results from both the water medium and the presence of suspended particles. Water induced attenuation (often also denoted as absorption), is primarily governed by viscous and thermal losses and depends on temperature, salinity, and pressure [42], which together determine the speed of sound in the medium. Water induced attenuation exhibits a strong linear frequency dependence, with low frequencies experiencing significantly less attenuation (i.e., a smaller negative slope of signal amplitude with range) than high frequencies. Consequently, for propagation through clear water, the two-way backscatter amplitude within 1 m can be reduced by more than 99% when the operating frequency is increased from 1 MHz to 10 MHz [29].

Particle-induced attenuation arises from a combination of viscous losses and scattering losses due to redirection of acoustic energy, described as α_{ss} and α_{sv} [43]. In suspensions composed of fine plate-like particles (clay and fine silts), viscous attenuation dominates, whereas for coarser sand-sized particles, scattering becomes the primary attenuation mechanism [30, 44]. For a frequency of 1.5 MHz the viscous to scattering transition occurs at a particle size of approximately 100 μm [45]. This distinction arises from two main factors: the relation between particle size and acoustic wavelength (further discussed in section 3.4.4), and the enhanced viscous shear associated with plate-shaped particles. The plate-like morphology of clay particles is characterised by low mass and a large surface area, which, when oscillating relative to the surrounding fluid, increases acoustic energy dissipation through viscous shear (heat) [23].

3.4.2. The Forward Formulation

The forward formulation describes what the theoretical amplitude of backscatter echo response would be if a known suspended sediment exists in suspension. It is commonly expressed by the root-mean-square voltage V_{rms}, as presented in equation 3.3 [42]. This formulation represents a reduced form of the classical sonar equation and is valid under the assumptions of incoherent scattering and negligible multiple scattering (MSCAT, no SSC threshold established in literature at which this assumption is no longer valid); assumptions are commonly adopted for low to moderate suspended sediment concentrations (approximately 0.5 - 18 g/L) [28, 30, 42, 46, 47, 48]. For elevated concentrations, exponential

attenuation terms dominate and the relation of V_{rms}, and concentration M becomes non-linear, causing the linear assumption to break down [29].

$$V_{\text{rms}} = \frac{k_t k_s M^{1/2}}{r\psi} e^{-2r(\alpha_w + \alpha_s)}, [Volts] \tag{3.3}$$

Equation 3.3 demonstrates that the measured backscattered signal, V_{rms} at range, r, depends explicitly on the system calibration constant, k_t ($V\, m^{3/2}$), the sediment backscattering parameter, k_s ($m\, kg^{-1/2}$), the near-field correction term, ψ, the particle-induced attenuation coefficient, α_s (m^{-1}), and the water induced attenuation, α_w (m^{-1}), of which the latter is dependent on temperature, salinity and pressure, and can be taken from literature formulae [49, 50, 51]. The near-field correction term, ψ, accounts for the complex geometric spreading in the near field, as described in Section 3.4.1. It is defined by Equation **??**, where $\psi = [2 + (\varepsilon r_n / r)]\,/3$ for the near field, and $\psi = 1$ for the far field.

The system calibration constant k_t characterises the instrument response and is independent of sediment properties. It accounts for the transducer sensitivity, electronic gain, and transducer beam pattern characteristics, and is therefore specific to each instrument. Its value is required to be obtained prior to measurements through a calibration procedure and is typically expressed as:

$$k_t = RT_v P_0 r_0 \left\{ \frac{3\pi c}{16} \right\}^{1/2} \frac{0.96}{k a_t} \tag{3.4}$$

Where, R is the transducer receive sensitivity, T_v, is the voltage transfer function, P_0, is the pressure reference level normally defined at $r_0 = 1\, m$, and, c is the speed of sound in the fluid medium [28, 42]. Its value may be obtained through a fully electro- acoustic calibration procedure, in which the individual parameters of Equation 3.4 are determined independently.

3.4.3. The Inversion Problem

While the Forward formulation (equation 3.3) describes the prediction of the acoustic response from known suspension properties, the primary objective of acoustic backscatter measurements is to infer the suspended sediment concentration (SSC), mathematically represented as M ($g\, L^{-1}$), from the measured backscatter signal V_{rms}, which defines the inversion problem.

Therefore, by rearranging Equation 3.3, the suspended sediment concentration can be expressed as:

$$M = \left(\frac{V_{\text{rms}}\, r\psi}{k_t k_s} \right)^2 e^{4r(\alpha_w + \alpha_s)} \tag{3.5}$$

Equation 3.5 demonstrates that the concentration, M, depends on the measured backscattered signal V_{rms}, the sediment-induced attenuation coefficient α_s, and the sediment backscattering coefficient k_s. The attenuation terms α_w and α_s influence the received signal exponentially and therefore strongly affect measurement sensitivity with increasing range and concentration [30]. As both k_s and α_s are determined by the characteristics of the suspended sediment, they form the fundamental sediment-dependent components of the inversion model and are discussed in the following sections.

The sediment scattering efficiency per unit mass is described by the coefficient k_s:

$$k_s = \frac{f}{\sqrt{\rho_s\, a_s}} \tag{3.6}$$

where ρ_s is the particle density, a_s is a representative particle radius, f is the dimensionless backscatter form function; whereas the energy loss due to sediment-induced attenuation is described by the attenuation coefficient α_s:

$$\alpha_s(r) = \frac{1}{r} \int_0^r \left(\frac{3\, \chi(r)\, M(r)}{4\, \rho_s\, a_s(r)} \right) \mathrm{d}r \tag{3.7}$$

which can be simplified under the assumption that the particle properties within the suspension remain homogeneous along the acoustic path [30]:

$$\alpha_s = \alpha_{sv} + \alpha_{ss} = \frac{3M}{4\rho_s a_s} \left(\chi_{sv} + \chi_{ss} \right) \tag{3.8}$$

where χ is the normalized total scattering cross-section which represents the combined scattering (χ_{ss}) and viscous attenuation (χ_{sv}) effects of the suspended sediment [47].

Although Equations 3.6 and 3.8 are expressed using a representative particle radius a_s, natural sediments consist of a distribution of particle sizes. Consequently, both the backscattering coefficient k_s and attenuation coefficient α_s are generally evaluated over the full particle size distribution $n(a)$ rather than for a single particle size. The assumed particle size distribution therefore forms an important component of the inversion.

Most inversion methods assume a log-normal particle size distribution (PSD), which is parametrized by a median particle size a_0 and distribution width σ (or the relative standard deviation, Rel. SD, a sorting value similar to that of Folk and Ward [52]. However, as natural fine sediments commonly contain multiple particle populations, more recent inversion approaches have adopted bimodal PSD formulations.

Log-normal Distribution

$$n_v(a) = \frac{1}{a\sigma\sqrt{2\pi}} \exp\left(-\frac{(\ln(a)-\mu)^2}{2\sigma^2}\right) \tag{3.9}$$

Bimodal Log-normal Distribution

$$\begin{aligned} n_v(a) = w_1 \frac{1}{a\sigma_1\sqrt{2\pi}} \exp\left(-\frac{(\ln(a)-\mu_1)^2}{2\sigma_1^2}\right) \\ + (1-w_2)\frac{1}{a\sigma_2\sqrt{2\pi}} \exp\left(-\frac{(\ln(a)-\mu_2)^2}{2\sigma_2^2}\right) \end{aligned} \tag{3.10}$$

$$\mu_1 = \ln(a_1), \qquad \mu_2 = \ln(a_2), \qquad 0 \leq w_1 \leq 1, \qquad 0 \leq w_2 \leq 1$$

The inversion furthermore depends on the formulation of the form function f and scattering cross-section χ, which describe the scattering and attenuation behaviour of suspended particles. These functions are obtained analytically for idealized spherical particles; however, for natural sediments they are typically represented through heuristic approximations derived from experimental observations, as scattering characteristics are sediment-specific.

A variety of scattering and attenuation models have therefore been proposed, including spherical particle models [53], mica-based formulations [42, 47, 48], multi-class particle size distribution models [48], oblate spheroidal particle models [54], and floc models [23, 55, 56]. Each model reflects different assumptions regarding particle shape, particle structure, and particle size distribution, and therefore exhibits varying applicability to natural marine sediments.

3.4.4. Single and Multiple Frequency Inversion, and their Limitations

The suspended sediment inversion can be performed with information from a single frequency which requires prescribed knowledge of the representative particle size a_s, and the particle size distribution width. The use of multiple frequencies has the additional capability to estimate the representative particle size a_s when the acoustic frequencies operate in an appropriate scattering regime.

The form function f, is an important concept here, as it describes how the scattering characteristics of a particle vary as a function of its geometric size relative to the acoustic wavelength (frequency) [42, 48], thereby, determining when particle size inversion through multi-frequency acoustics is possible and indicates which frequencies should be used for a given particle size range.

The scattering response behaviour of a particle is the result of reflection, diffraction, and transmission processes. The relative importance of these mechanisms depend on the ratio between the wavelength and particle size, which is captured by the form function, f; and is commonly expressed as a function of the dimensionless size parameter ka_s, where, $k = \frac{2\pi}{\lambda}$ [42, 48], is the acoustic wave number, and a_s, is the particle radius. The acoustic wavelength is given by $\lambda = \frac{c}{F}$, where, c, is the speed of sound in the fluid medium, and F, the acoustic frequency.

Based on this relationship, the scattering behaviour of particles are classified into the following regimes [50, 57, 58]:

$$\text{Scattering regime} = \begin{cases} \text{Rayleigh}, & ka \ll 1 \\ \text{Peak}, & ka \approx 1 \\ \text{Transitional}, & 1 < ka < 2 \sim 10 \\ \text{Geometric}, & ka \gg 2 \sim 10 \end{cases} \tag{3.11}$$

In the Rayleigh regime, the acoustic wavelength λ, is much larger than the particle radius a_s, and the response is defined by a monotonically increasing function with an approximate ka^2 dependence. When the acoustic wavelength and particle size become approximately equal, the backscatter intensity reaches its maximum [40, 59]. The transitional regime is characterised by the interference of diffracted and reflected waves, which results in a periodically varying response with distinct peaks and troughs. In the geometric regime, the wavelength λ is much smaller than the particle radius a_s, and the sound waves are now reflected by the particle surface rather than the volume and the strength is no longer dependent on the particle size nor frequency. The backscatter signal in this regime flattens to a asymptote. The boundary between the transitional and geometric regime varies depending on the suspended sediment characteristics. It commonly lies within $2 < ka < 10$ [60].

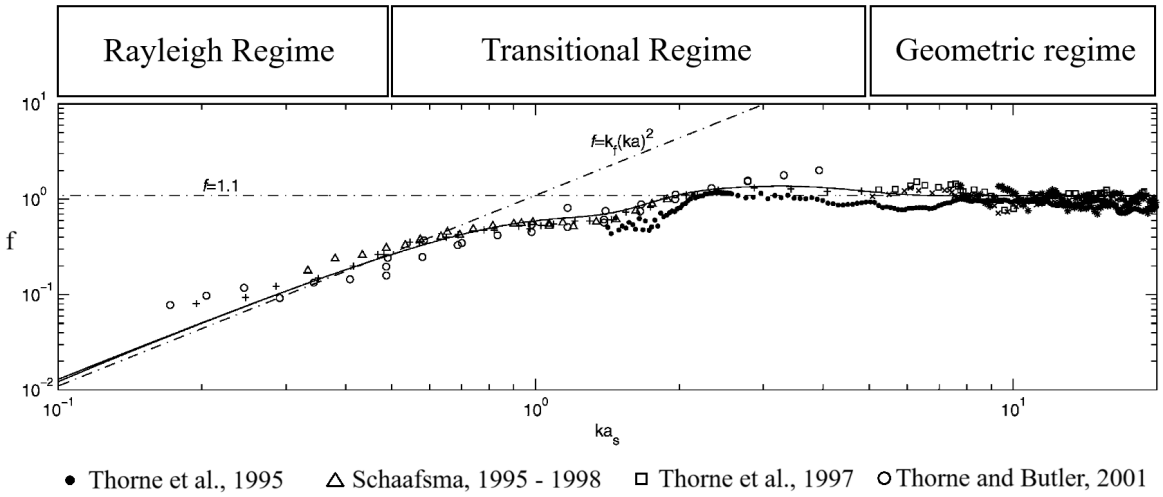

Figure 3.5: Dependence of the form function on the dimensionless size parameter ka_s for quartz sands of multiple experimental studies. The vertical dashed lines delimit the Rayleigh, transitional and Geometric regimes [42]

Frequencies operating in the Rayleigh regime ($ka \ll 1$) scale identically with particle size through the ka^2 dependence; consequently, when all frequencies lie within this regime, no unique size information can be obtained from their relative responses. However, when one or more frequencies lie within the transitional regime, the frequency-dependent scattering behaviour of the suspended sediment provides unique information that can be exploited to estimate the mean particle size a_s. This is achieved by evaluating the ratio of the form functions between frequencies. Since the form function is uniquely related to particle size through the size parameter ka_s, the corresponding particle radius can be determined by matching the measured form function ratio, obtained from Equation 3.12, to the theoretical response curve [61].

$$\frac{\langle f_i \rangle}{\langle f_j \rangle} = \frac{\left(\dfrac{\psi_i V_{\text{average},i}}{k_{t,i}} \right)}{\left(\dfrac{\psi_j V_{\text{average},j}}{k_{t,j}} \right)} e^{2r(\alpha_i - \alpha_j)} \tag{3.12}$$

The form-function ratio method represents one of the earliest multi-frequency inversion approaches. More recently, multi-frequency inversion is performed through a minimisation function, commonly referred to as the objective function. Rather than directly evaluating form-function ratios, the objective

function seeks the theoretical solution that provides the best agreement between the concentration estimates obtained from all frequencies.

Objective functions may be based on backscatter-derived concentrations, attenuation-derived concentrations, or a combination of both, and typically employ variance-based, absolute-difference, or weighted least-squares metrics (Φ, Γ, E) [30, 44, 48, 61].

The exact response for idealized spherical particles was defined [50], and a simplified model indicates a lower detection limit at $ka = 0.05$ [40, 59]. However, the exact response varies significantly for natural sediments and heuristic approximate formulations have therefore been developed for irregular shaped scatterers such as quartz sediments, based on data from various experimental studies. The general backscatter response per unit volume for quartz is illustrated in Figure 3.5.

Obtaining an approximate fit for cohesive fine sediments, such as Figure 3.5 does for quartz, is challenging, as sieving the material into discrete size fractions does not yield a particle size distribution that is representative of sediment behaviour in suspension.

However, under the assumption that cohesive deep-sea sediments can be approximated as idealised spherical particles, and that commonly used high-frequency ABS sensors operate predominantly within the Rayleigh and transitional scattering regimes, the lower detection limits and peak sensitivities can be estimated and are summarized in Table 3.1. Note that in reality, fine sediments are not ideal spheres and the particle radii values to which the frequencies are sensitive are expected to be higher.

Frequency [MHz]	**Lower limit** [μm]	**Peak sensitivity** [μm]
1	23.9	477.0
2	11.9	238.0
4	5.9	119.0
5	4.8	95.5

Table 3.1: Estimated particle diameters corresponding to the lower detection limit and peak sensitivity within the Rayleigh scattering regime for commonly used acoustic frequencies.

The five frequencies shown are among the highest commercially available acoustic frequencies. The highest frequency of 5 MHz has a theoretical lower detection limit of 4.8 μm, which in reality is expected to be higher, as fine sediments are more plate-like and therefore exhibit increased attenuation and poorer backscattering characteristics due to their lower mass. Deep-sea sediments typically contain a large fraction of particles below this limit, highlighting the challenges associated with acoustically measuring these sediments.

3.5. Acoustic Inversion Approaches

The acoustic inversion methods can be broadly divided into two approaches: an (implicit) bin-based inversion and an (explicit) profile-averaged inversion. The distinction lies in the underlying assumptions, solution procedure, spatial resolution, and computational stability.

The implicit bin-based approach is based on the assumption that the suspension that the measured suspension is homogeneous with a constant particle size within each individual range bin, allowing gradients within the suspension to be resolved. In contrast, the profile-averaged inversion requires the measured range to be approximately homogeneous and estimates a single representative particle size and SSC for the entire analysed range. These two approaches are described in more detail in the following sections.

3.5.1. Implicit Bin-based Inversion

The inversion problem, defined by Equation 3.5, is implicit, as the suspended sediment concentration M appears on both sides of the formulation through the sediment-induced attenuation coefficient α_s (Equation 3.8). Consequently, the concentration M cannot be solved directly when sediment attenuation is significant, which is often the case for fine-sediment suspensions. An iterative solution procedure

is therefore required.

In this approach, an initial concentration estimate M_0 is obtained by initially neglecting particle-induced attenuation ($\alpha_s = 0$) [62]:

$$M_0 = \left(\frac{V_{\text{rms}}\, r}{k_t k_s} \right)^2 e^{4r\alpha_w} \tag{3.13}$$

This estimate is subsequently used to evaluate

$$\alpha_{s,0} = \frac{3M_0}{4\rho_s a_s} \left(\chi_{sv} + \chi_{ss} \right) \tag{3.14}$$

after which an updated concentration estimate is computed according to

$$M_{n+1} = M_n e^{4r\alpha_{s,n}} \tag{3.15}$$

where $\alpha_{s,n}$ is the attenuation coefficient calculated from the previous concentration estimate. The procedure is repeated until two successive concentration estimates satisfy

$$|M_{n+1} - M_n| < \varepsilon \tag{3.16}$$

where ε is a prescribed convergence criterion [61].

The method exploits the fact that attenuation at short ranges is initially small and therefore provides a suitable starting estimate. Once convergence is achieved, the resulting concentration is considered self-consistent with the attenuation induced by the suspension.

The principal advantage of the iterative approach is that concentration profiles can be resolved at individual range bins throughout the acoustic range. However, this method can become unstable, as the strong exponential dependence on α_s can lead to large corrective updates between iterations when concentrations are elevated. This introduces a positive feedback mechanism, which may result in numerical instability and divergence of the solution.

3.5.2. Explicit Profile-Averaged Inversion

An alternative inversion approach assumes that the suspension remains approximately homogeneous in both concentration and particle size over the full measured profile. Under this assumption, the acoustic properties are considered constant along the measurement range, allowing the complete profile to be used to estimate a single particle size and concentration rather than determining these quantities for each individual range bin.

Applying the natural logarithm to Equation 3.3 yields the Fluid Corrected Backscatter (FCB):

$$FCB(r) = \ln(V_{\text{rms}}) + \ln(r) + 2\alpha_w r = \ln(k_t \sqrt{s_v}) - 2\alpha_s r \tag{3.17}$$

$$s_v = k_s^2 M \tag{3.18}$$

Where, parameter s_v is the volume backscattering coefficient and combines the sediment concentration and scattering properties into a single term. Under the assumption of homogeneity, all terms except α_s are constant, making the FCB expression linear with range, and the sediment attenuation coefficient (α_s) can therefore be obtained from the slope of a linear fit to the FCB profile:

$$FCB(r) = -2\alpha_s r + \ln(k_t \sqrt{s_v}) \tag{3.19}$$

which is equivalent to

$$y = Ax + B \tag{3.20}$$

A linear regression therefore provides a direct estimate of the sediment attenuation coefficient from the slope,

$$\alpha_s = -\frac{A}{2} \tag{3.21}$$

after which the volume backscattering coefficient s_v can be computed using the estimated α_s:

$$s_v = \frac{3}{16\pi} \frac{V_{\text{rms}}^2 r^2}{k_t^2} e^{4r(\alpha_s + \alpha_w)} \tag{3.22}$$

The measured pair (α_s, s_v) can subsequently be compared with theoretical values predicted by sediment scattering and attenuation models through an error minimization algorithm (the objective function as described in Section 3.4.4). The objective function determines the solution with the least error relative to theory, or in other words, the most probable values of M, D_{50}, and, in some cases, σ.

The objective function may be formulated using only the attenuation coefficient, α_s, commonly denoted as Γ or Φ, or as a weighted combination of the attenuation coefficient, α_s, and the backscattering coefficient, s_v, denoted as E. The difference between the Γ and Φ objective functions is that the Γ function minimizes the sum of the absolute residuals (which is the maximum likelihood estimate under the assumption of normally distributed measurements), whereas the Φ function minimizes the sum of the squared residuals (least-squares method). Consequently, the Γ function is less sensitive to outliers, as large residuals receive the same linear weighting as small residuals, whereas the Φ function penalizes large residuals more heavily due to the squaring operation. From previous studies, the E-function is suggested as a potential improved method by providing an additional constraint (s_v) in the solution space [30].

Unlike the iterative inversion approach, this method determines a representative α_s from the slope of the complete FCB profile, thereby sacrificing spatial resolution in exchange for increased robustness and reduced sensitivity to inversion divergence.

3.5.3. Controls on Acoustic Backscatter Response

In addition to backscattering from primary sediment particles, four additional sources may contribute to measured acoustic backscatter: flocs, air micro-bubbles, micro-organisms, and turbulence-induced microstructures [63]. The contribution of turbulence is commonly considered negligible, only found to affect measurements in strong currents exceeding $> 1\,ms^{-1}$ [21]. Air micro-bubbles, usually found in near surface measurements, such as surf-zones and laboratory settings, can increase backscatter intensity predominantly for high frequency measurements [63]. Micro-organisms, such as zooplankton and nekton, although generally insignificant by mass, have been shown to produce a relatively strong gain at low frequencies [15]. In deep-sea measurements, bubbles are not expected to form by the high pressures, turbulence is relatively low, and plankton is generally absent. The environment therefore presents itself as an idealised setting for ABS measurements.

Flocculation, however, represents a particularly important source of variability in deep-sea fine sediment plumes. Although effective floc density initially decreases with increasing floc size, acoustic backscatter intensity has been observed to increase with the degree of flocculation, and even more so with more mature flocs which can become denser. This occurs because backscatter strength is primarily governed by effective scatterer size and structure, which increases their acoustic scattering cross-section substantially, leading to higher backscatter form functions, k_s.

The exact backscatter mechanism in flocculated suspensions is not yet fully understood; however, it is found that the viscous attenuation depends on the particle–fluid density contrast, and that the reduced density contrast of flocs causes them to oscillate nearly in phase with the surrounding fluid, rendering viscous attenuation negligible and making water absorption the dominant attenuation mechanism [23]. How viscous attenuation scales with increasing floc size remains unresolved. It is hypothesized that viscous losses may either remain approximately constant or decrease with increasing floc size.

3.6. Supporting Instruments for Sediment Characterisation

To aid in interpretation and reduce uncertainties of acoustic and optical measurements, independent information of sediment characterisation are commonly obtained through supporting instruments such as a Laser In-Situ Scattering and Transmission (LISST) sensor, that can obtain the volumetric particle distribution information (d_{10}, d_{50}, d_{90}) for particle sizes between 2.25 to 381 μm for non spherical particles [41], and a particle camera for larger particles sizes such as flocs [12, 40].

3.7. Synthesis of Literature and Research Positioning

The current state-of-the-art for suspended sediment monitoring consists of optical and acoustic backscatter sensors, where each sensor exhibits a characteristic response that is influenced by the state of the suspension. Optical backscatter sensors are widely used for small volume (Range $\approx 5cm$) measurements of SSC (often referred to as point measurements) and are generally robust to concentrations up to 40 g/L; they rely on direct calibration, which is also their main limitation for deep sea nodule collection. The calibration may become invalid when sediment properties differ from the calibration conditions, for example due to variations in sediment composition between nodule collection sites or changes in particle size distribution resulting from aggregation and flocculation. Additionally, calibrations are performed on deck which makes it an operationally cumbersome and expensive procedure.

High-frequency acoustic backscatter sensors (ABS) provide non-intrusive, range-gated measurements and estimate concentration through theoretical formulations describing how acoustic energy is scattered by particles and attenuated within the suspension. Single-frequency acoustics still require prescribed particle-size information whereas multi-frequency acoustics exploit the frequency-dependent acoustic response of suspended particles to estimate particle size and SSC simultaneously; potentially eliminating the need for sediment-specific calibration and prescribed information.

Deep-sea sediment plumes consist largely of organic-enriched fine cohesive sediments that are prone to rapid, shear-dependent transitions between primary particles and flocculated aggregates. In such conditions, the interpretation of acoustic and optical observations becomes challenging, as the measured response is affected not only by suspended sediment concentration (SSC), but also by the evolving particle size distribution (PSD), particle structure, and attenuation or saturation effects.

The collector vehicle diffuser however, offers a potentially ideal measurement location for both sensors, as it provides a suspension of recently disaggregated material that has not yet undergone significant dynamic processes such as flocculation. This state could allow for increased performance as it can be bound by a single acoustic model. However, deep-sea sediments contain a significant fraction of particles below the theoretical sensitivity limit of the highest commercially available acoustic frequencies (1, 2, 4, 5 MHz) (e.g. approximately 25 % of the Bluefield box-core sample, mentioned in Section 4.2, is below the theoretical limit of the highest commercially available frequency transducer). This may cause particle-size estimation, and consequently SSC inversion, to become unfeasible or unreliable. Currently, the inversion capability of multi-frequency acoustics remains insufficiently validated for cohesive, organic-enriched suspensions in deep-sea nodule collection environments (a stable continuous flow of primary particles), presenting the research gap in which this thesis is situated.

The aim of this study is to bridge this gap by evaluating the applicability of state-of-the-art multi-frequency acoustic backscatter measurements for suspended sediment concentration (SSC) and particle-size inversion in representative deep-sea nodule collection plumes. Particular emphasis is placed on quantifying the accuracy, precision, uncertainty, and operational limitations of the acoustic inversion approaches, while identifying the factors governing inversion performance, including particle-size sensitivity, frequency selection, measurement noise, and inversion stability. To complement the deployment potential of acoustic monitoring, an optical backscatter sensor is assessed in parallel to assess the acoustic sensor in light of the accuracy of the optical sensor.

4

Inversion and Experimental Methods

The following sections describe the selected inversion methods and models evaluated in this study, followed by the experimental setup and the methods used to obtain the relevant data. In particular, the following topics are described: the experimental setup, the sediments and instruments used, preparations for the experiment, calibration and measurement procedures, data acquisition settings, and the filtering methods.

4.1. Selected Inversion Methods Under Evaluation

Section 3.4 describes the general approaches available for acoustic inversion and that the choice of inversion method depends on the sediment type, sediment composition, plume characteristics, and the required level of resolution. Accordingly, several modelling components must be selected, including the theoretical backscatter model (α_s and s_v; generic or oblate particles), the attenuation model (α_{sv}; spherical or mica particles), the assumed particle size distribution (log-normal or bimodal), the objective function (Φ, Γ, or E), the inversion strategy (implicit or explicit), and the parameters that are prescribed or estimated during the inversion.

The inversion methods and modelling approaches considered most suitable for the present application, based on both commercially available software and methods reported in the scientific literature, are summarized in Table 4.1. These methods are evaluated and compared in this study.

Table 4.1: Overview of the inversion methods evaluated in this study.

Case	PSD	Viscous att. model	Scattering models	Objective function	Fixed parameters	Estimated parameters
Method 1 *- Commercial software - Bin-based inversion*						
M1.1	Lognormal	Iterative	Irreg. part	Proprietary	σ	M, a_0
Method 2 *- Commercial software - Bin-based inversion (prescribed particle size)*						
M2.1	Lognorm.	Iterative	Irreg. part.	Proprietary	a_0, σ	M
Method 3 *- Python workflow - Profile-averaged inversion* (α_s & s_v)						
M3.1	Lognorm.	Oblate spher.	Mica-specific	E	$1/40 < h < 1$	M, a_0, σ
M3.2	Bimodal	Spheres	Generic	E	–	$M, a_1, a_2,$ $\sigma_1, \sigma_2, w_1, w_2$
Method 4 *- Python workflow - Profile-averaged inversion* (α_s)						
M4.1	Lognorm.	Spheres	Generic	Φ or Γ	σ	M, a_0
M4.2	Lognorm.	Spheres	Generic	Φ or Γ	–	M, a_0, σ
M4.3	Lognorm.	Oblate spher.	Mica-specific	Φ or Γ	$\sigma, h = 1/40$	M, a_0
M4.4	Lognorm.	Oblate spher.	Mica-specific	Φ or Γ	$h = 1/40$	M, a_0, σ

Note: The PSD model is either log-normal or bimodal log-normal; The applied procedure is either iterative (through the commercial Aquascat Toolkit) or non-iterative (Python), where the viscous attenuation is found through iterative correction or through linearization of the inverse Equation 3.5, respectively; When linearized, the attenuation model (α_{sv}) used is either the spherical model [53], or oblate spheroidal model [54]; The scattering models (s_v or α_{ss}) are either the irregular particle model [57], or the generic irregular particle model or the mica-specific model [47].

Methods 1 and 2 are implicit bin-based iterative inversion methods implemented in the commercially available software 'Aquascat Toolkit', as described in Section 3.5.1. They are based on a high resolution bin-based direct inversion of Equation 3.5, in which sediment attenuation is initially estimated and subsequently updated through an iterative procedure until convergence is achieved. These methods, as well as Method 2.1, use the acoustic scattering and attenuation models described by P. Thorne et al. [57], and Hay [46].

Method 1 is a multi-frequency method that determines particle size from frequency-dependent form-function ratios, after which SSC is determined through an iterative procedure where α_s is updated until convergence is achieved. **Method 2** comprises of both single-frequency and multi-frequency inversion methods, in which both the particle size and relative standard deviation are prescribed and assumed constant over the measured range. Consequently, the sediment sediment concentration (SSC) is the only parameter estimated.

Method 3, adapted from Vergne et al. [30], is a range-averaged inversion method in which the sediment attenuation coefficient (α_{sv}) is obtained from a linear regression of the fluid-corrected backscatter. The volume scattering coefficient (s_v) is subsequently determined using the estimated attenuation. Both α_{sv} and s_v at multiple frequencies are then included in the objective function to simultaneously estimate SSC and the particle size distribution parameters.

Method 3.1 represents the particle size distribution using a single log-normal distribution and combines an oblate-spheroidal viscous attenuation model with a mica-specific scattering model. Particle oblateness is described by the aspect ratio h, which increases from $1/40$ at a particle diameter of 2 μm to 1 at 60 μm. Here, $h = 1$ represents a spherical particle, whereas $h = 1/40$ corresponds to the aspect ratio of kaolin [54].

Method 3.2 instead combines a spheroidal viscous attenuation model ($h = 1$) with a generic scattering model, and represents the particle size distribution using two log-normal modes. As attenuation is primarily influenced by finer particles, and backscatter is more strongly influenced by larger particles, the bimodal representation can provides additional flexibility in describing their respective contributions to the measured acoustic response.

Method 4 is also a range-averaged inversion method; however, its objective function uses only the attenuation term (α_{sv}) in the minimization algorithm. Methods 4.1 and 4.2 use the generic scattering model of Moate and P. D. Thorne [47] in combination with the spherical viscous attenuation model. Methods 4.3 and 4.4 use the mica-specific scattering model and the oblate-spheroidal viscous attenuation model of S. Richards et al. [54]. Contrary to Method 3.1, where the oblateness varies linearly with particle diameter, the oblateness in Method 4.3, and 4.4 are fixed to 1/40.

4.2. Sediment Properties

Two deep-sea sediment box core samples were used in this study. The first sample, hereafter referred to as the CCZ sediment, was sourced from the NORI-D license area in the Clarion–Clipperton Zone (CCZ) at a depth of approximately 4000 m. The second sample, hereafter referred to as the Sediment B, was sourced from another representative deep-sea nodule field location at a depth of approximately 5500 m. Sediment B consisted of box core samples taken from the upper 15 cm sediment layer. For the CCZ sediment this information was not specified, however, derived from Wahab et al. [14], it is likely to be sourced from the top 30 cm.

The CCZ sediment has a D_{50} of 15.24 μm and a total loss on ignition (LOI) of 0.404 wt.%, while Sediment B has a d_{50} of 4.51 μm and an LOI of 0.581 wt.%. Both median particle sizes were determined through static light scattering, using a Malvern Mastersizer 3000 with a stirrer operating at 3250 rpm throughout the measurement. To ensure measurement of primary particles, the samples were disaggregated using an IKA T18 disperser during 10 seconds. The final particle size distribution was determined as the average of 10 profiles, which exhibited excellent agreement between one another.

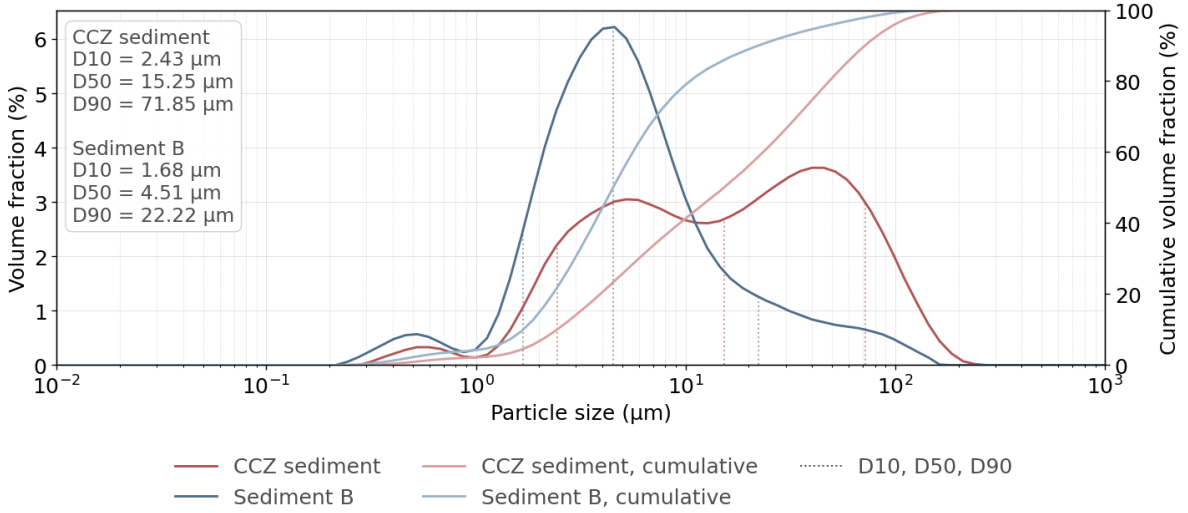

Figure 4.1: Malvern determined volume-based particle size distributions of the two sediment cases: CCZ sediment in red and Sediment B in blue.

A secondary particle size distribution measurement method was used during the experimental campaign through the use of an offline-configured LISST-100x. More information on the use of the LISST sensor is provided in the following sections. The most representative particle size distribution profiles for both sediments are shown in Figure 4.2.

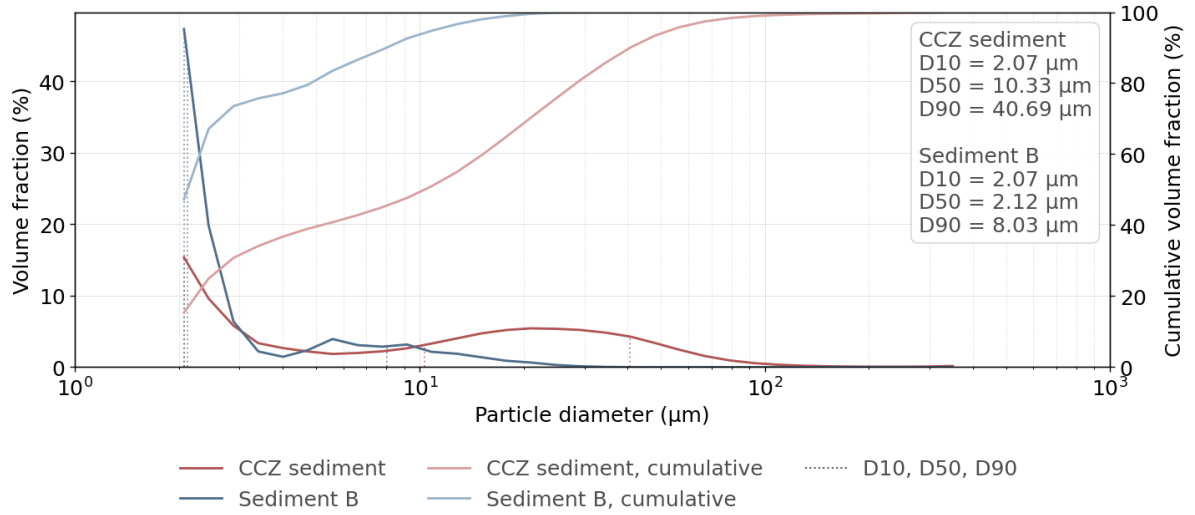

Figure 4.2: LISST determined volume-based particle size distributions of both sediment cases: the CCZ sediment in red and Sediment B in blue.

4.3. Sediment Particle Size Distribution Parameters

The methods described in Section 4.1, require the prescription of either the median particle diameter (D_{50}), or a measure of the particle distribution width , or both. The particle distribution width is defined through the relative standard deviation ($Rel.SD$), for methods 1 and 2, and the standard deviation (σ), for Methods 3 and 4. These are measures of the distribution width and therefore describe the degree of sorting within the sediment. A lower value of (e.g. $Rel.SD = 0.3$) defines a narrow well-sorted particle size distribution, whereas higher values indicate a broader distribution.

The particle size distribution parameters were measured with a Malvern Mastersizer 3000 as described in 4.2, as well as a LISST-100X. The median particle size was calculated from the cumulative volume distribution, while the standard deviation (σ) was determined through a log-normal RMSE minimization. The relative standard deviation (Rel. SD) was subsequently calculated by transforming the log-space standard deviation to linear space according to:

$$Rel.\ SD = \sqrt{\exp(\sigma^2) - 1} \tag{4.1}$$

The resulting median (D_{50}), standard deviation (σ), and relative standard deviation ($Rel.SD$) values are summarized in Table 6.1 and are used as input parameters and comparison parameters throughout this study.

Table 4.2: Summary of the measured and single-mode GMM fitted particle size distribution parameters used for the acoustic modelling.

Sediment	**Instrument**	D_{50} (μm)	σ	$Rel.SD$
CCZ sediment	LISST-100x	10.2	2.0	7.7
CCZ sediment	Malvern Mastersizer 3000	15.2	1.5	2.9
Sediment B	LISST-100x	2.1	0.2	0.2
Sediment B	Malvern Mastersizer 3000	4.5	0.8	1.0

4.4. Experimental Setup

The goal of the experimental setup is to perform acoustic measurements and acquire data representative of deep-sea nodule collection conditions. These measurements are used to evaluate the performance of the sensor and inversion methods over a wide range of suspended sediment concentrations,

thereby assessing their potential for future operational use. As discussed in previous sections and summarized in Section 3.7, the diffuser is the most promising location for acoustic measurements as dynamic effects such as flocculation here is minimal. Therefore, a new setup was designed and built to simulate the continuous flow conditions of the collector vehicle diffuser, where the plume over the entire viewing range of the sensor is approximately in its primary particle state. In addition, the setup could also be used in an alternative configuration, in which the pumps were turned off to allow settling to occur and evaluate the influence of flocculation. However, due to the poor inversion performance discussed in Sections 5.4.1 and 5.4.2, the assessment of flocculation was not considered in this study and is instead presented as a qualitative assessment in Appendix D.

The tank setup, hereinafter referred to the recirculation tank, consists of an acrylic tank with a square base of 0.38 meter and a height of 2 meters, allowing for a total volume of approximately 280 litres. The dimensions were determined based on the minimum proven working dimensions in previous experimental setups (e.g. the cylindrical water tower from [47] with a diameter of 0.3 m), while considering additional width to keep the tank accessible for other sensors and sampling methods and keeping the total volume to a minimum to enable elevated mixture concentrations (estimated approximately 50 g/L). An external dry centrifugal pump (Gardena 5000 Silent), with an inlet located at the bottom of the tank, was used to extract larger settling flocs and recirculate them to the top of the tank. During this process, elevated shear rates within the pump are assumed to fully disaggregate the flocs and reintroduce them into the water column as approximately primary particles. This created a continuous flow of disaggregated particles past the downward-looking mounted sensors, simulating in-diffuser jet-plume conditions.

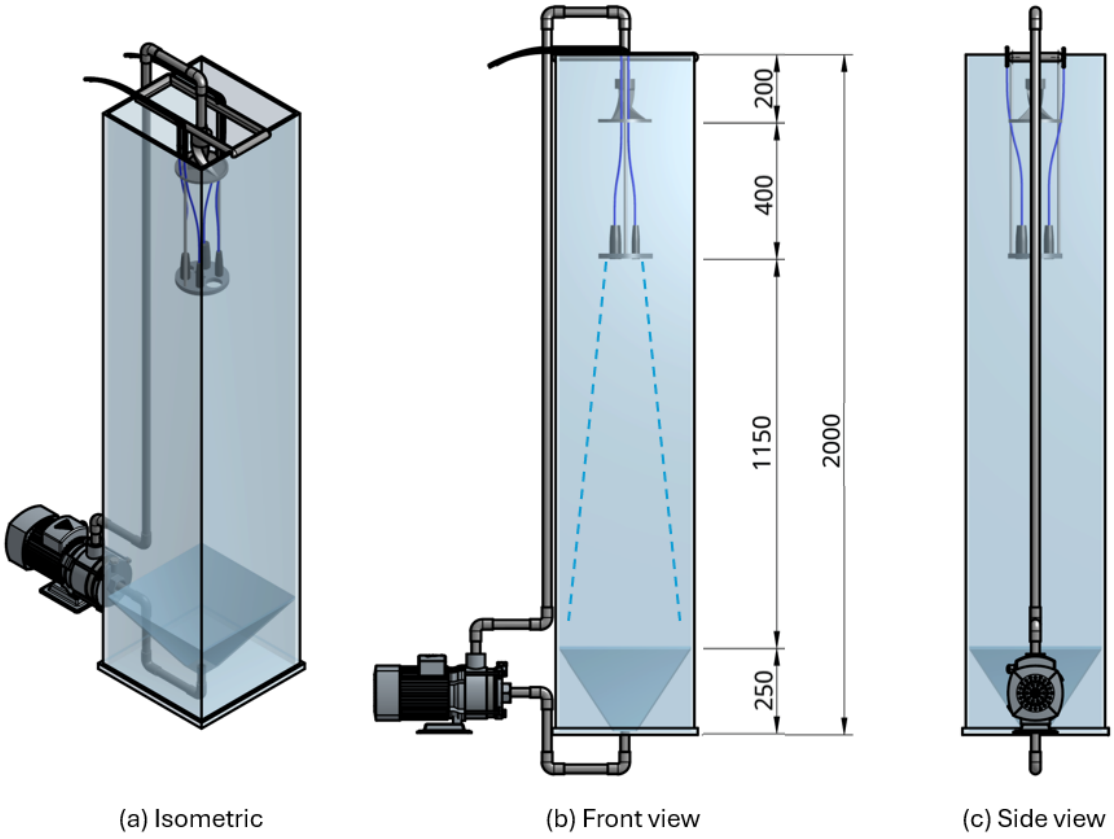

Figure 4.3: Schematic representation of the recirculation tank showing (a) the isometric view, (b) the front view, including the acoustic sensor's field of view (dashed light blue lines), and (c) the side view. The main components include the rectangular tank, accumulation funnel, transducer head assembly, deflector plate, and recirculation pump. The tank was filled with salt water to approximately 10 cm below the top edge.

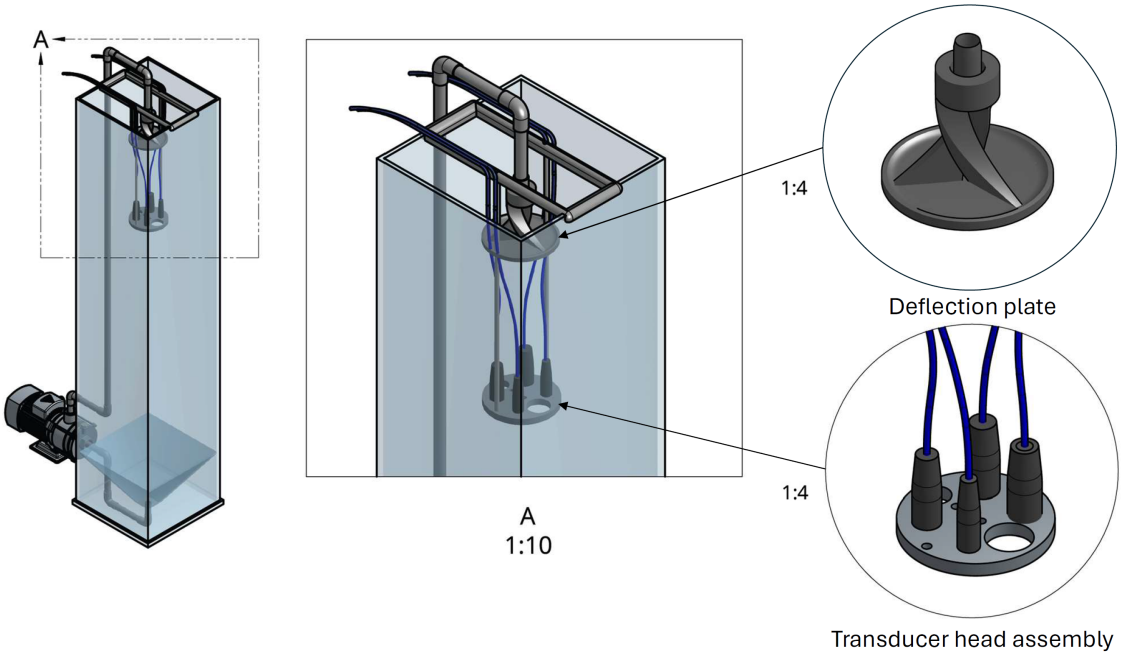

Figure 4.4: Schematic overview of the recirculation tank with a magnified view of the upper section. Enlarged details show the deflection plate, which redirects the inflow for improved mixture homogenization, and the transducer head assembly containing the four acoustic transducers.

An accumulation funnel was installed at the bottom of the tank to direct the sediment to the outlet of the tank and to prevent particle settling out of the water column and reducing the concentration over time. In addition, a 3D-printed dispersion nozzle was used to angle the flow outward and upward to homogenize the mixture in the tank and maximize the escape of any possible micro-bubbles present in the system.

The Gardena 5000 pump was selected for its high flow of 83.3 L min^{-1} and pressure of 3.7 bar which has a theoretical water turnover time of approximately 3.4 minutes and a bulk average vertical velocity of 0.96 cm s^{-1} , which was estimated to be sufficient to pump through elevated sediment concentration mixtures back to the top of the tank at a rate higher than the settling rate. The pump inlet consisted of 1” tubing to maximize inlet flow, the tubing running from the pump outlet to the tank consisted of 1/2” tubing to provide sufficient back pressure for the pump to operate in its optimal regime. Using a 1” inch tubing on the outlet resulted in cavitation and large amount of visible air-bubbles in the system.

Since temperature influences flocculation behaviour, the experiments were conducted in a thermoregulated room where the temperature was set to the lowest possible setting of 5 degrees Celsius to simulate deep-sea conditions as closely as possible.

4.5. Instruments

Acoustic Backscatter Sensor

The acoustic backscatter sensor (AQUAscat-R1000) consisted of four waterproof, cabled transducers operating at 1, 2, 4, and 5 MHz, mounted as an assembly in a vertical downward-looking configuration. To ensure the sensors could obtain the full expected working range of at least one meter at low concentrations, the transducers were mounted at a height of 1.4 m above the tank floor, corresponding to approximately 1.15 m above the top of the accumulation funnel. The large distance also minimized the probability of echoes from the tank floor and walls returning to the transducers, thereby reducing measurement noise.

Optical Backscatter Sensor

The optical backscatter sensor (AQUAlogger-310TY) was used to obtain point-concentration measurements at three selected distances below the transducer head, namely 0.2, 0.6, and 0.8 m, to obtain representative point measurements throughout the measurement range. The complete measurement

sequence is described in Section 4.7.

LISST-100X
A Sequoia LISST-100X (Type-C) was used to evaluate the spatial and temporal evolution of the particle size distribution (PSD) throughout the experiments. The instrument was deployed in an offline configuration, where the sensor was mounted horizontally on a laboratory bench and equipped with a measurement chamber positioned between the laser transmitter and receiver. This configuration allowed ex-situ analysis of suspension samples collected from the recirculation tank.

4.6. Experiment Preparation

A saline mixture of approximately 34.7 PSU was prepared in a buffer tank with a volume of 1000 litres and was stored in the thermo-controlled room of 5 degrees Celsius to ensure availability of cooled saline water throughout the experimental campaign. During the filling process into the test setup the water was filtered with a 63 micron filter to avoid any possible large debris and residues from the buffer tank. Prior to introducing the sediment into the test setup, the sediment was diluted with the saline mixture and moderately sheared with a paint mixer to dissolve any large clumps. When present, large nodule remains (>1 cm) were removed by hand to avoid clogging the system. After introducing the sediment in the tank, the tank was left to homogenize for 15 minutes before sensor measurements were taken. The concentration level was estimated with the OBS sensor through its real time turbidity/-concentration viewing function. The concentration homogenization stability was also verified through this method. Measuring the sediment in advance was preferred however during the test of Sediment B the accumulation funnel was not sealed sufficiently and allowed sediment to pass through and settle on the horizontal floor reducing the concentration over time. This issue was resolved during the test with the CCZ sediment, however the same method was applied as the sediment was a previously mixed sample and therefore the LOI (used to estimate the quantity of dry sediment) was no longer applicable to that sediment, while the optical sensor method was deemed sufficiently robust.

4.7. Measurement Procedures

Preliminary testing showed that the presence of the optical sensor in the tank interfered with the acoustic sensor, inducing noise in the acoustic measurements when mounted 0.2 m below the acoustic transducers as well as at the same height as the transducers. This effect was particularly pronounced for the 1 and 2 MHz frequencies and within the first 0.4 m below the transducers, after which the noise decreased, likely due to the wider acoustic beam angle and increased distance from the optical sensor.

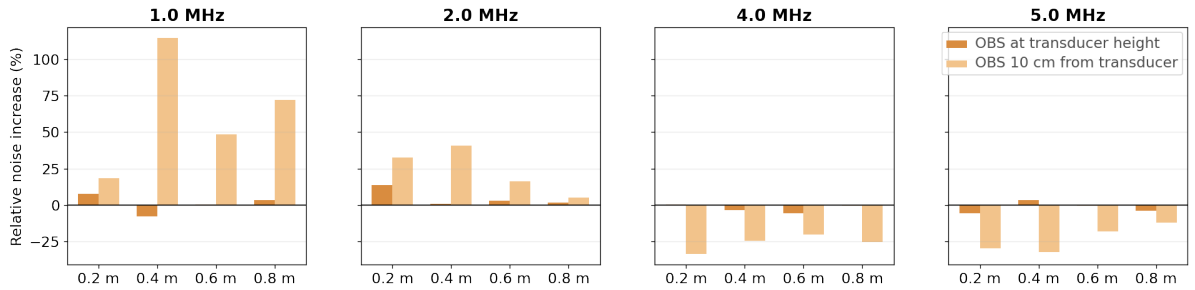

Figure 4.5: Relative increase in temporal noise in the acoustic beam due to the presence of the optical sensor at two locations: at transducer height and 10 cm below the transducers against the tank wall.

Consequently, to minimize interference effects between the optical and acoustic sensor, the measurements were not performed simultaneously. Instead, the optical measurements were performed intermittently between acoustic profile measurements, splitting the acoustic measurements into three measurements as described below.

Acoustic, Optical and Gravimetric Measurements
The measurement procedure started with the collection of three 50 mL gravimetric samples at distances of 0.2, 0.6, and 0.8 m below the transducer head. These samples served as reference concentrations against which the sensor-derived concentrations could be evaluated. Subsequently, OBS

point-concentration measurement were performed at the same distances, followed by three five-minute acoustic measurements over the full water column. Additional OBS measurements were made in between the acoustic measurements and after the final acoustic measurements, again at the three previously mentioned distances from the transducer head. Resulting in three acoustic measurements, twelve optical measurements and six gravimetric samples per concentration level. The measurement sequence is summarized in Figure 4.6.

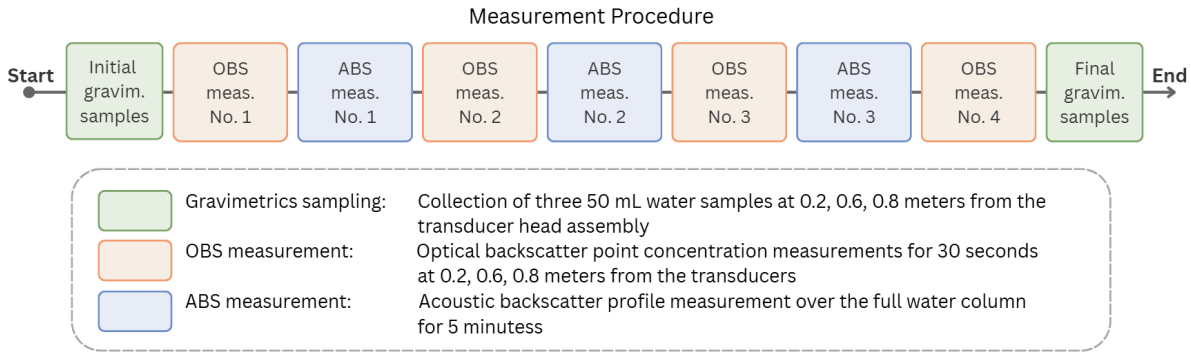

Figure 4.6: Overview of the sensor measurement procedure for each SSC step

LISST Measurements
The LISST was not deployed for all concentration experiments but rather for selected concentrations to evaluate the spatial and temporal evolution of the particle size distribution throughout the tank height. The measurements were used to assess whether particle aggregation and flocculation occurred during the experiments. The measurements consisted of sampling at 0.2 m and 0.8 m below the transducer head.

The LISST measurement procedure consisted of filling the offline measurement chamber with the premade saline solution from the buffer tank and allowing it to equilibrate for approximately 5 minutes to allow for micro-bubbles to escape and the temperature to adjust to the sensor. This step served to minimize temperature- and bubble-related measurement artefacts. Subsequently, a 50 mL sample was collected from the tank and gently poured into the funnel placed on top of the measurement chamber. A valve below the chamber was then opened to draw the sediment from the funnel into the chamber and allow the suspension to homogenize within the chamber. A minimum of 120 profiles was recorded and averaged to obtain a representative PSD measurement.

Initially, during the Sediment B tests, samples were collected from the recirculation tank using a 5 mm siphoning tube. However, after observing relatively narrow particle size distribution (PSD) profiles, it was decided to use a Niskin bottle during the CCZ sediment tests to minimize the shear applied to the sediment, which could potentially cause floc breakage.

The offline configuration of the LISST made it highly sensitive to artifacts. Further details regarding data quality control and filtering procedures are provided in Section 4.12.

Temperature Measurements
The experiments were conducted in a thermally-regulated room at 5 degrees Celsius, however the external recirculation pump introduced substantial energy into the water and thereby increasing the temperature. The water temperature varied between 4.8 and 17.1 degrees Celsius. Temperatures were recorded at each SSC step and were considered in the inversion accordingly.

4.8. Calibration of Optical Sensor

The optical backscatter sensor was previously calibrated to the CCZ sediment, however a new calibration curve was made for Sediment B. The calibration was performed by suspending the sensors in a beaker placed on top of a Heidolf MR3001 magnetic stirrer plate set to 700 rpm, the maximum stable speed to maintain the sediment in suspension even at higher concentrations. The calibration

procedure included: 1) adding sediment to the mixture and letting it homogenize for approximately 1-2 minute or until the FTU readings became visually stable enough to estimate an average value, 2) an optical measurement at a burst rate of 1 Hz for approximately 1 minute, 3) following a representative gravimetric sample was taken by rapidly submerging a 50 mL Falcon test tube to the height of the optical lens which is later filtered and weighed as described in section 4.9.

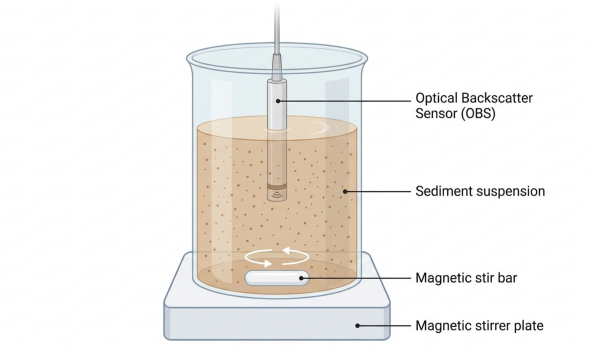

Figure 4.7: Schematic representation of the optical backscatter sensor calibration setup. The optical backscatter sensor suspended in a beaker, placed on a stirrer plate to maintain a homogenous suspension throughout the calibration process. Schematic generated with assistance of OpenAI ChatGPT and subsequently reviewed and modified for technical accuracy.

The calibration data show a linear increase in signal up to 5.089 g/L for the CCZ sediment and 4.993 g/L for Sediment B, after which the signal increased logarithmically with sediment concentration. For Sediment B, the signal began to saturate at concentrations above 26.58 g/L; therefore, data points beyond this concentration were excluded from the logarithmic fit and are represented by solely outlined markers in Figure 4.8. Statistical analysis was performed by fitting linear and logarithmic regression models using a least-squares optimization. The resulting best fit trend lines showed good agreement with the measured data, as indicated by the R^2 values in Figure 4.8. These results are consistent with the calibration fits reported by Tran et al. [64].

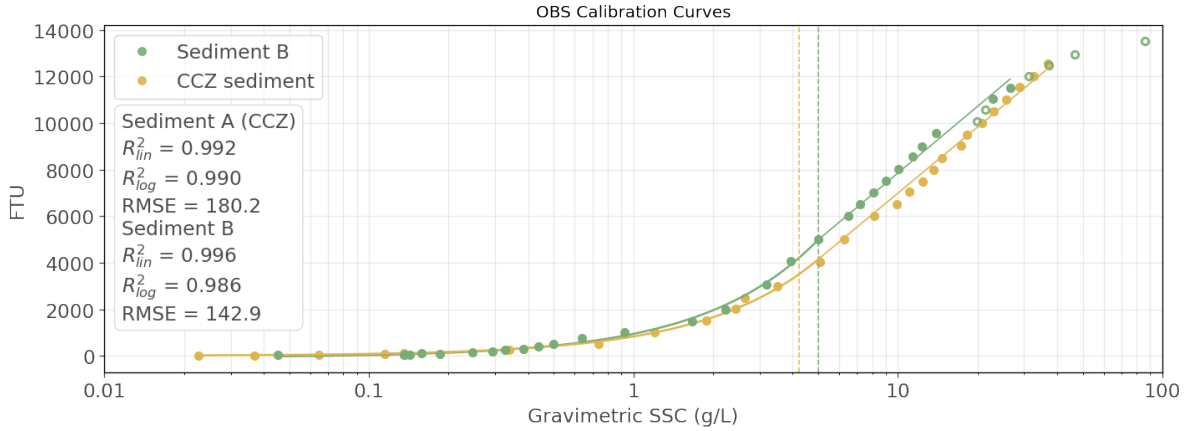

Figure 4.8: OBS calibration curves for Sediment A (CCZ) and Sediment B. Filled circles indicate data included in the fit, while crosses and empty circle symbols indicate excluded data points. The coloured dashed lines mark the transition between the linear and logarithmic fitting regimes.

CCZ sediment:

$$SSC = \begin{cases} \dfrac{\text{FTU} - 0.847}{828.64}, & \text{FTU} \leq 4217.80 \\ \exp\left(\dfrac{\text{FTU} + 2445.09}{4095.00}\right), & \text{FTU} > 4217.80 \end{cases} \tag{4.2}$$

Sediment B:

$$SSC = \begin{cases} \dfrac{\mathrm{FTU} + 68.12}{1010.82}, & \mathrm{FTU} \leq 4978.92 \\ \exp\left(\dfrac{\mathrm{FTU} + 1660.53}{4128.92}\right), & \mathrm{FTU} > 4978.92 \end{cases} \tag{4.3}$$

4.9. Gravimetric Analysis and Filtering

Samples collected during both the calibration procedure and the experiments were analysed using gravimetric methods to determine the reference suspended sediment concentration (SSC). For each sample, a known volume of suspension was filtered through pre-dried and pre-weighed membrane filters. Following filtration, the filters containing the retained sediment were dried and weighed again. The difference between the pre- and post-filtration filter masses represented the dry sediment mass contained in the measured sample volume. Subsequently, the suspended sediment concentrations were calculated and expressed in mg/L. This method has commonly been applied for this sensor and sediment grain size distribution [65, 66].

$$SSC = \frac{M_{sedimentladenfilter} - M_{Filter}}{V_{sample}}(g/L) \tag{4.4}$$

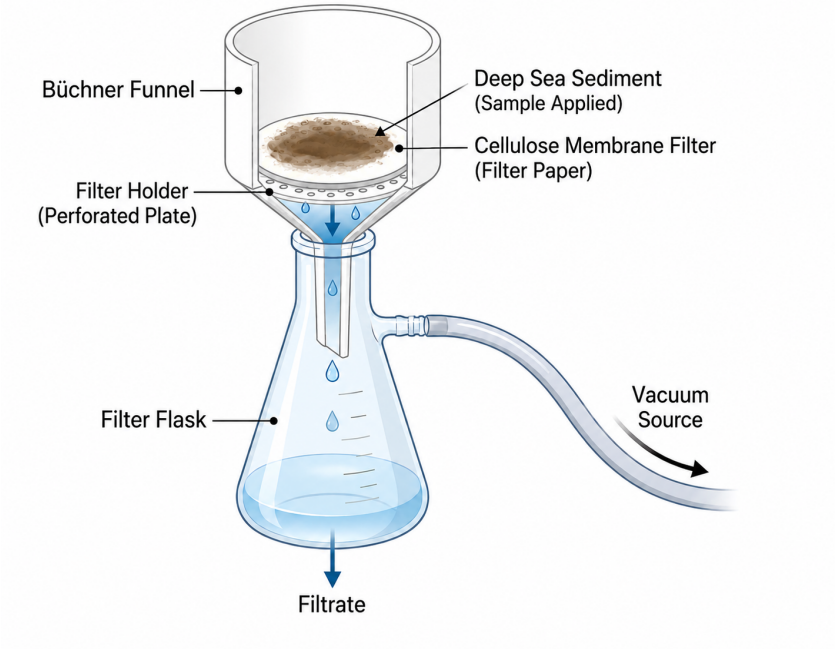

Figure 4.9: Schematic of the equipment used during the filtration process. The membrane filters were placed on top of the filter holder, onto which a known sample volume was applied. The vacuum ensured that the water was pulled through the filter, while the sediment was retained on the membrane filter, which was subsequently dried and weighed. Schematic generated with assistance of OpenAI ChatGPT and subsequently reviewed and modified for technical accuracy

The drying procedure ensured complete removal of residual moisture prior to weighing. Before filtration, the filters were dried for approximately 4 hours at $60°\mathrm{C}$, while after filtration the sediment-laden filters were dried overnight at the same temperature. The filters were weighed using a Mettler AT261 balance with a resolution of $\pm 0.01, \mathrm{mg}$. Sample volumes were measured with two pipettes depending on the sample volume, each with a maximum measuring volume and manufacturer uncertainty of 5 mL with $\pm 0,6\%$ uncertainty, and 10 mL with 5 % uncertainty.

The maximum relative error (Relative error $= \frac{\text{measurement uncertainty}}{\text{measured value}} \times 100$) associated with the measured weights and volumes was 1.19 % and 0.05 %, respectively, for the samples obtained during the OBS

calibration procedure, and 0.16 % and 0.016 %, respectively, for the samples collected during the experiment.

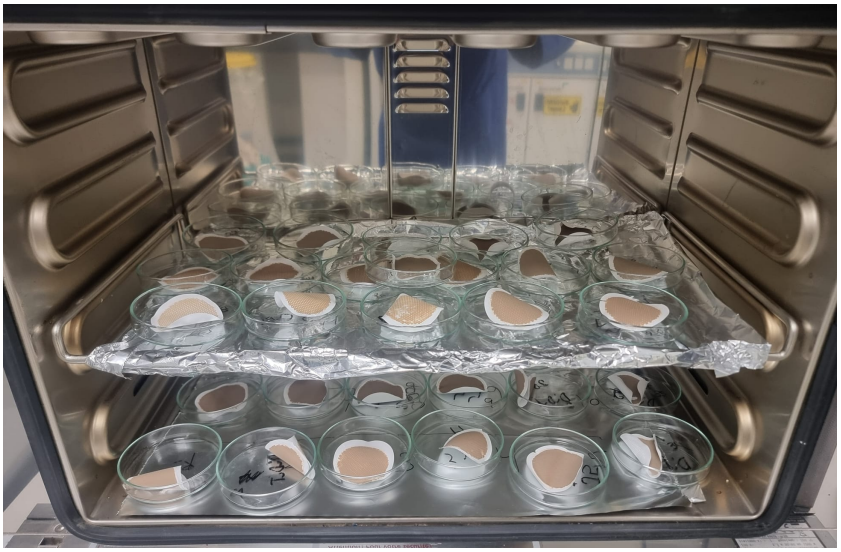

Figure 4.10: Batch of membrane filters placed in an oven for approximately 16 hours to remove residual moisture prior to weighing.

Due to restrictions in filter availability four types of filter membranes were used throughout the experiment:

- Whatman GF/F Glass microfiber filters 0.2 μm pore size and 47mm diameter (18192146)
- Nuclepore Track-Etch Membrane $0.4\mu m$ pore size and 25 mm diameter (10417112)
- Whatman Cellulose acetate membrane filters 0.2 μm pore size and 50mm diameter (10404001)
- Millipore 0.45 μm

Three samples from the CCZ Sediment with gravimetrically determined concentrations 1.250, 8.437 and 20.715 g/L were repeated and resulted in an uncertainty of 8.57 %, 1.54 %, and 1.43 %, respectively.

4.10. Acoustic Background Noise Measurements

Prior to the experiment, a 70-minute background measurement was performed under operating conditions identical to the conditions during the experiments, with the recirculation pump on but without sediments in the water column. The resulting signal, V_{noise}, was used to characterize background noise measurement of the setup conditions. The measurement captures contributions from air micro bubbles, electronic noise, inherent water turbidity, and acoustic reflections from the tank walls and floor. The resulting background profile was used for signal-to-noise ratio (SNR) calculations defined as:

$$\text{SNR} = \frac{V_{\text{signal}}^2}{V_{\text{noise}}^2} \tag{4.5}$$

where, V_{signal}, is the measured backscatter voltage in the presence of suspended sediment and, V_{noise}, is the background voltage obtained from clear-water background measurements.

The background file is used to subtract background noise from the measurement files. In the Aquascat Toolkit software, this is done by calculating an average background profile for each frequency and subtracting it from the corresponding measurement profile [67]. In the profile averaged Python analysis, where the attenuation term is first determined and the backscatter term is subsequently calculated, the background correction is applied differently. Since bubble backscatter is not expected to have a significant influence on the attenuation estimate, only the remaining electronic/background noise is

removed during the attenuation calculation. This noise level is estimated by selecting a representative range interval in the background profile and calculating the average signal amplitude over this section. The resulting mean value is then subtracted from the corresponding measurement files.

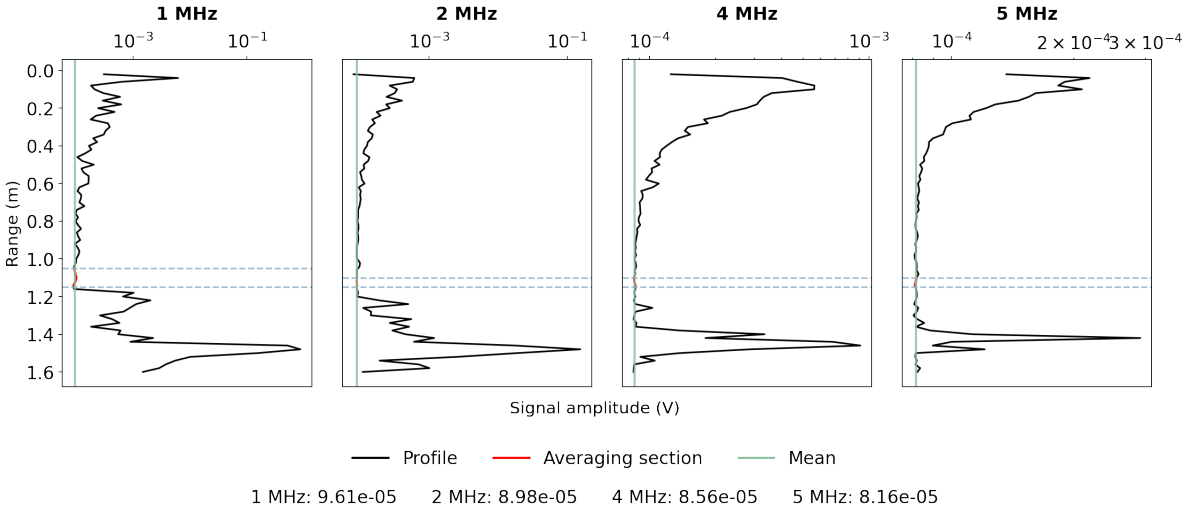

Figure 4.11: Signal amplitude in volts as a function of range for each frequency. The bounds of the selected interval used to estimate the average background noise level are defined by the blue dashed lines; the red section is the selected region, and the solid green line represents the final background noise.

In contrast, during the backscatter calculation, bubble scattering contributes directly to the measured signal and must therefore be removed. This is done by subtracting the quadratic mean background profile, V_{noise}, from the measured profile before calculating the backscatter coefficient.

To determine the maximum usable range for each frequency, an SNR threshold of 5 was applied. Measurements for which the SNR fell below this threshold were considered to be significantly affected by background noise and were excluded from further analysis. This method therefore identifies the maximum usable range for each frequency. The minimum valid range was defined by the theoretical near-field limit of each transducer, estimated as described in Section 3.4. Measurements outside these limits were excluded from further analysis. The transducer radii required for the near-field calculations were obtained from the acoustic data files provided by Vergne et al. [30], corresponding to an earlier software version that included this information. An SNR threshold of 5 was selected instead of the value of 10 used by Vergne et al. [30], as the lower receive gain (R_x) used during the present experiments reduced the received signal amplitude, causing valid measurements to fall below an SNR threshold of 10.

4.11. Data Acquisition Settings

The data was acquired through the sensor's communication software, Aquatalk, for both the optical and acoustic sensors.

ABS Settings

The acoustic sensor was configured to sample at a rate of 4 Hz, with a bin size of 2 mm, and a pulse rate of 2 us; these settings gave the most promising results from testing in clear water. The low sample rate and relatively high bin size are conservative settings set maximize the transmitted energy and to minimize crosstalk by allowing each transmission to fully dissipate before the next one. The measurement range was set to and 1.6 meters for Sediment B and later set to 1.1 meters for the CCZ sediment as the bins extending beyond the tank floor was found not to give additional information and it was assumed it could potentially cause increased noise due to unused bins.

For natural sediments the received acoustic echo amplitudes V follow Rayleigh statistics and the standard error therefore approximately follows $\epsilon = V_{rms}/2\sqrt{n}$ [57] where n is the number of independent profiles. The uncertainty decreases with the square root of the number of independent averaged profiles.

To obtain sufficient statistical accuracy in the acoustic backscatter measurements, the total measurement duration was set to 15 minutes, resulting in an estimated statistical uncertainty of approximately 0.77 % in V_{rms} and 1.53 % in the SSC inversion when no temporal averaging is applied; and to 1.33 % in V_{rms} and 2.66 % in SSC when the three 5-minute recordings are used independently.

OBS Settings
A single measurement made by the optical sensor consisted of a 30 second recording at rate of 4 Hz corresponding to a total of 120 samples per height.

LISST Settings
The LISST-100x (Type-C) was set to record profiles at approximately 1 Hz and for a minimum of 120 profiles. The randomly-shaped particle inversion method measures the PSD with a resolution of 32 bins with the centre of the bins logarithmically distributed from 2.25 to 381 microns, with upper bin size in each bin being 1.180 times the lower bin size, as per user manual.

4.12. Data Processing and Filtering

ABS Data
The acoustic sensor outputs binary '.aqa' files, which were subsequently processed using both the commercial Aquascat Toolkit software and a custom Python workflow. The Aquascat Toolkit software was used to apply Methods 1 and 2; The Python workflow was used for the remaining method 3 and 4, and the SNR analysis. The python workflow made use of an acoustic data loader file "AquascatDataLoader.py" obtained from Vergne et al. [30] to import the required information from the binary '.aqa' files.

ABS Background Profile Processing
The background measurement was performed in the water column prior to sediment injection. In a confined laboratory tank, the absence of sediment, and therefore attenuation, allowed the acoustic signal to propagate over larger distances with little energy dissipation. As a result, the reflections from the tank walls and floor contributed to the measured background signal, particularly at the lower frequencies due to their higher transmitted energy and wider acoustic beam angle. To reduce the influence of these reflections, the resulting background profiles (quadratically averaged profiles of a 70 minute recording) were de-spiked for each frequency using a median filter and subsequently smoothed using a Gaussian filter with frequency-specific parameters. The selected filter parameters are summarized in Table 4.3 and the resulting profile is shown in Figure 4.12.

Table 4.3: De-spiking and smoothing parameters applied to the background noise profile

Frequency (MHz)	Median filter size (-)	Gaussian smoothing σ (-)
1.0	7	3
2.0	4	1
4.0	3	1
5.0	3	1

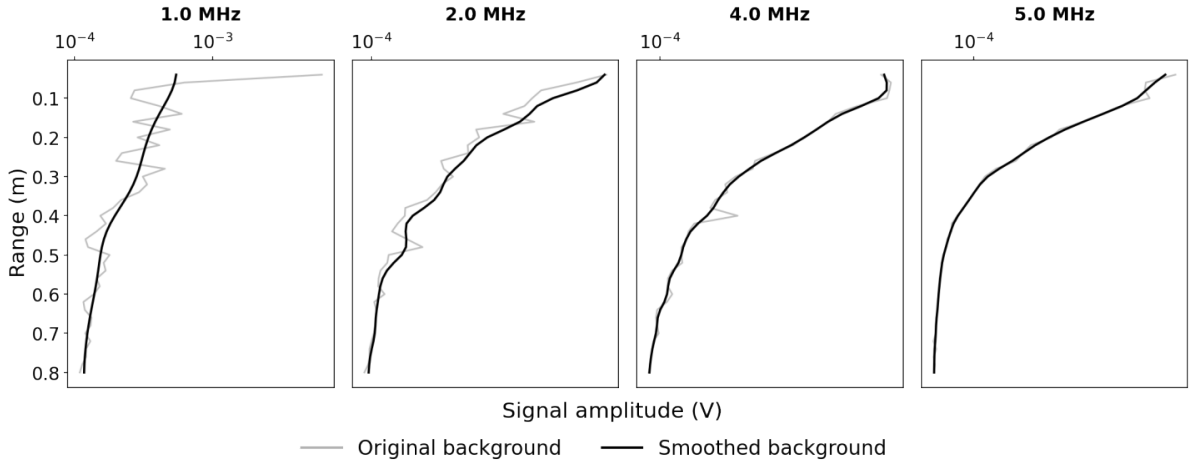

Figure 4.12: Quadratically averaged signal amplitude in volts as a function of range for each frequency. The raw profiles are shown in light grey, and the de-spiked and smoothed profiles are shown in black.

The filtered and smoothed background could only be used in python workflow however not in the commercial software. An attempt was made to apply the filter to the .mat files and apply it to the commercial Aquascat Toolkit software, however, the software only ran the inversion with raw '.aqa' files and not with modified '.mat' files. Using the unfiltered background file resulted in an unstable particle size inversion and did not contribute to improved SSC estimates and was therefore omitted in the commercial software. The standard background filter built into the software had a similar effect. Other filtering techniques such as threshold removed too many profiles often rendering the inversion not possible.

OBS Data

The optical sensor outputs '.csv' files, for which a data loader "AqualoggerDataLogger.py" was built to import the data into python. The optical sensor data included occasional spikes of high FTU values. An interquartile range (IQR) filter was applied prevent its influence to the mean calculation. The OBS sensor was also found to be sensitive to lens fouling, a common limitation of optical backscatter measurements. Fouling of the sensor lens resulted in a gradual decrease in the measured SSC over time. Repositioning the sensor to a different measurement height generated sufficient flow along the lens to remove the accumulated sediment, after which the FTU response recovered, as illustrated in Figure 4.13 (presented in already converted units of FTU to SSC (g/L)). To minimise the influence of lens fouling on the measurements, only the first 10 seconds of each OBS measurement burst were therefore used to determine the average FTU (See Appendix **??**). The filtered mean FTU values were then converted to suspended sediment concentration using the OBS calibration curve determined in Section 4.8.

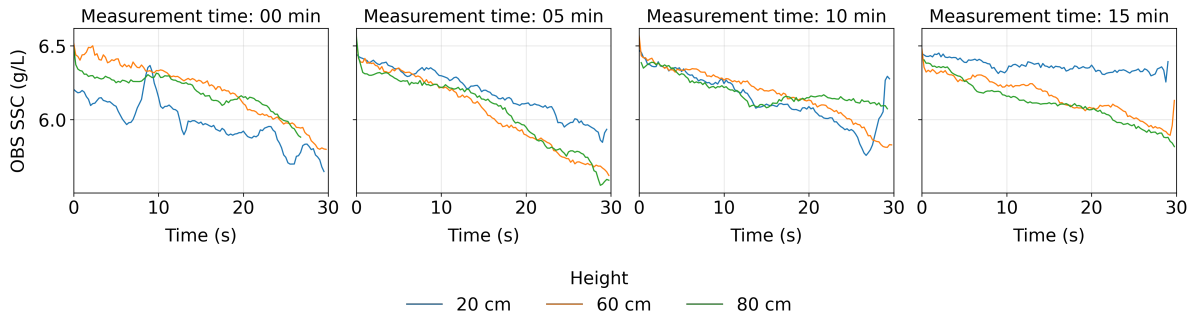

Figure 4.13: OBS measurements plots, representing the measurements at 3 measurement heights, and four measurement times. All measurements at gravimetric SSC= 8.873 g/L

LISST Data

The LISST-100X produced '.txt' files, which were imported and analysed in Python. Each measurement

consisted of a minimum of 120 profiles, from which representative particle size distributions were obtained. Due to the offline measurement configuration, the sensor was prone to measurement artefacts. Profiles containing these artefacts were excluded from further analysis. Affected profiles were identified based on PSD shapes that were inconsistent with physically realistic sediment size distributions.

In particular, these profiles exhibited a sudden increase in concentration in the largest size bins of the distribution following a large number of nearly empty bins, or showed strong variability from profile to profile. This behaviour was often correlated with measurements conducted at excessively high or low concentrations, or with profiles that had insufficient mixing within the chamber.

The affected profiles were flagged and removed prior to averaging to obtain a representative PSD for each measurement location and concentration. Examples of profiles affected by excessively high concentrations in the larger size bins, and strongly varying profiles due to concentration effects, are illustrated in Figure 4.14a and Figure 4.14b, respectively.

Therefore, three filters were applied to remove profiles affected by measurement artefacts:

- **Bin-wise standard deviation filter:** Profiles were removed when a particle size bin deviated by more than ± 2 standard deviations from the ensemble mean profile.
- **Low- and high-total-volume filter:** Profiles with a total particle volume below $10\,\mu L L^{-1}$ or above $50\,\mu L L^{-1}$ were removed.
- **Gap filter:** Profiles were removed when no particles were detected between 90 and 120 μm, while particles were simultaneously detected at sizes larger than 120 μm, indicating an anomalous discontinuity in the particle size distribution.

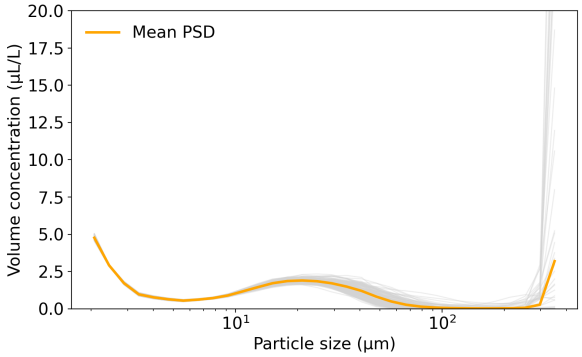

(a) Example of a faulty LISST profile exhibiting an artificial coarse-particle tail.

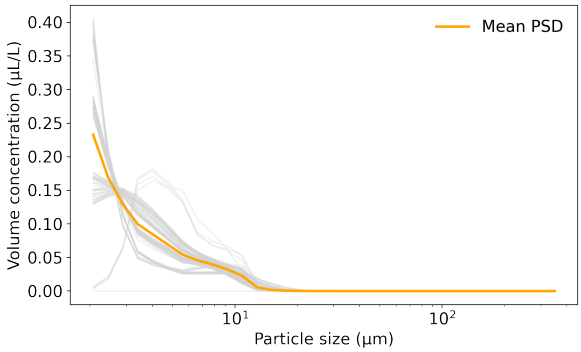

(b) Example of LISST profiles exhibiting distinct shapes due to differing total particle volume concentrations.

Figure 4.14: Examples of particle size distributions measured by the LISST-100X, containing large variations in distribution shape and final bin

5

Results and Analysis

The following chapter first presents the experimental conditions, followed by an evaluation of the optical sensor performance, the acoustic sensor range, and the four acoustic inversion methods investigated in this study. The chapter concludes with a comparison and summary of the inversion performance.

The experimental conditions are assessed to establish the achieved homogeneity and particle size evolution within the measured water column and thereby verify the assumptions underlying the acoustic analysis. The optical sensor performance is evaluated for comparison with the acoustic SSC measurements, while the acoustic sensor range establishes the range over which reliable acoustic measurements can be obtained. The four inversion methods are subsequently evaluated in terms of their ability to estimate particle size and SSC.

5.1. Experimental Conditions

5.1.1. Test Matrix

The suspended sediment concentration (SSC) is the primary parameter varied in this study. The SSC ranged from 0.576 to 31.98 g/L for the CCZ sediment and 0.160 to 17.38 g/L for Sediment B, with smaller SSC increments in the lower range and larger increments at higher concentrations. The suspended sediment concentrations were measured by the OBS sensor during the experiment and by gravimetric analysis in post processing. The gravimetrically determined SSC is considered the reference SSC throughout the present study, to which the OBS and ABS determined SSC are evaluated.

The gravimetrically determined SSC and the OBS-determined SSC are summarized in Table 5.1. All reported values represent the mean concentration over all measurement heights and measurement times for each concentration step. The SSC values are reported as the mean $\pm$ standard deviation. When only a single gravimetric sample was processed for a given SSC, the standard deviation is omitted. There are more OBS measurements than gravimetric measurements as not all gravimetric samples could be processed due to time and material constraints.

Table 5.1: Test matrix summarizing the target concentration, gravimetrically determined reference SSC, and OBS-derived SSC for both sediments.

Sediment	**Gravimetric SSC** (g/L)	**OBS SSC** (g/L)
CCZ Sediment	0.576 ± 0.073	0.598 ± 0.015
CCZ Sediment	1.250 ± 0.166	1.240 ± 0.027
CCZ Sediment	3.205	2.383 ± 0.031
CCZ Sediment	7.835	5.125 ± 0.128
CCZ Sediment	8.437 ± 0.612	6.309 ± 0.074
CCZ Sediment	14.920 ± 0.227	9.837 ± 0.281
CCZ Sediment	20.715	12.370 ± 0.396
CCZ Sediment	31.980	15.589 ± 0.322
Sediment B	–	0.120 ± 0.003
Sediment B	0.160	0.165 ± 0.005
Sediment B	0.247	0.288 ± 0.008
Sediment B	0.499	0.574 ± 0.015
Sediment B	0.626	0.828 ± 0.018
Sediment B	0.850 ± 0.019	1.028 ± 0.023
Sediment B	–	1.438 ± 0.039
Sediment B	–	2.079 ± 0.063
Sediment B	3.330	2.807 ± 0.085
Sediment B	–	4.338 ± 0.245
Sediment B	6.997 ± 0.195	5.460 ± 0.209
Sediment B	–	7.105 ± 0.167
Sediment B	9.514	9.251 ± 0.246
Sediment B	12.452 ± 0.129	10.728 ± 0.179
Sediment B	–	12.374 ± 0.611
Sediment B	17.377 ± 0.268	14.911 ± 0.397

5.1.2. Suspension Homogeneity

Suspension concentration homogeneity was assessed using OBS measurements taken at various locations along the tank walls and at the centre of the tank for two cases: CCZ sediment at 2 g/L and Sediment B at 0.8 g/L. The maximum variability in percentage from the total mean for Sediment B was 5.46 % and for the CCZ Sediment 1.82 % indicating a reasonably well mixed tank.

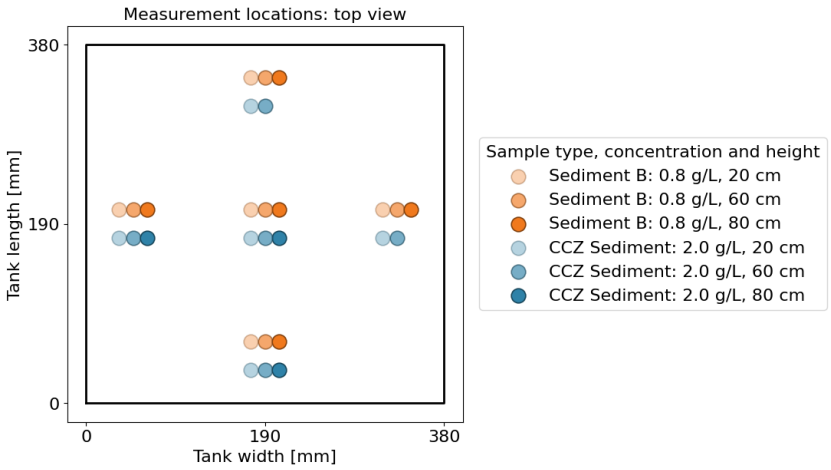

Figure 5.1: Gravimetric measurement locations inside the recirculation tank

Similarly, the spatio-temporal suspension concentration homogeneity was verified through gravimetric analysis during post-processing. At four concentration steps, samples were collected at three locations within the water column, namely, 0.2, 0.6, and 0.8 meters below the transducer. At each concentration step, a total of six samples were analysed (three at the beginning and three at the end of the experiment, with one sample collected at each height, described in Section **??**). The SSC gradient over the water column varied by an average of 4.93%, with a maximum deviation of 15.1%. The largest deviations were predominantly observed at the beginning of the experiments. No consistent vertical trend of SSC gradient with height was observed (See Appendix **??**), suggesting that the SSC fluctuated dynamically throughout the water column over time.

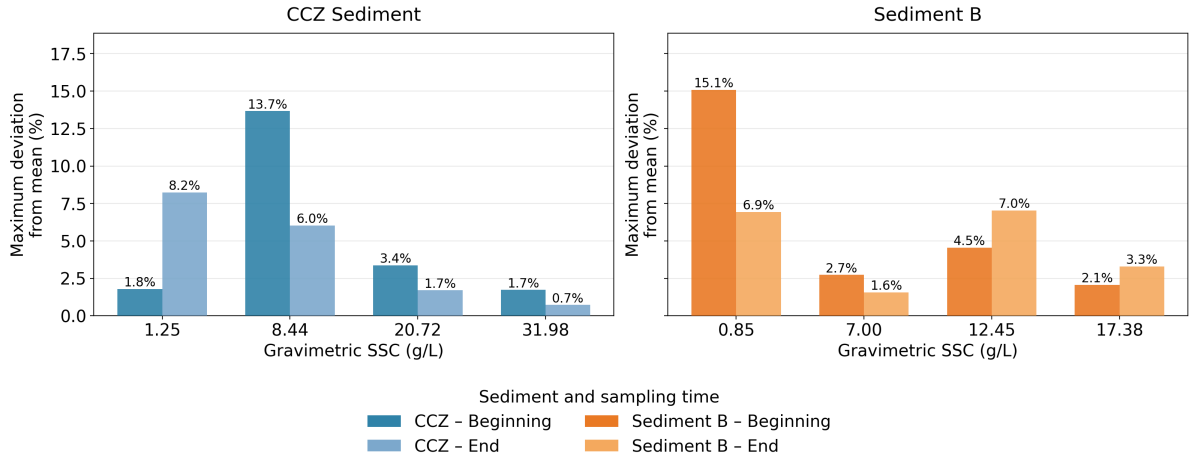

Figure 5.2: Maximum deviation from the mean gravimetric concentration across the three sampling heights at the beginning and end of the experiments for CCZ sediment and Sediment B.

The temporal stability of the SSC was assessed by comparing the mean gravimetrically determined SSC across all sampling heights at the beginning and end of each concentration step. The measured SSC remained within 10.2 % of its initial value, indicating that the suspension concentration remained relatively stable throughout the experiment.

5.1.3. Particle Size Evolution

Particle size distributions were measured at selected suspended sediment concentrations at ranges of 0.2 and 0.8 m below the transducers. In no case did the measured D_{10} increase. However, both the D_{50} and D_{90} increased with range in all cases indicating the occurrence of minor flocculation within the

water column. The largest observed increase in D_{50} was 23.9 % (2.4 μm), while the largest increase in D_{90} was 24.7 % (8.3 μm). Based on the tank's vertical bulk velocity of 0.96 cm/s, these changes developed over a transport time of approximately 62.5 seconds.

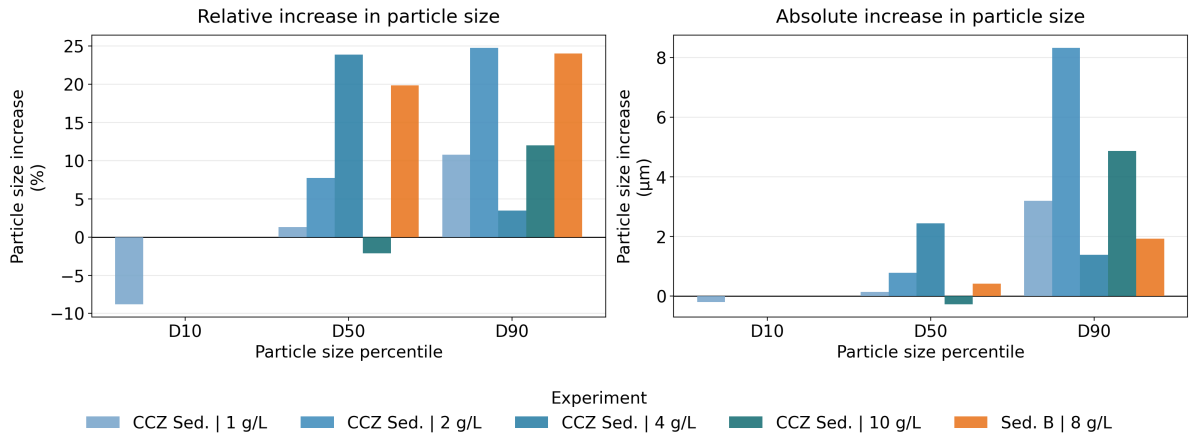

Figure 5.3: Relative and absolute increases in the D_{10}, D_{50}, and D_{90} particle size percentiles between measurement distances of 0.2 m and 0.8 m from the transducer (over 62.5 seconds). Positive values indicate an increase in particle size with distance from the transducer.

Although these results demonstrate measurable particle aggregation, the overall changes in particle size distribution remained relatively modest and within the natural variability typically observed for cohesive sediment plumes, indicating only a limited degree of flocculation during the experiments.

5.2. Evaluation Metrics

The investigated measurement and inversion methods are evaluated against the gravimetrically determined SSC and, where applicable, the measured particle parameters. As Methods 1 and 2 were assessed using commercial software and did not provide viable inversions over the investigated SSC range, their quantitative evaluation against the reference measurements is limited and focuses primarily on inversion sensitivity.

In contrast, Methods 3 and 4 provided quantifiable range-averaged SSC estimates and are therefore evaluated extensively using statistical metrics against the gravimetrically determined SSC. The point-based OBS measurements are evaluated using the same metrics to enable direct comparison. For both, the measured or inverted SSC is plotted against the gravimetrically determined SSC on a log-log scale to accommodate the wide investigated concentration range.

In these plots, perfect agreement is represented by the 1:1 relationship, shown as a solid black line. The performance of the investigated method is primarily evaluated using two metrics: the slope of the linear fit, which indicates the proportional bias relative to the ideal 1:1 relationship and therefore provides **a measure of accuracy**; and the coefficient of determination (R^2), which describes how well the linear model explains the observed data and therefore provides **a measure of precision**.

To assist the visual interpretation of the inversion performance, the uncertainty of the linear regression is represented by the $\pm 2\sigma_{\log}$ bounds, shown as a shaded region around the fitted line. Assuming normally distributed logarithmic residuals, these correspond to approximately 95.4 % confidence bounds. These uncertainty bounds can be visually compared with the $\pm 50\%$ bounds about the 1:1 relationship to assess whether the inversion results fall within this evaluation criterion. The $\pm 50\%$ bounds were selected as they represent a commonly accepted performance criterion for acoustic SSC measurements.

Additionally, the Root Mean Square Error (RMSE) and the Mean Absolute Relative Error (MARE) relative to the 1:1 line are reported to provide additional measures of overall model performance. The RMSE quantifies the average absolute deviation from the gravimetric SSC and is therefore dominated by larger errors at higher concentrations; whereas, the MARE quantifies the average relative deviation,

which assigns comparable weight to proportional errors across the entire concentration range, and therefore providing a more representative measure of performance at lower concentrations.

5.3. Sensor Performance

5.3.1. Optical Backscatter Sensor

In the following analysis, only the first and last OBS measurements were considered, as these correspond directly to the gravimetric samples. Figure 5.4 compares the OBS-derived SSC with the gravimetrically determined SSC, while Figure 5.5 shows the corresponding relative error, calculated as

$$\text{Relative error}(\%) = \frac{SSC_{\text{OBS}} - SSC_{\text{grav}}}{SSC_{\text{grav}}} \times 100 \tag{5.1}$$

For both sediments, the OBS generally overestimated SSC below approximately 1.2 g/L and underestimated SSC at higher concentrations. For Sediment B, the underestimation remained relatively proportional over the investigated range, resulting in a strong linear relationship with a slope of 0.857 and an R^2 of 0.993.

For the CCZ sediment, the underestimation became increasingly pronounced with increasing SSC. Over the full investigated range of $1.2 - 32.4$ g/L, this resulted in a slope of 0.546 and an R^2 of 0.884.

Restricting the CCZ sediment to $1.2 - 18.0$ g/L, thereby providing a consistent concentration range for comparison with Sediment B, increased the slope to 0.664 and the R^2 to 0.958. Thus, although the larger investigated concentration range partly explains the lower linearity observed for the CCZ sediment, the OBS continued to exhibit substantially greater underestimation than for Sediment B over the same SSC range.

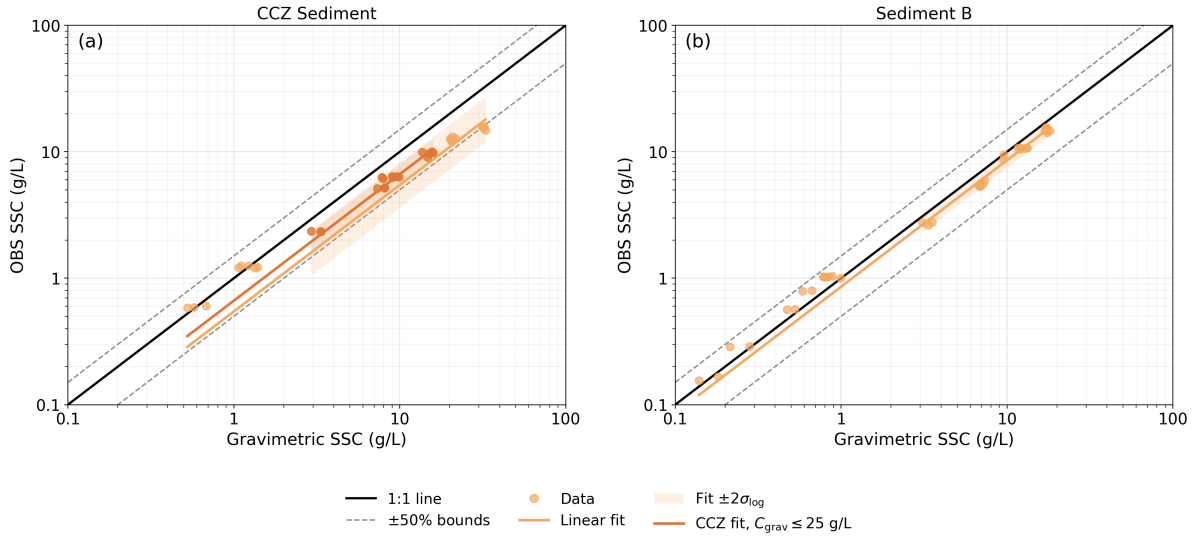

Figure 5.4: Comparison of the OBS-derived SSC with the gravimetrically determined SSC both the CCZ sediment (left) and Sediment B (right).

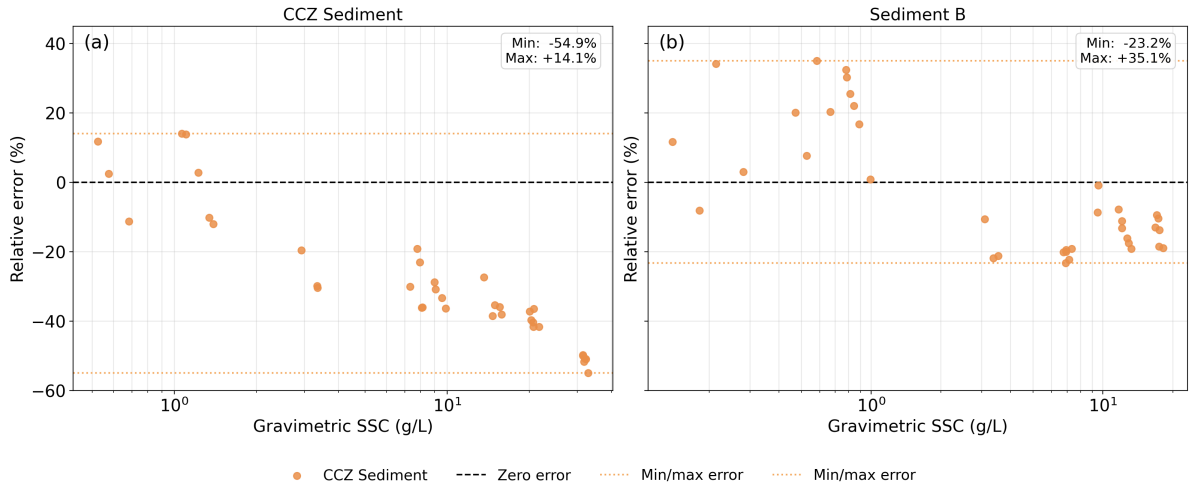

Figure 5.5: Relative error of the OBS-derived SSC as a function of the gravimetrically determined SSC.

Table 5.2: Performance metrics of the OBS measured SSC relative to the gravimetrically determined SSC

Case	**Slope**	R^2	**MARE** (%)	**RMSE** (g/L)
CCZ sediment $1.2 - 32.4$ g/L	0.546	0.884	37.0	8.77
CCZ sediment $1.2 - 18.0$ g/L	0.664	0.958	31.1	3.5
Sediment B $1.2 - 18.0$ g/L	0.857	0.993	15.4	1.79

5.3.2. Acoustic Sensor Range

The acoustic signal is subject to attenuation through viscous absorption and scattering losses. This effect is sediment specific and increases with increasing SSC, and higher frequencies are additionally more prone to attenuation. To evaluate the valid range in which inversion remains feasible, the maximum valid range per frequency is determined using an SNR threshold of 5, as described in Section 4.12. The resulting maximum ranges per frequency over the investigated SSC range are plotted for both sediments in Figure 5.6, where the horizontal dashed lines indicate the theoretical near-field limits of the transducers.

The maximum sensor acquisition range during the experimental campaign was set to 1.1 m for the CCZ sediment, and 1.6 m for Sediment B; and lower frequencies in low SSC ranges are restricted by this range rather than the actual measurement capability.

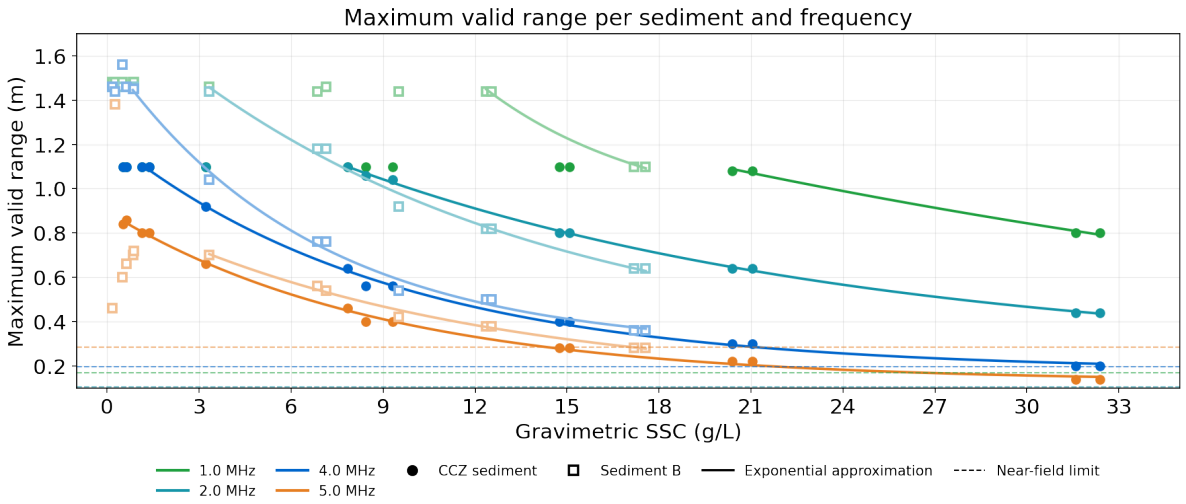

Figure 5.6: Maximum valid acoustic measurement range as a function of SSC for the 1, 2, 4, and 5 MHz transducers, shown for both CCZ sediment and Sediment B. Horizontal dashed lines indicate the theoretical near-field limits of each transducer, while solid lines represent exponential approximations of the measured trends.

At low concentrations, the 5 MHz transducer is limited by the weak backscatter signal generated by the suspension. Consequently, the received signal falls below the SNR threshold at shorter ranges and can no longer be reliably distinguished from the the noise generated by the micro-bubbles. For Sediment B, the maximum range reached 0.77 m at approximately 0.8 g/L, while for the CCZ sediment it reached 0.86 m at 0.5 g/L.

With increasing SSC, the valid maximum range decreases approximately exponentially, validating the expected attenuation behaviour described by the sonar equation (Equation 3.5). This behaviour is approximated by the regression $R_{max} = C + Ae^{-Bx}$, of which the constant parameters are summarized in Appendix B, which may assist in estimating the maximum valid measurement range for future experiments conducted under similar conditions. The 5 MHz transducer was affected most strongly by attenuation and therefore became entirely restricted to the near-field region at approximately 15 g/L for the CCZ sediment, whereas for Sediment B this occurred at approximately 17.5 g/L. Sediment B exhibited a slightly larger valid measurement range than the CCZ sediment, which is inconsistent with theory, as larger particle sizes are expected to experience lower attenuation and stronger backscatter. However, this difference is considered negligible given the uncertainty in the Python workflow, which determines the maximum valid range using the first range bin below the SNR threshold, potentially introducing a noticeable discretization error.

The maximum range over which the following inversions are performed are therefore limited by the maximum valid range of the highest included transducer frequency. For the CCZ sediment at 32.4 g/L, this range is reduced to only 5 cm, effectively limiting the inversion to a point measurement.

5.4. Bin-Based Inversion Methods

5.4.1. Method 1 - SSC and Particle Size Inversion

The following section presents the particle size estimates and SSC inversion results obtained with Method 1 using the commercial 'AQUAscat Toolkit' software. First, the particle size inversion results are presented, followed by the corresponding SSC inversion results.

The commercial software merely supports graphical outputs within the software environment, which limits the extent of the quantitative analysis through visual interpretation of the output plots. The values presented in the following sections were estimated as accurately as possible through visual interpretation of the plots.

Particle Size Inversion

Method 1 consistently overestimated the median particle size for both sediments. The closest agreement was obtained for the CCZ sediment at 0.576 g/L, where the inverted particle diameter was 4.1 and 6.1 times larger than the Malvern- and LISST-measured D_{50}, respectively. For Sediment B, the minimum overestimation was at 0.499 g/L and is substantially greater, with factors of 18.2 and 39.0 relative to the Malvern and LISST measurements, respectively. The inversion performance deteriorated further outside the intermediate SSC range, with estimates increasingly approaching the upper inversion bound of $D_{50} = 400\mu m$. Overall, Method 1 did not provide representative particle-size estimates for either sediment.

Effect of Frequency Combinations on the Particle Size Inversion

Selecting specific frequency combinations slightly improved the inversion stability over range, however the median particle diameters maintained similar overestimated values to the previous section. The closest agreement with the reference particle diameters was obtained using the 4 and 5 MHz for Sediment B, and 2 and 4 MHz for the CCZ sediment, yielding median particle diameters of 36 μm in both cases which is an overestimation of 8 and 2.4 relative to the Malvern.

For Sediment B, adding 2 MHz to the 4 and 5 MHz combination improved the inversion stability over range and time, but also increased the estimated particle size to 42 μm. In contrast, adding the 5 MHz to the 2 and 4 MHz combination for the CCZ sediment had little influence on the inversion. The complete frequency sensitivity analysis is presented in Appendix **??**.

Effect of Relative Standard Deviation ($Rel.SD$) on $D_{50}Inversion$

The particle size inversion also shows a strong sensitivity to the prescribed relative standard deviation. As an example, for Sediment B, the LISST-derived $Rel.SD$ of 0.2 resulted in an unstable particle size inversion, with the estimated particle radius exceeding 40 μm, whereas the Malvern-derived $Rel.SD$ of 1.0 resulted in particle radius estimates of approximately $10 - 15$ μm, representing a reduction of approximately 68.8 %. Generally, increasing $Rel.SD$ yielded lower particle radius estimates. With an artificial $Rel.SD$ of 3.0, the inverted particle radius reached its minimum of approximately 7 μm, which remains approximately 3.1 and 6.7 times larger than the equivalent particle radii measured by the Malvern and LISST, respectively.

SSC Inversion

The SSC was underestimated by approximately 1.2 and 2.0 orders of magnitude for the CCZ sediment at 0.576 g/L and Sediment B at 0.499 g/L, respectively. These results correspond to the cases with the lowest particle-size overestimation, for which the inverted particle diameter was still overestimated by factors of 4.1 and 18.2 relative to the Malvern measurements. Thus, even under the most favourable conditions, the method did not provide meaningful SSC estimates.

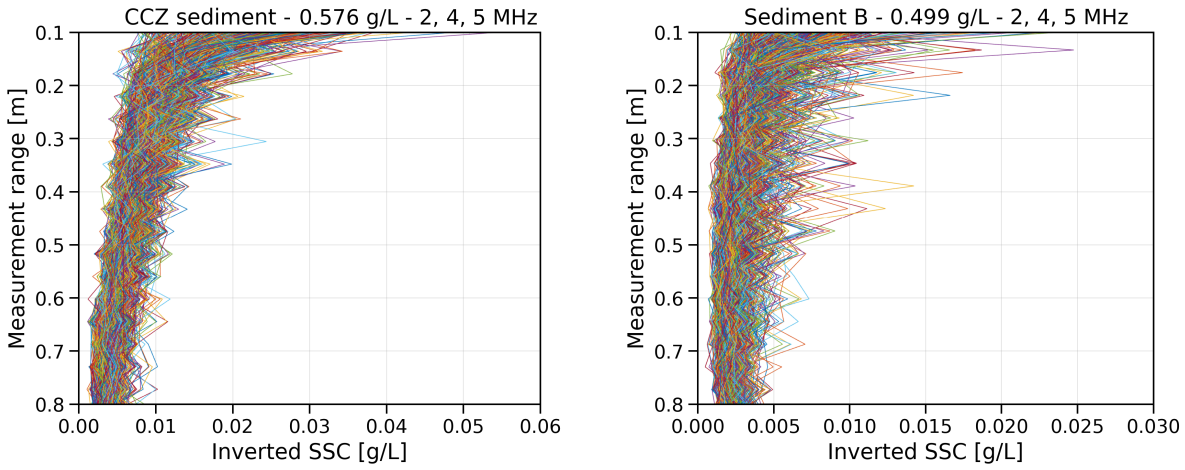

Figure 5.7: Multi-frequency SSC inversion results obtained using the 2, 4, and 5 MHz frequencies.

5.4.2. Method 2 - Prescribed Particle Size SSC Inversion

Similar to Method 1, Method 2 is also found to be highly sensitive to the prescribed particle parameters (D_{50} and $Rel.SD$), as well as to the selected frequency combination. Small deviations in the median particle diameter or Relative Standard Deviation lead to significant deviations in the mean inverted SSC over the measurement range, as well as significant SSC gradients over range, making it challenging to estimate a single representative inverted SSC for each test. These effects become increasingly unstable at suspended sediment concentrations above approximately 2 g/L, making meaningful quantification of the inversion performance impossible. Therefore, rather than quantifying inversion performance over the full concentration range, the following sections present the sensitivity of the inversion to the input parameters D_{50} and σ.

Sensitivity Assessment

The sensitivity to the prescribed particle parameters is evaluated by varying the median particle diameter (D_{50}) by $\pm 1\,\mu m$ and the Relative Standard Deviation ($Rel.SD$) by ± 0.1 about their Malvern-measured values. For Sediment B at 0.85 g/L, underestimating D_{50} by $1\mu m$ resulted in an SSC deviation of 185.7 %, while underestimating the $Rel.SD$ by 0.1 resulted in a deviation of up to 100 %. These results demonstrate the high sensitivity of the inversion to both prescribed particle parameters.

In addition, various frequency combinations were evaluated. Although the inversion response differed between the two sediments, consistent trends were observed. Lower frequencies generally produced higher SSC estimates with greater variation over the measurement range, whereas higher frequencies resulted in smoother, more consistent profiles with lower SSC estimates. Using the Malvern-measured particle parameters, the most accurate and stable results were obtained with the 1 and 2 MHz combination for the CCZ sediment at 1.25 g/L, and the 4 and 5 MHz combination for Sediment B at 0.85 g/L. However, the differing response to frequency selection should not be interpreted as evidence that specific frequency combinations are inherently better suited to either sediment. Rather, these differences are likely related to uncertainties in the prescribed particle parameters and the general instability of the inversion, which also varied with SSC.

The complete sensitivity analysis with representative examples are provided in Appendix D.

5.5. Profile-Averaged Inversion Methods

Methods 3 and 4 derive SSC and particle-size parameters from the intermediate acoustic parameters α_{sv} and s_v. This section therefore first evaluates the behaviour and reliability of the obtained parameters over range and with SSC, before assessing their influence on the performance of the following inversion methods 3 and 4.

5.5.1. Acoustic Parameter Assessment

Attenuation and Backscatter over Range

The linear regression to the FCB, and the average backscatter, fit the data reasonably well over the valid range, which reaffirms the suspension homogeneity assumption. Figure 5.8 shows an example of the fitted lines corresponding to the CCZ sediment at 3.21 g/L where the regression range still extends to the full data set of 0.7 meter. However, elevated concentrations rapidly decreased the range and data points over which the regression could be performed.

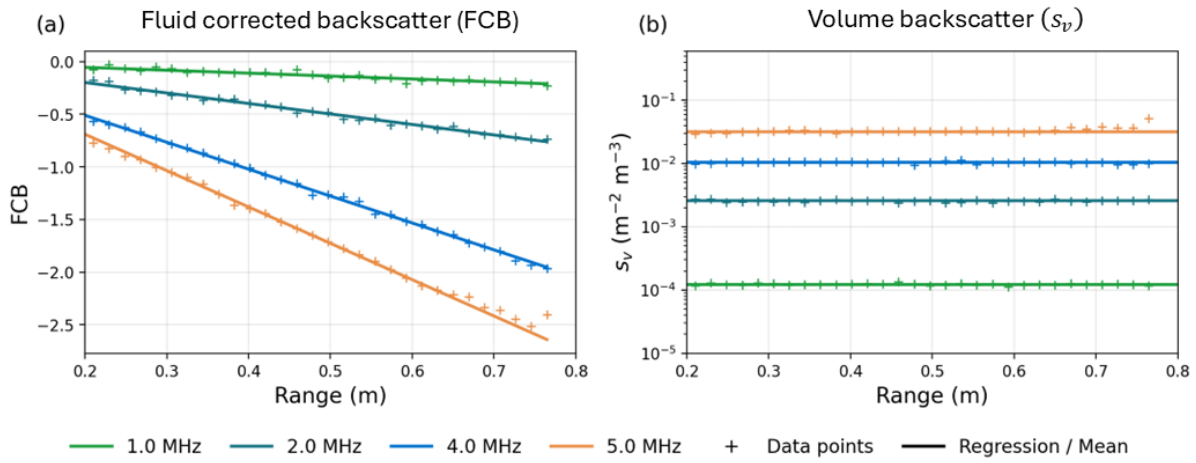

Figure 5.8: Example regressions for the CCZ sediment at 3.21 g/L. Plot (a) shows the linear regression to the Fluid corrected backscatter (FCB) of which the slope is used to derive the viscous sediment attenuation. Plot (b) shows the linear horizontal average regression to the micro-bubble corrected signal to obtain the volume backscatter coefficient.

Attenuation and Backscatter with SSC

The resulting α_{sv} and s_v are plotted as a function of SSC in Figure 5.9, together with the trend lines represented by the dotted lines. In both sediment cases, α_{sv} follows a steady near-linear increase with SSC, particularly for the 2, 4, and 5 MHz frequencies, which is consistent with the assumption that multiple scattering (MSCAT) remained limited over the measurement range. However, the weaker and sometimes non-linear trends between s_v and SSC do not provide equally strong support for this assumption. Specifically, for the CCZ sediment, which extends to higher SSC values up to 32.4 g/L, the 4 and 5 MHz backscatter coefficients decrease above approximately 18.0 g/L, whereas the 1 and 2 MHz frequencies continue to increase with SSC. The greater variability in volume backscatter, s_v, may also reflect the intrinsically weak backscatter response of fine sediments, variations in scattering properties, and the propagation of uncertainty from the estimated attenuation term. These factors and the potential physical causes of the observed behaviour are discussed in Section 6.

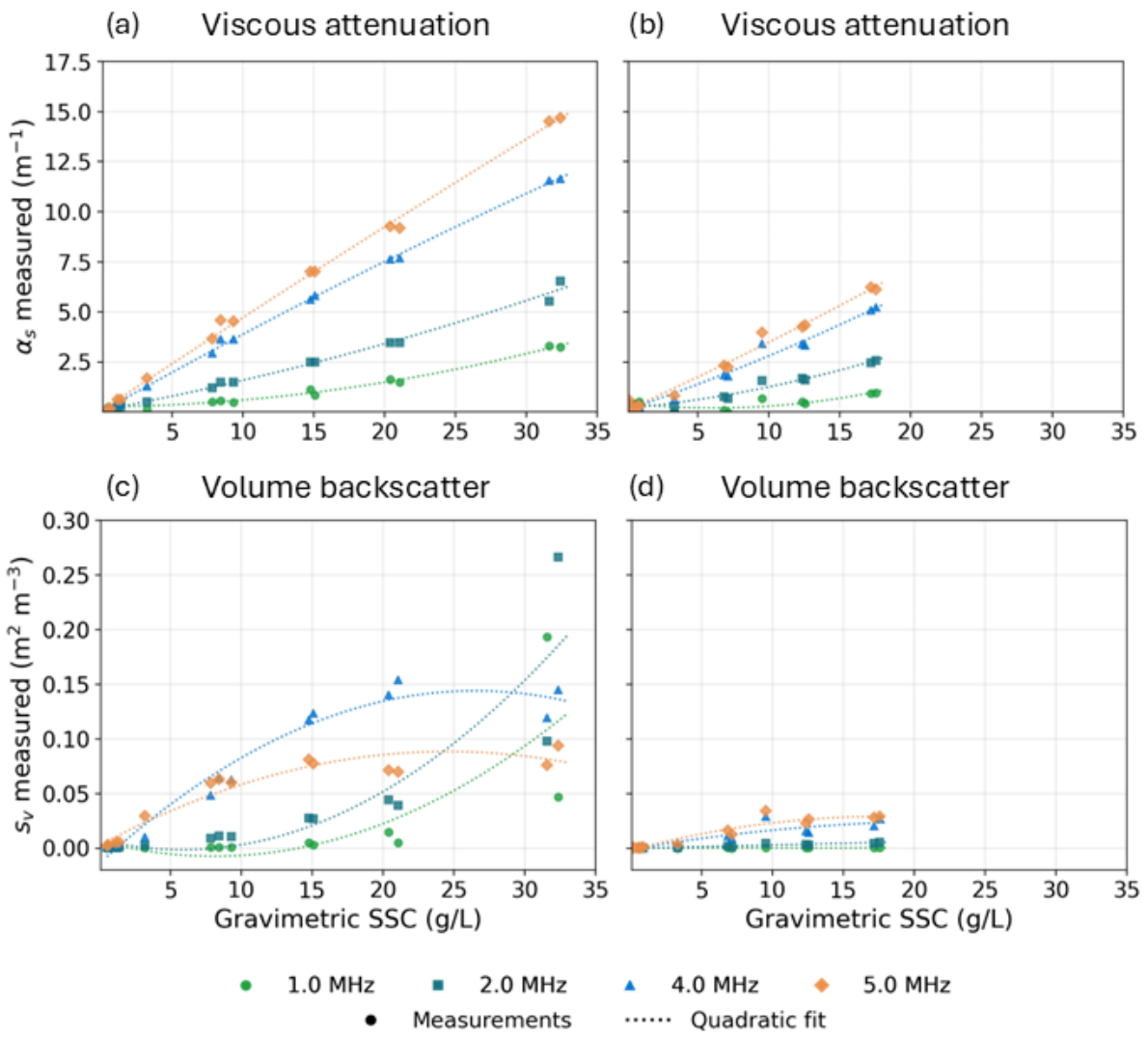

Figure 5.9: Plots (a) and (b) show the viscous sediment attenuation as a function of suspended sediment concentration for the CCZ sediment and Sediment B, respectively. Plots (c) and (d) show the corresponding volume backscatter coefficient as a function of suspended sediment concentration. The dotted lines represent quadratic least-squares fits included as visual guides to the observed trends.

Figure 5.10 presents the attenuation and backscatter results in log-log space. The logarithmic representation provides greater resolution over the full investigated SSC range and reveals that the 2, 4, and 5 MHz frequencies exhibit an approximately linear relationship with SSC between 0.5 and 18.0 g/L (shaded region in Figure 5.10). Below and above this range, the measurements increasingly deviate from the fitted linear trends. The 1 MHz frequency exhibits the greatest scatter, particularly below 1.4 g/L.

Based on these observations, the concentration range of $0.5 - 18.0$ g/L is adopted as the primary analysis range for the regression analyses and uncertainty bounds presented in the remainder of this study. Measurements below 0.5 g/L are excluded because they fall outside the intended operational concentration range and exhibit increased variability. Since the CCZ sediment was investigated up to 32.4 g/L, whereas Sediment B extended to approximately 18.0 g/L, regression statistics for the CCZ sediment are presented for both the full 0.532 g/L range and the reduced $0.518.0$ g/L range to enable a consistent comparison between the two sediments.

Although the 1 MHz frequency exhibits greater variability than the higher frequencies below approximately 1.4 g/L, its relatively low contribution to the inversion generally limits its impact on the estimated SSC, with only a limited effect on inversion performance in most cases.

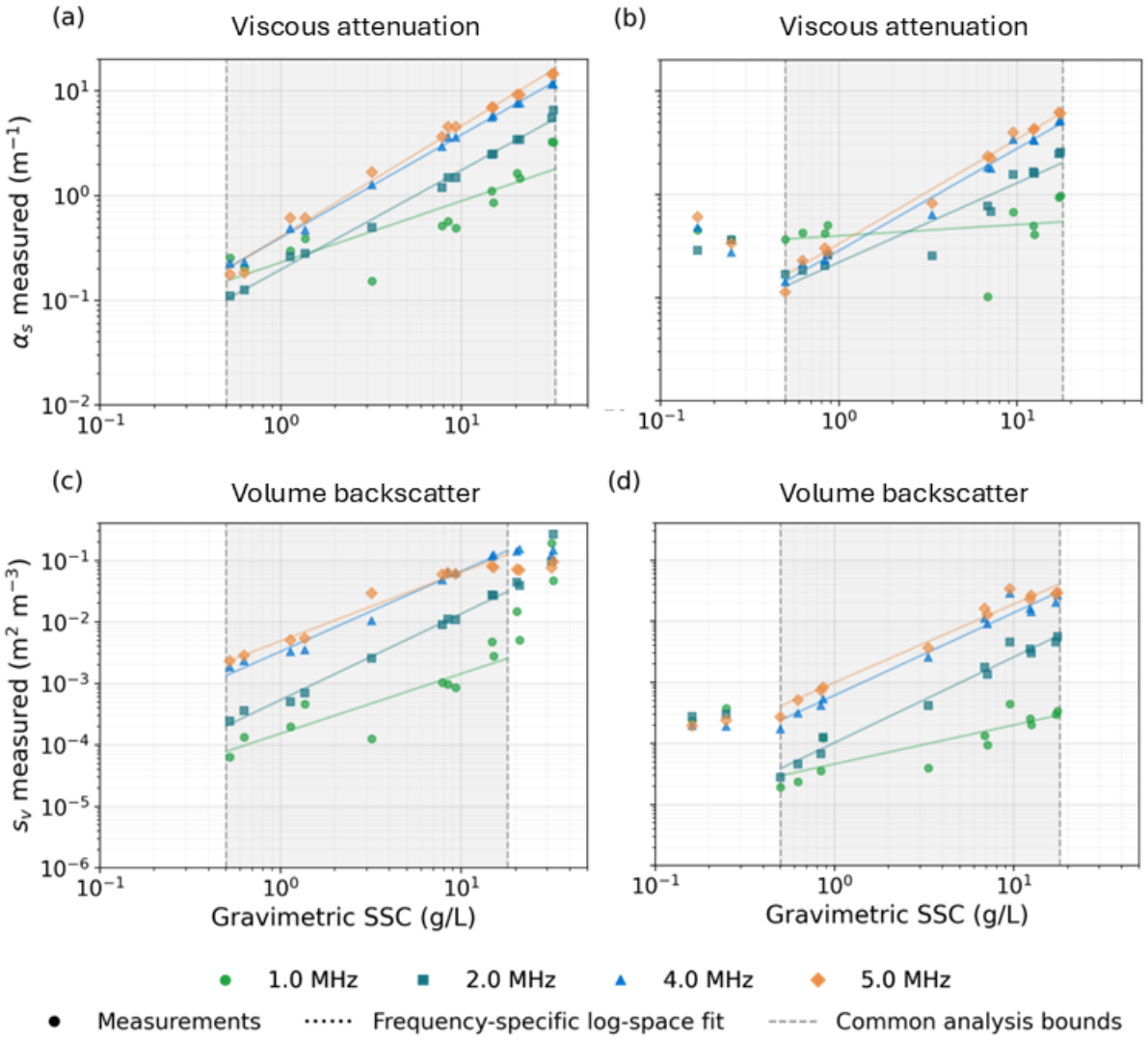

Figure 5.10: Plots (a) and (b) show viscous sediment attenuation as a function of suspended sediment concentration for the CCZ sediment and Sediment B, respectively. Plots (c) and (d) show the corresponding volume backscatter coefficient as a function of suspended sediment concentration. The shaded region indicates the range in which the frequencies give the most consistent results. All plots are in log-log scale.

For consistency with previous studies [30], the slope and R^2 values of the linear regressions are summarized in Appendix A.

5.5.2. Method 3 - Attenuation α_{sv} and Backscatter s_v Based Inversion

This method applies a minimization function to both the attenuation and backscatter estimates through the objective function (E) to determine the suspended sediment concentration (SSC), median particle diameter (D_{50}), and standard deviation of the log-normal distribution (σ).

Method 3.1: Single Log-Normal Distribution

Method 3.1 represents the particle size distribution using a single log-normal distribution, characterized by the median particle diameter (D_{50}) and distribution width (σ). As the solution space may not be unique, the sensitivity of the inversion to prescribed information of the particle parameters is evaluated using four cases: (1) both D_{50} and σ unconstrained, (2) D_{50} constrained, (3) σ constrained, and (4) both D_{50} and σ constrained. The unconstrained iteration ranges are $1 - 40\mu m$ for D_{50} in 60 logarithmic steps and $0.1 - 2.0$ for σ in steps of 0.05, while the constrained ranges are defined by the minimum and maximum particle parameters measured using the LISST and Malvern. Larger search ranges,

extending to 100 μm, were attempted as well, however this did not affect the inversion results, therefore the previously defined range was maintained to reduce computational time.

Unconstrained Inversion

Without particle parameter constraints the inversion overestimated the SSC for both sediments. Over the range of $0.5-18.0$ g/L, slopes of 1.530 and 1.090 were obtained for the CCZ sediment and Sediment B, respectively. The corresponding R^2 values of 0.872 and 0.889 indicate that the general SSC trend was captured despite the proportional bias. In the case of the CCZ sediment, extending the range to 32.4 g/L improved the proportional bias and precision to a slope of 1.311 and an R^2 value of 0.916, indicating that the results up to this concentration can still be viable.

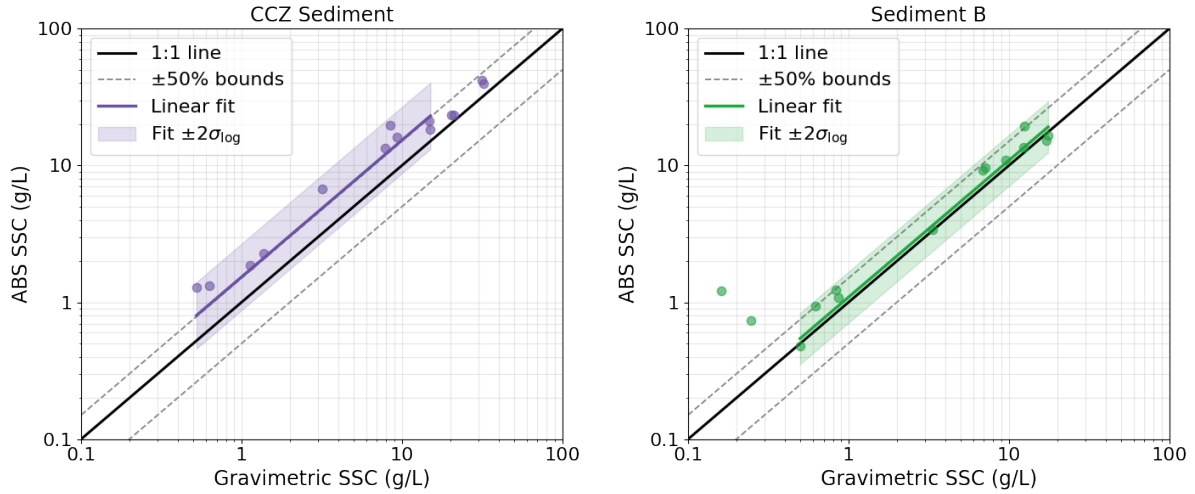

Figure 5.11: Comparison of the inverted SSC against the gravimetric SSC model outputs for the CCZ sediment and Sediment B

For the CCZ sediment the inverted D_{50} was underestimated by approximately a factor of two relative to the LISST measurements and a factor of three relative to the Malvern measurements.

For Sediment B the estimated median particle diameter and standard deviation is 4.51 μm and 0.94 (-), respectively. These parameters correspond well with the parameters measured by the Malvern, which measured a particle size of 4.5 μm and distribution width of 0.8 (-).

Overall, the inverted particle parameters were considerably less stable and relatively scattered around the mean value. Below 0.8 g/L for Sediment B and 1.4 g/L for the CCZ sediment, the inversion estimated larger particle diameters and low distribution widths. Above this concentration, the opposite occurred. Overall, the particle diameter and distribution widths exhibited an inverse relationship to each other, where one parameter compensated in value for the other.

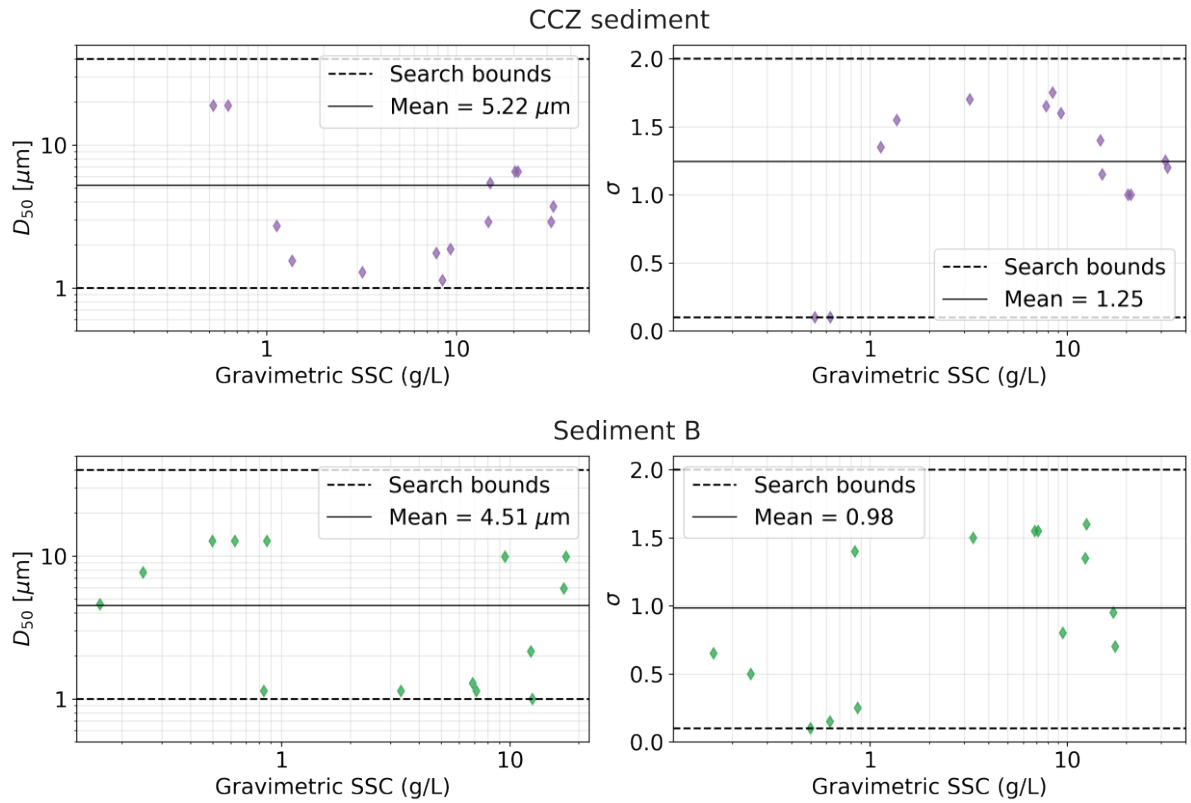

Figure 5.12: Inverted particle-size distribution parameters without constraints for the CCZ sediement (purple) and Sediment B (green). The left panels present the particle-size inversion and the right panels the distribution-width inversion.

It was found that the inversion method is highly sensitive to small errors and that multiple combinations of particle size and distribution width can produce similar SSC solutions. This non-uniqueness is illustrated in Figure 5.13. A 2 % variation in the objective function around the minimum corresponds to a D_{50} range of approximately $4.5 - 9\ \mu m$ (a 100 % variation) and a σ range of $0.9 - 1.2$ (a 33.3 % variation), while the corresponding SSC remains within approximately 2 %. The inverted particle parameters are therefore considerably more sensitive than the SSC estimate to small variations in the objective function, with minor changes in error potentially resulting in large changes in the estimated D_{50} and σ.

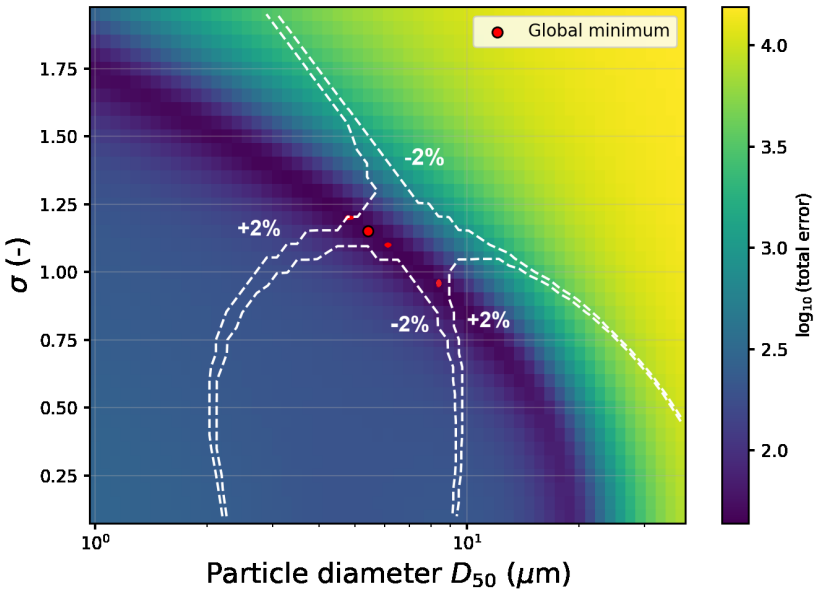

Figure 5.13: Overlay of the total objective-function error and best-fit SSC solution space for the CCZ sediment. The red contours (appearing as dots at this scale) indicate a $2\,\%$ increase relative to the minimum objective-function error, while the white contours indicate a $\pm 2\,\%$ variation in inverted SSC relative to the global minimum.

Influence of Particle-Parameter Constraints

Figure 5.14 compares the four solution-space constraint cases. Constraining D_{50} produced the most consistent improvement in SSC inversion performance. For the CCZ sediment, the R^2 increased from 0.872 to 0.995 over $0.5 - 18.0$ g/L, while the proportional overestimation relative to the 1:1 relationship decreased from 53.0 % to 36.1 %. A similar improvement was observed for Sediment B, for which constraining D_{50} reduced the proportional overestimation from 9.0 % to only 1.2 %.

Constraining only σ consistently improved precision but had a less consistent effect on accuracy. For the CCZ sediment, the SSC overestimation increased, whereas for Sediment B the slope decreased to 0.947, corresponding to an underestimation of 5.3 %. Constraining both parameters resulted in SSC underestimation for both sediments and, for the CCZ sediment, a substantial deterioration in performance above 18.0 g/L. Overall, constraining D_{50} provided the most consistent improvement in both accuracy and precision, whereas constraining σ primarily improved precision without consistently improving accuracy.

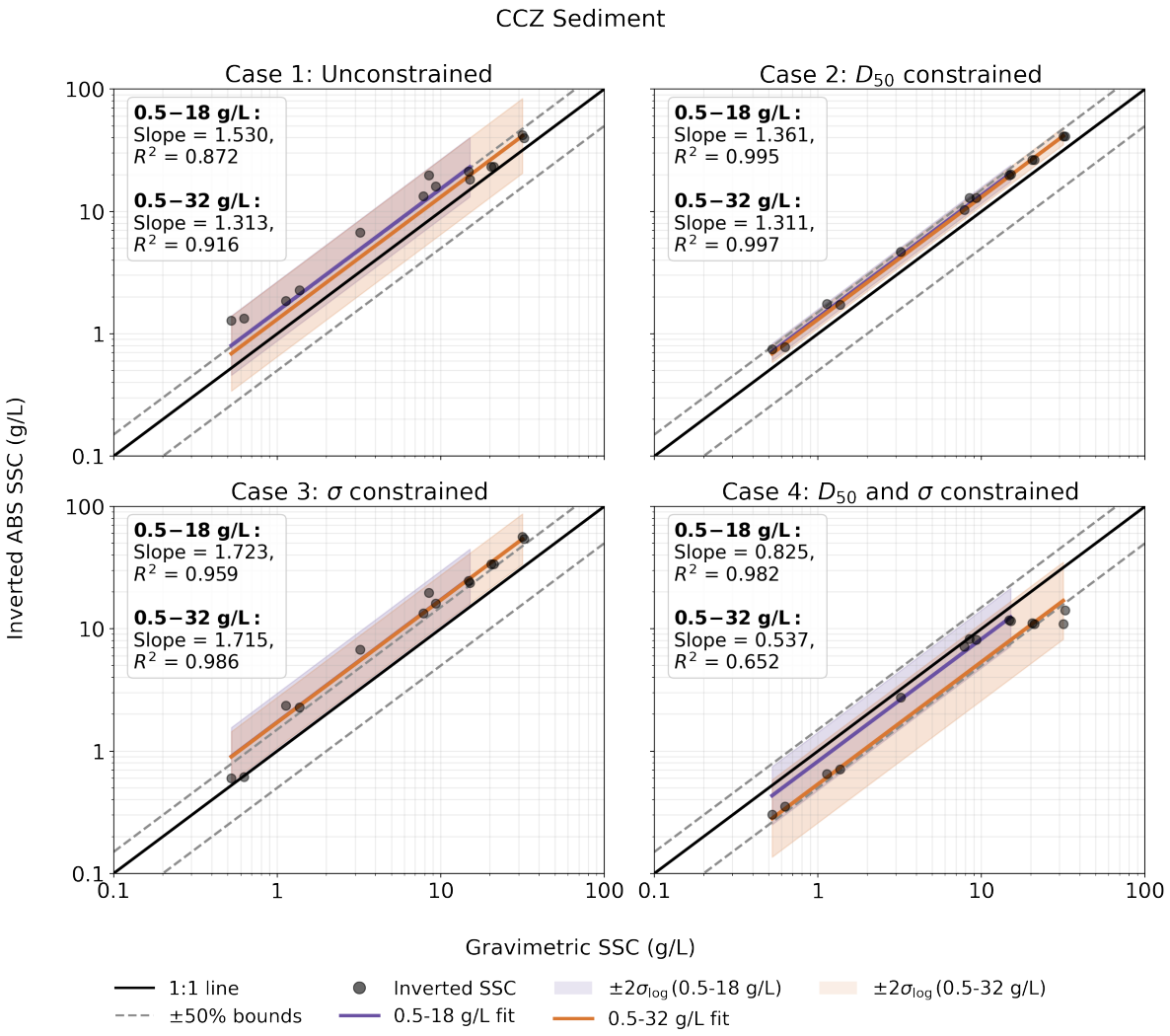

Figure 5.14: Influence of particle-size distribution constraints on the Method 3.1 SSC inversion. Case 1 is unconstrained, Case 2 constrains D_{50}, Case 3 constrains σ, and Case 4 constrains both parameters. For the CCZ sediment, regressions are presented over both $0.5 - 18.0$ g/L and the full $0.5 - 32.4$ g/L concentration range.

The complete performance metrics and inverted particle-size parameters for all constraint cases are provided in Appendix E.

Effect of Frequency Combinations

The effect of various frequency combinations was evaluated using the unconstrained inversion (Case 1). For both sediments over $0.5 - 18.0$ g/L, combinations containing the higher frequencies generally resulted in the highest accuracy. For the CCZ sediment, the 4 and 5 MHz combination produced the lowest overestimation, with a slope of 1.367 ($R^2 = 0.957$). For Sediment B, additionally including the 2 MHz frequency resulted in the highest accuracy, with a slope of 1.079 ($R^2 = 0.895$).

The improved performance at higher frequencies is consistent with their greater sensitivity to finer particles in the sediment. However, including lower frequencies generally increased rather than decreased the inverted SSC. For the particle-size and distribution-width inversions, frequency selection did not substantially improve either the accuracy or stability of the estimates.

Method 3.2: Bi-modal Distribution

The bi-modal inversion underestimated SSC for both sediments, with slopes of 0.847 and 0.590 for the CCZ sediment and Sediment B, respectively. A similar tendency towards underestimation was

observed for the spherical model applied in Method 4 (next section), an effect of the spherical particle approximation. The corresponding R^2 values of 0.924 and 0.962 were comparable to those of the unconstrained single log-normal inversion (Method 3.1, Case 1). Thus, the additional flexibility in representing the particle size distribution did not improve the SSC inversion performance.

The resulting particle size distributions are provided in Appendix E.

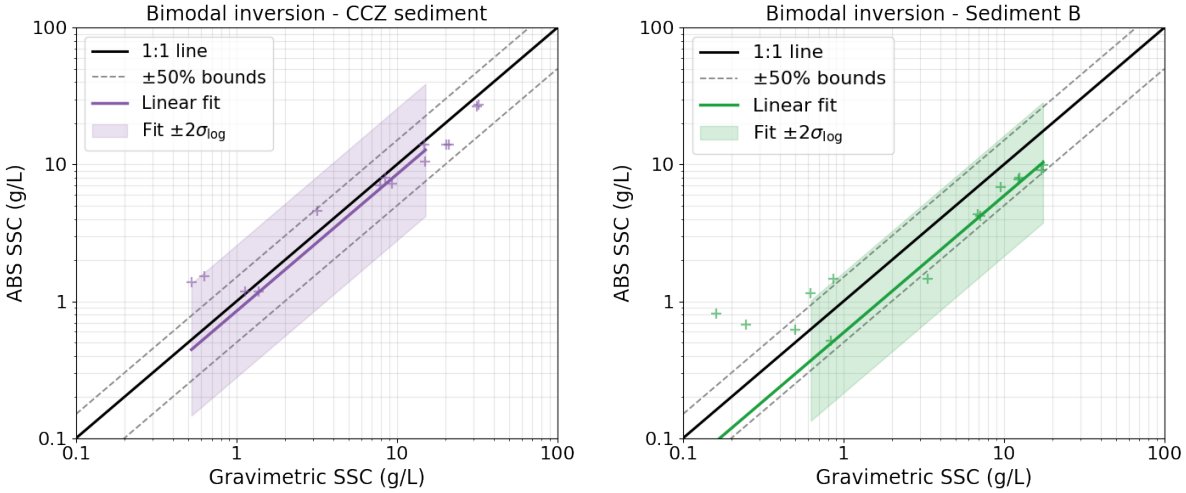

Figure 5.15: Comparison of the bi-modal distribution model against the gravimetric SSC for the CCZ sediment and Sediment B

Table 5.3: Performance metrics of Method 3 for the CCZ sediment and Sediment B with a bi-modal defined distribution.

Sediment	Slope	R^2	MARE (%)	RMSE (g/L)
CCZ sediment $0.5 - 32.4$ g/L	0.804	0.966	38.2	3.5
CCZ sediment $0.5 - 18.0$ g/L	0.847	0.924	43.8	1.72
Sediment B $0.5 - 18.0$ g/L	0.590	0.962	80.6	3.72

5.5.3. Method 4 - Attenuation(α_{sv}) Based Inversion

In contrast to Method 3, Method 4 applies a minimization algorithm based solely on the attenuation term (α_{sv}), omitting the more noise-sensitive backscatter term (s_v). The objective function therefore contains less acoustic information, but potentially information of higher quality. Methods 4.2 and 4.4 are evaluated using the same four solution-space constraint cases as Method 3 (Section 5.5.2). Methods 4.1 and 4.3 require the distribution width to be fixed to a single value and are therefore evaluated using the exact values measured by the LISST and Malvern.

The combination of four sub-methods and multiple constraint cases resulted in a large number of inversion results. The complete set of plots and performance metrics (slope, R^2, MARE, and RMSE) is therefore provided in Appendix F, while the most representative results are summarized in Table F.7. All summarized results are based on the Φ objective function, which generally produced higher and more consistent SSC estimates than the Γ objective function.

Effect of Attenuation Model

Between the two attenuation models, the oblate-spheroidal model (Methods 4.3 and 4.4) produced the most accurate results for both sediments (Table F.7). In contrast, the spherical model (Methods 4.1 and 4.2) consistently underestimated the SSC and generally with lower precision.

Effect of D_{50} and σ Constraints

The two sediments responded differently to the particle-size and distribution-width constraints. For the CCZ sediment, the highest accuracy and precision were obtained without constraining either parameter, whereas Sediment B performed best when both the particle size and distribution width were constrained to the Malvern-measured values. Nevertheless, prescribing only the particle size resulted in comparable performance for the CCZ sediment and substantially improved performance for Sediment B relative to the respective unconstrained cases. Further constraining the distribution width reduced the accuracy for the CCZ sediment and provided only a minor additional improvement for Sediment B. This again demonstrates the strong influence of the prescribed particle size on the inversion performance, whereas constraining the distribution width provides limited additional benefit or even a decrease in accuracy.

Table 5.4: Effect of particle-size and distribution-width constraints on the performance of the oblate-spheroidal attenuation model.

Sediment	Constraint	Method	Slope	$\mathbf{R^2}$	MARE (%)	RMSE (g/L)
CCZ	None	4.4	1.046	0.952	34.5	1.20
CCZ	D_{50}	4.4	1.098	0.944	62.6	1.50
CCZ	D_{50} + σ Malvern	4.3	1.344	0.966	74.7	3.11
Sediment B	None	4.4	0.721	0.573	189.4	3.91
Sediment B	D_{50}	4.4	0.845	0.867	272.3	2.20
Sediment B	D_{50} + σ (Malvern)	4.3	0.871	0.884	253.3	2.03

The inverted median particle diameters and distribution widths for all cases remained highly scattered. Both parameters frequently reached their prescribed upper bounds of $D_{50} = 40$ µm and $\sigma = 2$, indicating that the lack of backscatter information yields a reduction in inversion performance of the particle size and distribution width.

This is particularly noticeable in Sediment B, measurements below 0.84 g/L demonstrated significantly higher SSC inversions and varying particle size results than above this concentration. This can be observed visually in the plots (See Appendix F) but also through the MARE and RMSE values.

Effect of LISST and Malvern Prescribed Distribution Width

In Method 4.1 and 4.3 the distribution width was constrained to the single value of either the LISST or the Malvern. Constraining the distribution width to the Malvern-measured value consistently resulted in better inversion performance than using the LISST-measured value. This difference was particularly pronounced for Sediment B, which showed greater sensitivity to the prescribed distribution width. This is likely related to the substantial difference between the distribution widths measured by the Malvern ($\sigma = 0.8$) and LISST ($\sigma = 0.2$).

5.6. Summary of Inversion Results

Combining the findings from the analysis of the inversion method results, it can be concluded that Methods 1 and 2 are of insufficient quality for meaningful inversions of both particle size and SSC. In contrast, Methods 3.1, 4.3, and 4.4 yielded consistent and quantifiable estimates of SSC, particle size, and distribution width.

Method 3.1 yielded a very strong fit to the linear approximation over the entire range. Including measurements above 18.0 g/L improved the fit even further. Overall, excellent precision was obtained when the particle size was constrained. In the best case, it produced excellent accuracy for Sediment B (slope = 1.012, R^2 = 0.978) and reduced accuracy for the CCZ sediment (slope = 1.361, R^2 = 0.995).

Methods 4.3 and 4.4, which are based on the oblate sphere model, consistently showed the improved accuracy and precision relative to Methods 4.1 and 4.2. The overall precision of the linear fit was lower compared to Method 3.1, and the particle parameter inversion included a larger overall scatter, indicating that the backscatter term in Method 3.1 has a beneficial effect on precision and particle parameter inversion. Again, like Method 3.1, constraining the particle size had a significant beneficial

effect, whereas constraining the distribution width resulted in little improvement or even performance degradation.Considering the D_{50} constrained case as the preferred configuration, Method 4.4 produced excellent accuracy for the CCZ sediment (slope = 1.098, $R^2 = 0.944$) and good agreement for Sediment B (slope = 0.845, $R^2 = 0.867$).

Methods 4.1 and 4.2, based on the spherical model, consistently underestimated SSC and demonstrated decreased performance relative to the oblate sphere model, confirming that the spherical approximation is not an appropriate approximation for fine deep-sea sediments.

Like Method 4.1 and 4.2, Method 3.2 reflected the underestimation associated with the spherical model as well; and the bi-modal distribution, which allows for more flexibility in particle size characterization, did not improve the inversion of the particle size parameters. Instead it yielded an even greater scatter.

Overall, constraining only D_{50} provided the most consistent improvement in inversion performance across both sediments and inversion methods. Constraining σ generally provided limited additional benefit to accuracy and, in some cases, reduced the inversion accuracy, while constraining both parameters led to over constraining the inversion above 18.0 g/L. This indicates that D_{50} is the most dominant and reliable PSD parameter controlling SSC inversion performance. Therefore, the D_{50}-constrained configurations of Methods 3.1 and 4.4 are selected as the representative configurations in the Discussion and Conclusion.

Over the common SSC range of $0.5 - 18.0$ g/L, with particle size constrained, Method 3.1 showed a proportional bias of $+1.2\,\%$ for Sediment B and $+36.1\,\%$ for the CCZ sediment. Method 4.4 showed a proportional bias of $-15.5\,\%$ and $+9.8\,\%$, respectively. For the CCZ sediment, extending the evaluated range to $0.5 - 32.4$ g/L changed the proportional bias to $+31.1\,\%$ for Method 3.1 and $+19.2\,\%$ for Method 4.4.

Overall, the proportional bias of the selected D_{50}-constrained inversion methods remained within $\pm 36.1\%$ across both sediments and evaluated SSC ranges.

Table F.7 summarizes the performance metrics of Methods 3.1, 3.2, 4.3, and 4.4. Only the results of Method 4.3 and 4.4 using the Φ objective function are presented, as it consistently outperformed the Γ function. To improve readability and interpretation, Methods 4.1 and 4.2 are omitted from the summary, as they produced comparable or poorer results. The complete set of inversion results is provided in Appendix F.

Table 5.5: Performance metrics of Methods 3 and 4 for the CCZ sediment and Sediment B. Method 3 evaluates different particle size distribution constraints, while Method 4 evaluates the attenuation-based sub-methods for different constraints on D_{50} and σ. Method 4 results are based on the Φ objective function.

Sediment	SSC range	Constraint	Model	Slope	R^2	MARE (%)	RMSE (g/L)
Method 3.1 - Single-mode distribution							
CCZ sediment	0.5–32	–	Oblate	1.311	0.916	69.0	5.49
CCZ sediment	0.5–18.0	–	Oblate	1.530	0.872	84.0	5.20
Sediment B	0.5–18.0	–	Oblate	1.090	0.889	24.5	2.35
CCZ sediment	0.5–32	D_{50}	Oblate	1.311	0.997	36.2	4.39
CCZ sediment	0.5–18.0	D_{50}	Oblate	1.361	0.995	38.4	3.02
Sediment B	0.5–18.0	D_{50}	Oblate	1.012	0.978	10.7	0.92
CCZ sediment	0.5–32	σ	Oblate	1.715	0.986	69.8	10.16
CCZ sediment	0.5–18.0	σ	Oblate	1.723	0.959	70.3	6.24
Sediment B	0.5–18.0	σ	Oblate	0.947	0.976	18.5	1.09
CCZ sediment	0.5–32	D_{50}, σ	Oblate	0.537	0.652	32.1	7.02
CCZ sediment	0.5–18.0	D_{50}, σ	Oblate	0.825	0.982	25.9	1.56
Sediment B	0.5–18.0	D_{50}, σ	Oblate	0.762	0.987	26.5	2.46
Method 3.2 - Bi-modal distribution							
CCZ sediment	0.5–32	–	Spherical	0.804	0.966	38.2	3.50
CCZ sediment	0.5–18.0	–	Spherical	0.847	0.924	43.8	1.72
Sediment B	0.5–18.0	–	Spherical	0.590	0.962	80.6	3.72
Method 4.3 - Single-mode distribution							
CCZ sediment	0.5–32	σ (LISST)	Oblate	1.301	0.902	71.0	6.31
CCZ sediment	0.5–18.0	σ (LISST)	Oblate	1.657	0.860	91.7	6.41
Sediment B	0.5–18.0	σ (LISST)	Oblate	0.728	0.594	185.8	3.80
CCZ sediment	0.5–32	D_{50}, σ (Malvern)	Oblate	1.264	0.985	59.5	4.51
CCZ sediment	0.5–18.0	D_{50}, σ (Malvern)	Oblate	1.344	0.966	74.7	3.11
Sediment B	0.5–18.0	D_{50}, σ (Malvern)	Oblate	0.871	0.884	253.3	2.03
Method 4.4 - Single-mode distribution							
CCZ sediment	0.5–32	–	Oblate	0.901	0.956	29.0	2.47
CCZ sediment	0.5–18.0	–	Oblate	1.046	0.952	34.5	1.20
Sediment B	0.5–18.0	–	Oblate	0.721	0.573	189.4	3.91
CCZ sediment	0.5–32	D_{50}	Oblate	1.192	0.983	49.9	3.49
CCZ sediment	0.5–18.0	D_{50}	Oblate	1.098	0.944	62.6	1.50
Sediment B	0.5–18.0	D_{50}	Oblate	0.845	0.867	272.3	2.20

6

Discussion

6.1. Influence of Echo Statistics on Acoustic Inversion

The sonar equation (Equation 3.12) assumes that the received echo is the result of many randomly distributed scatterers (incoherent scattering). Under these conditions, and provided that no individual scatterer dominates the received signal, the echo amplitude is expected to approximately follow a Rayleigh distribution.

Figure 6.1 provides a representative example of a measurement for which all frequencies contained sufficient information up to 0.6 m from the transducer. Deviations from the theoretical Rayleigh distribution are observed at both ends of the echo-amplitude spectrum, becoming more pronounced at lower frequencies and larger ranges. In particular, the deviation at high echo amplitudes indicates that the received signal was influenced by a relatively small number of strong scatterers, violating the assumption of randomly distributed scatterers underlying the Rayleigh distribution.

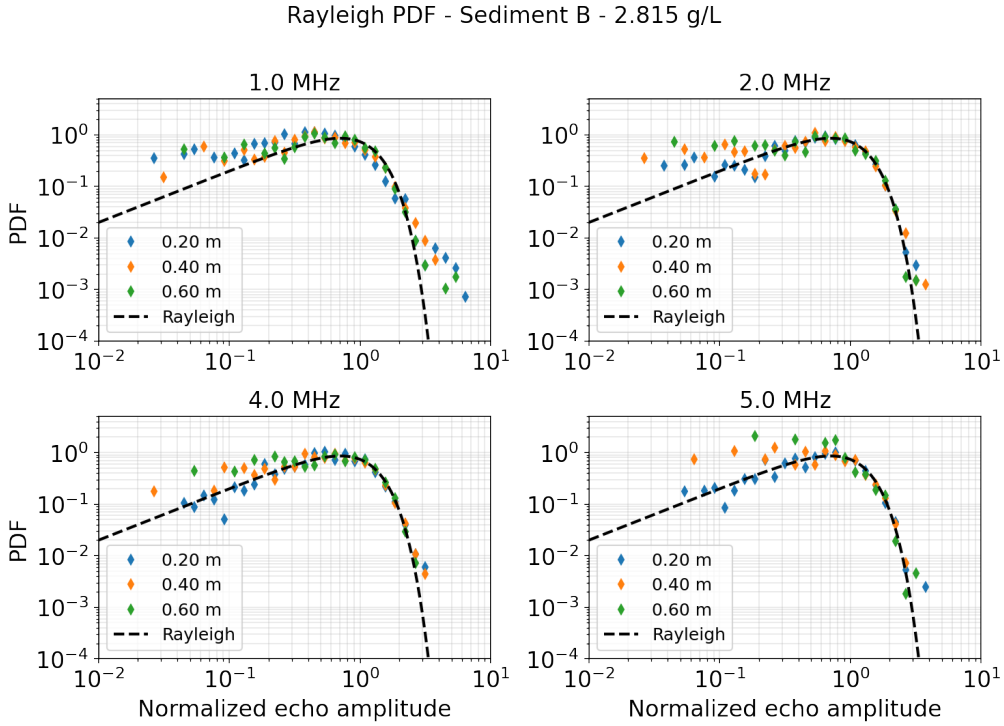

Figure 6.1: Probability density function of the normalized echo amplitude for the 1, 2, 4, and 5 MHz transducers at measurement ranges of 0.2, 0.4, and 0.6 m. The dashed black line represents the theoretical Rayleigh distribution.

It was also considered that the stronger deviation observed at 1 MHz may be partially influenced by reflections from the tank walls. However, similar deviations are observed at higher suspended sediment concentrations and at higher frequencies, for which wall reflections are less likely to dominate. Wall reflections are therefore unlikely to be the sole cause of the observed deviations.

The raw acoustic measurements shown in Figure 6.2 give further insight to the origin of these strong scatterers. The 1, 2, and 4 MHz transducers show distinct diagonal features corresponding to larger particle fragments settling through the water column over time. Additional smaller features close to the transducers also appear to move upwards and may represent particles transported by the turbulent flow at the top or larger micro-bubbles. The continuous recirculation of the suspension, including larger nodule fragments, may therefore have contributed to the departure from Rayleigh-distributed scattering observed in Figure 6.1.

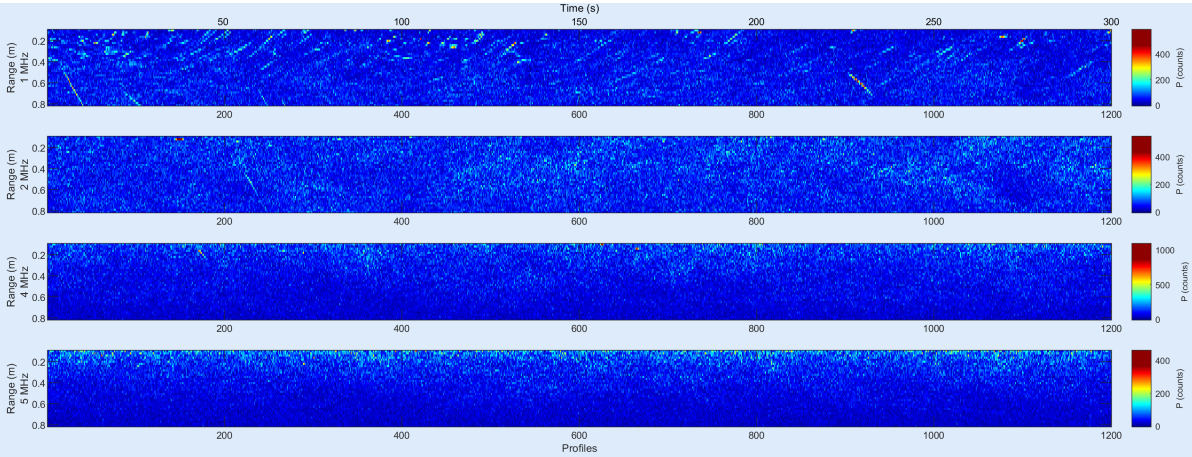

Figure 6.2: Raw acoustic data in counts over time and range, showing scattering structures associated with larger particles moving through the water column. A larger scale version of this figure can be found in Appendix **??**

Deviations from Rayleigh-distributed scattering are a known challenge when applying acoustic methods to natural sediments with broad particle size distributions. Although the fine sediment fraction investigated in this study, dominated by clay and silt, can generally be considered relatively narrow, the presence of nodule fines and larger fragments introduces strong scatterers that may produce similar effects to broad distribution sediments. The strong scatterers may therefore have affected the inferred form function ratio and contributed to the particle-size overestimation observed for Method 1. Methods 3 and 4 are expected to be less sensitive to individual strong scatterers because the full measurement period is temporally averaged into a single quadratically averaged profile, with α_{sv} subsequently determined from a linear regression.

6.2. Influence of α_{sv} and s_v on Inversion Performance

By back-calculating the theoretical attenuation (α_{sv}) and backscatter (s_v) from the best-fit inverted SSC and particle-size parameters (D_{50} and σ), the measured acoustic parameters can then be compared directly with their best-fit theoretical values to determine whether the deviations observed in the measured attenuation and backscatter (Section 5.5.2) can be explained by the theoretical sediment response.

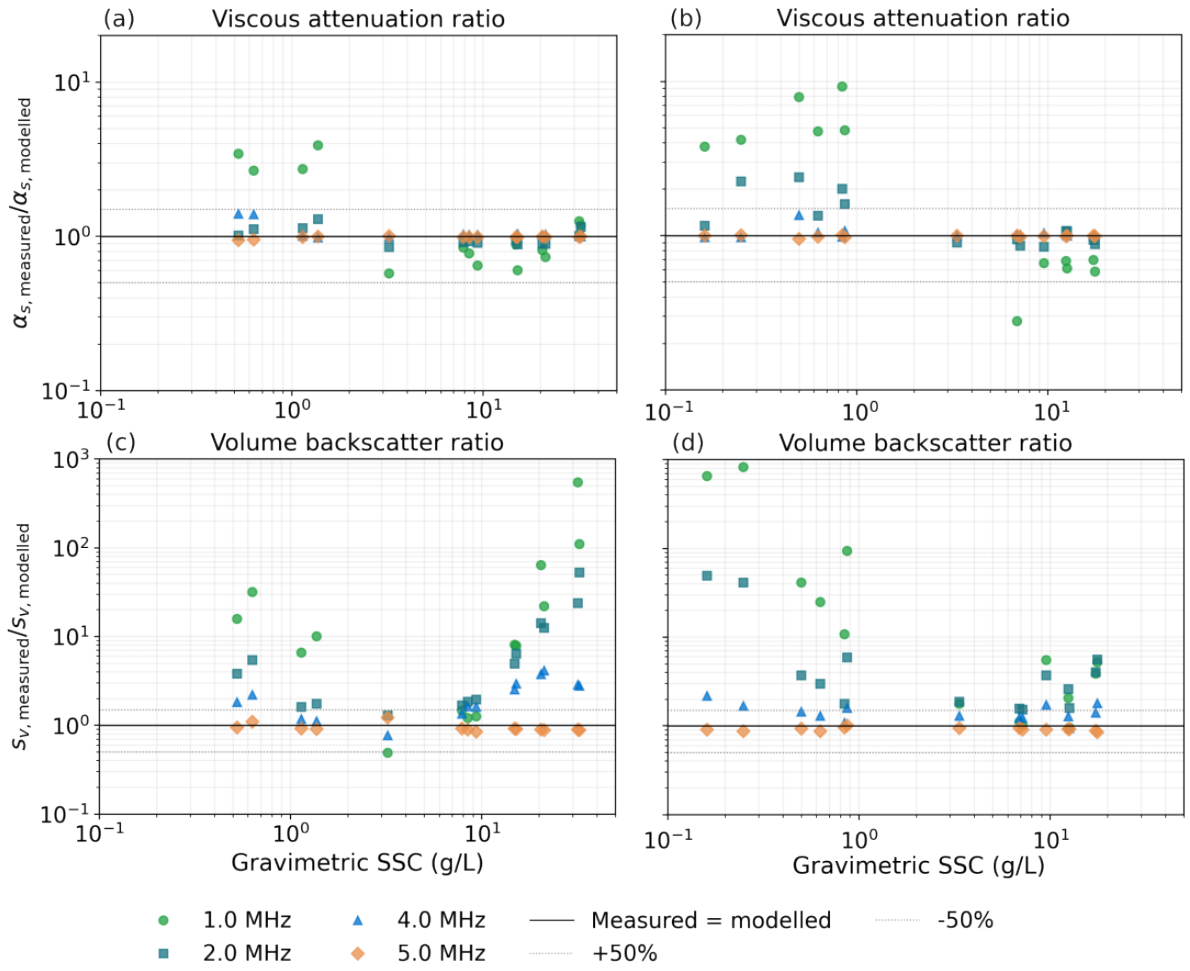

Figure 6.3: Plots (a) and (b) show the ratio of measured to modelled viscous sediment attenuation for the CCZ sediment and Sediment B, respectively, while plots (c) and (d) show the corresponding ratios for the volume backscatter coefficient.

Figure 6.3 shows that the 1 and 2 MHz frequencies deviate substantially from the theoretical attenuation and backscatter, particularly below approximately 1.5 g/L and above 18.0 g/L. In contrast, the 4 and 5 MHz frequencies generally show better agreement with the theoretical values. The poor linearity previously observed for the lower frequencies can therefore not be explained by the expected theoretical sediment response, suggesting that these measurements are more strongly affected by experimental or signal-related uncertainty rather than representing a physical sediment response. This interpretation is also consistent with the improved precision of Method 3.1 when the 1 MHz frequency is omitted (Section 5.5.2).

The deviations outside $0.5 - 18.0$ g/L are likely associated with limitations of the experimental setup. Below 0.5 g/L, reflections from the tank may have contributed to the deviations particularly in lower frequencies. Above 18.0 g/L, the reduced valid measurement range increases sensitivity to local SSC variations and near-field effects. Additionally, uncertainty in the backscatter term may be the result of changes in sediment composition due to the potential increased amount of nodule fragments present in higher SSC. Finally, the increased overestimation of the backscatter term relative to the attenuation term is, however, also inherent to this method, as errors in measured attenuation propagate into the backscatter calculation.

Effect of Particle Size Oblateness (h)

The oblateness of the particles is defined by the spheroidal aspect ratio (h), which is the ratio between the radii of the two principal axes. In Method 3, the ratio increases linearly from $h = 1/40$ to $h = 1$ for

particle diameters between 1 μm and 30 μm, whereas in Method 4 the particle oblateness is constrained to either $h = 1$ (spheres) or $h = 1/40$ (oblate spheroids). This difference in the particle shape definition should be considered when comparing the two methods. This study did not attempt to implement a variable oblateness in Method 4; however, doing so would make the comparison between Methods 3 and 4 more consistent. The effect of introducing a variable oblateness is therefore expected to yield SSC estimates between those obtained for the spherical and oblate assumptions. Based on the results obtained for these two limiting cases, this would likely reduce the inversion accuracy for both sediments.

6.3. Experimental Uncertainty

Uncertainty in SSC Measurements

The inversion results should be interpreted in the context of the experimental uncertainties present throughout this study. The repeated gravimetric measurements showed uncertainties of 8.57 % at 1 g/L, decreasing to $1.43 - 1.54$% at $6 - 12$ g/L. In addition, vertical SSC variations within the tank were generally below 8%, although local deviations reached 15.1 %, while temporal variations of up to 10.2 % were observed during the experiments.

Although these uncertainties do not directly accumulate, they demonstrate that variability in the reference SSC remained even under controlled experimental conditions. Therefore, deviations between the inverted and gravimetrically determined SSC cannot be attributed solely to the performance of the inversion method. Variability up to 15.1 % should be considered with caution, whereas systematic deviations exceeding this variability are more likely to represent limitations in the inversion method.

Uncertainty in PSD Measurements

The particle size distributions measured by the LISST and Malvern should also be interpreted with caution. The LISST, in it's offline configuration introduces several potential sources of uncertainty due to temperature, salinity, and concentration gradients, which can lead to erroneous particle size distribution profiles and skew the results. Handling the samples from the tank to the LISST measurement chamber may also introduce flocculation or floc breakup. Even the Malvern, which has a larger measurement range and more measurement steps, and is commonly considered to provide the representative particle size distribution, yielded largely varying particle size distributions depending on the disaggregation method. The disaggregation by vibration yielded a D_{50} of 20.36 μm, whereas the disaggregation by shear yielded a D_{50} of 15.24 μm, a 33.6 % variation.

Even the post-processing method can have a significant influence on the determined particle parameters. Fitting a single-mode Gaussian Mixture Model (GMM) [68], to the measured particle size distributions resulted in noticeable deviations from the parameters determined by means of RMSE minimization cumulative and RMSE optimization determined distributions. The largest differences were observed for the Sediment B LISST measurements, where the fitted median particle diameter differed by 47.6% and the distribution width by 200% relative to cumulative and RMSE determined parameters.

Table 6.1: Summary of the measured and single-mode Gaussian mixture model (GMM) [30, 68] fitted particle size distribution parameters used for the acoustic modelling.

Sediment	Instrument	Method	D_{50} (μm)	σ
CCZ sediment	LISST-100X	Measured	10.2	2.0
CCZ sediment	LISST-100X	Single-mode GMM	9.6	1.2
CCZ sediment	Malvern Mastersizer 3000	Measured	15.2	1.5
CCZ sediment	Malvern Mastersizer 3000	Single-mode GMM	14.3	1.3
Sediment B	LISST-100X	Measured	2.1	0.2
Sediment B	LISST-100X	Single-mode GMM	3.1	0.6
Sediment B	Malvern Mastersizer 3000	Measured	4.5	0.8
Sediment B	Malvern Mastersizer 3000	Single-mode GMM	5.4	1.1

6.4. Factors Influencing OBS Measurement Performance

The OBS overestimated SSC below approximately 1.2 g/L and underestimated the SSC above this SSC threshold. The underestimation increased with SSC for the CCZ sediment, whereas the Sediment B exhibited a relatively constant proportional bias over the lower and higher investigated SSC range (See Figure5.4).

A first possible explanation is a change in suspension characteristics between the calibration and concentration experiments. Optical backscatter sensors are sensitive not only to sediment concentration but also to particle size, shape, and optical properties. Theory indicates that an increased fraction of larger particles leads to a decreased sensor output [26, 69]. If the sediment used during the experiments contained relatively coarser particles than during calibration, a lower backscatter signal would be produced for the same suspended sediment concentration, resulting in an underestimation during the experiment. However, during the calibration process the degree of flocculation in the beaker was not assessed, and it is therefore not possible to conclusively assess the degree of flocculation relative to the experimental setup.

Another possible explanation is that the gravimetric samples collected during the calibration procedure underestimated the true SSC. During calibration, samples were collected by submerging the sampling bottle from the top into the beaker. If a vertical concentration gradient was present, with lower SSC near the surface, these samples may have contained a lower sediment concentration than the water measured by the OBS. Consequently, the OBS response would have been calibrated against artificially low reference SSC values, resulting in a systematic underestimation of SSC during the experimental campaign. This calibration method is currently the industry standard and would benefit of an uncertainty assessment.

Errors during the filtration and drying process are excluded, as these procedures were identical for both the calibration and experimental samples. The differences between filter types was 1.54 % and is therefore also excluded.

Another hypothesis for the underestimation observed for both sediments is an increased fraction of low-reflectivity and/or larger nodule fines during the experiments. Nodule fines were audibly observed to undergo mechanical degradation in the pumps, potentially altering the suspension composition and reducing the OBS response. This may also explain the increasing underestimation observed for the CCZ sediment, which contained substantially more nodules than Sediment B and therefore introduced more nodule fines at higher SSC. Research into the optical response to nodule fines is required.

For the CCZ sediment, an additional source of uncertainty is that the sensor calibration was performed in 2020 during the experimental campaign of Gillard et al. Gillard and Laurenz [19] and was assumed to remain representative of the sediment properties. Between the calibration and the current exper-

imental campaign, the sediment underwent substantial handling, which may have altered its particle characteristics and reduced the representativeness of the original calibration.

These results demonstrate that although the sensor possesses a high sensitivity to fine sediments, its reliability is only as strong as the quality of the calibration. They highlight the challenges of calibrating an optical backscatter sensor for specific sediment plumes, where even small differences in sediment properties between the calibration and testing measurement conditions can impose significant uncertainties.

6.5. Representativeness of Experimental Setup

The experimental conditions should also be interpreted in the context of their representativeness for deep-sea nodule collection operations. As previously described, it is likely that the recirculation of sediments in this experiment may have produced more nodule fines through pump induced nodule breakage and reintroduced them at the top of the water column. These conditions may have contributed to the OBS underestimation through changes in sediment optical properties, while simultaneously causing the heavy-tailed echo statistics observed in the ABS measurements. During actual nodule collection operations, the horizontal flow in the diffuser is expected to allow larger particles to settle out to a larger extent before reaching the sensors. additionally, the laboratory experiments were performed under relatively low vertical bulk velocity of 0.96 cm/s, whereas local velocities within the diffuser of a deep-sea nodule collector are expected to reach approximately $0.3 - 0.5$ m/s. Consequently, the sensor will continuously sample freshly discharged sediment rather than recirculated sediment. Based on a transport distance of 1.55 m in the laboratory and approximately 6 m in the diffuser, the residence time prior to measurement decreases from approximately 78 s to 12 s. As a result, particle aggregation and flocculation are expected to be less developed under operational conditions. Furthermore, micro-bubbles are not expected under hydrostatic pressures present in the deep sea, removing an additional source of acoustic measurement uncertainty.

6.6. Suitability of Multi-Frequency ABS for Deep-sea Nodule Collection

The primary objective of monitoring the diffuser is to quantify the average discharged sediment load and, if possible, also the particle size. These parameters define the initial conditions of the emitted plume and therefore influence its subsequent transport, dilution, aggregation, and settling behaviour (see Section 2). The monitoring system should therefore be capable of measuring suspended sediment concentrations up to 18.0 g/L, and preferably higher to account for potential fluctuations, while providing measurements representative of the entire diffuser height.

Consequently, the commercially available inversion approaches investigated in this study, Methods 1 and 2, are not considered suitable for operational deployment under the investigated conditions. Method 1 consistently overestimated the particle size, which propagated into unrealistic SSC estimates. Method 2, based on a prescribed particle size, remained highly sensitive to the prescribed particle size and distribution width, resulting in unrealistic SSC values and gradients throughout the measurement range. Furthermore, both methods only produced interpretable results up to approximately 7.8 g/L, which is considerably below the upper SSC expected during nodule collection operations. These methods may remain suitable for applications involving coarser sediments, where the frequency-dependent form function is more pronounced, but they are not considered technically feasible for monitoring deep-sea nodule collection plumes.

Methods 3.1 and 4.4, however, are considered more promising for this application. Based on the D_{50} constrained cases the proportional bias remained within $\pm 36\,\%$ across both sediments and investigated ranges.

Under operational conditions, all methods are expected to perform better than observed in this study, as micro-bubbles are not expected under deep-sea hydrostatic pressures, removing an additional source of acoustic measurement uncertainty. The horizontal flow may also allow larger fragments to settle before reaching the sensor.

One of the least favourable and under-reported characteristics of this sensor is the loss of measure-

ment range when operating at the highest frequencies. The maximum profile range is restricted by the maximum range of the highest frequency, which is approximately 0.3 m at 18.0 g/L, reducing the effectiveness of a profile measurement. The range could potentially be slightly improved by increasing the receive gain (R_x) [30], although this was not assessed in the present study.

A key consideration for operational monitoring is the installation location and orientation of the acoustic sensor. The vertically mounted configuration used in this study is not recommended for operational conditions, as a potential vertical concentration gradient can bias the attenuation estimate in Methods 3 and 4 and subsequently influence the inversion. A horizontal installation is expected to minimize this effect and provide measurements that are more representative of the bulk diffuser discharge. Because the acoustic beam width is approximately 0.3 m, it should be noted that a single sensor would observe only part of the approximately 1 meter wide diffuser. Installing multiple sensors within a single diffuser is not considered feasible due to inter-sensor interference. Furthermore, the experiments demonstrated that confined environments particularly affect the lower two frequency transducers through wall reflections. Consequently, mounting the sensor in high proximity, but outside, the diffuser is expected to provide a better compromise between representative plume measurements and measurement quality.

Overall, the results demonstrate that multi-frequency acoustic backscatter inversions through Methods 3.1 and 4.4 is a promising technique for monitoring suspended sediment plumes. Compared to conventional optical backscatter sensors, it provides a larger measurement range, reduced sensitivity to lens fouling, the potential to estimate particle size and distribution width (although currently with considerable uncertainty), and most importantly, does not require sediment-specific calibration beforehand. Therefore, the results of this study indicate that, with further development and validation under representative operational conditions, multi-frequency acoustic sensors have significant potential as a practical monitoring technology for deep-sea nodule collection plumes.

7

Conclusions

This study investigated the applicability of a multi high-frequency acoustic backscatter sensor for the inversion of the suspended sediment concentration (SSC) and representative particle size parameters (D_{50} and σ) in deep-sea sediment plumes. Experimental tests were conducted using a newly developed recirculation tank and two representative deep-sea box-core sediment samples: referred to as CCZ sediment and Sediment B. The sensor was evaluated over a suspended sediment concentration range of $0.16 - 32.37$ g/L to generate data representative of deep-sea mining plume conditions. Four inversion methods were evaluated. Method 1 and 2 were implemented using the most advanced commercially available inversion software, whereas Method 3 and 4 were implemented in a python workflow based on the most promising inversion methodology currently reported in the literature. This section summarizes the main findings while addressing the research questions.

Sub-question 1 - What sediment properties and plume characteristics are expected in deep-sea nodule collecting operations, and how do they affect acoustic measurements?

Sediment properties encountered in deep-sea conditions are characterized by fine-grained siliceous sediments such as clays, silts, and oozes. The representative deep-sea sediments under investigation within this study have median particle diameters of 15.4 μm and 4.5 μm for the CCZ sediment and Sediment B, respectively. During nodule collection operations, the suspension may additionally contain nodule fines and larger nodule fragments generated during the collection process.

The discharged sediment plume evolves from a high-suspended sediment concentration, shear and turbulent energy towards a progressively more diluted and flocculated plume, defined by the near-field, transitional, and far-field regions (described in Section 2). As the plume develops, it undergoes dynamic processes of particle aggregation, dilution, and settling; continuously altering the spatio-temporal particle size distribution and suspended sediment concentration.

Acoustic suspended sediment measurements are directly influenced by suspended sediment concentration, particle size distribution, particle shape, and the degree of flocculation. Therefore, the spatio-temporal development of the plume increases the uncertainty in both particle size and SSC inversion, as the evolving suspension can no longer be adequately characterized by a single theoretical model. Consequently, the more suitable location for reliable acoustic SSC measurements and particle-size inversion is inside or in close proximity to the diffuser, where the particle properties remain relatively stable and flocculation is expected to be minimal.

Sub-question 2 - Which acoustic inversion approaches are available for estimating suspended sediment concentration and particle size, and what are their theoretical capabilities and limitations?

Acoustic inversion approaches for suspended sediment measurements can generally be divided into profile-based and range-averaged inversion methods. Profile-based approaches determine the SSC

and particle size for individual range bins, thereby providing spatially resolved measurements of concentration and particle-size gradients. In contrast, range-averaged approaches determine a single representative SSC and particle size over the complete measurement range, assuming that the suspension is sufficiently homogeneous. These approaches are described in Section 3.4.

Four inversion methods representative of the current state of the art were evaluated in this study. Methods 1 and 2 involve the commercially available bin-based inversion approaches, whereas Methods 3 and 4 apply a range-averaged inversion method based on recent research developments. The methods are described in Section 3.5.

Method 1 and **Method 2** have the theoretical advantage of resolving spatial variations in SSC and particle size throughout the measurement range. However, these methods rely on an iterative bin-based inversion, making them inherently more sensitive to measurement noise and inversion instabilities. Furthermore, the particle-size inversion, applied in Method 1, is fundamentally limited by the frequency-dependent form-function response, which for the investigated 5 MHz transducer limits the minimum measurable particle diameter to approximately 4.8 μm (See Section 3.4.4). In addition, these methods assume generic quartz particle attenuation and backscatter properties.

Methods 3 and **Method 4**, in contrast, assume that SSC and particle size remain constant over the analysed measurement range and therefore cannot resolve spatial gradients. In return, they provide a substantially more stable inversion by using a quadratically averaged acoustic profile. These methods also incorporate oblate-sphere attenuation and mica-based scattering models, making them more suitable for representing the plate-like particle shapes expected in deep-sea sediments.

Sub-question 3 - What is the achievable accuracy of the investigated inversion methods for inverting suspended sediment concentration for representative deep-sea sediments, and which factors govern their performance?

The achievable inversion accuracy strongly depends on the selected inversion methodology, the prescribed particle parameters, and the sediment type. Of the four investigated methods, only Methods 3 and 4 proved capable of reliably estimating SSC over the concentration range representative of deep-sea nodule collection operations.

Method 1 and **Method 2** failed to provide reliable inversion results. Between 0.5 g/L and 7.8 g/L, the inversions remained numerically stable but consistently overestimated particle size, while outside this range the estimated particle size and SSC gradients became unrealistically high. Even in the cases of best agreement, Method 1 consistently overestimated the median particle diameter by factors of 4.1 and 18.2 relative to the Malvern measurements for the CCZ sediment and Sediment B, respectively. These particle size overestimations propagated into SSC underestimations of approximately 1.2 orders of magnitude for the CCZ sediment and 2 orders of magnitude for Sediment B. Method 2 did not yield any reliable particle size estimations and proved to be highly sensitive to small errors in the prescribed particle parameters. Deviations of only 1 μm in median particle diameter and a deviation of 0.1 in relative standard deviation yielded a SSC error of 58.8 % and 117.7 % relative to the Malvern-measured parameters, respectively.

Methods 3.1 and 4.4 demonstrated the greatest potential for SSC inversion over the investigated range of $0.16 - 32.37$ g/L. For the selected D_{50} constrained configurations, Method 3.1 achieved proportional biases of $+36.1\,\%$ and $+1.2\,\%$, with R^2 values of 0.995 and 0.978 for the CCZ sediment and Sediment B, respectively, while Method 4.4 achieved proportional biases of $+9.8\,\%$ and $-15.5\,\%$ with R^2 values of 0.944 and 0.867, respectively. Across the selected sediments, methods and constraint, the proportional bias therefore remained within approximately $\pm 36\,\%$.

The inversion performance was governed primarily by prescribed median particle diameter (D_{50}). It provided the most consistent improvement across both sediments and inversion methods, whereas constraining σ provided limited additional benefit and, in some cases, reduced inversion accuracy. Constraining both parameters could over-constrain the inversion. This identifies D_{50} as the dominant PSD parameter controlling SSC inversion performance.

Method 3.1 consistently showed higher R^2 values and less scatter in the D_{50} parameter inversion, relative to Methods 4.3 and 4.4, indicating that use of the backscatter s_v in the inversion can have a benefi-

cial effect on precision and particle parameter inversion. However, the accuracy is primarily dependent on the quality of the acoustic measurement. Noise caused by acoustic reflections, micro-bubbles, or nodule fragments increases uncertainty in the attenuation term, which subsequently propagates to the backscatter term.

Sub-question 4 - What are the practical capabilities and limitations of optical and multi-frequency acoustic sensors for monitoring suspended sediment concentration and particle size in deep-sea mining plumes?

A practical capability of the optical backscatter sensor is that, when calibrated against a specific sediment, it provides a point measurement of suspended sediment concentration without theoretical assumptions or computationally intense algorithms. For Sediment B, the OBS achieved a relatively good performance, yielding a slope of 0.857 and an R^2 value of 0.983. In contrast, the CCZ sediment resulted in a slope of 0.546 and an R^2 value of 0.884. The poorer performance for the CCZ sediment is attributed to differences between the sediment conditions during calibration and those during testing, likely caused by the presence of nodule fines. Consequently, the accuracy of the OBS is highly dependent on the representativeness of the sediment-specific calibration and the frequency at which recalibration is performed. Furthermore, the OBS provides only a point measurement and is therefore unable to resolve concentration gradients across the diffuser or provide particle size information, requiring multiple sensors to be installed to characterize the discharged plume.

The practical capability of the multi-frequency acoustic backscatter sensor is that it provides continuous range averaged measurements of SSC without requiring sediment-specific calibration, with the Methods 4.4 and 3.1 achieving SSC inversions with proportional biases within $+1.2\,\%$ to $+36.1\,\%$ for Method 3.1 and from -15.5% to $+9.8\%$ for Method 4.4. Furthermore, the multi-frequency approach offers the potential to simultaneously estimate the median particle diameter and the distribution width, although these parameters could not yet be reliably quantified under the investigated conditions.

The main practical limitations are the reduction in measurement range with increasing SSC, with a maximum range of approximately 0.3 m at 15 g/L; its reduced performance due to wall reflections in confined environments; and its potential interference with nearby acoustic sensors. Additionally, although a sideways looking sensor configuration for methods 3 and 4, this configuration implies independent of SSC the maximum measurable range of the vertical SSC gradient is the acoustic beam width, which with its maximum range of 1 meter is approximately 0.3 meters, preventing a single sensor from characterizing the full cross-section of a 1 m wide diffuser.

Main Research Question - How can multi-frequency acoustic backscatter measurements be used to reliably quantify suspended sediment concentration and particle size in deep-sea nodule collection plumes, and how does their performance compare with existing optical measurement techniques?

Multi-frequency acoustic backscatter measurements are most reliable within or in close proximity to the nodule collector vehicle diffuser, where the plume has not yet developed complex behaviour such as flocculation. The relatively stable suspension of primary particles can therefore be more reliably approximated using theoretical attenuation and scattering models.

Of the investigated approaches, the range-averaged Methods 3.1 and 4.4 showed the greatest potential. Over the investigated range of $0.5 - 18$ g/L, Method 3.1 achieved proportional biases between $+1.2\,\%$ and $+36.1\,\%$ when D_{50} was constrained, while Method 4.4 achieved biases between -15.5% and $+9.8\,\%$. The extended SSC range of the CCZ sediment also showed good results, with proportional biases of $31.1\,\%$ and 19.2% for Methods 3.1 and 4.4, respectively. The results demonstrate that appropriate representation of the median particle size has the greatest effect on SSC inversion performance. A priori information on the median particle diameter improved the inversion in all cases. In contrast, constraining the distribution width yielded inconsistent improvements in accuracy and precision.

Relative to the SSC inversion, the particle-size and distribution-width inversions were found to be much more sensitive to uncertainties in the objective function. Small deviations of $2\,\%$ in the objective function led to 100% variations in particle size, while resulting in only a $2\,\%$ variation in SSC. Multi-frequency acoustic measurements should therefore currently be considered a viable method for range-averaged

SSC estimation, with particle-size inversion remaining a potential capability requiring further development.

Reliable acoustic SSC inversion below 0.5 g/L and above 18 g/L depends on the quality of the measured acoustic attenuation and backscatter terms (α_{sv} and s_v). In laboratory settings, low-SSC inversions are prone to noise from wall reflections and micro-bubbles, while at elevated SSC, the increased presence of nodule fragments interfered with the quality of the backscatter term. Deep-sea operational conditions are expected to reduce these issues.

Compared with the OBS, multi-frequency acoustic backscatter achieved .comparable SSC accuracy and precision without requiring sediment-specific calibration, while additionally offering the potential to estimate median particle diameter and distribution width over a larger representative measurement volume. Its main limitation is the reduction in effective measurement range at elevated SSC, which is particularly relevant for applications in high-concentration regions of deep-sea nodule collection plumes. In contrast, the OBS provides a simpler and highly precise local SSC ”point” measurement when a representative sediment-specific calibration is available, but provides no particle-size information and its accuracy remains strongly dependent on the validity of this calibration. This dependence was identified as a key limitation in the present study, as the applied calibration did not adequately represent the conditions encountered during the experiments simulating a nodule collector diffuser.

Overall, the results demonstrate that multi-frequency acoustic backscatter provides a more comprehensive and potentially more robust approach for operational plume monitoring, particularly within and close to the diffuser where complex plume dynamics such as flocculation have not yet developed. However, further development is required to improve inversion reliability and measurement range at elevated SSC, followed by validation under representative deep-sea conditions.

8

Recommendations

8.1. Improvements to the Experimental Setup

Should the experimental campaign be repeated using the current setup, several modifications are recommended to improve both the quality of the acoustic measurements and the practicality of the experiments.

From an acoustic perspective, the limited dimensions of the current recirculation tank resulted in wall reflections and increased signal noise, particularly for the 1 and 2 MHz transducers. To improve signal quality, which is especially critical at low suspended sediment concentrations (e.g. < 2 g/L), a wider and taller tank is recommended. Alternatively, acoustic absorbing panels could be installed along the tank walls and bottom. To minimise sediment accumulation, the panels should preferably have a pyramidal geometry with the vertices oriented upwards.

Several practical improvements would also simplify maintenance of the system. Installing a valve on the outlet of the recirculation tank would allow the pump and connecting pipework to be removed without draining the tank, facilitating the removal of accumulated coarse nodule particles from the pipework. Furthermore, the addition of a T-junction with two valves at the pump outlet would allow the flow either to be directed towards the top of the tank during normal operation or recirculated towards the bottom during maintenance. The latter would facilitate backwashing of the system in the event of complete sediment settling.

The current setup required continuous pump operation throughout both the day and night to prevent sediment deposition and clogging of the system, which resulted in premature pump failure. The proposed valve configuration would allow the pump to be switched off overnight and restarted by first backwashing the system. Besides reducing mechanical wear, this would also reduce the cumulative shear imposed on the sediment, thereby limiting changes in the particle size distribution and optical properties of the sediment during long-duration experiments.

8.2. Alternative Experimental Configuration

To reduce the influence of coarse nodule fines and more closely simulate the flow conditions within the diffuser, an alternative horizontal flow setup could be considered. A flow perpendicular to the transducer would continuously refresh the sediment within the acoustic path and allow coarse nodule fines to settle out before reaching the measurement volume, thereby improving signal quality. Such a setup would however require a larger dimensional footprint and careful consideration of how to maintain a sufficiently homogeneous suspension. Vertical concentration gradients are also more likely to develop under these conditions. Consequently, a downward-facing transducer would introduce additional uncertainty in the attenuation-based inversion methods 3 and 4, whereas a horizontally mounted transducer measuring across the water column would minimise the influence of these vertical gradients.

8.3. Optimisation of Acoustic Measurement Settings

In this study, the acoustic sensor was operated at a ping frequency of 4 Hz. However, preliminary tests indicated that higher ping frequencies were possible without a reduction in performance. Increasing the ping frequency to 8 or 16 Hz would reduce the measurement time from 15 minutes to 7.5 or 3.75 minutes, respectively. This would reduce the time between intermittent OBS measurements and is therefore expected to improve the accuracy of the comparison by minimizing temporal differences between the measurements.

The sensor receive gain (R_x) is another parameter that could improve the measurement range. After completion of the experimental campaign, it was found that Vergne et al. [30] used an increased receive gain, whereas no receive gain was applied in the present study. Although the usable measurement range found in the measurement data was slightly larger [30], this difference may also be attributed to differences in sediment properties.

8.4. Future Research

Further Development of the Acoustic Inversion Models

The current acoustic inversion frameworks (Methods 3.1-3.2 and 4.1-4.4) are not directly comparable, as two model assumptions differ simultaneously. First, Method 3 performs an inversion based solely on viscous attenuation, whereas Method 4 jointly inverts both viscous attenuation and the volume scattering parameter. Second, the particle oblateness is defined differently. In Method 3, the aspect ratio varies linearly from $h = 1/40$ at $D_{50} = 2$ μm to $h = 1$ at $D_{50} = 60$ μm. In contrast, Method 4 assumes a constant particle shape throughout the entire particle size range, with the aspect ratio fixed at either $h = 1$ or $h = 1/40$. Consequently, differences in inversion performance between the two frameworks cannot be attributed solely to the inclusion of the volume scattering parameter. Isolating the two parameters would give improved insight to their influences.

Furthermore, two additional improvements to the model should be considered. First, a more accurate characterisation of the sediment density is required. Currently, a density representative of quartz sand (2650 kg/m^3) is assumed for all sediments. Second, Method 4 includes a weighting parameter, A_j^2, which increases the influence of attenuation relative to backscatter. This parameter was introduced by Vergne et al. [30]; however, its value was chosen rather arbitrarily. A more physically based definition or calibration of this weighting factor is therefore recommended.

Validation Using Control Sediments

Currently, Methods 3 and 4 have only been applied to natural sediments. The use of artificial control sediments with well-defined particle size distributions would facilitate a more systematic assessment of inversion performance with respect to particle size, distribution width, and flocculation.

Field Validation of Multi-Frequency ABS

The performance of the acoustic measurements and inversion methods should be evaluated during field deployments or large-scale hydraulic testing. Such validation would establish whether the laboratory performance observed in this study is representative of deep-sea conditions, where factors such as pressure, ambient noise, natural turbulence, and particle transport may influence the acoustic response. Furthermore, the absence of micro-bubbles at depth may improve signal quality and measurement accuracy.

Improved Calibration of Optical Backscatter Sensors

Although this thesis primarily focused on acoustic sensing, the OBS measurements demonstrated that conventional optical calibration procedures are of great importance and should adequately represent both the diffuser flow conditions and sediment characteristics to obtain accurate results. It is suspected that the current calibration procedure, performed in a small beaker, did not sufficiently represent the experimental conditions. In particular, the influence of deep-sea nodule fines may have been underestimated due to their potentially different optical properties, including surface colour, surface roughness, and particle geometry. Future work should therefore investigate the optical properties of nodule fines and develop calibration procedures using more representative sediment compositions and flow condi-

tions. This would provide a more appropriate benchmark for comparing conventional optical monitoring with acoustic methods.

References

[1] Josh, D. (2025, March). Evidence of deep-sea mining still visible over four decades later. https://www.nhm.ac.uk/discover/news/2025/march/evidence-of-deep-sea-mining-visible-over-four-decades-later.html

[2] Kuhn, T., Wegorzewski, A., Rühlemann, C., & Vink, A. (2017). Composition, Formation, and Occurrence of Polymetallic Nodules. In R. Sharma (Ed.), *Deep-Sea Mining: Resource Potential, Technical and Environmental Considerations* (pp. 23–63). Springer International Publishing. https://doi.org/10.1007/978-3-319-52557-0_2

[3] Lèbre, É., Kung, A., Savinova, E., & Valenta, R. K. (2023). Mining on land or in the deep sea? Overlooked considerations of a reshuffling in the supply source mix. *Resources, Conservation and Recycling*, *191*, 106898. https://doi.org/https://doi.org/10.1016/j.resconrec.2023.106898

[4] Vink, A., Aigner, T., Bardenhagen, M., Barz, J., Bouriat, A., Charlet, F., de Stigter, H., Gazis, I., Goossens, J., Haeckel, M., Hagedorn, D., Heger, K., Janssen, F., Kefel, O., Luongo, G., Maschmann, N., Mohrmann, J., Molari, M., Rossel, S., … Yapan, B. (2022). *MANGAN 2021 Cruise Report: Independent scientific monitoring of two collector tests in the BGR and GSR contract areas for the exploration of polymetallic nodules in the equatorial NE Pacific* (A. Vink, Ed.). Bundesanstalt für Geowissenschaften und Rohstoffe. https://doi.org/10.25928/HW7D-FS42

[5] Gazis, I.-Z., De Stigter, H., Mohrmann, J., Heger, K., Diaz, M., Gillard, B., Baeye, M., Veloso-Alarcón, M. E., Purkiani, K., Haeckel, M., Vink, A., Thomsen, L., & Greinert, J. (2025). Monitoring benthic plumes, sediment redeposition and seafloor imprints caused by deep-sea polymetallic nodule mining. *Nature Communications*, *16*(1), 1229. https://doi.org/10.1038/s41467-025-56311-0

[6] ISA. (2023, November). NORI Collector Test Environmental Impact Statement. Retrieved December 1, 2025, from https://www.deepseamining.ac

[7] Ali, W. (2024). *Flocculation and deep-sea mining plumes* [Doctoral dissertation, Delft University of Technology]. https://doi.org/10.4233/UUID:155B3071-C74C-4296-9DD2-512CCB2E1006

[8] Muñoz-Royo, C., Ouillon, R., El Mousadik, S., Alford, M. H., & Peacock, T. (2022). An in situ study of abyssal turbidity-current sediment plumes generated by a deep seabed polymetallic nodule mining preprototype collector vehicle. *Science Advances*, *8*(38), eabn1219. https://doi.org/10.1126/sciadv.abn1219

[9] Guo, X., Liu, Y., Liu, X., Li, Z., Liang, D., Sousa, R. L., Lai, Y., Yin, J., & Stoesser, T. (2025). Rheology of deep-sea mining plumes: Dependence on properties of sediments in Western Pacific Ocean. *Journal of Rock Mechanics and Geotechnical Engineering*. https://doi.org/10.1016/j.jrmge.2025.08.034

[10] Sharma, R. (Ed.). (2025). *Deep-Sea Mining Management, Policy and Regulation: Data Management, Environmental Monitoring, Techno-Economic Assessment, Law of the Sea and Regulatory Regimes*. Springer Nature Switzerland. https://doi.org/10.1007/978-3-031-92737-9

[11] Haalboom, S., de Stigter, H. C., Mohn, C., Vandorpe, T., Smit, M., de Jonge, L., & Reichart, G.-J. (2023). Monitoring of a sediment plume produced by a deep-sea mining test in shallow water, Málaga Bight, Alboran Sea (southwestern Mediterranean Sea). *Marine Geology*, *456*, 106971. https://doi.org/10.1016/j.margeo.2022.106971

[12] Gillard, B., Purkiani, K., Chatzievangelou, D., Vink, A., Iversen, M. H., & Thomsen, L. (2019). Physical and hydrodynamic properties of deep sea mining-generated, abyssal sediment plumes in the Clarion Clipperton Fracture Zone (eastern-central Pacific) (J. W. Deming & S. F. Ackley, Eds.). *Elementa: Science of the Anthropocene*, *7*, 5. https://doi.org/10.1525/elementa.343

[13] The Mining Code: Standards and Guidelines - International Seabed Authority. (2022, March). Retrieved February 4, 2026, from https://isa.org.jm/the-mining-code/standards-and-guidelines/

[14] Wahab, S. A., Ali, W., Chassagne, C., & Helmons, R. (2024). Role of Organic Matter Present in the Water Column on Turbidity Flows. *Journal of Marine Science and Engineering*, *12*(10), 1884. https://doi.org/10.3390/jmse12101884

[15] Haalboom, S. (2024, May). *Monitoring Strategies of Suspended Matter after Natural and Deep-Sea Mining Disturbances* [dr.]. Utrecht University. https://doi.org/10.33540/2217

[16] BGR Geoportal - Detailseite. (n.d.). https://geoportal.bgr.de/mapapps/resources/apps/geoportal/index.html?lang=de#/datasets/portal/201888

[17] Fractionation Trends and Variability of Rare Earth Elements and Selected Critical Metals in Pelagic Sediment from Abyssal Basin of NE Pacific (Clarion-Clipperton Fracture Zone). (n.d.). https://www.mdpi.com/2075-163X/10/4/320

[18] Jones, D. O. B., Simon-Lledó, E., Amon, D. J., Bett, B. J., Caulle, C., Clément, L., Connelly, D. P., Dahlgren, T. G., Durden, J. M., Drazen, J. C., Felden, J., Gates, A. R., Georgieva, M. N., Glover, A. G., Gooday, A. J., Hollingsworth, A. L., Horton, T., James, R. H., Jeffreys, R. M., … Huvenne, V. A. I. (2021). Environment, ecology, and potential effectiveness of an area protected from deep-sea mining (Clarion Clipperton Zone, abyssal Pacific). *Progress in Oceanography*, *197*, 102653. https://doi.org/10.1016/j.pocean.2021.102653

[19] Gillard, B., & Laurenz, T. (2020). Characterization of sediment plumes behind mining vehicles in the NORI area (laboratory analyses). https://metals.co/wp-content/uploads/dlm_uploads/2022/12/NORI-D-Collector-Test-EIS-Final-Appendix-6.pdf

[20] Pearson, S. G., Verney, R., van Prooijen, B. C., Tran, D., Hendriks, E. C. M., Jacquet, M., & Wang, Z. B. (2021). Characterizing the Composition of Sand and Mud Suspensions in Coastal and Estuarine Environments Using Combined Optical and Acoustic Measurements. *Journal of Geophysical Research: Oceans*, *126*(7), e2021JC017354. https://doi.org/10.1029/2021JC017354

[21] Fettweis, M., Riethmüller, R., Verney, R., Becker, M., Backers, J., Baeye, M., Chapalain, M., Claeys, S., Claus, J., Cox, T., Deloffre, J., Depreiter, D., Druine, F., Flöser, G., Grünler, S., Jourdin, F., Lafite, R., Nauw, J., Nechad, B., … Vereecken, H. (2019). Uncertainties associated with in situ high-frequency long-term observations of suspended particulate matter concentration using optical and acoustic sensors. *Progress in Oceanography*, *178*, 102162. https://doi.org/10.1016/j.pocean.2019.102162

[22] Elerian, M., Huang, Z., van Rhee, C., & Helmons, R. (2023). Flocculation effect on turbidity flows generated by deep-sea mining: A numerical study. *Ocean Engineering*, *277*. https://doi.org/10.1016/j.oceaneng.2023.114250

[23] MacDonald, I. T., Vincent, C. E., Thorne, P. D., & Moate, B. D. (2013). Acoustic scattering from a suspension of flocculated sediments. *Journal of Geophysical Research: Oceans*, *118*(5), 2581–2594. https://doi.org/10.1002/jgrc.20197

[24] Sahin, C. (2014). Investigation of the variability of floc sizes on the Louisiana Shelf using acoustic estimates of cohesive sediment properties. *Marine Geology*, *353*, 55–64. https://doi.org/10.1016/j.margeo.2014.03.022

[25] IAEA. (2005, August). Fluvial Sediment Transport: Analytical Techniques for Measuring Sediment Load. Retrieved December 2, 2025, from http://www.iaea.org/publications/7294/fluvial-sediment-transport-analytical-techniques-for-measuring-sediment-load

[26] Downing, J. (2006). Twenty-five years with OBS sensors: The good, the bad, and the ugly. *Continental Shelf Research*, *26*(17), 2299–2318. https://doi.org/10.1016/j.csr.2006.07.018

[27] Conevski, S. (2016). Testing the LISST-ABS capabilities and verifying its usage for measuring suspended sediment concentration in large rivers. *5th Particles in Europe Conference (PiE2016)*, 1–13.

[28] Betteridge, K. F. E., Thorne, P. D., & Cooke, R. D. (2008). Calibrating multi-frequency acoustic backscatter systems for studying near-bed suspended sediment transport processes. *Continental Shelf Research*, *28*(2), 227–235. https://doi.org/10.1016/j.csr.2007.07.007

[29] Thorne, P. D., Vincent, C. E., Hardcastle, P. J., Rehman, S., & Pearson, N. (1991). Measuring suspended sediment concentrations using acoustic backscatter devices. *Marine Geology*, *98*(1), 7–16. https://doi.org/https://doi.org/10.1016/0025-3227(91)90031-X

[30] Vergne, A., Berni, C., Le Coz, J., & Tencé, F. (2021). Acoustic Backscatter and Attenuation Due to River Fine Sediments: Experimental Evaluation of Models and Inversion Methods. *Water Resources Research*, *57*(9). https://doi.org/10.1029/2021WR029589

[31] Sutherland, T. F., Lane, P. M., Amos, C. L., & Downing, J. (2000). The calibration of optical backscatter sensors for suspended sediment of varying darkness levels. *Marine Geology*, *162*(2), 587–597. https://doi.org/10.1016/S0025-3227(99)00080-8

[32] Hatcher, A., Hill, P., Grant, J., & Macpherson, P. (2000). Spectral optical backscatter of sand in suspension: Effects of particle size, composition and colour. *Marine Geology*, *168*(1), 115–128. https://doi.org/10.1016/S0025-3227(00)00042-6

[33] Maa, J. P. Y., Xu, J., & Victor, M. (1992). Notes on the performance of an optical backscatter sensor for cohesive sediments. *Marine Geology*, *104*(1), 215–218. https://doi.org/10.1016/0025-3227(92)90096-Z

[34] Ha, H. K., Hsu, W. .-., Maa, J. P. .-., Shao, Y. Y., & Holland, C. W. (2009). Using ADV backscatter strength for measuring suspended cohesive sediment concentration. *Continental Shelf Research*, *29*(10), 1310–1316. https://doi.org/10.1016/j.csr.2009.03.001

[35] Gibbs, R. J., & Wolanski, E. (1992). The effect of flocs on optical backscattering measurements of suspended material concentration. *Marine Geology*, *107*(4), 289–291. https://doi.org/https://doi.org/10.1016/0025-3227(92)90078-V

[36] Bunt, J. A. C., Larcombe, P., & Jago, C. F. (1999). Quantifying the response of optical backscatter devices and transmissometers to variations in suspended particulate matter. *Continental Shelf Research*, *19*(9), 1199–1220. https://doi.org/10.1016/S0278-4343(99)00018-7

[37] Wang, Y., Peng, Y., Du, Z., Lin, H., & Yu, Q. (2020). Calibrations of Suspended Sediment Concentrations in High-Turbidity Waters Using Different In Situ Optical Instruments. *Water*, *12*(11), 3296. https://doi.org/10.3390/w12113296

[38] Guillén, J., Palanques, A., Puig, P., Durrie de Madron, X., & Nyffeler, F. (2000). Field calibration of optical sensors for measuring suspended sediment concentration in the western Mediterranean. *Scientia Marina*, *64*(4), 427–435. https://doi.org/10.3989/scimar.2000.64n4427

[39] Kineke, G. C., & Sternberg, R. W. (1992). Measurements of high concentration suspended sediments using the optical backscatterance sensor. *Marine Geology*, *108*(3), 253–258. https://doi.org/https://doi.org/10.1016/0025-3227(92)90199-R

[40] Haalboom, S., de Stigter, H., Duineveld, G., van Haren, H., Reichart, G.-J., & Mienis, F. (2021). Suspended particulate matter in a submarine canyon (Whittard Canyon, Bay of Biscay, NE Atlantic Ocean): Assessment of commonly used instruments to record turbidity. *Marine Geology*, *434*, 106439. https://doi.org/10.1016/j.margeo.2021.106439

[41] Agrawal, Y. C., & Pottsmith, H. C. (2000). Instruments for particle size and settling velocity observations in sediment transport. *Marine Geology*, *168*(1), 89–114. https://doi.org/10.1016/S0025-3227(00)00044-X

[42] Thorne, P. D., & Hanes, D. M. (2002). A review of acoustic measurement of small-scale sediment processes. *Continental Shelf Research*, *22*(4), 603–632. https://doi.org/10.1016/S0278-4343(01)00101-7

[43] Guerrero, M., Conevski, S., Baranya, S., & Ruther, N. (2017). Combining Backscatter and Attenuation Measurements for Suspended Sediment Concentration Assessment. *ResearchGate*. https://www.researchgate.net/publication/351374193_COMBINING_BACKSCATTER_AND_ATTENUATION_MEASUREMENTS_FOR_SUSPENDED_SEDIMENT_CONCENTRATION_ASSESSMENT

[44] Moore, S. A., Le Coz, J., Hurther, D., & Paquier, A. (2013). Using multi-frequency acoustic attenuation to monitor grain size and concentration of suspended sediment in rivers. *The Journal of the Acoustical Society of America*, *133*(4), 1959–1970. https://doi.org/10.1121/1.4792645

[45] Ha, H. K., Maa, J. P. .-., Park, K., & Kim, Y. H. (2011). Estimation of high-resolution sediment concentration profiles in bottom boundary layer using pulse-coherent acoustic Doppler current profilers. *Marine Geology*, *279*(1), 199–209. https://doi.org/10.1016/j.margeo.2010.11.002

[46] Hay, A. E. (1991). Sound scattering from a particle laden, turbulent jet. *The Journal of the Acoustical Society of America*, *90*(4), 2055–2074. https://doi.org/10.1121/1.401633

[47] Moate, B. D., & Thorne, P. D. (2012). Interpreting acoustic backscatter from suspended sediments of different and mixed mineralogical composition. *Continental Shelf Research*, *46*, 67–82. https://doi.org/10.1016/j.csr.2011.10.007

[48] Thorne, P. D., & Hurther, D. (2014). An overview on the use of backscattered sound for measuring suspended particle size and concentration profiles in non-cohesive inorganic sediment transport studies. *Continental Shelf Research*, *73*, 97–118. https://doi.org/10.1016/j.csr.2013.10.017

[49] Doonan, I., Coombs, R., Doonan, S., Coombs, I., Mcclatchie, S., & Niwa. (2003). The absorption of sound in seawater in relation to the estimation of deep-water fish biomass. *Ices Journal of Marine Science - ICES J MAR SCI*, *60*. https://doi.org/10.1016/S1054–3139(03)00120-6

[50] Medwin, H., & Clarence, C. S. (1998). *Fundamentals of Acoustical Oceanography*. Elsevier. https://doi.org/10.1016/B978-0-12-487570-8.X5000-4

[51] Richards, S. D., Heathershaw, A. D., & Thorne, P. D. (1996). The effect of suspended particulate matter on sound attenuation in seawater. *The Journal of the Acoustical Society of America*, *100*(3), 1447–1450. https://doi.org/10.1121/1.415991

[52] Folk, R. L., & Ward, W. C. (1957). Brazos River bar [Texas]; a study in the significance of grain size parameters. *Journal of Sedimentary Research*, *27*(1), 3–26. https://doi.org/10.1306/74D70646-2B21-11D7-8648000102C1865D

[53] Urick, R. J. (1948). The Absorption of Sound in Suspensions of Irregular Particles. *The Journal of the Acoustical Society of America*, *20*(3), 283–289. https://doi.org/10.1121/1.1906373

[54] Richards, S., Leighton, T., & Brown, N. (2003). Visco–inertial absorption in dilute suspensions of irregular particles. *Proceedings of the Royal Society A: Mathematical, Physical and Engineering Sciences*, *459*(2037), 2153–2167. https://doi.org/10.1098/rspa.2003.1126

[55] Vincent, C. E., & MacDonald, I. T. (2015). A flocculi model for the acoustic scattering from flocs. *Continental Shelf Research*, *104*, 15–24. https://doi.org/10.1016/j.csr.2015.05.002

[56] Thorne, P. D., MacDonald, I. T., & Vincent, C. E. (2014). Modelling acoustic scattering by suspended flocculating sediments. *Continental Shelf Research*, *88*, 81–91. https://doi.org/10.1016/j.csr.2014.07.003

[57] Thorne, P., Hardcastle, P., & Soulsby, R. (1993). Analysis of Acoustic Measurements of Suspended Sediment. *J. Geophys. Res.*, *98*, 899–910. https://doi.org/10.1029/92JC01855

[58] Thorne, P. D., & Meral, R. (2008). Formulations for the scattering properties of suspended sandy sediments for use in the application of acoustics to sediment transport processes. *Continental Shelf Research*, *28*(2), 309–317. https://doi.org/10.1016/j.csr.2007.08.002

[59] Lohrmann, A. (2001, October). Monitoring Sediment Concentration with acoustic backscattering instruments. https://www.nortekgroup.com/assets/documents/Monitoring-sediment-concentration-with-acoustic-backscattering-instruments.pdf

[60] Hurther, D., Thorne, P. D., Bricault, M., Lemmin, U., & Barnoud, J.-M. (2011). A multi-frequency Acoustic Concentration and Velocity Profiler (ACVP) for boundary layer measurements of fine-scale flow and sediment transport processes. *Coastal Engineering*, *58*(7), 594–605. https://doi.org/10.1016/j.coastaleng.2011.01.006

[61] Thorne, P. D., & Hardcastle, P. J. (1997). Acoustic measurements of suspended sediments in turbulent currents and comparison with in-situ samples. *The Journal of the Acoustical Society of America*, *101*(5), 2603–2614. https://doi.org/10.1121/1.418501

[62] Aquatec Subsea Limited. (2002). Inversion Technique [Revision: 1.0]. https://doi.org/https://www.aquatecsubsea.com

[63] Vergne, A., Le Coz, J., Berni, C., & Pierrefeu, G. (2020). Using a Down-Looking Multifrequency ABS for Measuring Suspended Sediments in Rivers. *Water Resources Research*, *56*(2), e2019WR024877. https://doi.org/10.1029/2019WR024877

[64] Tran, D., Jacquet, M., Pearson, S., Van Prooijen, B., & Verney, R. (2024). Estimation of Mud and Sand Fractions and Total Concentration From Coupled Optical-Acoustic Sensors. *Earth and Space Science*, *11*(11), e2024EA003694. https://doi.org/10.1029/2024EA003694

[65] Champagne, B., & Xu, K. (2017). Calibrations Of Optical And Acoustic Sensors For Coastal Protection And Restoration Research. https://repository.library.noaa.gov

[66] Shao, Y. Y., & Maa, J. P. .-. (2017). Comparisons of Different Instruments for Measuring Suspended Cohesive Sediment Concentrations. https://www.mdpi.com/2073-4441/9/12/968

[67] Aquatec Group Limited. (2021, January). AQUAscat Toolkit User Manual [Version: 2.20 | Document Ref: 910-5000]. https://www.aquatecgroup.com

[68] Masson, M., Angot, H., Le Bescond, C., Launay, M., Dabrin, A., Miège, C., Le Coz, J., & Coquery, M. (2018). Sampling of suspended particulate matter using particle traps in the Rhône River: Relevance and representativeness for the monitoring of contaminants. *Science of The Total Environment*, *637-638*, 538–549. https://doi.org/10.1016/j.scitotenv.2018.04.343

[69] Crossouard, N., Taylor, J., & Lee, M. (2017). Potential sources and magnitude of errors associated with the measurement of suspended sediment concentration. https://eprints.hrwallingford.com/1222/

A

Attenuation and Backscatter Linear Regression Parameters

Table A.1: Linear regression parameters for the relationships between viscous sediment attenuation (α_{sv}) and SSC, and between the volume backscatter coefficient (s_v) and SSC, for the CCZ sediment and Sediment B. The reported parameters comprise of the slope and the coefficient of determination (R^2). All regressions were forced through the origin for consistency with previous studies.

Sediment	**Frequency**	**Attenuation** (α_s)		**Backscatter** (s_v)	
		Slope ($\mathrm{L\,g^{-1}\,m^{-1}}$)	R^2	**Slope** ($\mathrm{L\,g^{-1}\,m^{-1}}$)	R^2
CCZ	1.0 MHz	0.089	0.90	2.20×10^{-3}	0.49
	2.0 MHz	0.179	0.98	4.06×10^{-3}	0.59
	4.0 MHz	0.369	1.00	5.51×10^{-3}	0.79
	5.0 MHz	0.459	1.00	3.47×10^{-3}	0.56
Sediment B	1.0 MHz	0.047	-0.16	2.06×10^{-5}	-0.06
	2.0 MHz	0.139	0.95	2.91×10^{-4}	0.90
	4.0 MHz	0.290	0.98	1.46×10^{-3}	0.80
	5.0 MHz	0.352	0.99	1.86×10^{-3}	0.87

Note: The slopes were obtained from linear regression constrained through the origin.

B

Acoustic Measurement Range Regression Parameters

Summary of the exponential regression parameters used to approximate the maximum valid measurement range.

$$R_{\max} = C + Ae^{-B\,\mathrm{M}}.$$

Table B.1: Parameters of the exponential regression used to approximate the maximum valid measurement range.

Sediment	**Frequency**	A	B	C	**Regression**
CCZ	1.0 MHz	1.871	0.0265	0.000	$R_{\max} = 0.000 + 1.871e^{-0.0265\,\mathrm{M}}$
CCZ	2.0 MHz	1.375	0.0565	0.214	$R_{\max} = 0.214 + 1.375e^{-0.0565\,\mathrm{M}}$
CCZ	4.0 MHz	1.048	0.1097	0.183	$R_{\max} = 0.183 + 1.048e^{-0.1097\,\mathrm{M}}$
CCZ	5.0 MHz	0.760	0.1153	0.137	$R_{\max} = 0.137 + 0.760e^{-0.1153\,\mathrm{M}}$
Sediment B	1.0 MHz	5.361	0.1785	0.859	$R_{\max} = 0.859 + 5.361e^{-0.1785\,\mathrm{M}}$
Sediment B	2.0 MHz	1.608	0.0780	0.221	$R_{\max} = 0.221 + 1.608e^{-0.0780\,\mathrm{M}}$
Sediment B	4.0 MHz	1.335	0.1469	0.266	$R_{\max} = 0.266 + 1.335e^{-0.1469\,\mathrm{M}}$
Sediment B	5.0 MHz	0.799	0.0890	0.109	$R_{\max} = 0.109 + 0.799e^{-0.0890\,\mathrm{M}}$

C

Method 1 Analysis

Effect of Averaging for Median Particle Diameter Estimation

The median particle diameter inversion is inherently more sensitive to measurement variability than the SSC inversion and therefore requires greater profile averaging to obtain stable results. The profile averaging of the raw data was set to 5 profiles (1.25 seconds), and 2 bin-averaging. The particle estimate averaging was set to 250 profiles, and no further bin averaging. Figure C.2 illustrates the effect of averaging for particle size estimates. Averaging by more profiles results in more stable inversion. In this case, above 20 averaged profiles, the inversion becomes stable, with no sudden deviations to the prescribed inversion bounds. However, for the subsequent analysis, 100 profiles are averaged to ensure stable results across all measurements, while retaining 6 profiles per measurement to provide insight in the variations of the inversion results over the measurement period.

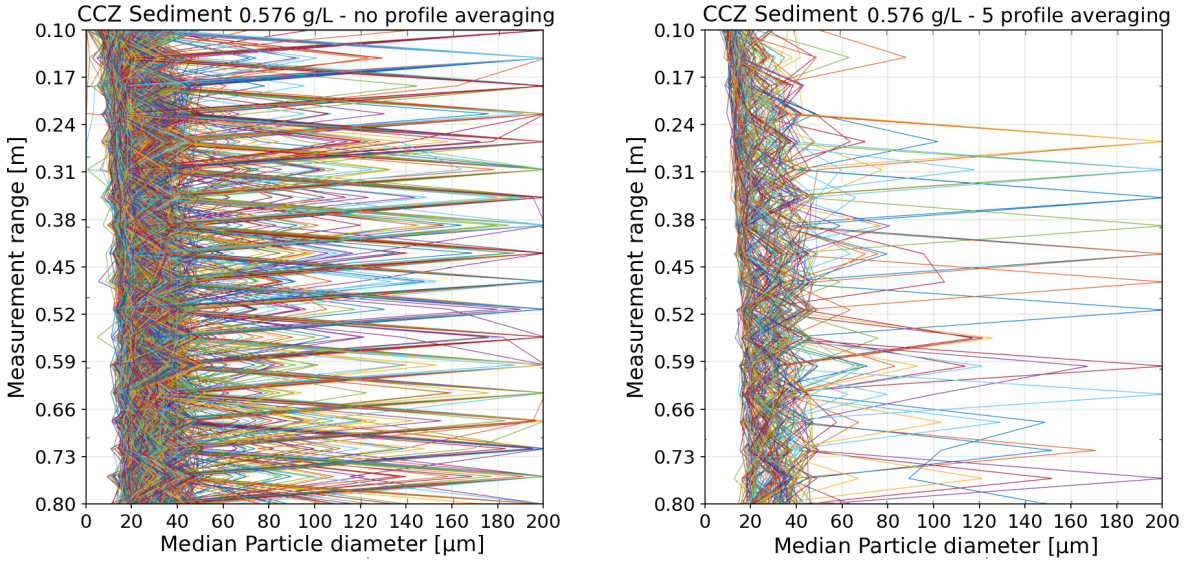

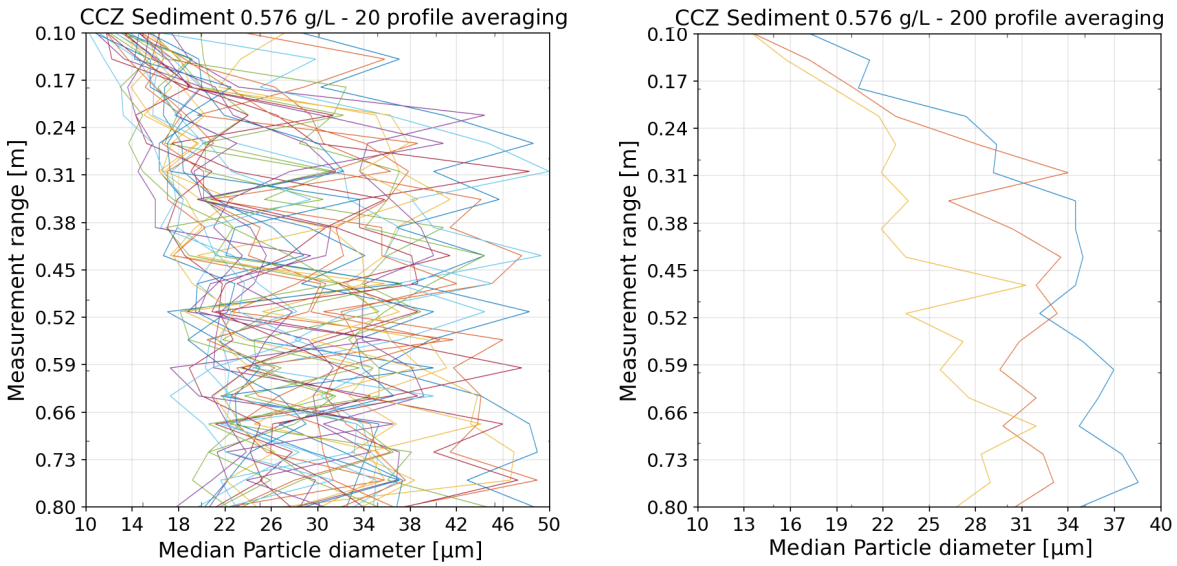

Figure C.2: Particle size estimates for the 0.576 g/L CCZ sediment case, using different levels of profile averaging

Effect of Frequency Combinations

Various frequency combinations were tested for both sediment cases and at various suspended sediment concentrations, with the Relative Standard Deviation ($Rel.SD$) set to that measured by the Malvern ($\sigma = 1$). The optimal frequency selection differs per sediment. Sediment B has a improved accuracy with the 4 and 5 MHz frequency combination, whereas the CCZ Sediment gives an improved accuracy with the 2 and 4 MHz frequency combination (Relative to all other frequency combinations).

Using a third frequency (2 MHz) for Sediment B improved the inversion stability over both range and time, eliminating sudden deviations to the measurement bounds. However, it also increased the estimated particle size. In contrast, including a third frequency (5 MHz) in the inversion of the CCZ sediment did not influence the inversion performance. These results indicate that including additional frequencies can improve inversion stability, as expected, since it provides additional information; however, care should be taken, as it may not improve the results relative to the LISST and Malvern.

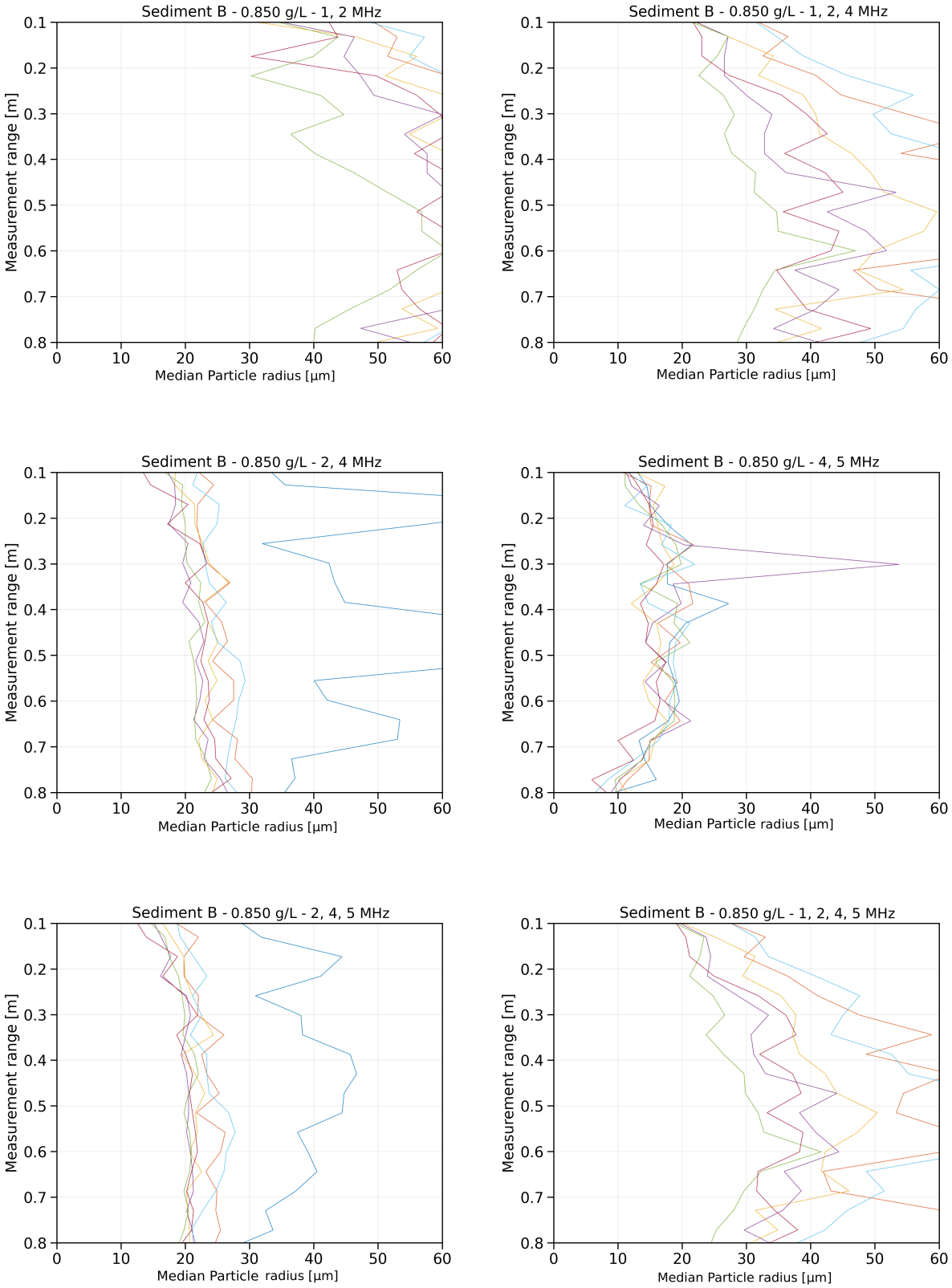

Figure C.3: Particle size estimates for the 0.850 g/L Sediment B measurement obtained using different frequency combinations: the two lowest frequencies (1 and 2 MHz), the three lowest frequencies (1, 2, and 4 MHz), the two middle frequencies (2 and 4 MHz), the two highest frequencies (4 and 5 MHz), the three highest frequencies (2, 4, and 5 MHz), and all four frequencies (1, 2, 4, and 5 MHz).

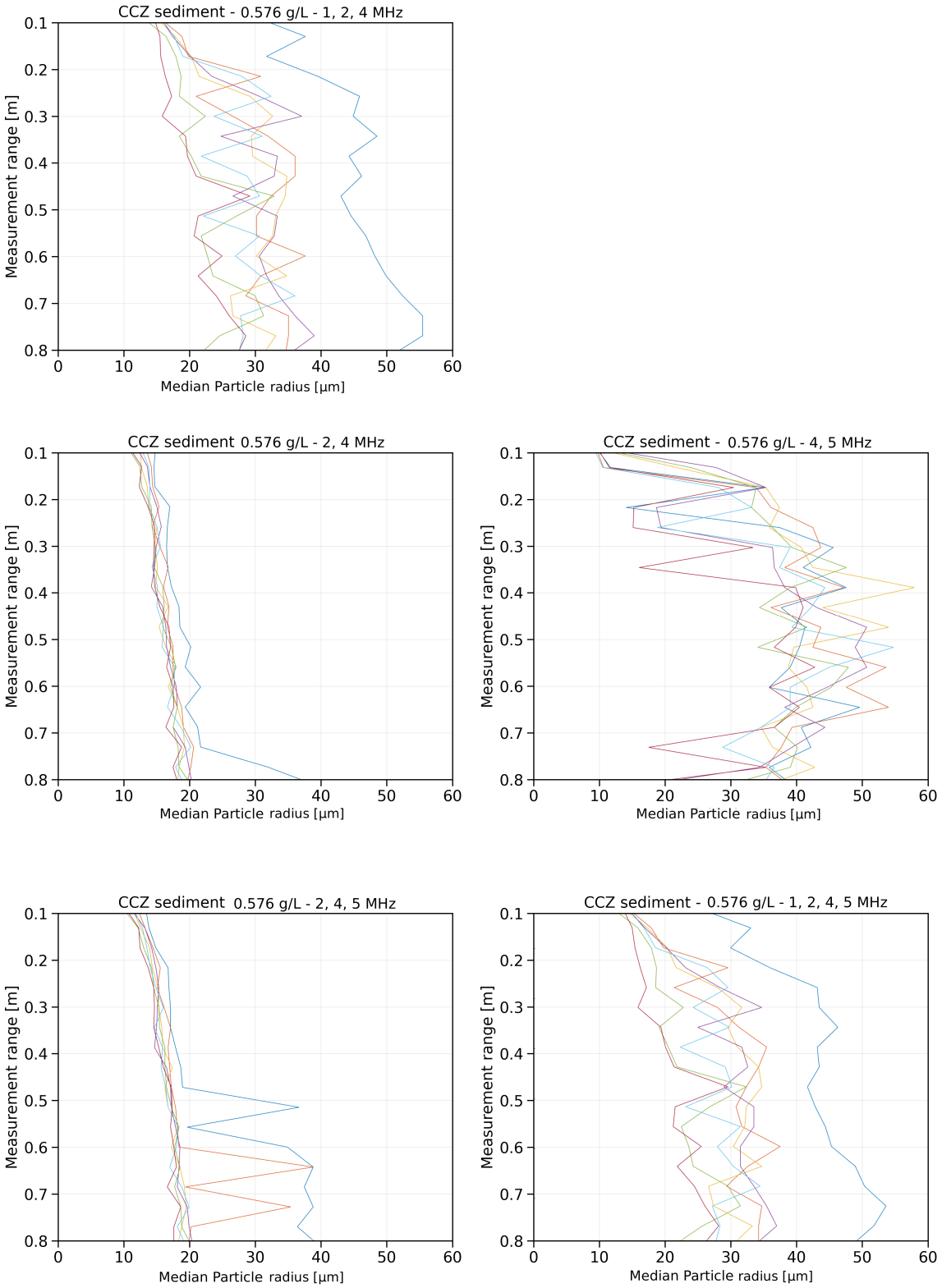

Figure C.4: Particle size estimates for the 0.576 g/L CCZ sediment measurement obtained using different frequency combinations: the two lowest frequencies (1 and 2 MHz), the three lowest frequencies (1, 2, and 4 MHz), the two middle frequencies (2 and 4 MHz), the two highest frequencies (4 and 5 MHz), the three highest frequencies (2, 4, and 5 MHz), and all four frequencies (1, 2, 4, and 5 MHz).

Particle Size Inversion Evaluation

The analysis reveals that this method consistently overestimates the particle size. The inversion results are therefore quantified using an overestimation ratio, defined as the average inverted particle size divided by the corresponding Malern or LISST measured D_{50}. The results are summarized in Table C.1 and visualized in Figure C.5. The reported particle size is defined by the minimum and maximum particle size obtained across the six averaged profiles. A single unstable profile is disregarded as an outlier, whereas two or more unstable profiles are included in the reported range. For the following analysis, the inversion is performed using all four frequencies, with the Relative standard deviation ($Rel.SD$) prescribed to the Malvern measured value.

Above approximately 1.250 g/L, the inverted particle diameter would increased with range, with the gradient becoming steeper as SSC increased. In some cases, the inverted radius increased from approximately 30 µm near the transducer to the upper inversion bound of 200 µm at greater range. Suspended sediment concentrations above 7.8 g/L did not provide resolved particle-size estimates and were therefore excluded from the analysis.

The lowest particle-size overestimation occurred at SSCs of $0.499 - 0.850$ g/L for Sediment B and $0.576 - 1.250$ g/L for the CCZ sediment. The CCZ sediment showed the closest agreement with the reference measurements, with the lowest inverted particle diameter overestimated by factors of 4.1 and 6.1 relative to the Malvern and LISST measurements, respectively. For Sediment B, the lowest overestimation factors were substantially higher, at 18.2 and 39.0 relative to the Malvern and LISST measurements, respectively. At SSCs outside these ranges, the inversion performance deteriorated, with particle-size estimates increasingly approaching the software's upper particle-radius inversion bound of 400 μm. For both sediments, the inverted particle sizes showed consistently closer agreement with the Malvern measurements than with the LISST measurements.

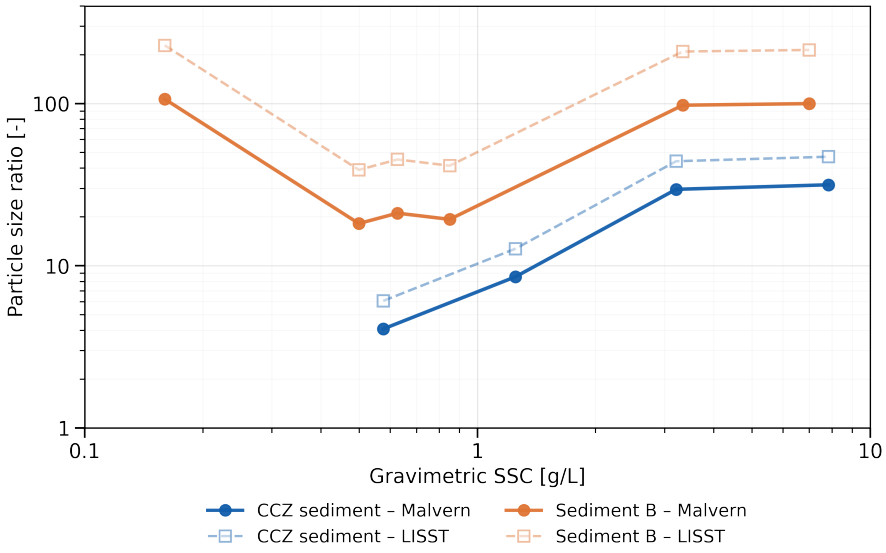

Figure C.5: Particle size ratio relative to the LISST and Malvern measured D_{50}, as a function of gravimetric SSC (g/L)

Table C.1: Minimum and maximum estimated particle radii and corresponding mean median particle diameter obtained with Method 1 using the 1, 2, 4, and 5 MHz frequencies. The overestimation ratios are calculated relative to the Malvern- and LISST-determined median particle diameters.

SSC	**Sediment**	**Particle radius range**	**Mean diameter**	**Malvern**		**LISST**	
(g/L)		(μm)	(μm)	D_{50} (μm)	Ratio	D_{50} (μm)	Ratio
0.576	CCZ sediment	25–37	62	15.2	4.1	10.2	6.1
1.250	CCZ sediment	30–100	130	15.2	8.6	10.2	12.7
3.205	CCZ sediment	50–400	450	15.2	29.6	10.2	44.1
7.835	CCZ sediment	80–400	480	15.2	31.6	10.2	47.1
0.160	Sediment B	80–400	480	4.5	106.7	2.1	228.6
0.499	Sediment B	30–52	82	4.5	18.2	2.1	39.0
0.626	Sediment B	35–60	95	4.5	21.1	2.1	45.2
0.850	Sediment B	35–52	87	4.5	19.3	2.1	41.4
3.330	Sediment B	40–400	440	4.5	97.8	2.1	209.5
6.997	Sediment B	50–400	450	4.5	100.0	2.1	214.3

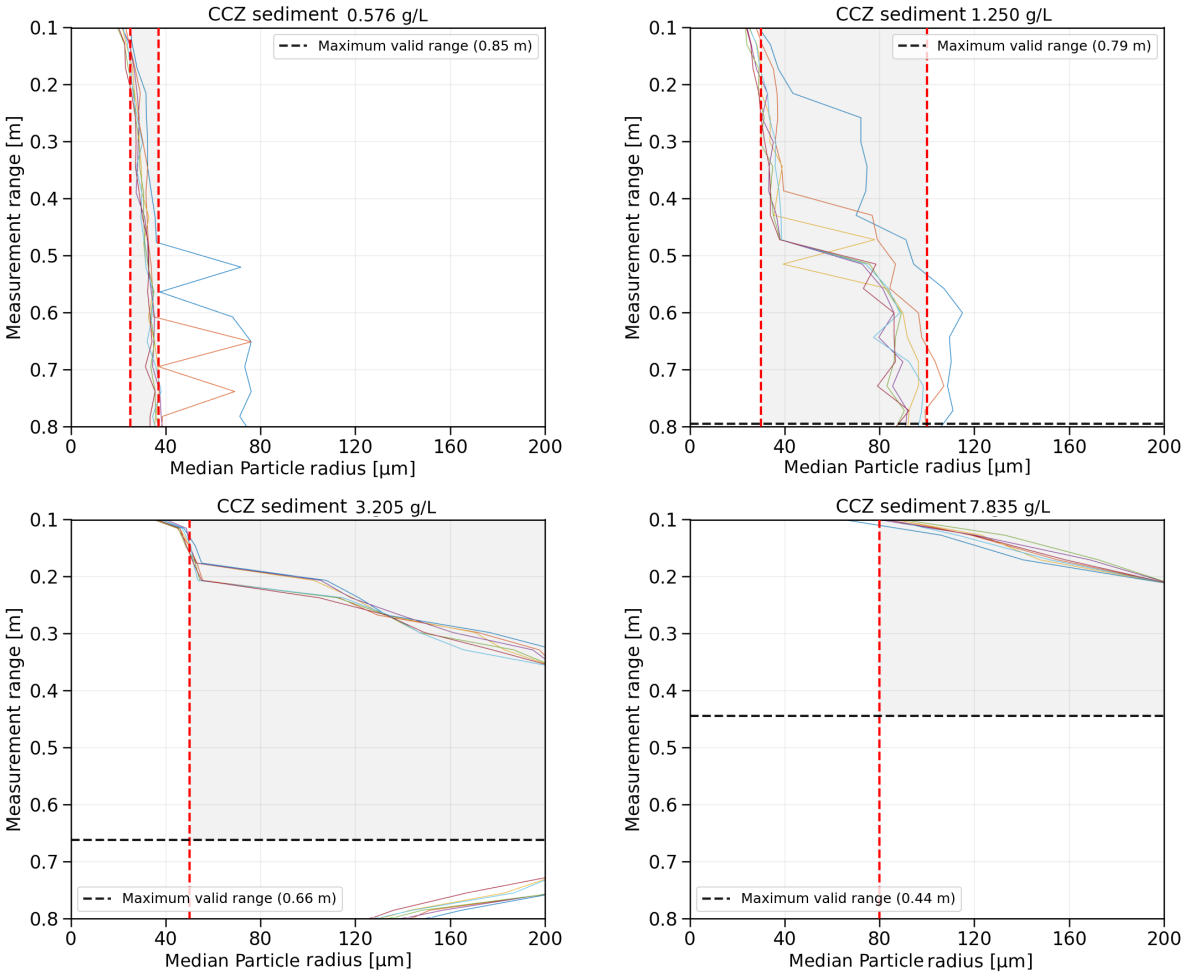

Figure C.6: Particle-size inversion of the CCZ sediment through Method 1. Horizontal plot indicates the maximum range set by SNR=5. Vertical lines indicate the maximum and minimum estimated value.

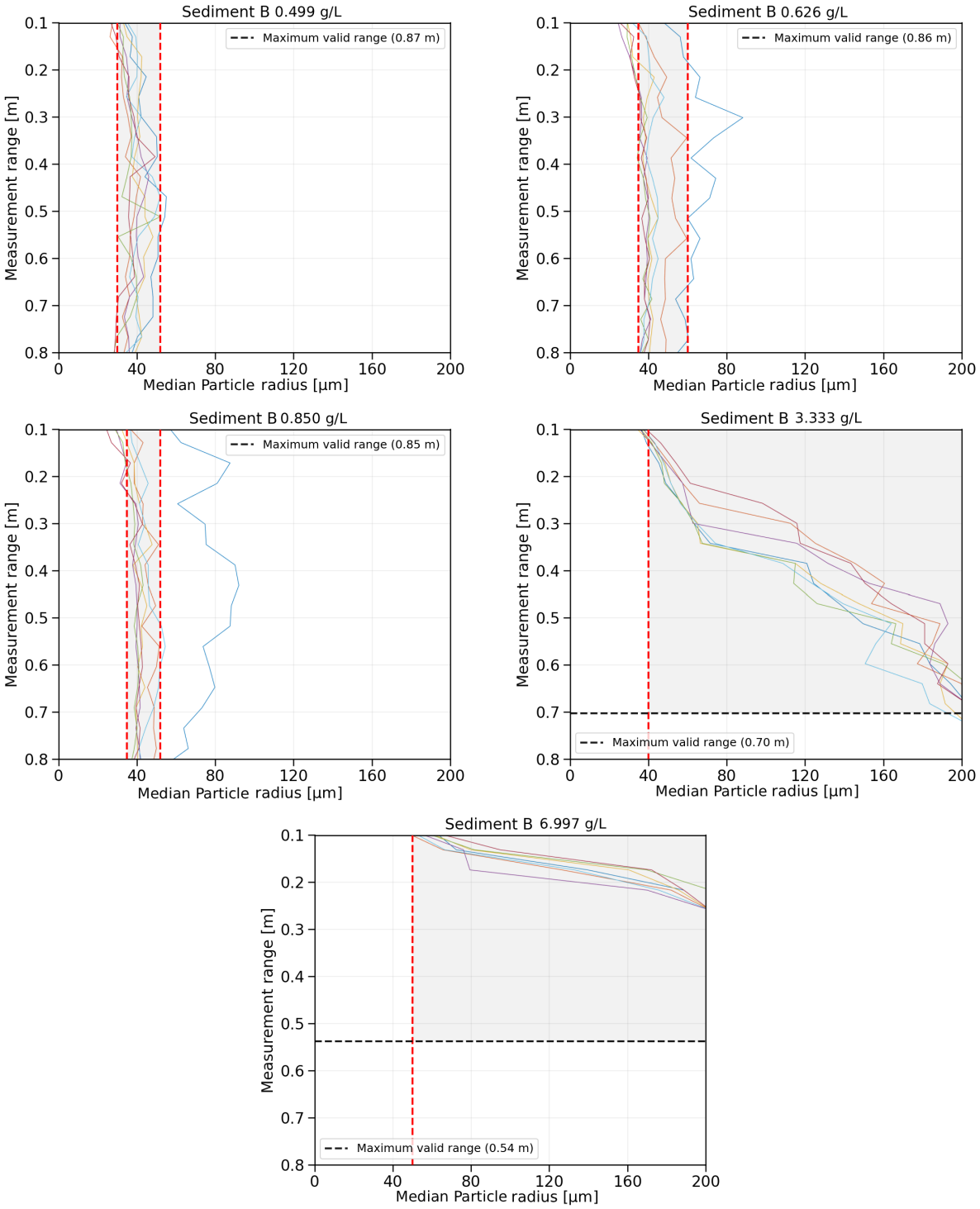

Figure C.7: Particle-size inversion of Sediment B through Method 1. Horizontal plot indicates the maximum range set by SNR=5. Vertical lines indicate the maximum and minimum estimated value.

Effect of Relative Standard Deviation

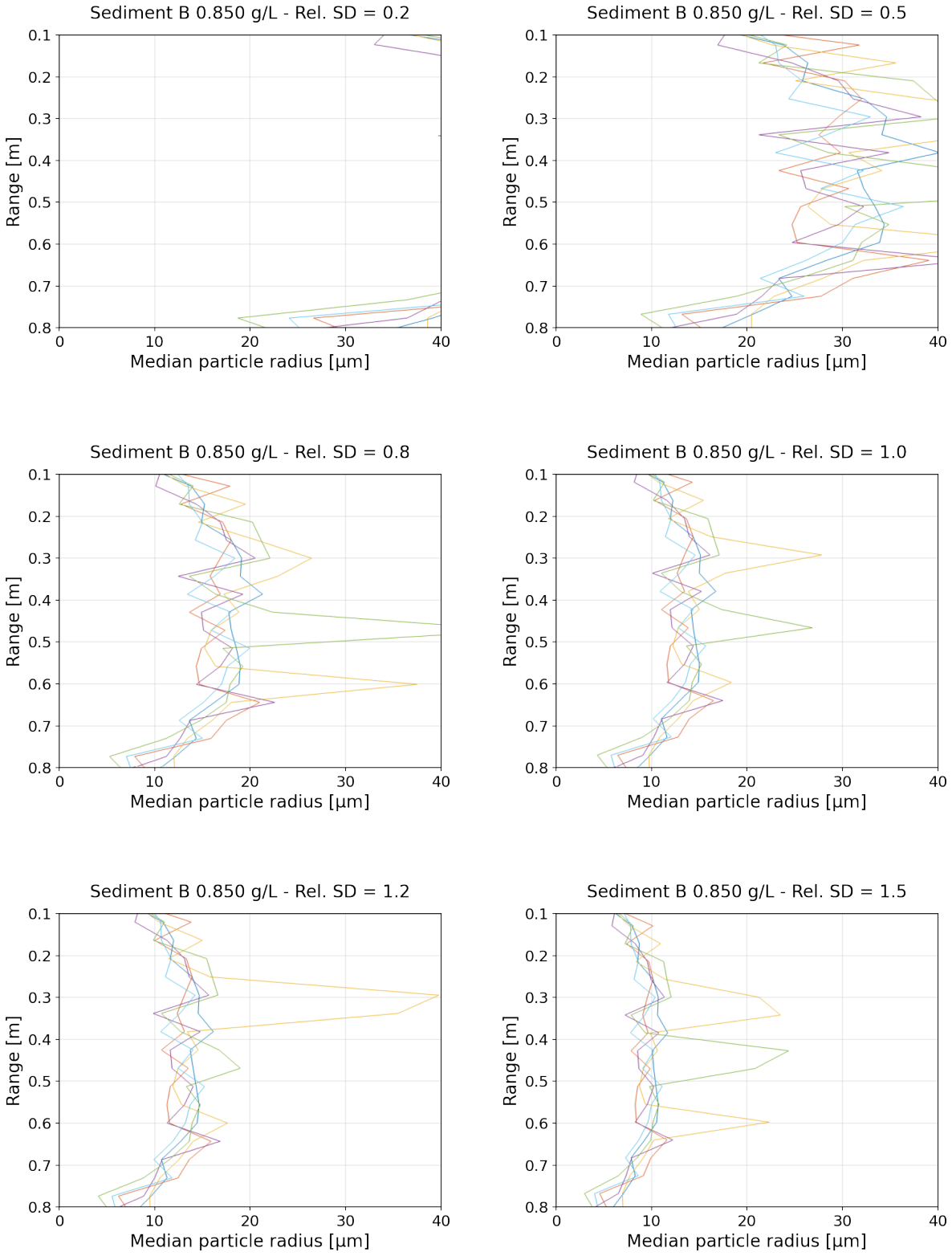

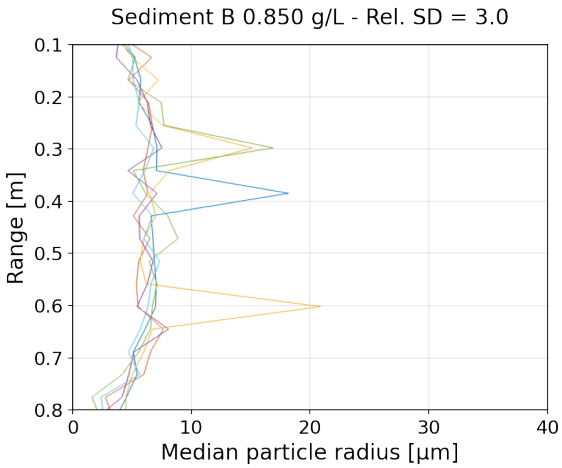

Figure C.9: Particle size estimates for the Sediment B measurement using a prescribed relative standard deviation of 3.0 for the lognormal particle size distribution.

D

Method 2 Analysis

The following section presents the results of Method 2. Due to time-intensive post-processing and preparation of the figures, it was not feasible to include the case for all sediment types, SSC levels, and frequency combinations. Instead, the most representative cases were selected to illustrate the key findings, as the remaining cases exhibited similar trends.

Effect of Frequency Combinations

In the following plots, the inverted SSC for the CCZ sediment is consistently underestimated for all frequency combinations. The lower 1 and 2 MHz frequencies did result in slightly higher SSC values, with approximately half of the profiles estimating a concentration above 0.5 g/L (See Figure D.1 for a more intuitive interpretation). For Sediment B, the inverted SSC is overestimated by the lower frequency combinations; the 4 and 5 MHz frequencies yielded the most accurate SSC inversion.

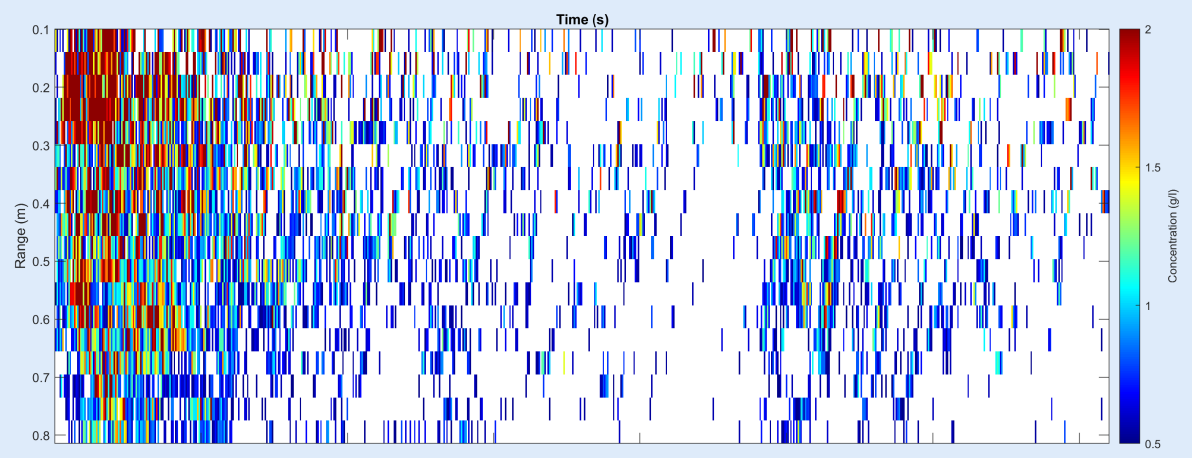

Figure D.1: Inverted SSC profile for the CCZ sediment at a measured SSC of 1.25 g/L using only the 1 MHz frequency, illustrating the effect of the lowest-frequency selection.

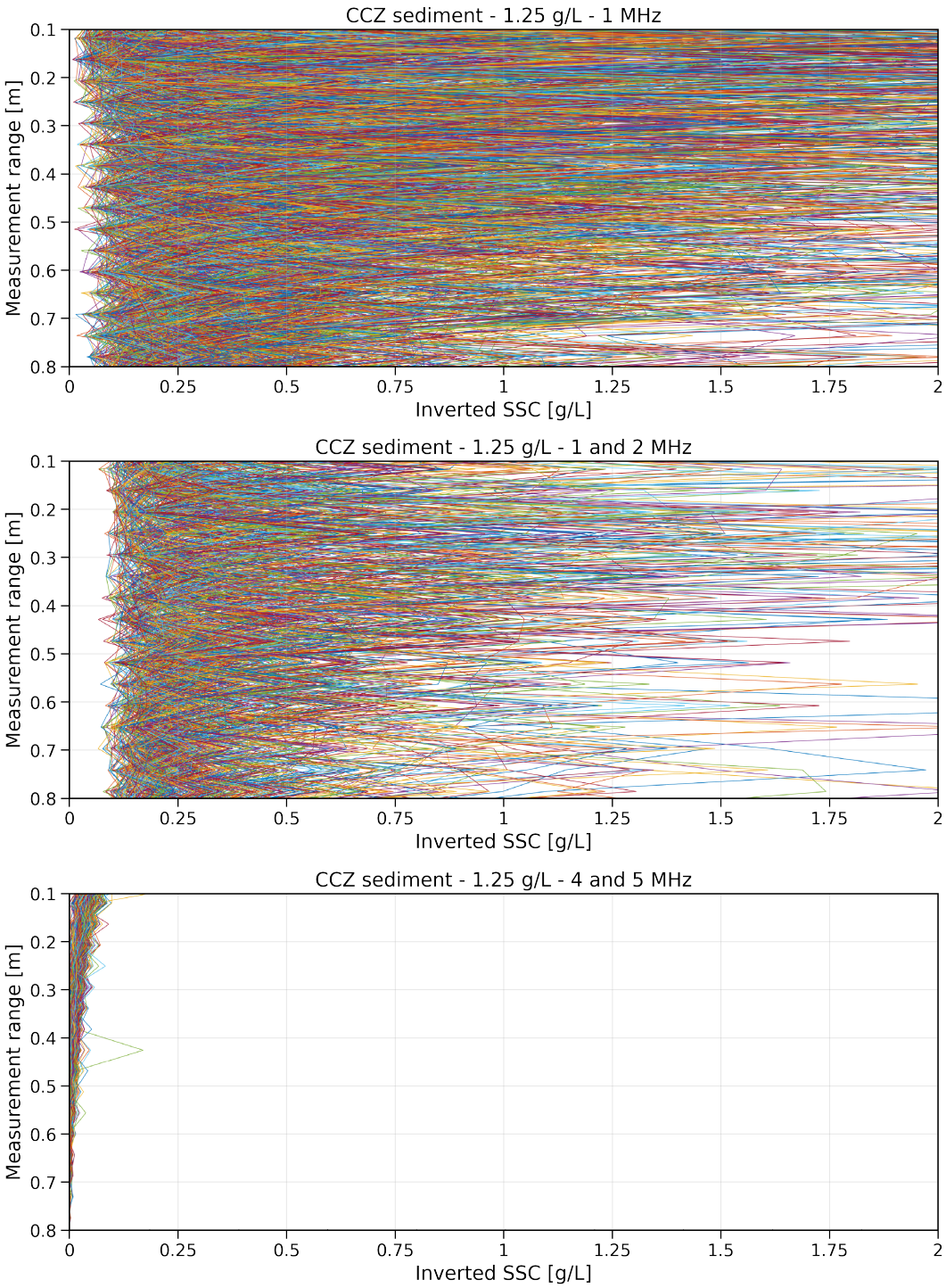

Figure D.2: Inverted SSC profiles for the CCZ sediment at gravimetrically measured SSC = 1.250 g/L using different frequency combinations (part 1).

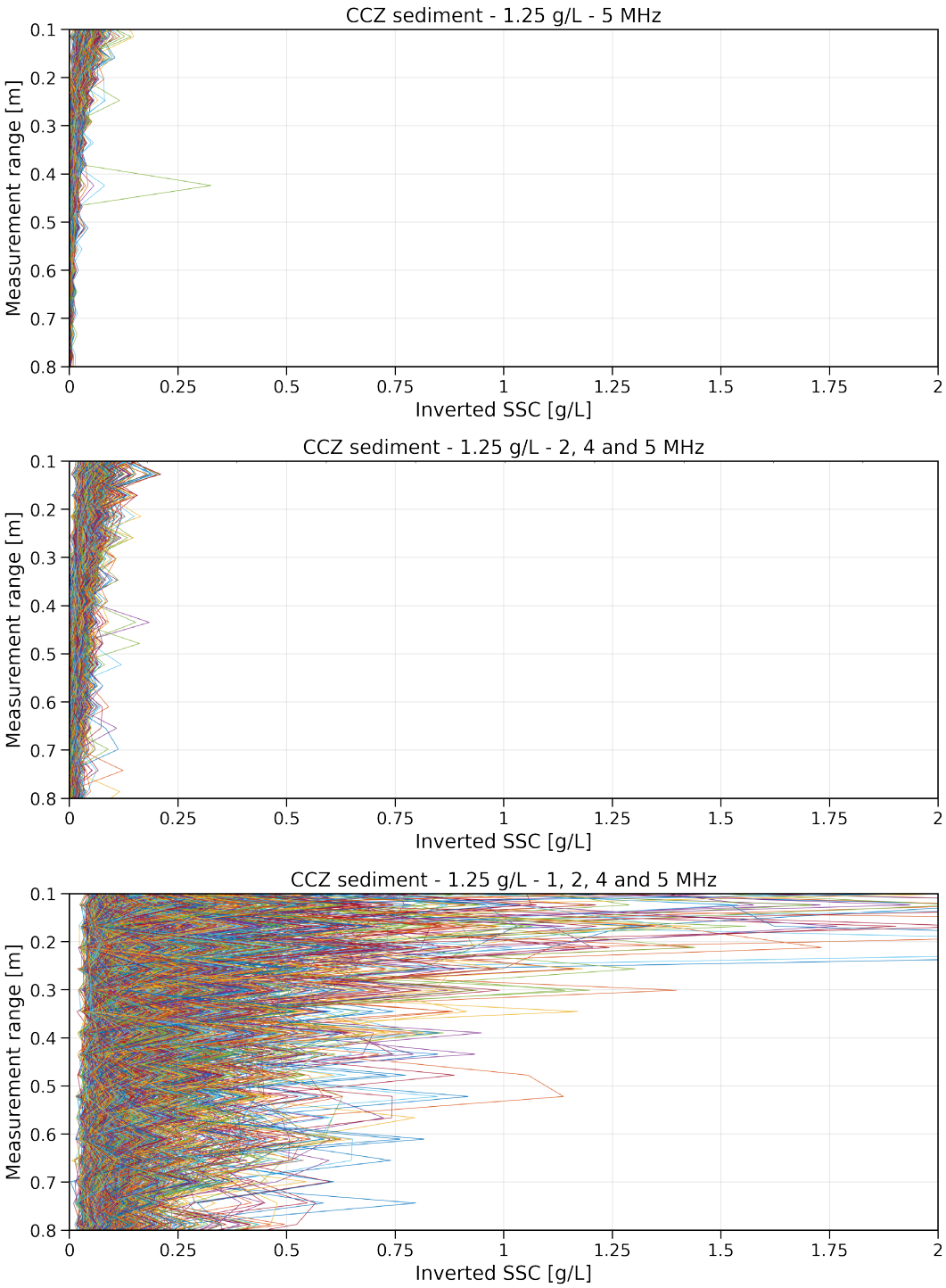

Figure D.3: Inverted SSC profiles for the CCZ sediment at gravimetrically measured SSC = 1.250 g/L using different frequency combinations (part 2).

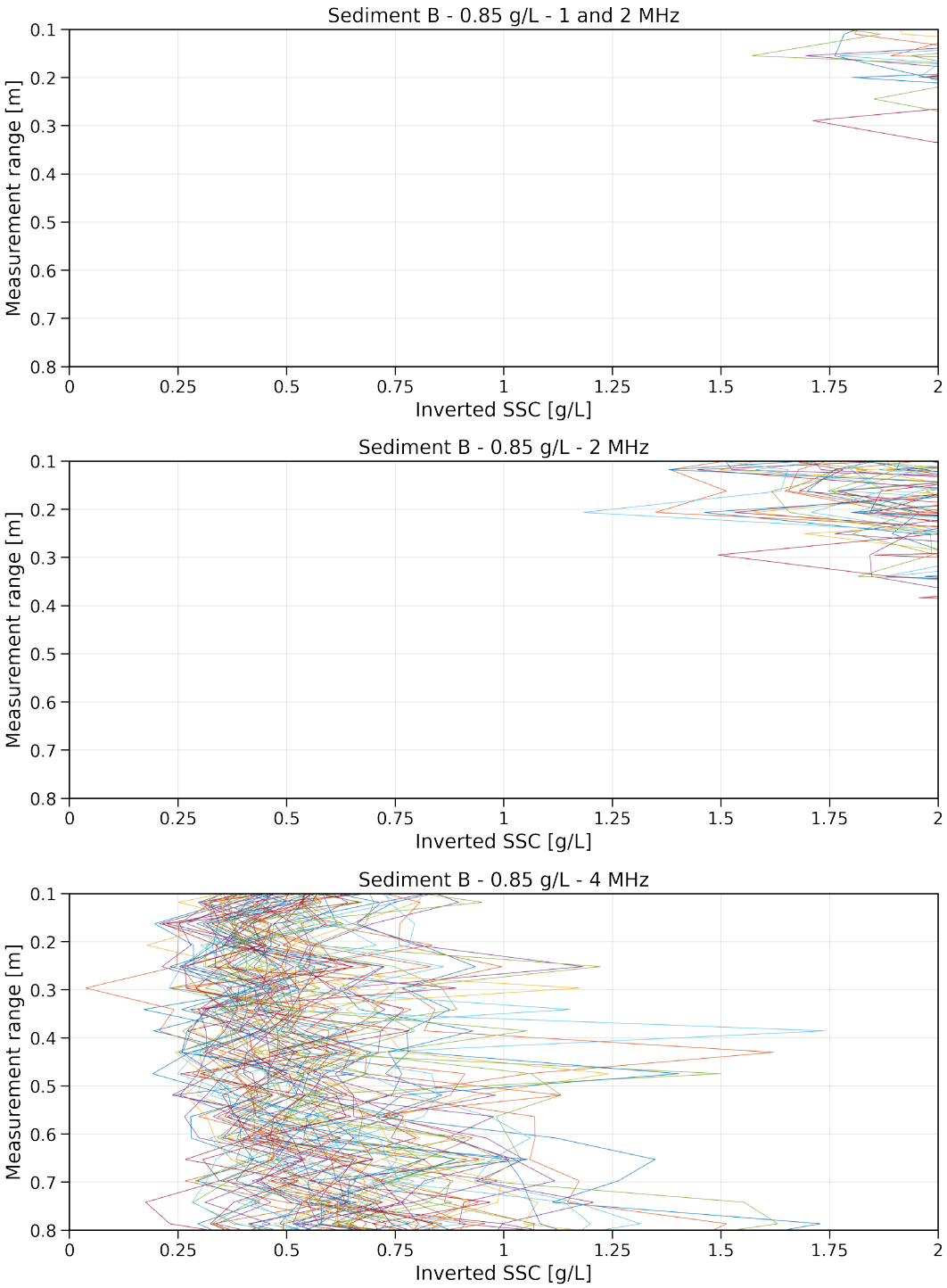

Figure D.4: Inverted SSC profiles for Sediment B at gravimetrically measured SSC = 0.850 g/L using different frequency combinations (part 1).

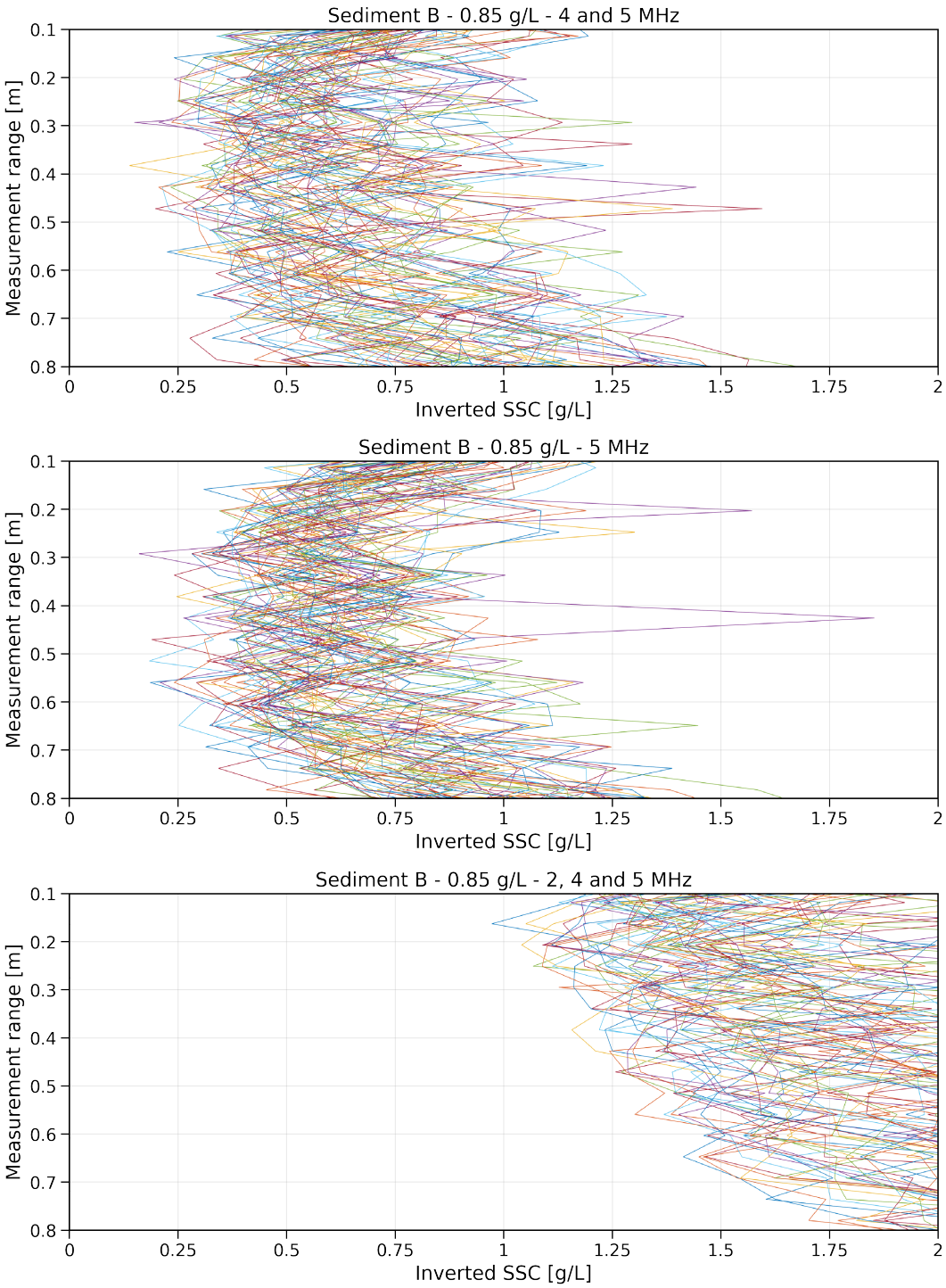

Figure D.5: Inverted SSC profiles for Sediment B at gravimetrically measured SSC = 0.85 g/L using different frequency combinations (part 2).

Effect of Particle Size

Table D.1: Sensitivity of the inverted SSC to the prescribed median particle diameter (D_{50}). The measured SSC was 0.85 g/L. The relative error with respect to the reference case ($D_{50} = 4.5$ μm) was calculated as $\left(SSC_{D_{50}} - SSC_{4.5}\right) / SSC_{4.5} \times 100$.

D_{50} (μm)	**Inverted SSC** (g/L)	**Relative error to** $D_{50} = 4.5\mu m$ $(\%)$
3.5	$\geq$1.00	$\geq$+185.7
4.5	0.35	0
5.5	0.20	-42.9

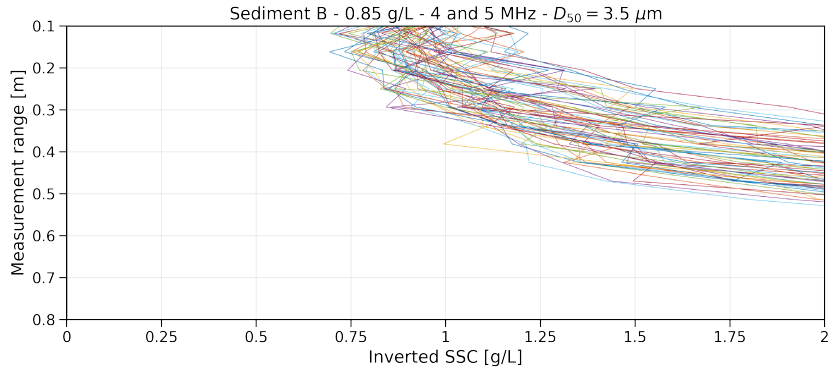

(a) $D_{50} = 3.5\ \mu\mathrm{m}$

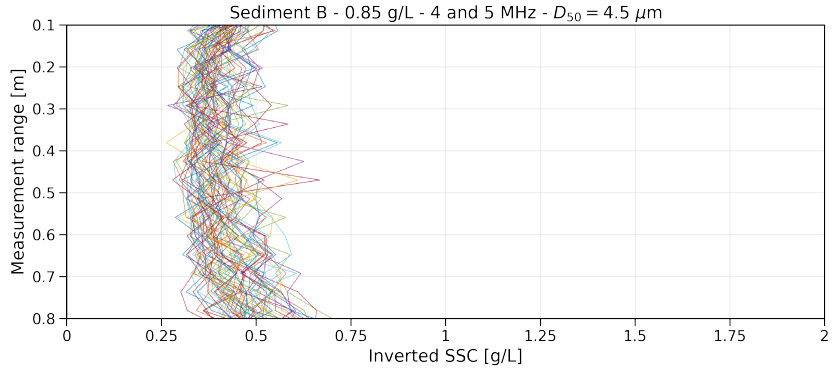

(b) $D_{50} = 4.5\ \mu\mathrm{m}$

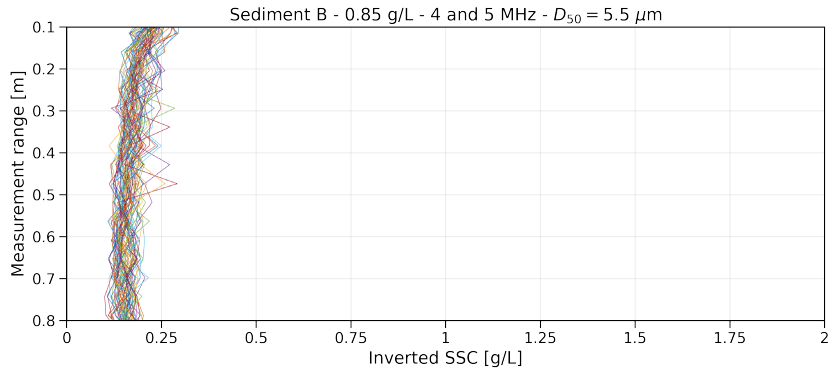

(c) $D_{50} = 5.5\ \mu\mathrm{m}$

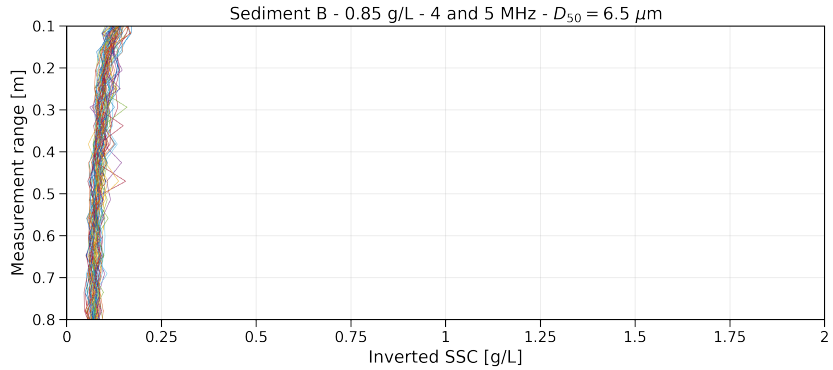

(d) $D_{50} = 6.5\ \mu\mathrm{m}$

Figure D.6: Inverted SSC profiles for Sediment B using the 4 and 5 MHz frequencies for fixed median particle diameters ranging from 3.5 to 6.5 μm. The cases are ordered from the smallest to the largest prescribed particle size.

Effect of Distribution Width

Similarly, the relative standard deviation was varied by ± 0.1 about the Malvern-measured value of 0.8. An overestimation of by 0.1 in the Relative Standard Deviation can lead up to a deviation in SSC of 117.7 % relative to the Malvern-measured SSC; demonstrating its sensitivity to the the relative standard deviation.

Table D.2: Sensitivity of the inverted SSC to the prescribed relative standard deviation. The measured SSC was 0.85 g/L.

Rel. SD (-)	Inverted SSC (g/L)	Error (g/L)	Relative error (%)
0.7	2.0	+1.15	+135.3
0.8	1.0	+0.15	+17.6
0.9	0.6	-0.25	-29.4

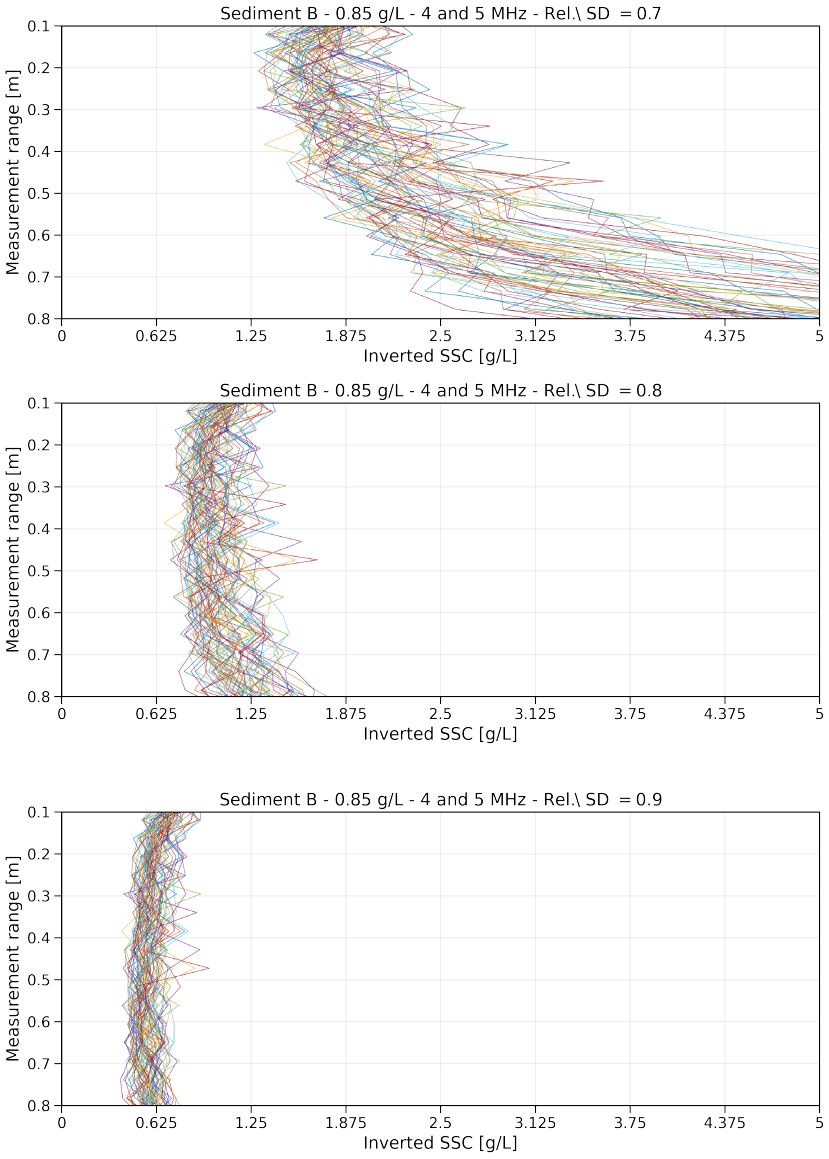

Figure D.7: Inverted SSC profiles for Sediment B using the 4 and 5 MHz frequencies for prescribed relative standard deviations ranging from 0.7 to 0.9. The cases are ordered from the lowest to the highest relative standard deviation.

Qualitative Assessment Through Method 1 & 2

The experimental campaign additionally included settling experiments, initially intended to assess sensor performance under flocculating suspensions using Methods 1 and 2. Following the shift in research scope after the experimental campaign, these experiments were excluded from the main analysis. Nevertheless, the observed sensor response during a settling plume is briefly assessed qualitatively to provide additional insight into its performance and interpretation challenges.

In this analysis the settling behaviour of Sediment B at 1 g/L is assessed over a period of approximately 2 hours, measured in recordings of 15 minutes each. This section begins by analysing the plume using Method 2, illustrating the challenge of measuring plumes without particle size information. It then explores the particle size estimation and SSC inversion limits of Method 1, after which it concludes with a manual interpretation of the individual frequency responses.

Method 2 Qualitative Analysis

Figure D.9 illustrates the results of the Method 2 settling measurement. The particle size is set so that the inverted SSC corresponded best to the initial SSC measured by the OBS, attempting to give some sort of reference SSC. The increase of SSC within the first 10 minutes is likely the effect of increasing particle size due to flocculation. Flocs result in increased backscatter. from 13:10 it can be observed that the sediment begins to settle over time starting from the top and slowly decreasing in height. This plot illustrates the development of the plume, however the causing factor can not be distinguished between SSC and flocculation, and therefore no quantitative information can taken from this plot.

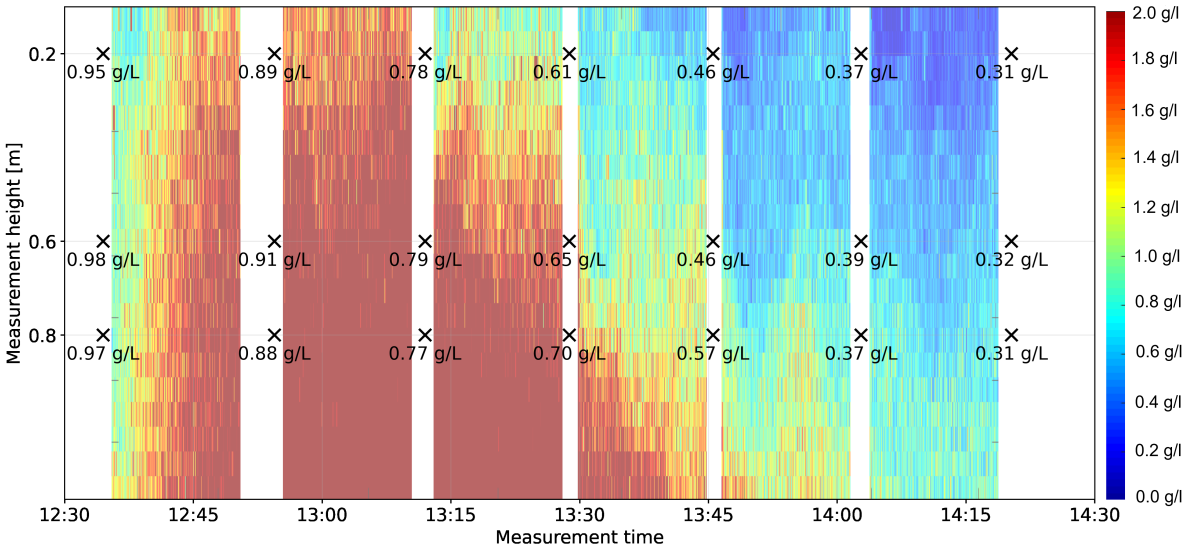

Figure D.8: Multi-frequency inversion of Sediment B settling out starting from approximately 1 g/L for approximately 2 hours, in 6 recordings of 10 minutes

Method 1 - Qualitative Analysis

The multi-frequency SSC and particle size inversion (Method 1) evaluates the particle size first and subsequently the SSC; therefore, the SSC is a result of the estimated particle size. The particle size inversion indicates an increase in particle size within the first 10 minutes, increasing from approximately 30 μm to 110 μm and beyond, after which it remains at this size for the remainder of the experiment. At the beginning of the experiment, the SSC inversion is highest when the particle size is smallest. Once the particle size starts to increase, the SSC can be observed to decrease slightly. From 13:10 onwards, the SSC starts to decrease with both time and height, similar to the inversion with the prescribed particle size. However, the SSC decreases to lower value estimates than in the prescribed particle size method, which is a result of the increased particle size estimate. Since the software restricts particle size estimation to 200 μm, the particle size cannot be tracked to larger sizes and the SSC estimate is likely to be even lower than what is qualitatively visualized.

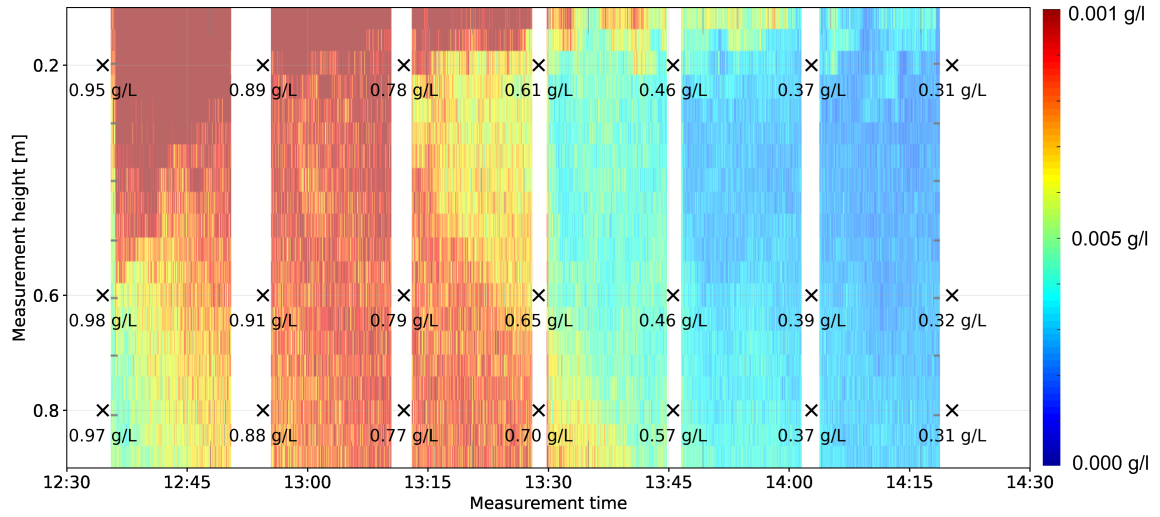

(a) Estimated concentration over the settling experiment.

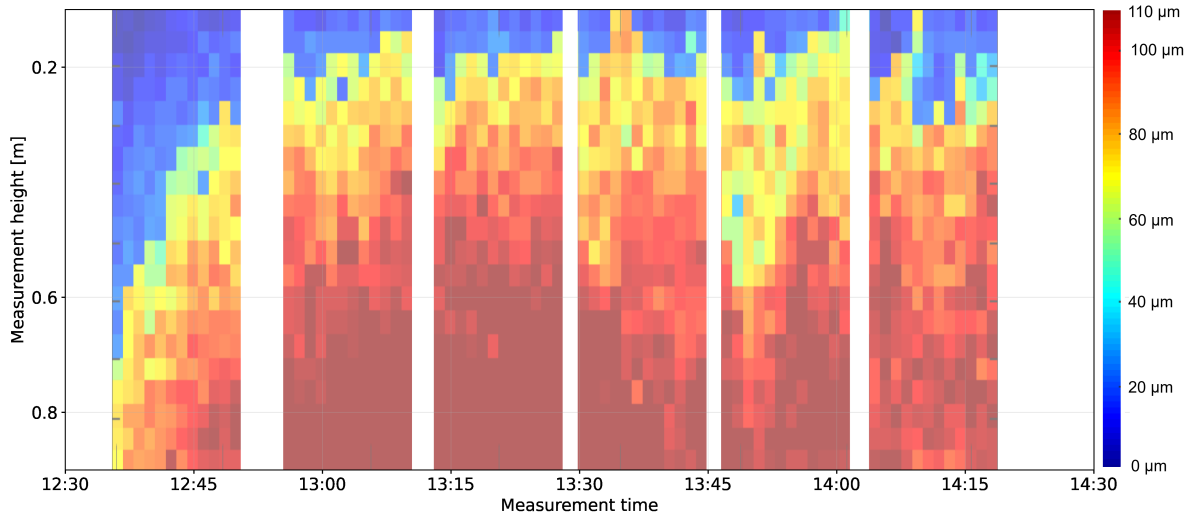

(b) Estimated particle size distribution parameters over the settling experiment.

Figure D.9: Multi-frequency inversion results for Sediment B settling from an initial concentration of approximately 1 g/L over a period of approximately 2 hours. Six 10-minute inversion windows are shown, illustrating the temporal evolution of the estimated suspended sediment concentration (top) and particle size parameters (bottom).

The previous analysis indicate the complexity of plume characterization, where Method 2 can not distinguish the causing factor of SSC increase due to actual SSC increase or due to flocculation. And Method 1 can distinguish this to some extent but quickly loses any credibility once particle sizes increase beyond 200 μm due to software restrictions. Although, multi-frequency particle size estimation and SSC inversion do not result in an solid overall analysis. Visually, interpreting the raw acoustic voltage data for each individual frequency can give some intuitive information on plume characteristics.

Qualitative Analysis Through Analysis of the Raw Acoustic Signal

The profile time series plots for each frequency, more specifically the low frequencies, visualize a sudden increase in voltage, while the high frequencies slightly decrease in voltage, indicating a shift towards larger particle sizes, to which the lower frequencies are more responsive. Over time, all transducer signals decrease, indicating a decrease in SSC.

This analysis illustrates the complexity of plume analysis, even under controlled laboratory conditions. For in-situ measurements, this analysis is most likely not feasible, as the plume is not confined within the volume of a tank, making it highly dynamic and unpredictable. Furthermore, there are no reference start

and end conditions, making the interpretation of the measurements considerably more challenging.

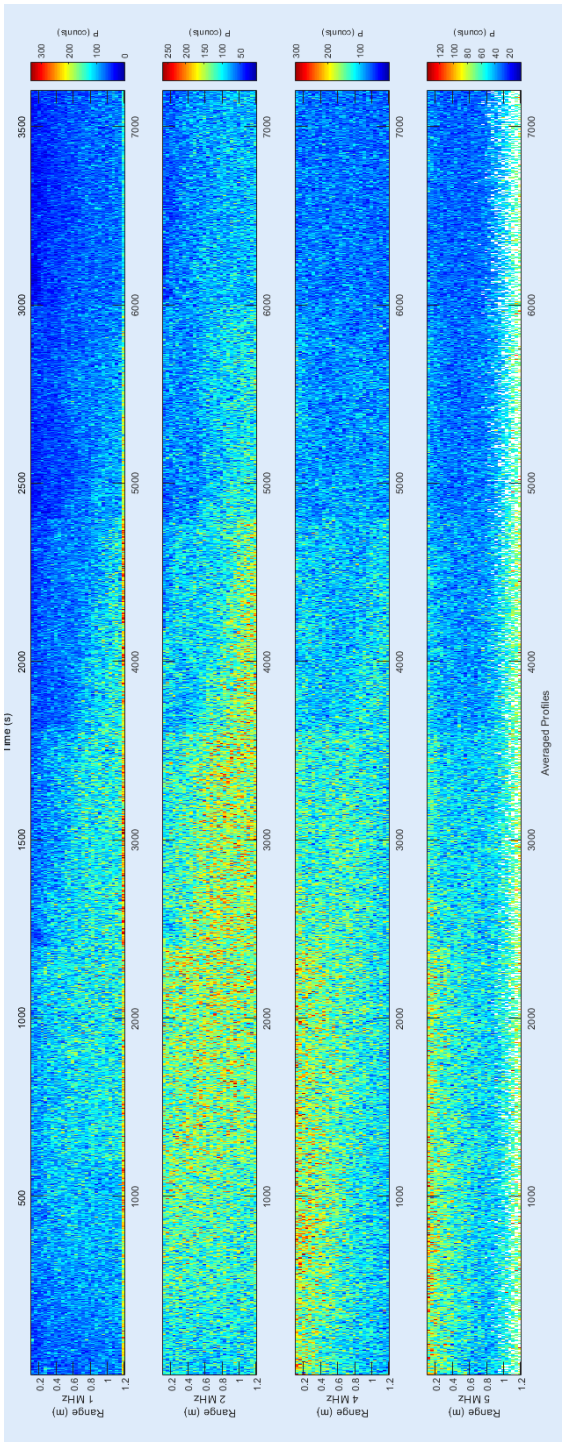

Figure D.10: Time series of the raw acoustic voltage profiles for 1, 2, 4, and 5 MHz frequencies during the 1 g/L Sediment B settling experiment.

E

Method 3 Analysis

The results of Method 3.1 are first presented for the four investigated constraint cases: no constraints, D_{50} constrained, σ constrained, and both D_{50} and σ constrained. For each case, the inverted SSC, D_{50}, and σ are presented as a function of the gravimetrically determined SSC. The inverted D_{50} and σ are additionally used to reconstruct and visualize the corresponding particle-size distributions in logarithmic space.

This is followed by the comparison with the OBS-derived SSC and the frequency selection analysis. Finally, the results of Method 3.2 are presented using the bi-modal particle-size distribution.

Table E.1: Performance metrics of Methods 3 and 4 for the CCZ sediment and Sediment B. Method 3 evaluates different particle size distribution constraints, while Method 4 evaluates the attenuation-based sub-methods for different constraints on D_{50} and σ. Method 4 results are based on the Φ objective function.

Sediment	SSC range	Constraint	Model	Slope	R^2	MARE (%)	RMSE (g/L)
Method 3.1 - Single-mode distribution							
CCZ sediment	0.5–32	–	Oblate	1.311	0.916	69.0	5.49
CCZ sediment	0.5–18	–	Oblate	1.530	0.872	84.0	5.20
Sediment B	0.5–18	–	Oblate	1.090	0.889	24.5	2.35
CCZ sediment	0.5–32	D_{50}	Oblate	1.311	0.997	36.2	4.39
CCZ sediment	0.5–18	D_{50}	Oblate	1.361	0.995	38.4	3.02
Sediment B	0.5–18	D_{50}	Oblate	1.012	0.978	10.7	0.92
CCZ sediment	0.5–32	σ	Oblate	1.715	0.986	69.8	10.16
CCZ sediment	0.5–18	σ	Oblate	1.723	0.959	70.3	6.24
Sediment B	0.5–18	σ	Oblate	0.947	0.976	18.5	1.09
CCZ sediment	0.5–32	D_{50}, σ	Oblate	0.537	0.652	32.1	7.02
CCZ sediment	0.5–18	D_{50}, σ	Oblate	0.825	0.982	25.9	1.56
Sediment B	0.5–18	D_{50}, σ	Oblate	0.762	0.987	26.5	2.46
Method 3.2 - Bi-modal distribution							
CCZ sediment	0.5–32	–	Spherical	0.804	0.966	38.2	3.50
CCZ sediment	0.5–18	–	Spherical	0.847	0.924	43.8	1.72
Sediment B	0.5–18	–	Spherical	0.590	0.962	80.6	3.72

Method 3.1

Case 1: No Constraints

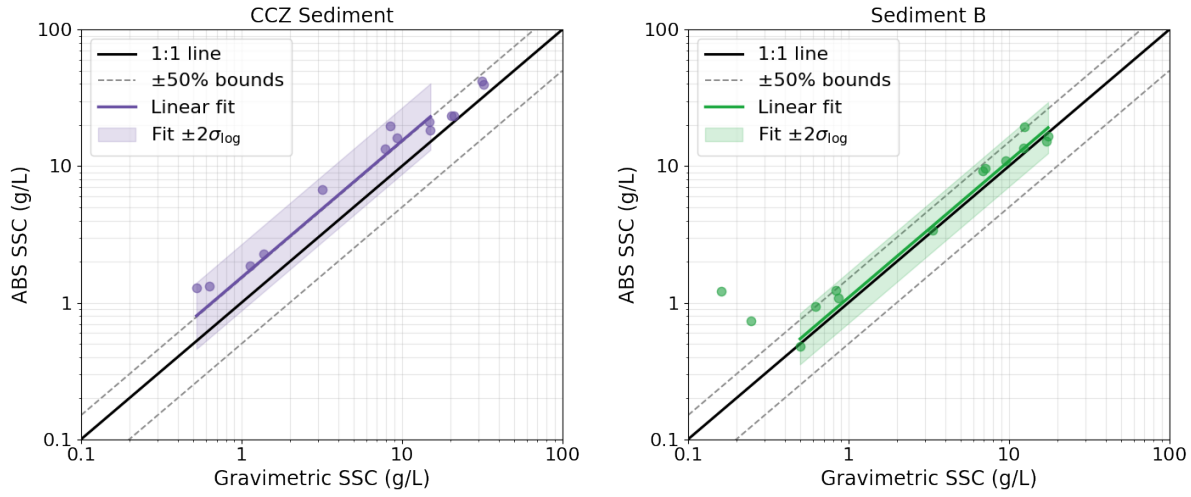

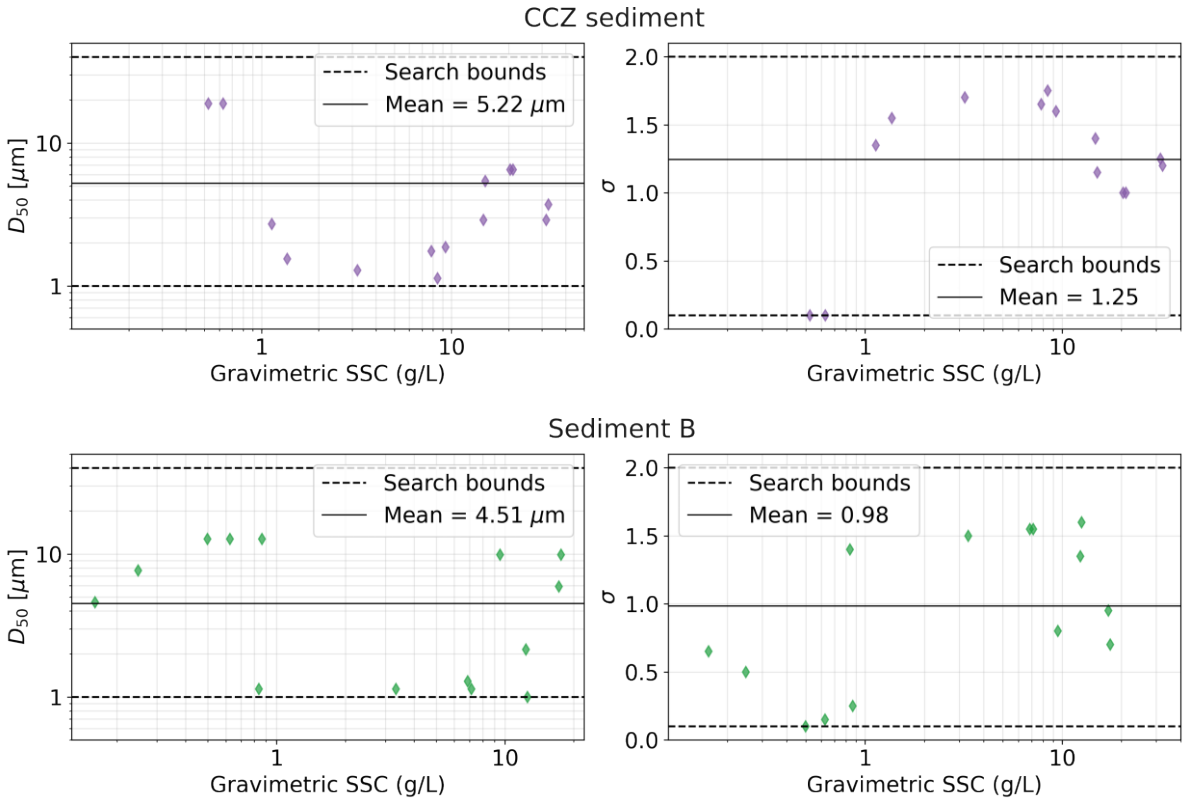

Figure E.2: Inverted particle-size distribution parameters without constraints. In each subplot, the left panel presents the particle-size inversion and the right panel the distribution-width inversion. Purple curves correspond to the CCZ sediment and green curves to Sediment B.

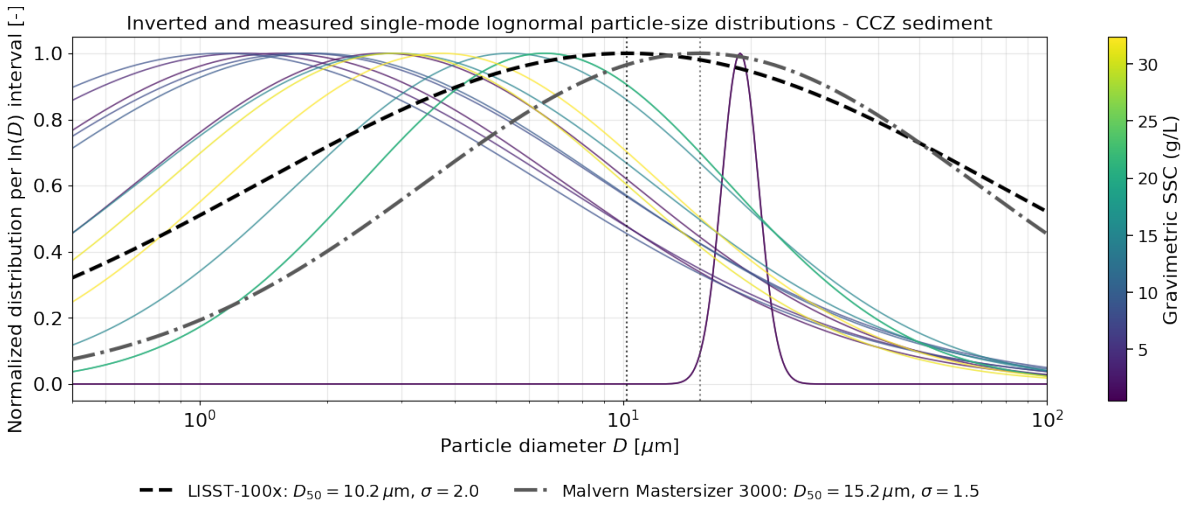

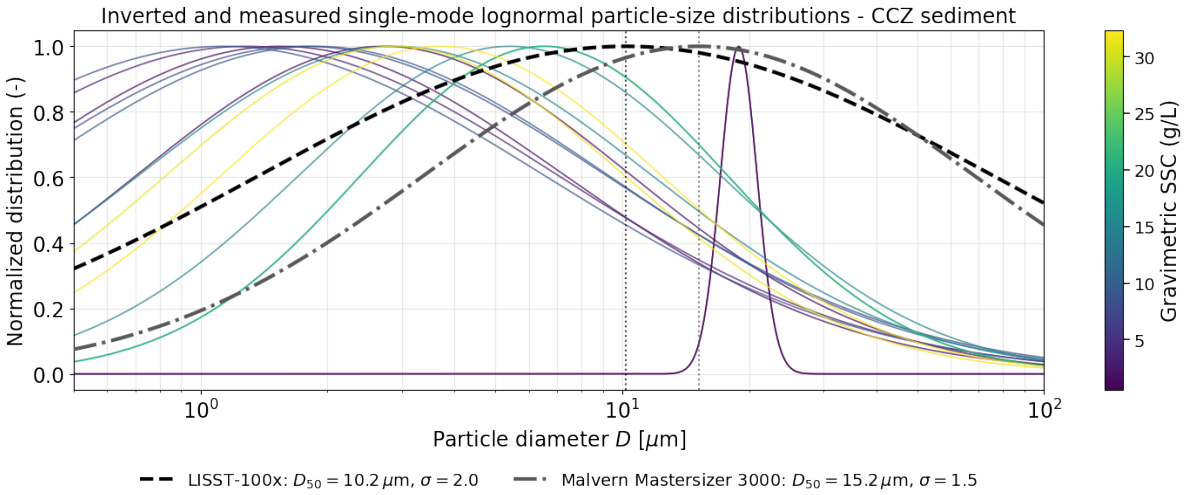

Case 2: Particle Size Constrained

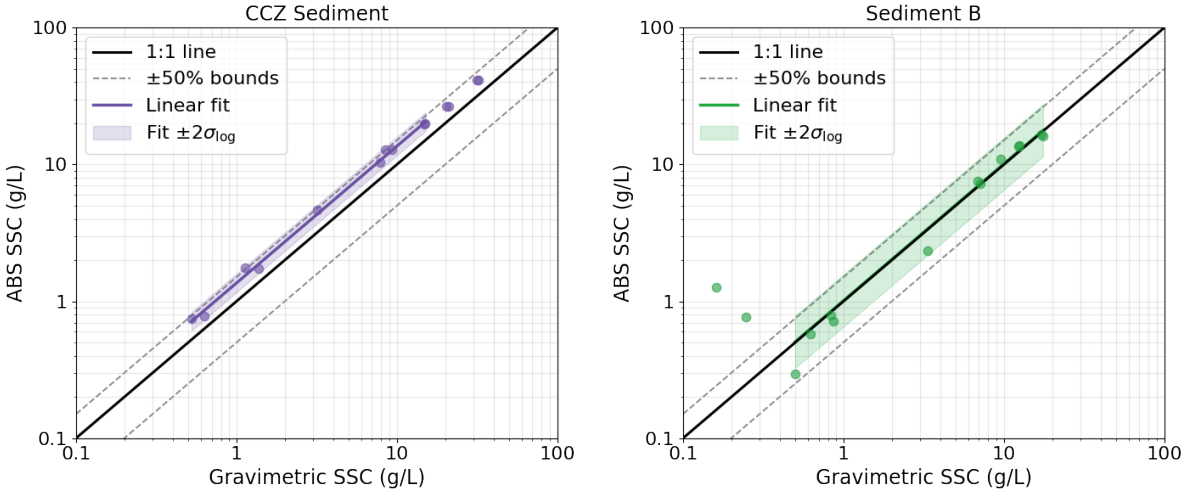

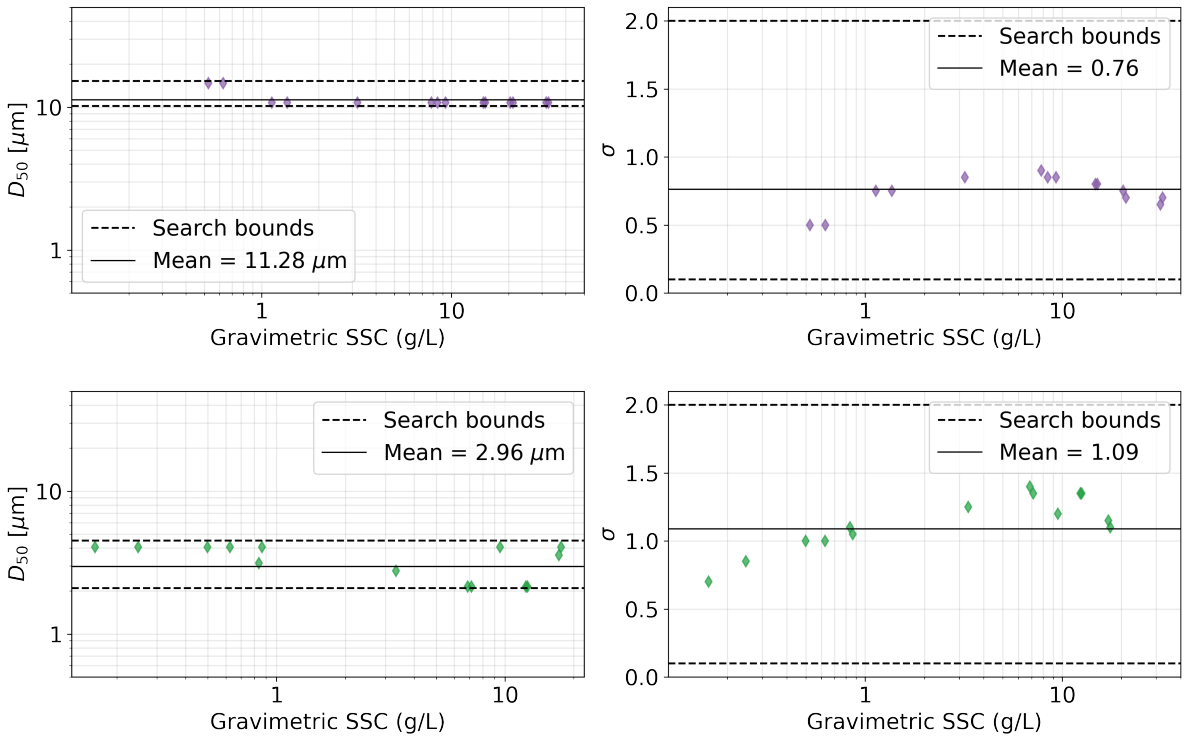

Figure E.4: Inverted particle-size distribution parameters with the particle size constrained. In each subplot, the left panel presents the particle-size inversion and the right panel the distribution-width inversion. Purple curves correspond to the CCZ sediment and green curves to Sediment B.

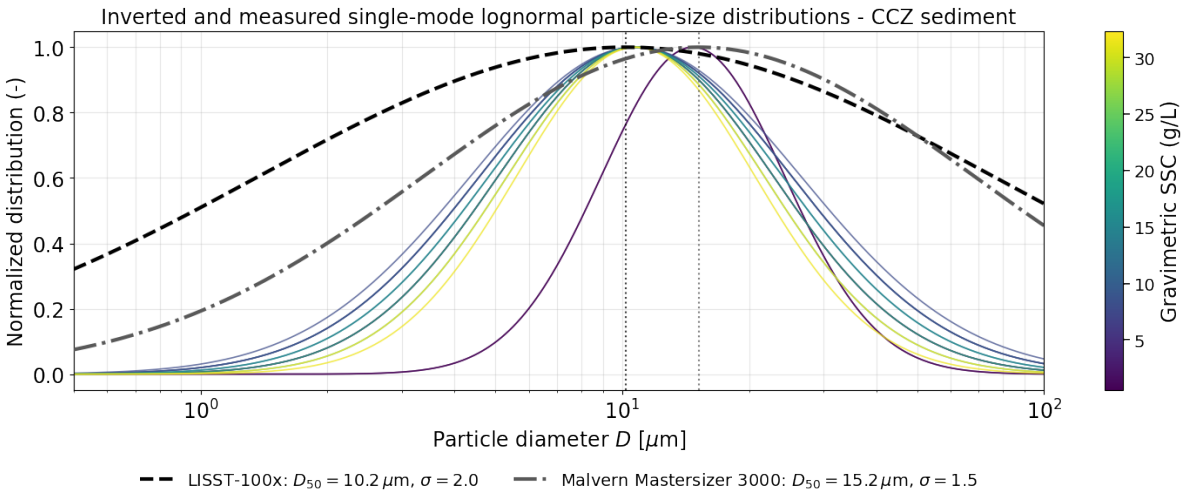

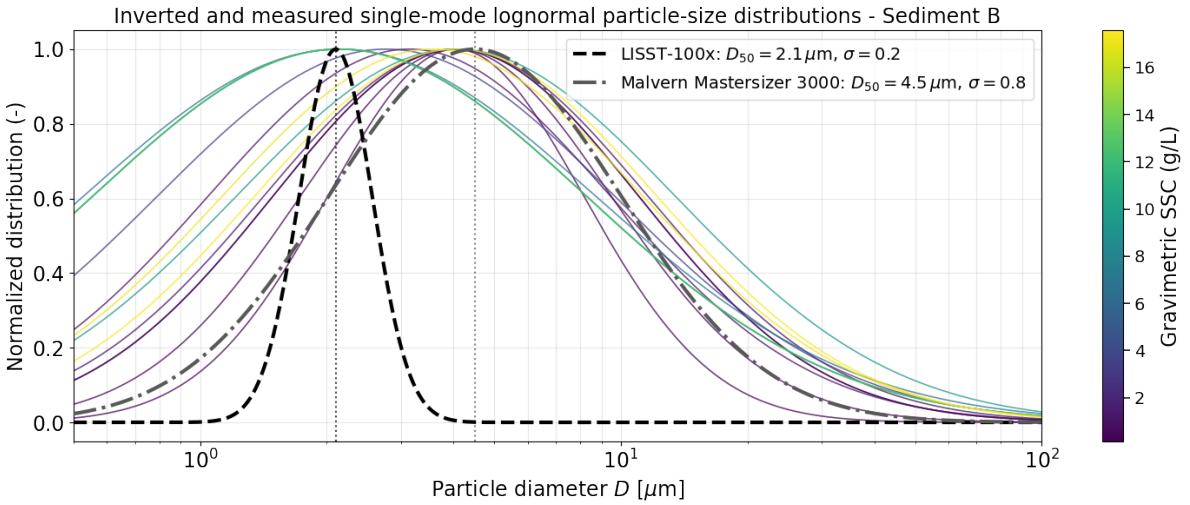

Case 3: Distribution Width Constrained

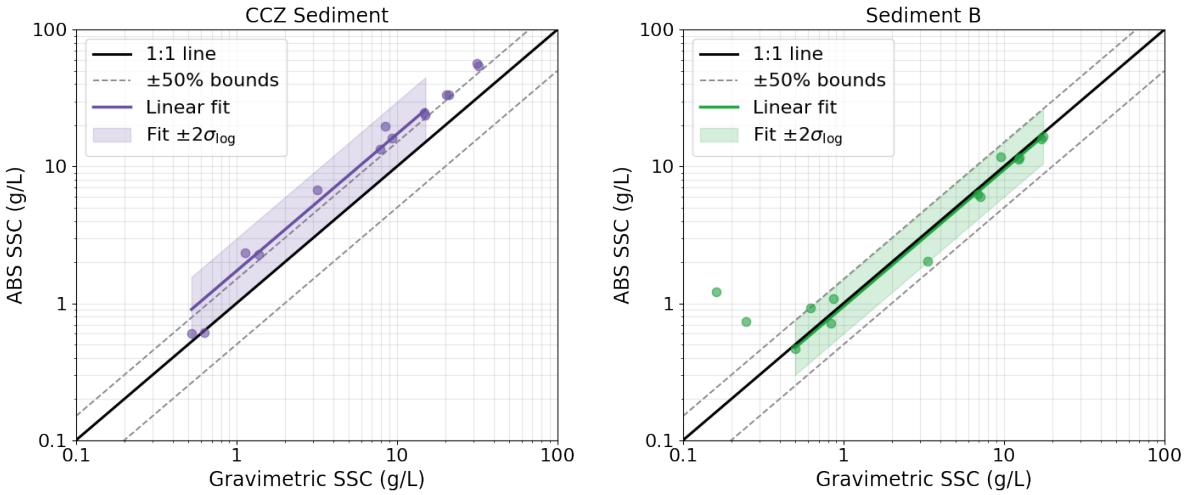

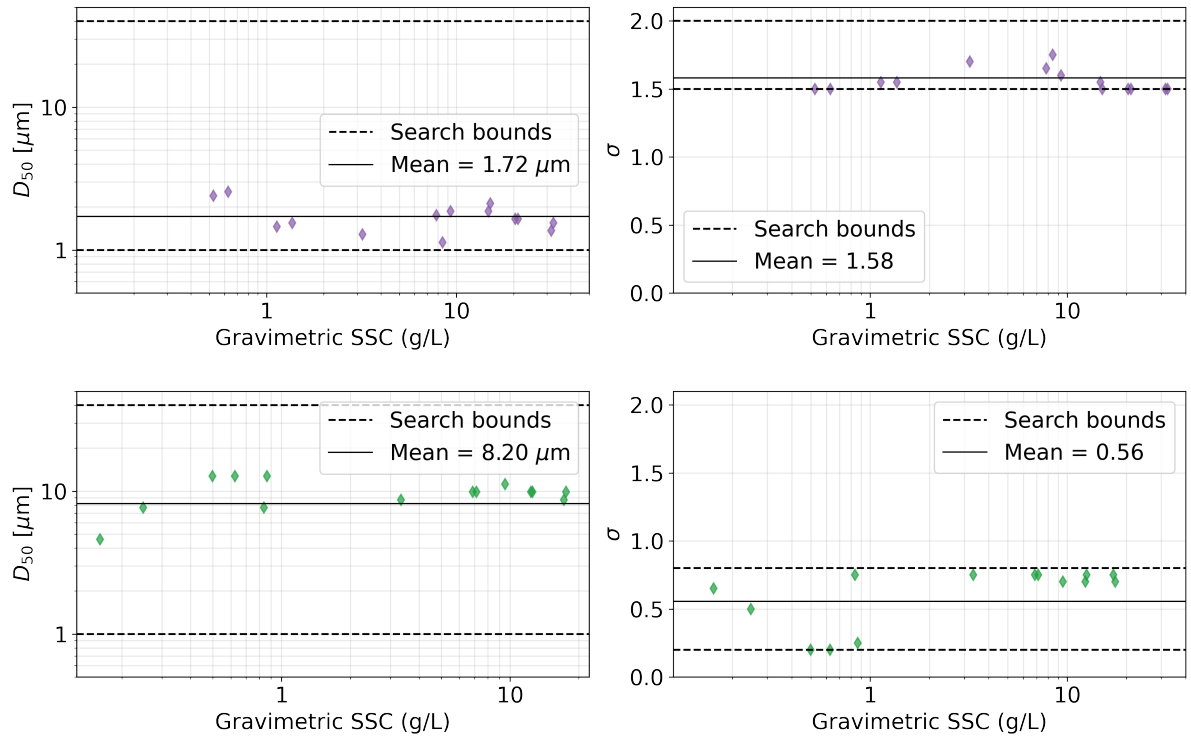

Figure E.6: Inverted particle-size distribution parameters with the distribution width constrained. In each subplot, the left panel presents the particle-size inversion and the right panel the distribution-width inversion. Purple curves correspond to the CCZ sediment and green curves to Sediment B.

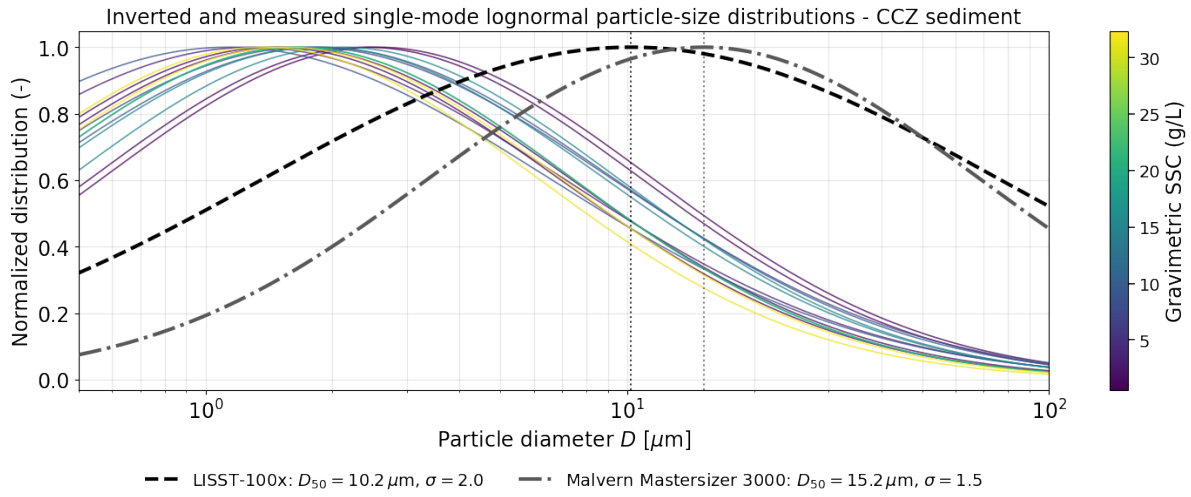

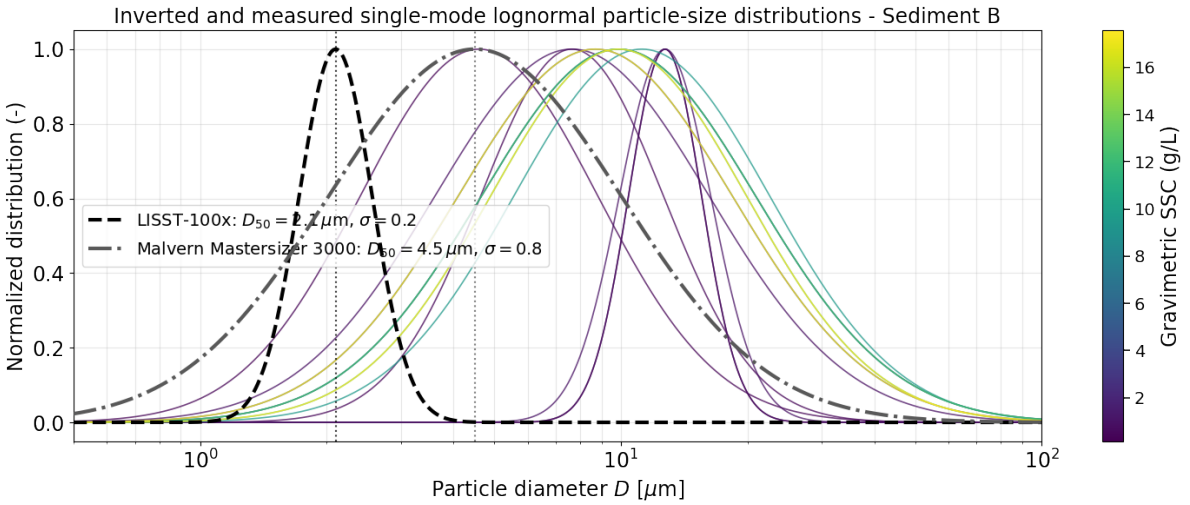

Case 4: Particle Size and Distribution Width Constrained

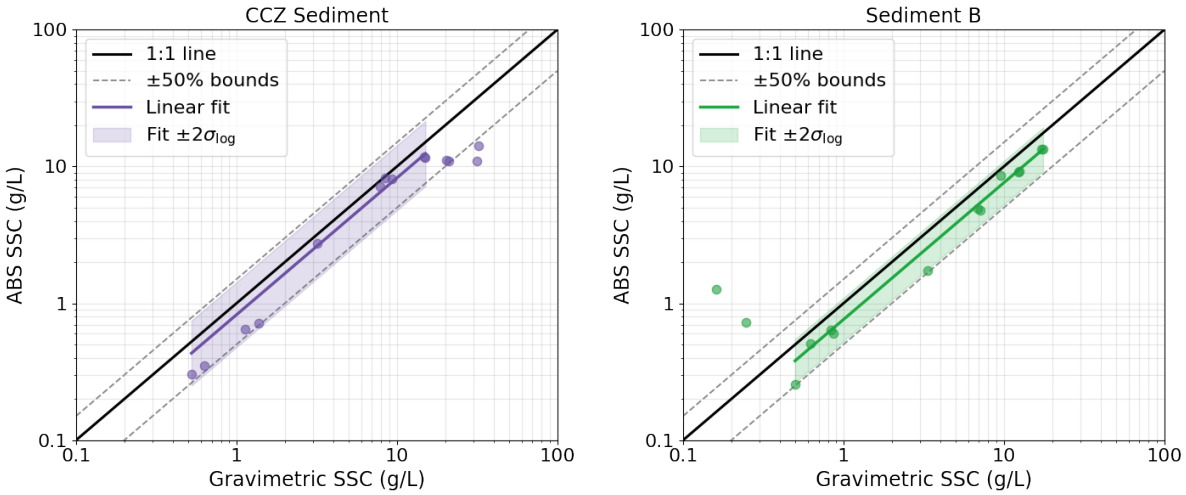

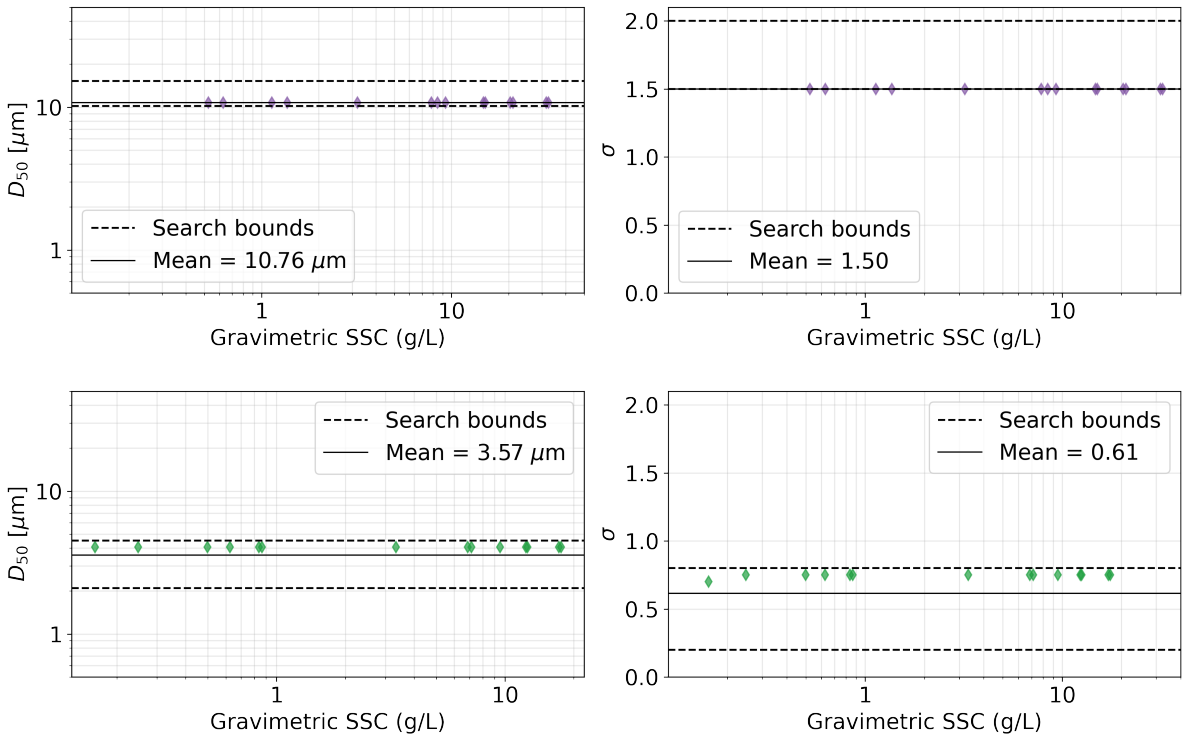

Figure E.8: Inverted particle-size distribution parameters with both the particle size and distribution width constrained. In each subplot, the left panel presents the particle-size inversion and the right panel the distribution-width inversion. Purple curves correspond to the CCZ sediment and green curves to Sediment B.

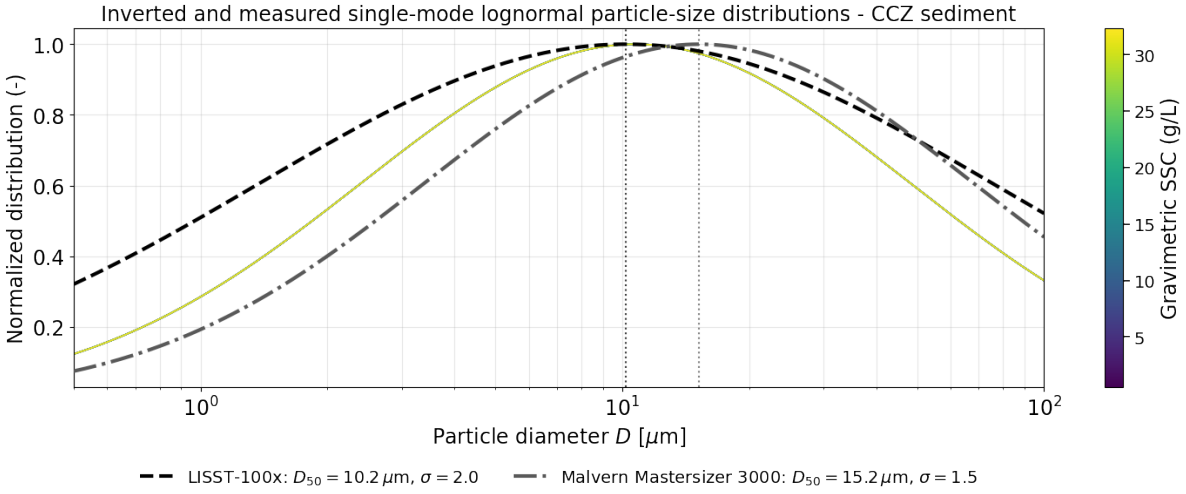

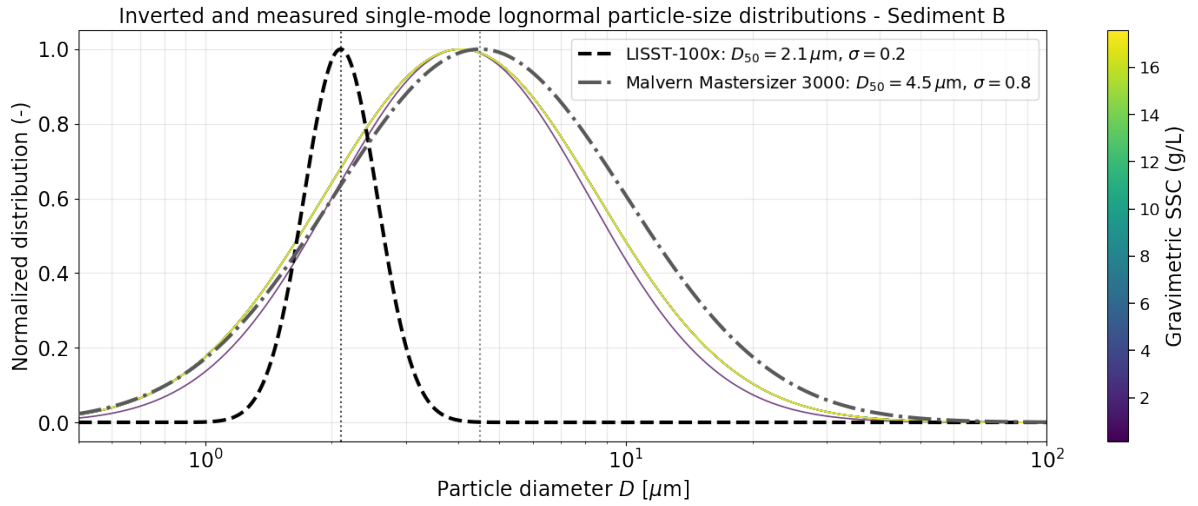

Comparison to OBS determined SSC - Single-mode No-Constraints

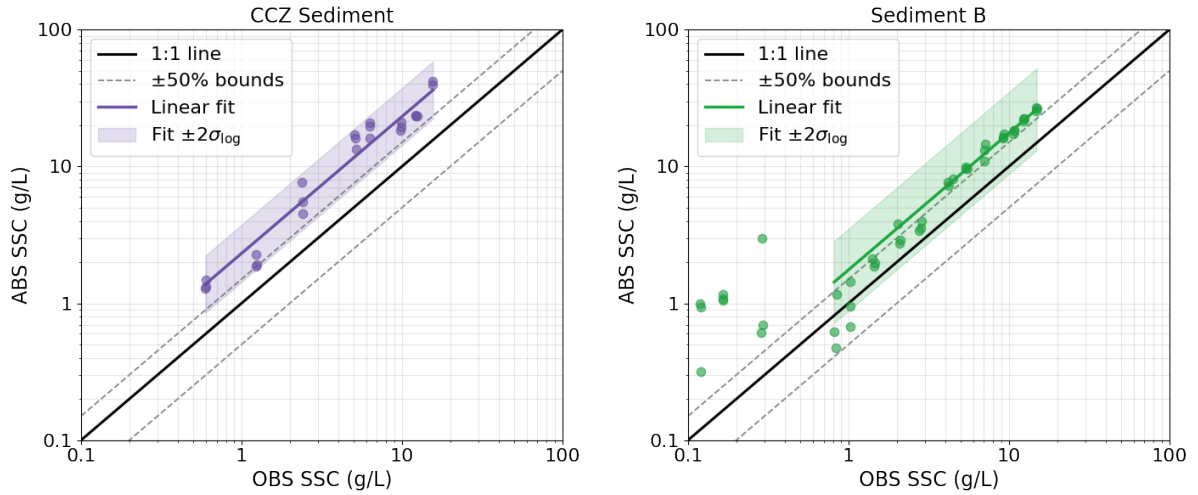

Figure E.9: Comparison of the ABS-inverted SSC against the reference SSC for the CCZ sediment and Sediment B using the attenuation-based inversion.

Table E.2: Performance metrics of Method 3 for the CCZ sediment and Sediment B relative to the OBS derived SSC with particle size constrained

Sediment	Slope	R^2	MARE (%)	RMSE (g/L)
CCZ sediment	2.315	0.906	135.1	11.03
Sediment B	1.756	0.989	147.5	5.20

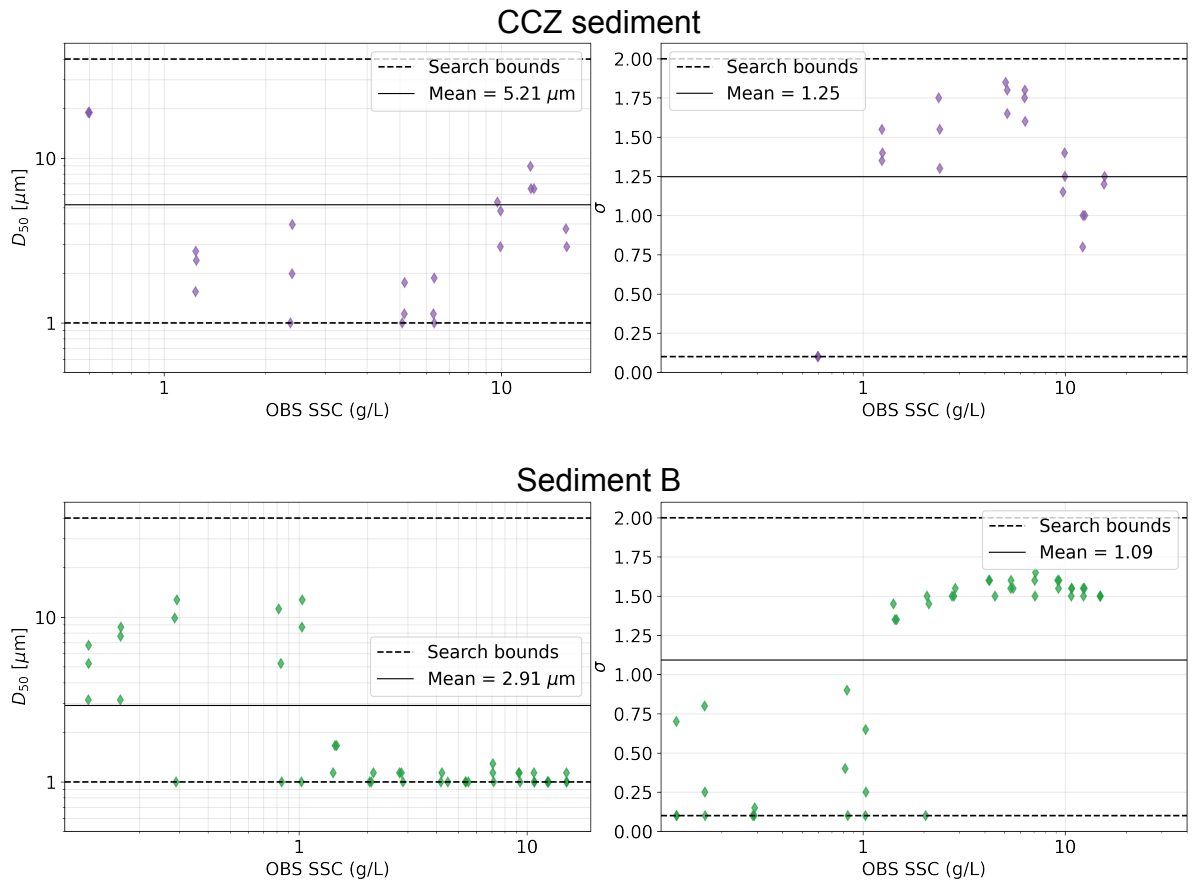

Figure E.10: ABS-OBS Inverted particle-size distribution parameters with no constraint. In each subplot, the left panel presents the particle-size inversion and the right panel the distribution-width inversion. Purple curves correspond to the CCZ sediment and green curves to Sediment B.

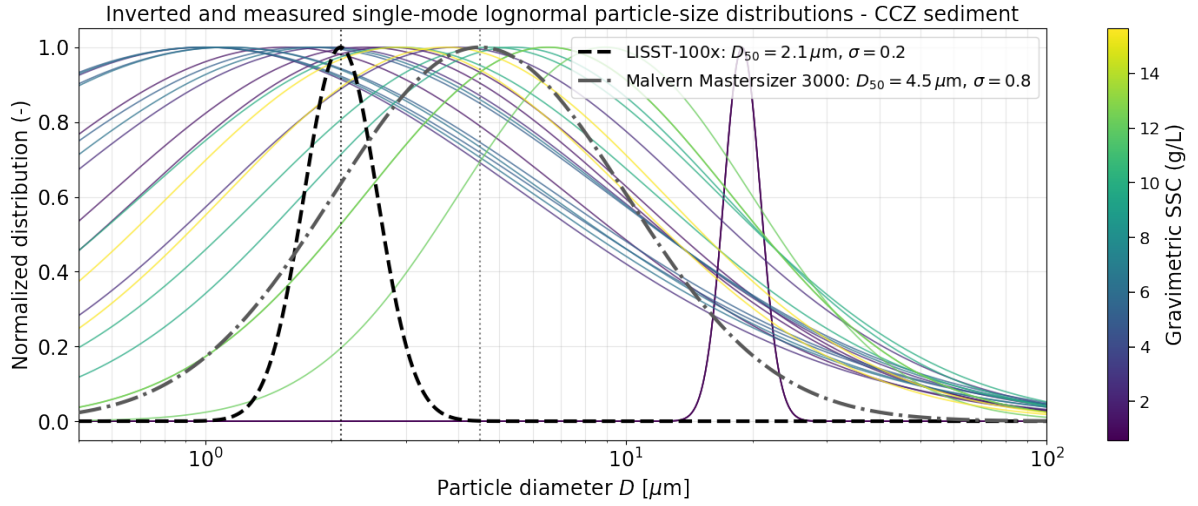

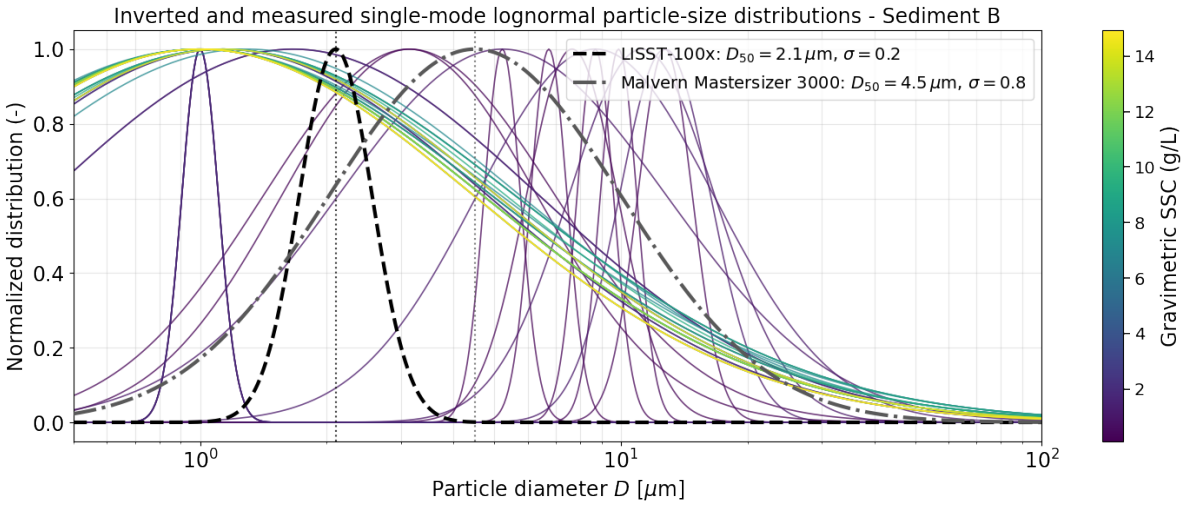
Inverted and measured single-mode lognormal particle-size distributions - Sediment B
LISST-100x: $D_{50} = 2.1\,\mu$m, $\sigma = 0.2$
Malvern Mastersizer 3000: $D_{50} = 4.5\,\mu$m, $\sigma = 0.8$
Normalized distribution (-)
Particle diameter D [μm]
Gravimetric SSC (g/L)

Frequency analysis

Table E.3: Performance metrics of the selected single-mode inversion method for the CCZ sediment and Sediment B.

Selected frequencies	Slope	R^2	MARE (%)	RMSE (g/L)
CCZ sediment (0.5–32 g/L)				
1, 2 MHz	1.596	0.945	84.3	10.40
1, 4 MHz	1.828	0.955	95.6	13.88
1, 5 MHz	1.515	0.905	68.5	9.54
2, 4 MHz	1.807	0.906	89.8	14.09
2, 5 MHz	1.461	0.852	79.1	9.20
1, 2, 4 MHz	1.799	0.911	88.6	13.90
1, 2, 5 MHz	1.460	0.855	76.7	9.17
1, 4, 5 MHz	1.286	0.983	55.4	4.90
4, 5 MHz	1.373	0.964	55.7	6.60
2, 4, 5 MHz	1.289	0.953	63.3	5.40
1, 2, 4, 5 MHz	1.288	0.935	65.7	5.65
CCZ sediment (0.5–18 g/L)				
1, 2 MHz	1.427	0.876	93.4	4.50
1, 4 MHz	1.787	0.961	96.6	6.77
1, 5 MHz	1.841	0.981	77.4	7.07
2, 4 MHz	2.162	0.989	91.8	9.65
2, 5 MHz	2.097	0.993	96.6	9.09
1, 2, 4 MHz	2.143	0.994	90.5	9.46
1, 2, 5 MHz	2.092	0.993	93.2	9.05
1, 4, 5 MHz	1.394	0.961	68.2	3.54
4, 5 MHz	1.367	0.957	65.5	3.36
2, 4, 5 MHz	1.492	0.898	80.0	4.73
1, 2, 4, 5 MHz	1.530	0.872	84.0	5.20
Sediment B (0.5–18 g/L)				
1, 2 MHz	1.004	0.948	57.6	1.33
1, 4 MHz	1.464	0.981	46.3	4.64
1, 5 MHz	1.182	0.984	23.6	1.98
2, 4 MHz	1.515	0.973	47.9	5.20
2, 5 MHz	1.126	0.934	24.4	2.13
1, 2, 4 MHz	1.515	0.973	47.9	5.20
1, 2, 5 MHz	1.186	0.899	28.8	2.92
1, 4, 5 MHz	1.111	0.884	24.5	2.59
4, 5 MHz	1.111	0.884	24.5	2.59
2, 4, 5 MHz	1.079	0.895	22.4	2.26
1, 2, 4, 5 MHz	1.090	0.889	24.5	2.35

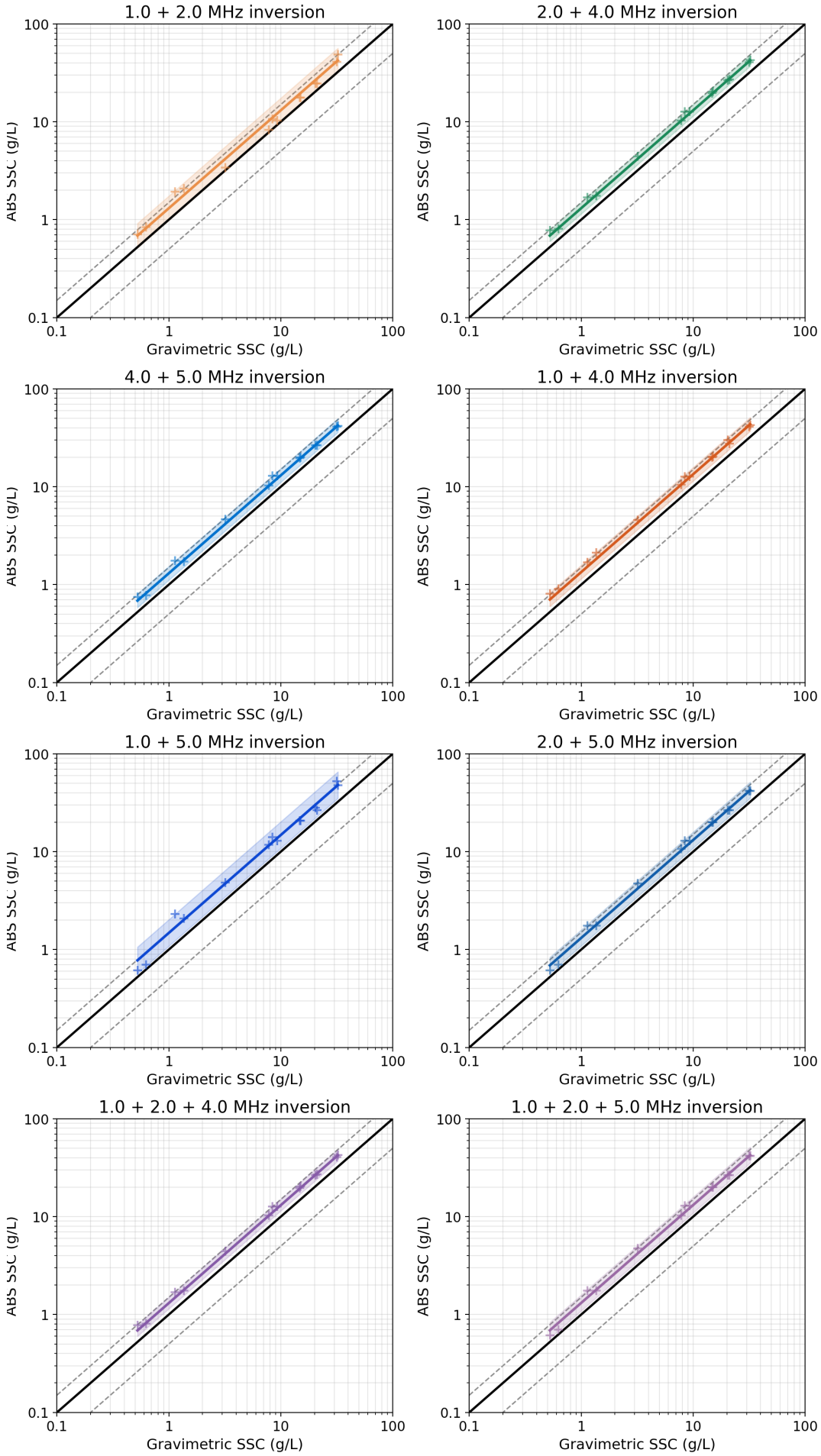

Figure E.11: CCZ sediment inversion results using various frequency combinations $0.5 - 32$ g/L

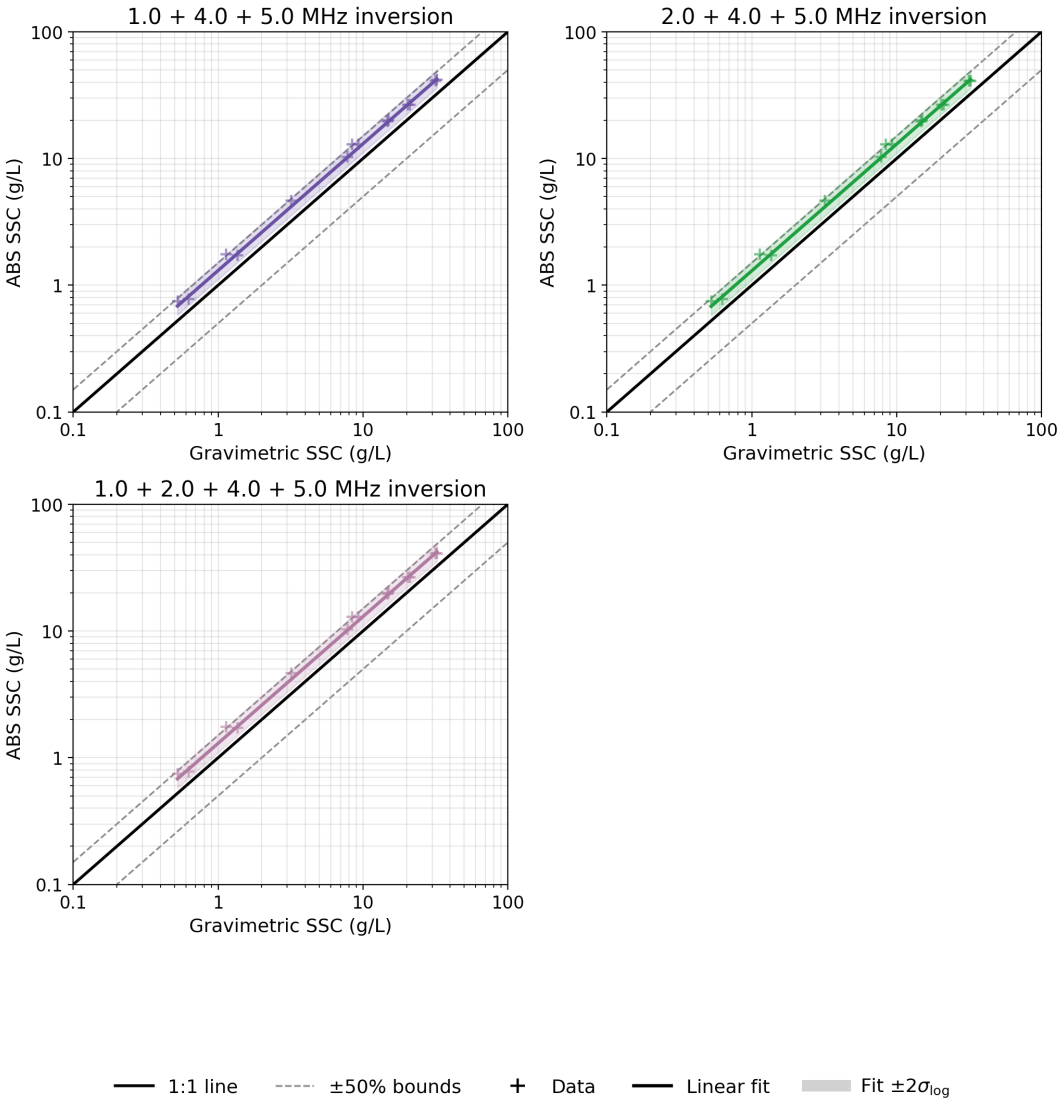

Figure E.12: CCZ sediment inversion results using various frequency combinations $0.5 - 32$ g/L

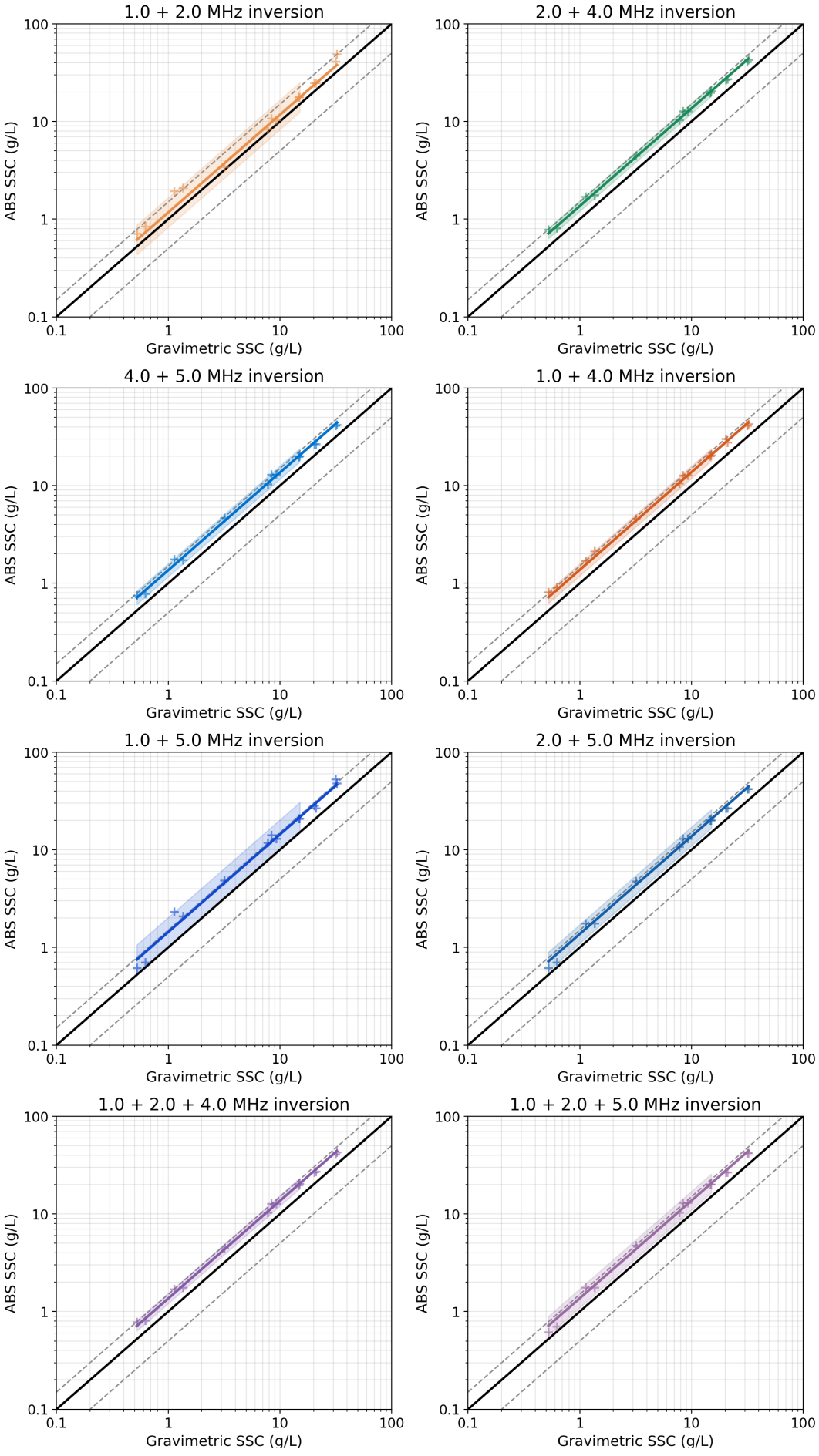

Figure E.13: CCZ sediment inversion results using various frequency combinations $0.5 - 18$ g/L

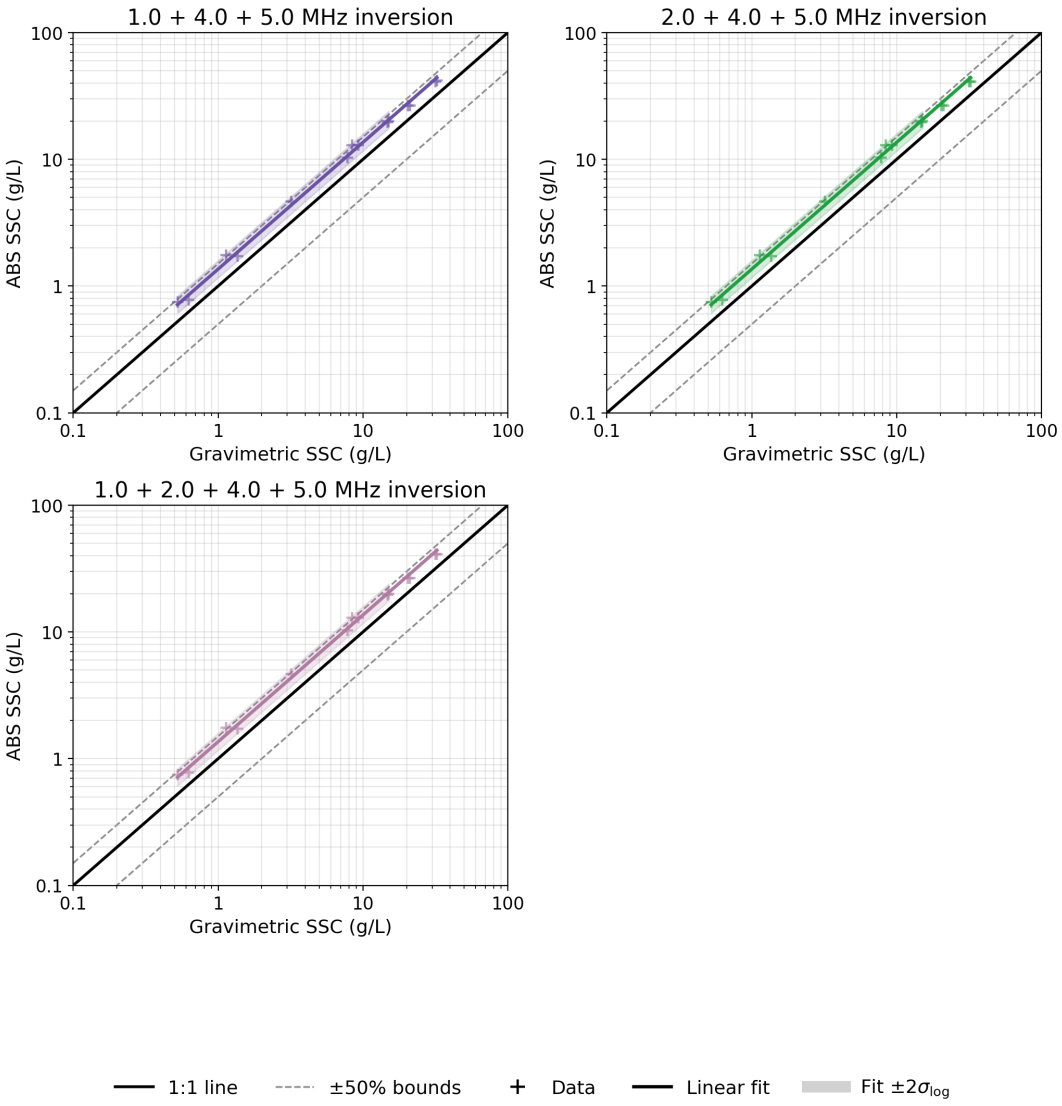

Figure E.14: CCZ sediment inversion results using various frequency combinations $0.5 - 18$ g/L

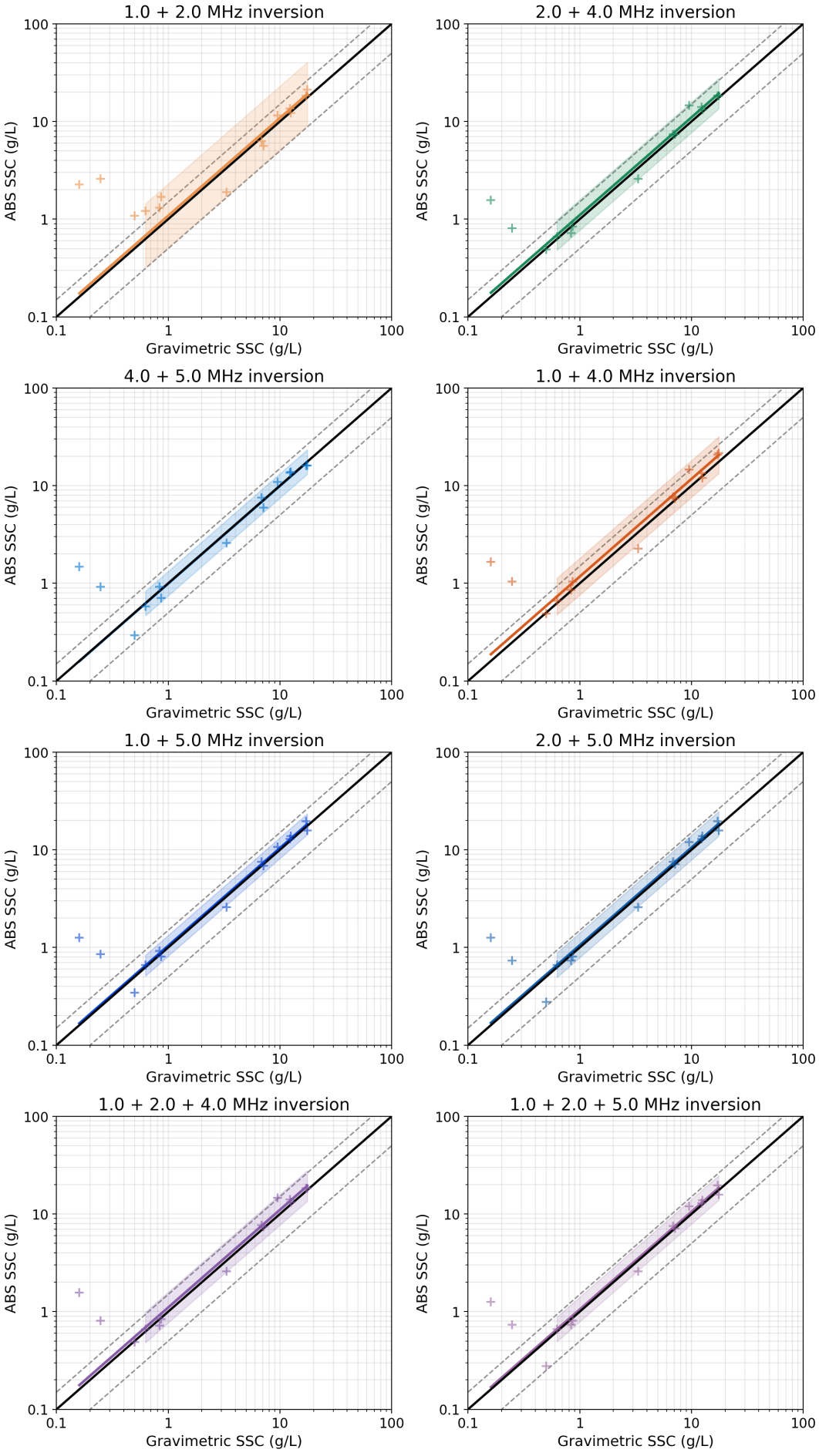

Figure E.15: Sediment B inversion results using various frequency combinations $0.5 - 18$ g/L

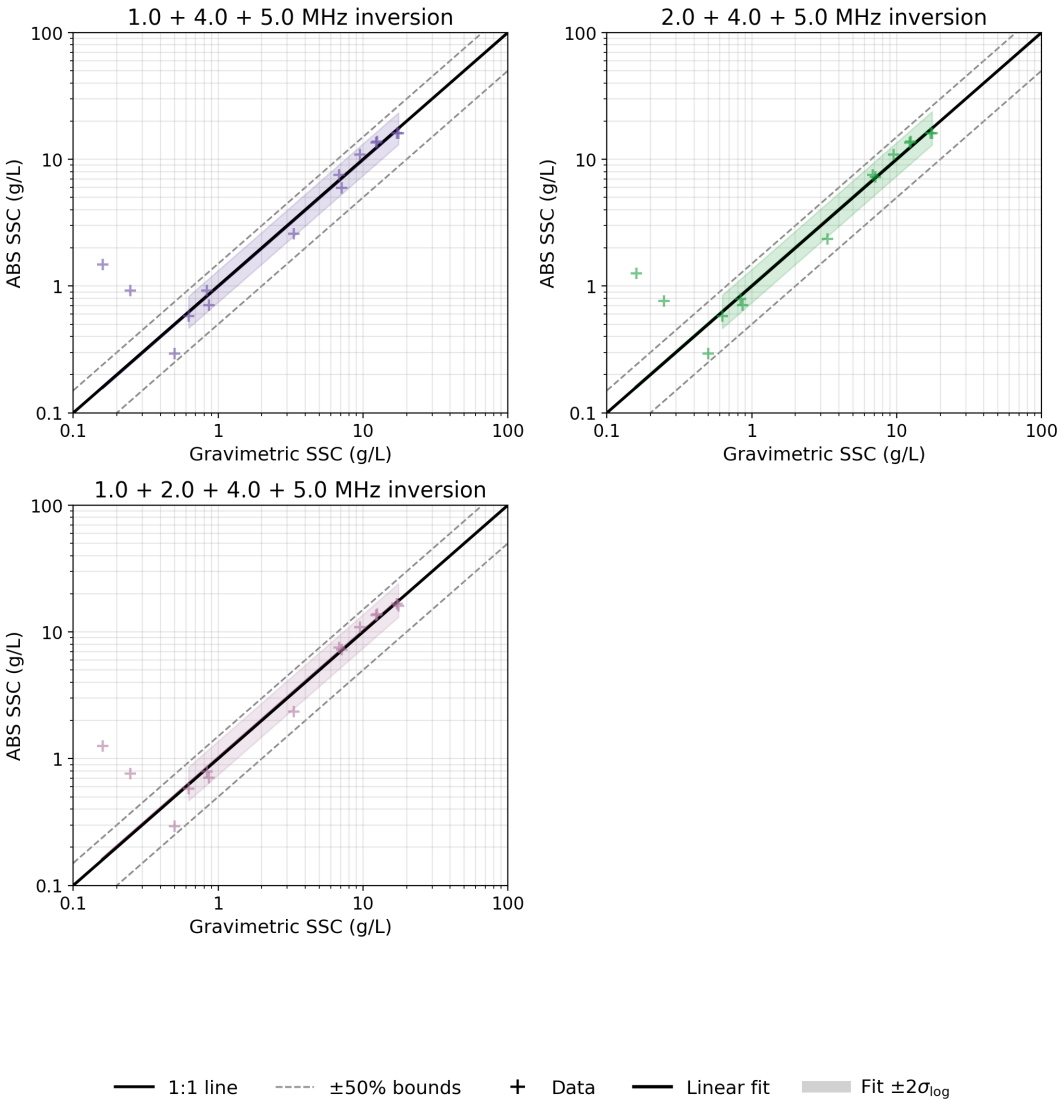

Figure E.16: Sediment B inversion results using various frequency combinations $0.5 - 18$ g/L

Method 3.2 - Bi-modal Distribution

The prescribed iteration boundaries for the median particle diameter in the following inversion is set from 1- 80 μm in 30 logarithmic steps for each mode, with an additional criterion that the second particle size must always be larger than the first. The standard deviation (σ) of both modes are bound between 0.2 and 2 (-) in step sizes of 0.2.

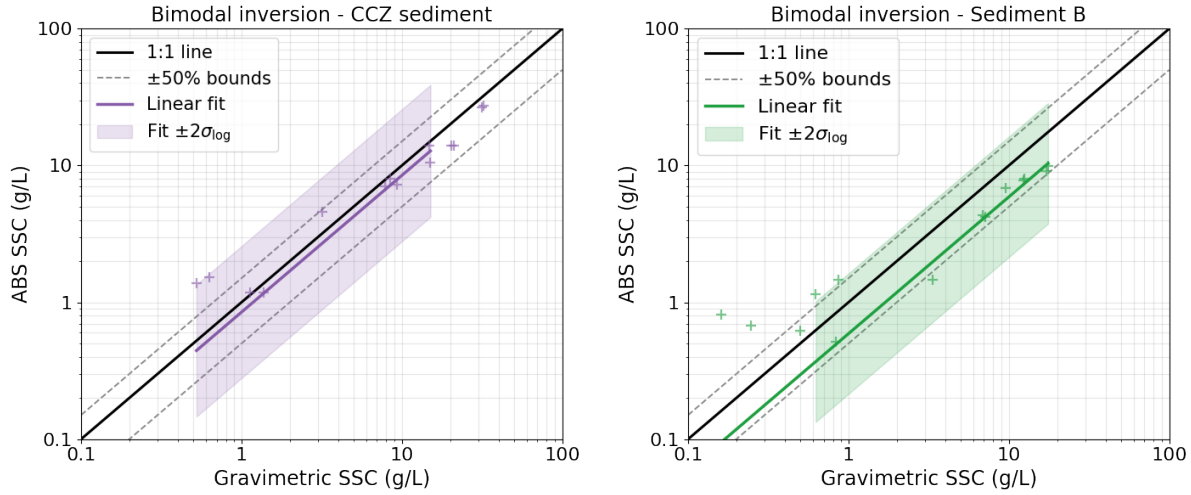

Figure E.17: Comparison of the bi-modal distribution model against the gravimetric SSC for the CCZ sediment and Sediment B

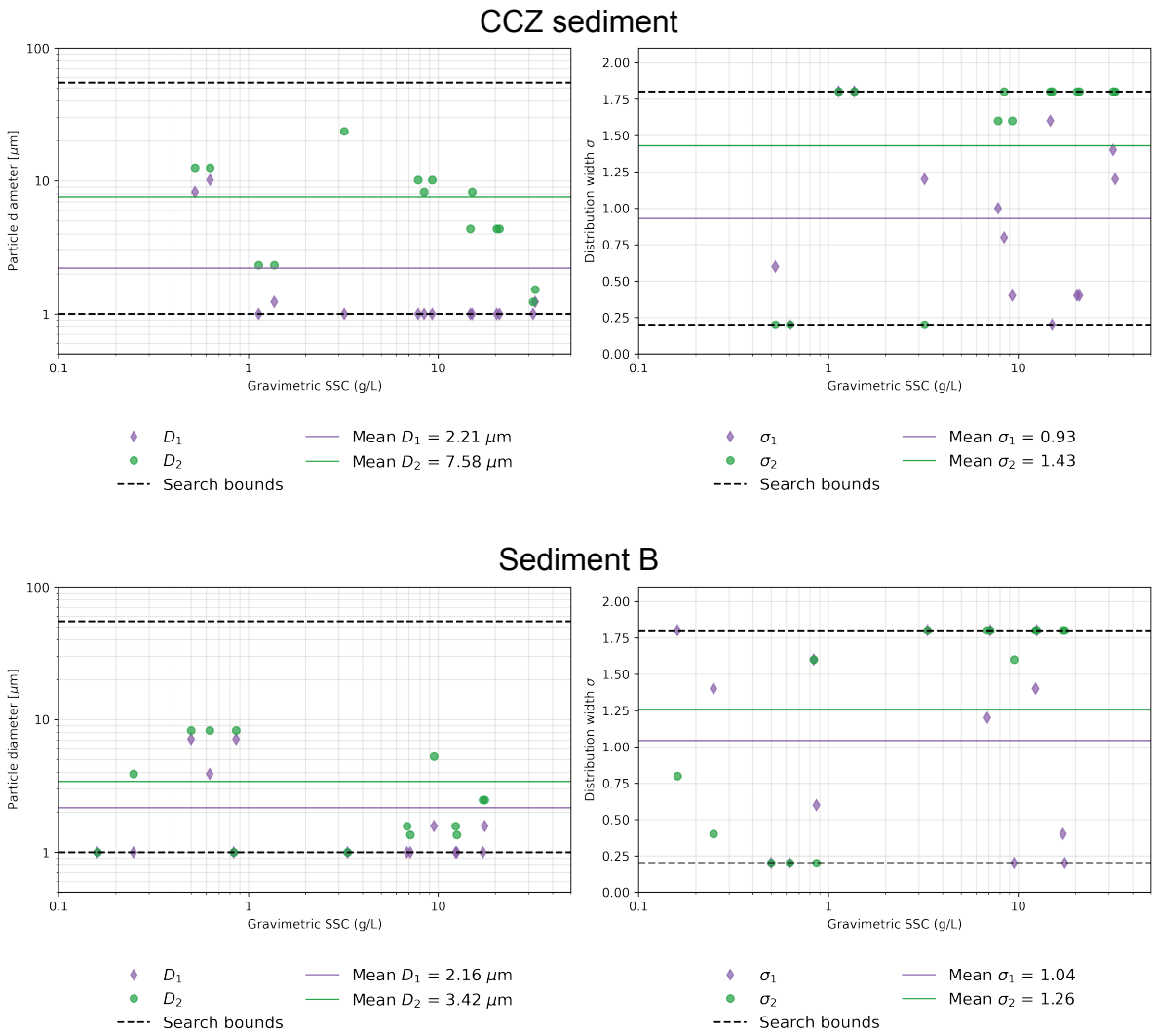

Figure E.18: ABS Inverted particle-size distribution parameters obtained through the bimodal inversion. In each subplot, the left panel presents the particle-size inversion and the right panel the distribution-width inversion. Purple curves correspond to the CCZ sediment and green curves to Sediment B.

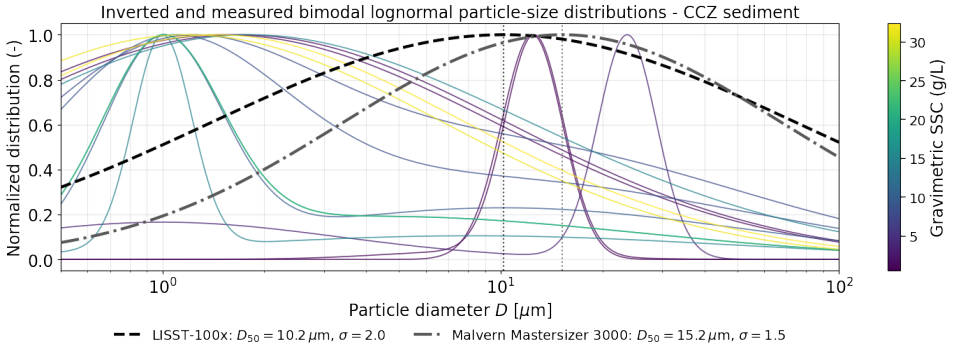

Figure E.19: Graphical representation of the obtained particle size distribution shapes per SSC step for the CCZ sediment.

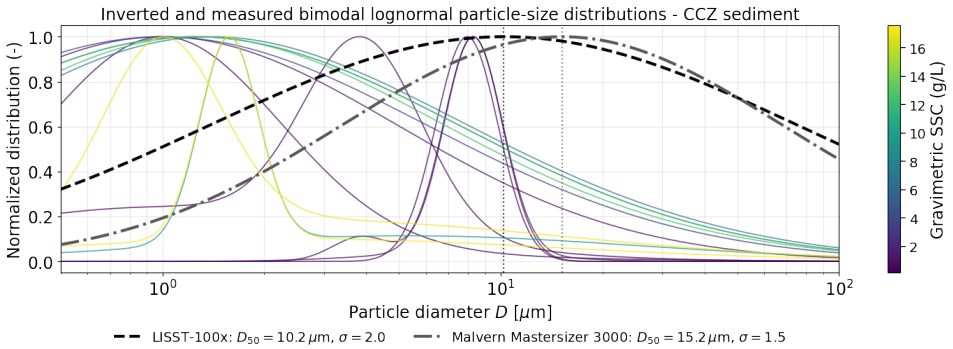

Figure E.20: Graphical representation of the obtained particle size distribution shapes per SSC step for Sediment B.

F

Method 4 Analysis

For interpretability of the evaluating metrics relative to the plots the metrics are presented below each plot and in order of the plot. At the end a overview table is summarized to ease the overall interpretation of the metrics.

Note: The x-axis label ”Reference SSC (g/L)”, refers to the gravimetrically obtained SSC.

No Constraint on Median Particle Diameter

CCZ sediment

0.5 - 18 g/L

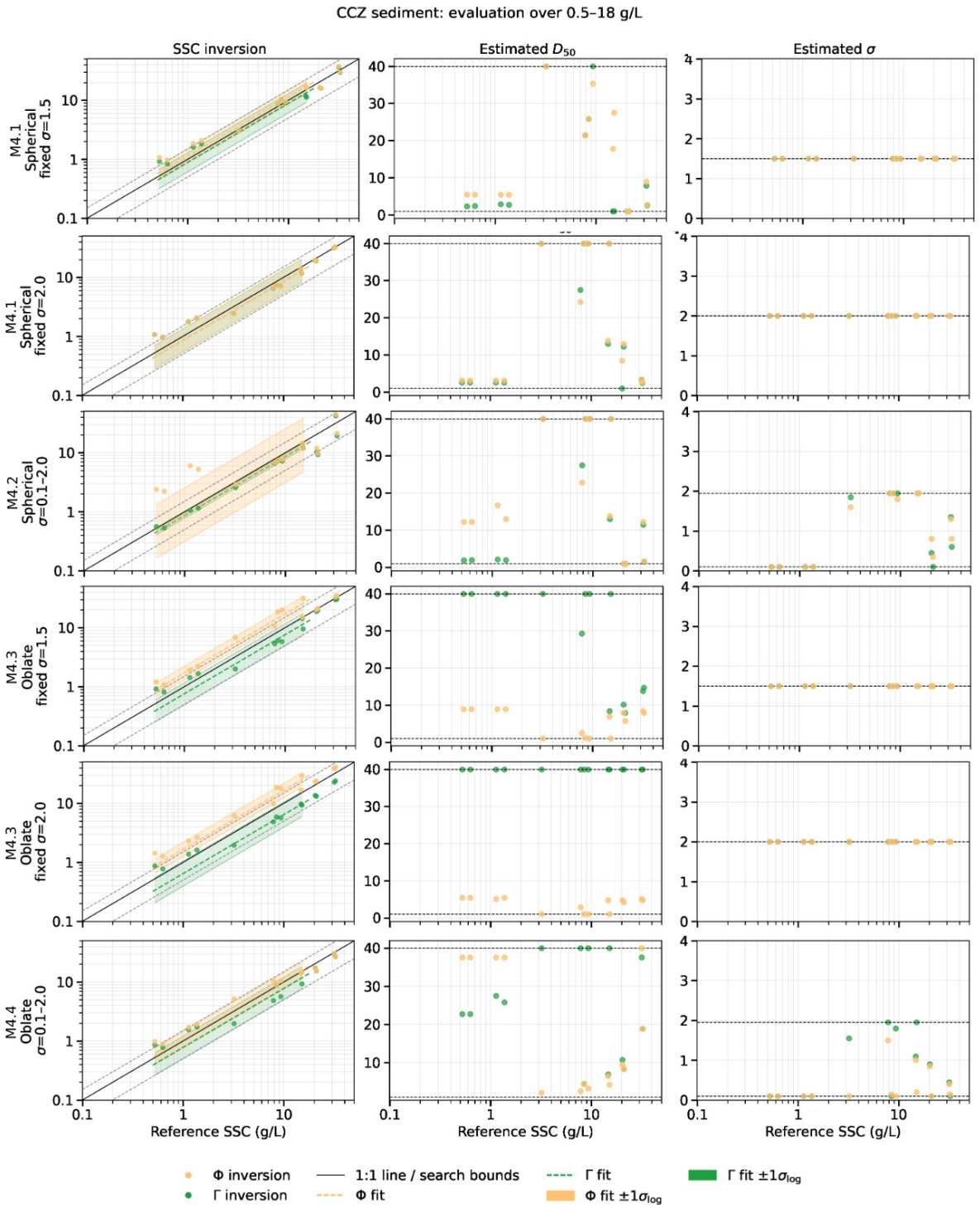

Figure F.1: Comparison of the Method 4 inversions applied to the CCZ sediment between 0.5-18 g/L, together with the estimated particle diameter and the estimated distribution widths.

Table F.1: Performance metrics of Methods 4.1, 4.2, 4.3, and 4.4 applied to the CCZ sediment over the SSC range of 0.5–18 g/L.

Model	PSD	Inv.	Slope	R^2	MARE (%)	RMSE (g/L)
M4.1 (Spherical)	LISST ($\sigma = 2.0$)	Φ	0.857	0.968	37.0	1.42
		Γ	0.856	0.968	36.9	1.43
	Malvern ($\sigma = 1.5$)	Φ	1.133	0.987	34.5	1.30
		Γ	0.887	0.901	27.2	1.68
M4.2 (Spherical)	$\sigma = 0.1$–2.0	Φ	0.894	0.634	140.5	2.44
		Γ	0.866	0.981	13.5	1.29
M4.3 (Oblate)	LISST (fixed $\sigma = 2.0$)	Φ	1.657	0.860	91.7	6.41
		Γ	0.644	0.981	35.0	2.97
	Malvern (fixed $\sigma = 1.5$)	Φ	1.704	0.807	83.7	7.22
		Γ	0.758	0.907	32.9	2.36
M4.4 (Oblate)	$\sigma = 0.1$–2.0	Φ	1.046	0.952	34.5	1.20
		Γ	0.780	0.868	31.5	2.40

0.5-32 g/L

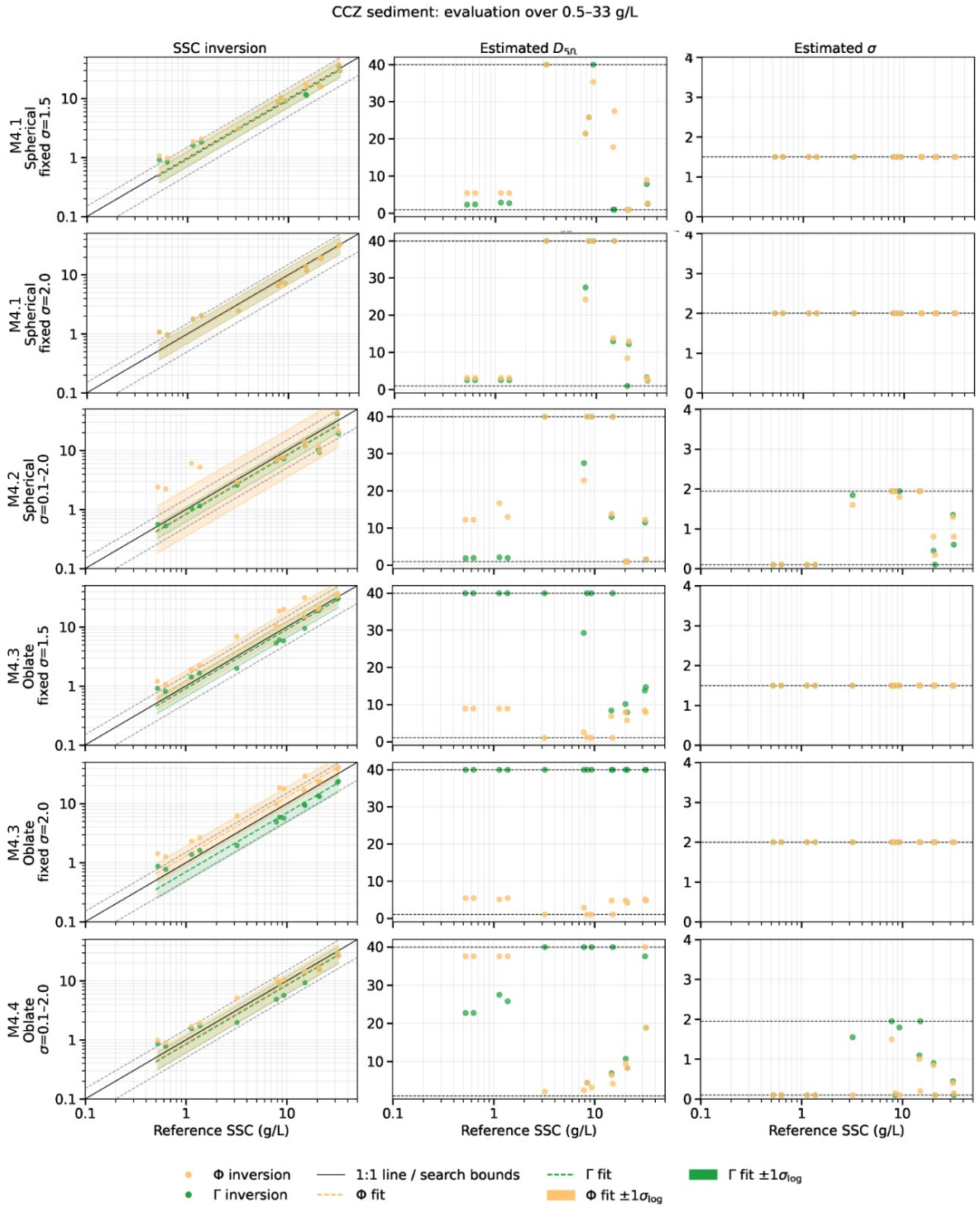

Figure F.2: Comparison of the Method 4 inversions applied to the CCZ sediment between 0.5-33 g/L, together with the estimated particle diameter and the estimated distribution widths.

Table F.2: Performance metrics of Methods 4.1, 4.2, 4.3, and 4.4 applied to the CCZ sediment over the SSC range of 0.5–32 g/L.

Model	PSD	Inv.	Slope	R^2	MARE (%)	RMSE (g/L)
M4.1 (Spherical)	LISST ($\sigma = 2.0$)	Φ	0.961	0.987	27.5	1.33
		Γ	0.960	0.987	27.4	1.35
	Malvern ($\sigma = 1.5$)	Φ	1.001	0.937	29.7	2.68
		Γ	0.943	0.939	24.3	2.70
M4.2 (Spherical)	$\sigma = 0.1$–2.0	Φ	0.882	0.684	112.4	6.23
		Γ	0.829	0.726	22.4	6.21
M4.3 (Oblate)	LISST (fixed $\sigma = 2.0$)	Φ	1.301	0.902	71.0	6.31
		Γ	0.698	0.988	33.8	4.90
	Malvern (fixed $\sigma = 1.5$)	Φ	1.177	0.782	61.0	6.18
		Γ	0.905	0.976	25.3	2.18
M4.4 (Oblate)	$\sigma = 0.1$–2.0	Φ	0.901	0.956	29.0	2.47
		Γ	0.844	0.963	27.1	3.06

Sediment B

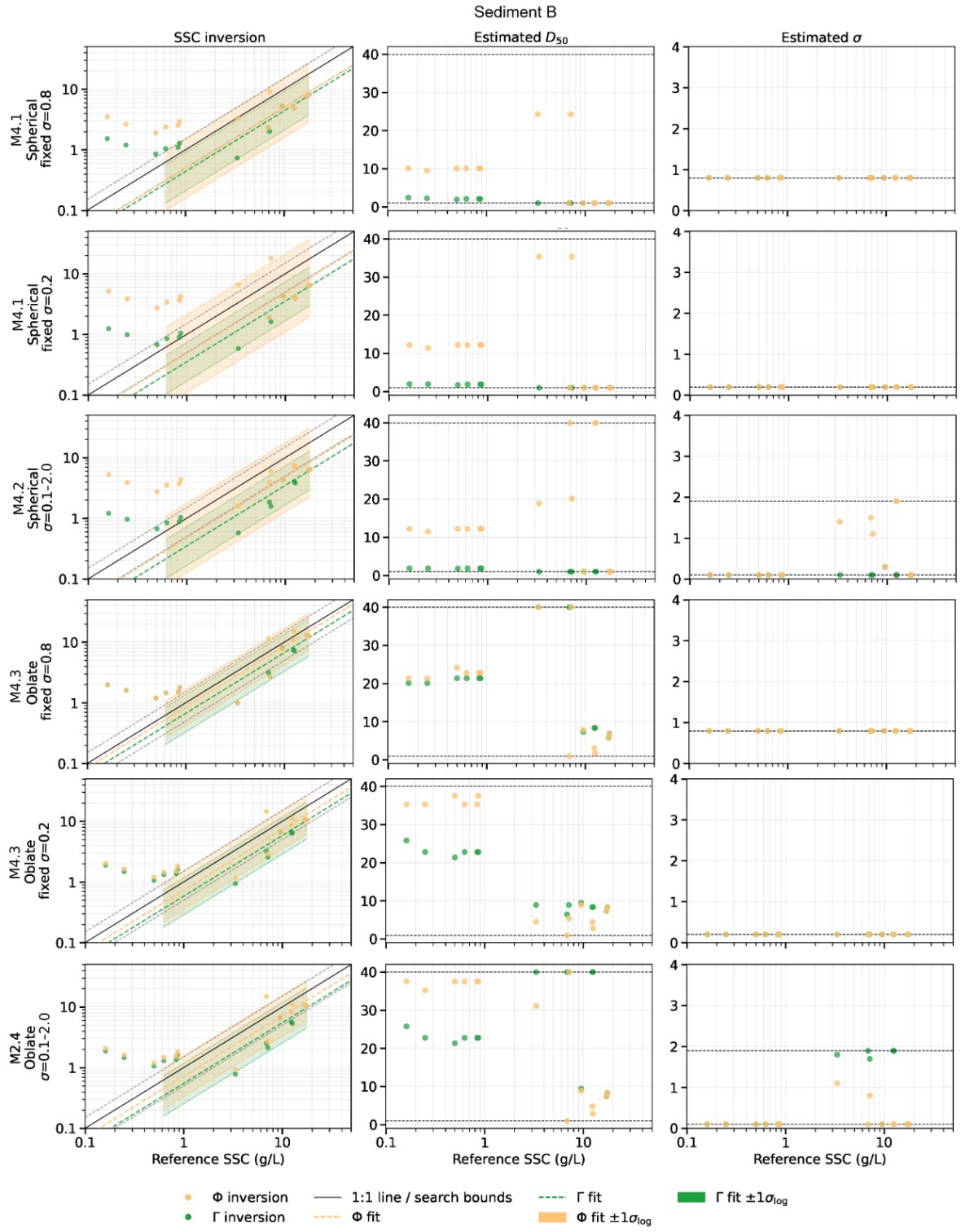

Figure F.3: Comparison of the Method 4 inversions applied to the Sediment B between 0.5-18 g/L, together with the estimated particle diameter and the estimated distribution widths.

Table F.3: Performance metrics of Methods 4.1, 4.2, 4.3, and 4.4 applied to Sediment B using a particle-size search range of 1–40 μm.

Model	PSD	Inv.	Slope	R^2	MARE (%)	RMSE (g/L)
M4.1 (Spherical)	LISST (fixed $\sigma = 0.2$)	Φ	0.484	-0.693	493.2	6.76
		Γ	0.352	0.887	116.8	5.82
	Malvern (fixed $\sigma = 0.8$)	Φ	0.495	-0.010	318.7	5.07
		Γ	0.438	0.890	139.4	5.09
M4.2 (Spherical)	$\sigma = 0.1$–1.9	Φ	0.475	-1.755	480.5	5.42
		Γ	0.348	0.884	113.7	5.86
M4.3 (Oblate)	LISST (fixed $\sigma = 0.2$)	Φ	0.728	0.594	185.8	3.80
		Γ	0.581	0.902	167.1	3.89
	Malvern (fixed $\sigma = 0.8$)	Φ	0.849	0.781	174.4	2.80
		Γ	0.671	0.893	176.9	3.22
M4.4 (Oblate)	$\sigma = 0.1$–1.9	Φ	0.721	0.573	189.4	3.91
		Γ	0.549	0.855	168.9	4.22

Median Particle Diameter Constrained

CCZ Sediment

0.5-18 g/L

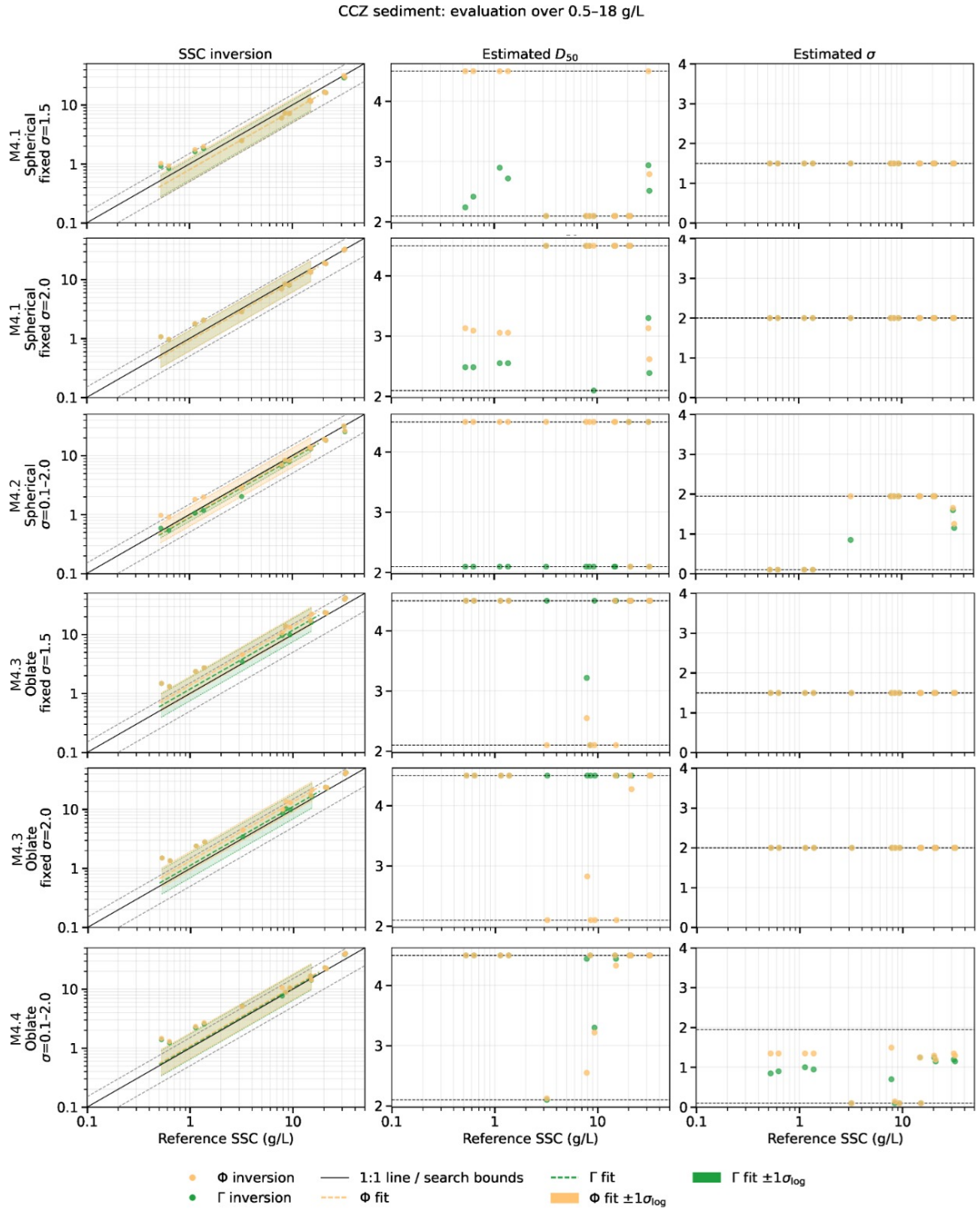

Figure F.4: Comparison of the Method 4 inversions applied to the CCZ sediment between 0.5-18 g/L, together with the estimated particle diameter and the estimated distribution widths.

Table F.4: Performance metrics of Methods 4.1, 4.2, 4.3, and 4.4 applied to the CCZ sediment over the SSC range of 0.5–18 g/L using particle-size constraints based on the LISST and Malvern measurements.

Model	PSD	Inv.	Slope	R^2	MARE (%)	RMSE (g/L)
M4.1 (Spherical)	LISST (fixed $\sigma = 2.0$)	Φ	0.921	0.988	32.2	0.83
		Γ	0.919	0.987	32.1	0.86
	Malvern (fixed $\sigma = 1.5$)	Φ	0.801	0.982	36.9	1.73
		Γ	0.800	0.987	30.8	1.71
M4.2 (Spherical)	$\sigma = 0.1$–2.0	Φ	0.922	0.989	29.2	0.82
		Γ	0.887	0.993	13.6	1.02
M4.3 (Oblate)	LISST (fixed $\sigma = 2.0$)	Φ	1.344	0.966	74.7	3.11
		Γ	1.128	0.982	59.0	1.30
	Malvern (fixed $\sigma = 1.5$)	Φ	1.376	0.960	75.6	3.40
		Γ	1.184	0.937	63.1	2.14
M4.4 (Oblate)	$\sigma = 0.1$–2.0	Φ	1.098	0.944	62.6	1.50
		Γ	1.058	0.956	55.2	1.19

0.5-32 g/L

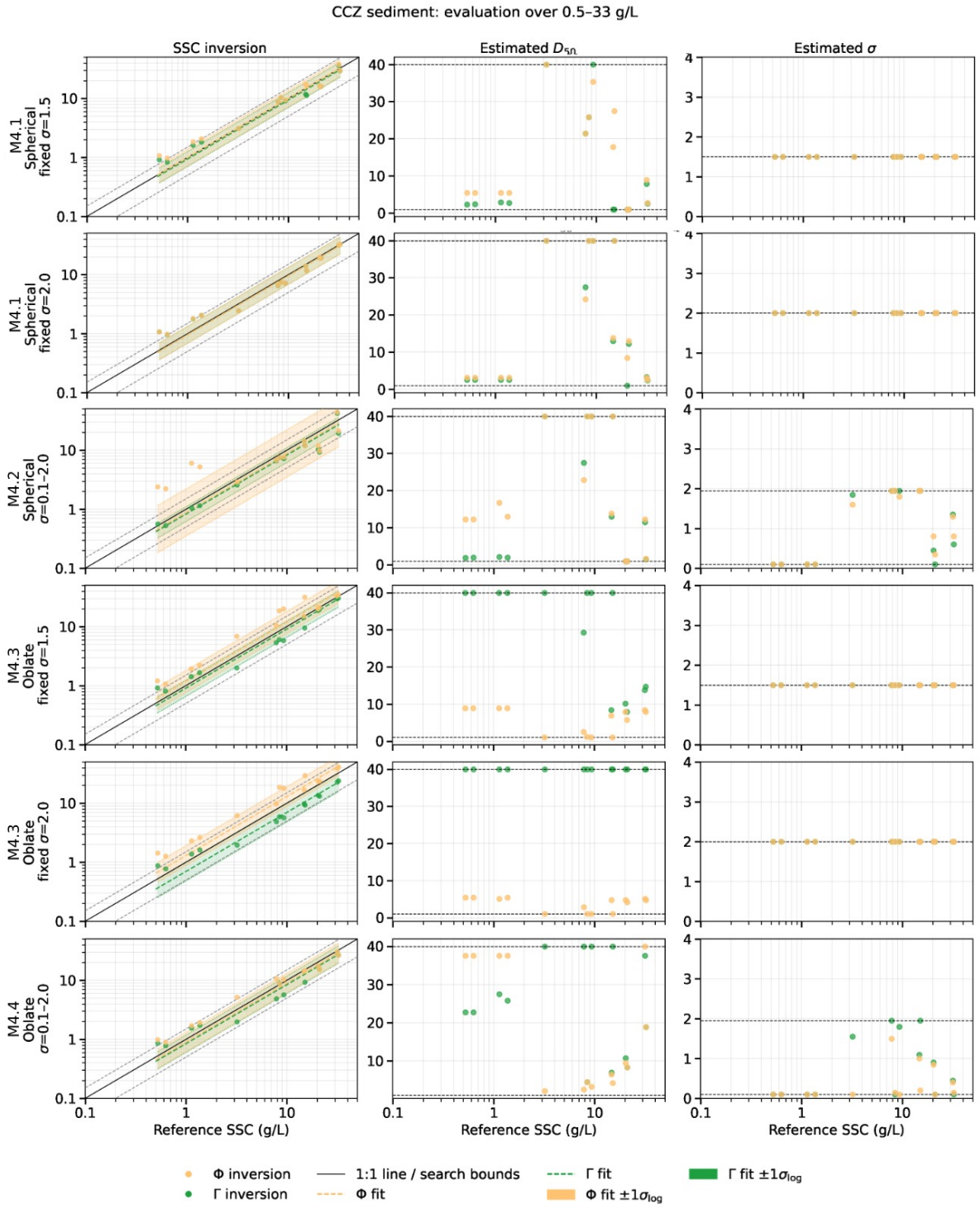

Figure F.5: Comparison of the Method 4 inversions applied to the CCZ sediment between 0.5-32 g/L, together with the estimated particle diameter and the estimated distribution widths.

Table F.5: Performance metrics of Methods 4.1, 4.2, 4.3, and 4.4 applied to the CCZ sediment over the SSC range of 0.5–32 g/L using particle-size constraints based on the LISST and Malvern measurements.

Model	PSD	Inv.	Slope	R^2	MARE (%)	RMSE (g/L)
M4.1 (Spherical)	LISST (fixed $\sigma = 2.0$)	Φ	0.970	0.993	24.3	0.98
		Γ	0.970	0.993	24.2	0.99
	Malvern (fixed $\sigma = 1.5$)	Φ	0.893	0.977	29.9	2.27
		Γ	0.864	0.988	26.2	2.41
M4.2 (Spherical)	$\sigma = 0.1$–2.0	Φ	0.912	0.982	23.6	1.91
		Γ	0.897	0.979	12.6	2.17
M4.3 (Oblate)	LISST (fixed $\sigma = 2.0$)	Φ	1.264	0.985	59.5	4.51
		Γ	1.221	0.988	48.2	3.81
	Malvern (fixed $\sigma = 1.5$)	Φ	1.262	0.981	59.9	4.57
		Γ	1.226	0.983	51.0	3.98
M4.4 (Oblate)	$\sigma = 0.1$–2.0	Φ	1.192	0.983	49.9	3.49
		Γ	1.169	0.984	44.2	3.13

Sediment B

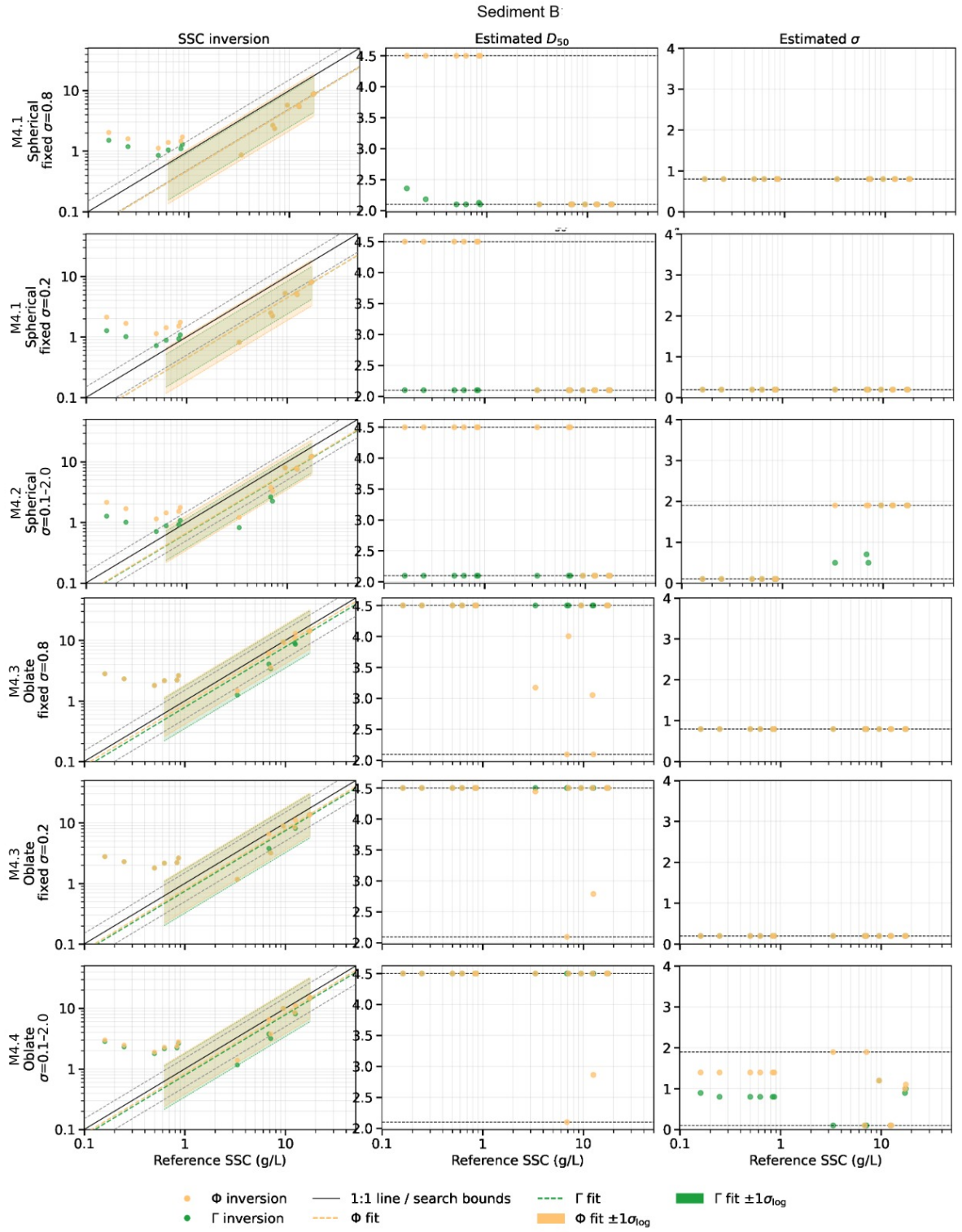

Figure F.6: Comparison of the Method 4 inversions applied to the Sediment B between 0.5-18 g/L, together with the estimated particle diameter and the estimated distribution widths.

Table F.6: Performance metrics for the four inversion models applied to Sediment B using the LISST and Malvern particle size distributions. M4.1 and M4.3 use prescribed particle size distributions, whereas M4.2 and M4.4 estimate the distribution width during the inversion. The slope is obtained from a linear regression forced through the origin.

Model	PSD	Inv.	Slope	R^2	MARE (%)	RMSE (g/L)
M4.1 (Spherical)	LISST ($\sigma = 0.2$)	Φ	0.447	0.811	195.4	5.05
		Γ	0.445	0.927	115.2	5.01
	Malvern ($\sigma = 0.8$)	Φ	0.487	0.853	184.9	4.70
		Γ	0.486	0.913	136.0	4.67
M4.2 (Spherical)	$\sigma = 0.1$–1.9	Φ	0.676	0.913	184.9	3.12
		Γ	0.659	0.922	105.5	3.27
M4.3 (Oblate)	LISST (fixed $\sigma = 0.2$)	Φ	0.795	0.864	253.4	2.45
		Γ	0.743	0.851	258.0	2.81
	Malvern (fixed $\sigma = 0.8$)	Φ	0.871	0.884	253.3	2.03
		Γ	0.782	0.864	259.0	2.55
M4.4 (Oblate)	$\sigma = 0.1$–1.9	Φ	0.845	0.867	272.3	2.20
		Γ	0.783	0.842	261.5	2.66

Overview of Evaluation Metrics

Table F.7: Performance metrics of Methods 3 and 4 for the CCZ sediment and Sediment B. Method 3 evaluates different particle size distribution constraints, while Method 4 evaluates the attenuation-based sub-methods for different constraints on D_{50} and σ. For Methods 4.1 and 4.3, the prescribed distribution width is identified by its measurement source (LISST or Malvern). Method 4 results are based on the Φ objective function.

Sediment	SSC range	Constraint	Model	Slope	R^2	MARE (%)	RMSE (g/L)
Method 3.1 - Single-mode distribution							
CCZ sediment	0.5–32	–	Oblate	1.311	0.916	69.0	5.49
CCZ sediment	0.5–18	–	Oblate	1.530	0.872	84.0	5.20
Sediment B	0.5–18	–	Oblate	1.090	0.889	24.5	2.35
CCZ sediment	0.5–32	D_{50}	Oblate	1.311	0.997	36.2	4.39
CCZ sediment	0.5–18	D_{50}	Oblate	1.361	0.995	38.4	3.02
Sediment B	0.5–18	D_{50}	Oblate	1.012	0.978	10.7	0.92
CCZ sediment	0.5–32	σ	Oblate	1.715	0.986	69.8	10.16
CCZ sediment	0.5–18	σ	Oblate	1.723	0.959	70.3	6.24
Sediment B	0.5–18	σ	Oblate	0.947	0.976	18.5	1.09
CCZ sediment	0.5–32	D_{50}, σ	Oblate	0.537	0.652	32.1	7.02
CCZ sediment	0.5–18	D_{50}, σ	Oblate	0.825	0.982	25.9	1.56
Sediment B	0.5–18	D_{50}, σ	Oblate	0.762	0.987	26.5	2.46
Method 3.2 - Bi-modal distribution							
CCZ sediment	0.5–32	–	Spherical	0.804	0.966	38.2	3.50
CCZ sediment	0.5–18	–	Spherical	0.847	0.924	43.8	1.72
Sediment B	0.5–18	–	Spherical	0.590	0.962	80.6	3.72

Method 4.1 - Φ-function							
CCZ sediment	0.5–32	σ (LISST)	Spherical	0.961	0.987	27.5	1.33
CCZ sediment	0.5–18	σ (LISST)	Spherical	0.857	0.968	37.0	1.42
Sediment B	0.5–18	σ (LISST)	Spherical	0.484	-0.693	493.2	6.76
CCZ sediment	0.5–32	D_{50}, σ (Malvern)	Spherical	0.970	0.993	24.3	0.98
CCZ sediment	0.5–18	D_{50}, σ (Malvern)	Spherical	0.921	0.988	32.2	0.83
Sediment B	0.5–18	D_{50}, σ (Malvern)	Spherical	0.487	0.853	184.9	4.70
Method 4.1 - Γ-function							
CCZ sediment	0.5–32	σ (LISST)	Spherical	0.960	0.987	27.4	1.35
CCZ sediment	0.5–18	σ (LISST)	Spherical	0.856	0.968	36.9	1.43
Sediment B	0.5–18	σ (LISST)	Spherical	0.352	0.887	116.8	5.82
CCZ sediment	0.5–32	D_{50}, σ (Malvern)	Spherical	0.970	0.993	24.2	0.99
CCZ sediment	0.5–18	D_{50}, σ (Malvern)	Spherical	0.919	0.987	32.1	0.86
Sediment B	0.5–18	D_{50}, σ (Malvern)	Spherical	0.486	0.913	136.0	4.67
Method 4.2 - Φ-function							
CCZ sediment	0.5–32	–	Spherical	0.882	0.684	112.4	6.23
CCZ sediment	0.5–18	–	Spherical	0.894	0.634	140.5	2.44
Sediment B	0.5–18	–	Spherical	0.475	-1.755	480.5	5.42
CCZ sediment	0.5–32	D_{50}	Spherical	0.912	0.982	23.6	1.91
CCZ sediment	0.5–18	D_{50}	Spherical	0.922	0.989	29.2	0.82
Sediment B	0.5–18	D_{50}	Spherical	0.676	0.913	184.9	3.12
Method 4.2 - Γ-function							
CCZ sediment	0.5–32	–	Spherical	0.829	0.726	22.4	6.21
CCZ sediment	0.5–18	–	Spherical	0.866	0.981	13.5	1.29
Sediment B	0.5–18	–	Spherical	0.348	0.884	113.7	5.86
CCZ sediment	0.5–32	D_{50}	Spherical	0.897	0.979	12.6	2.17
CCZ sediment	0.5–18	D_{50}	Spherical	0.887	0.993	13.6	1.02
Sediment B	0.5–18	D_{50}	Spherical	0.659	0.922	105.5	3.27

Sediment	SSC range	Constraint	Model	Slope	R^2	MARE (%)	RMSE (g/L)
Method 4.3 - Φ-function							
CCZ sediment	0.5–32	σ (LISST)	Oblate	1.301	0.902	71.0	6.31
CCZ sediment	0.5–18	σ (LISST)	Oblate	1.657	0.860	91.7	6.41
Sediment B	0.5–18	σ (LISST)	Oblate	0.728	0.594	185.8	3.80
CCZ sediment	0.5–32	D_{50}, σ (Malvern)	Oblate	1.264	0.985	59.5	4.51
CCZ sediment	0.5–18	D_{50}, σ (Malvern)	Oblate	1.344	0.966	74.7	3.11
Sediment B	0.5–18	D_{50}, σ (Malvern)	Oblate	0.871	0.884	253.3	2.03
Method 4.3 - Γ-function							
CCZ sediment	0.5–32	σ (LISST)	Oblate	0.698	0.988	33.8	4.90
CCZ sediment	0.5–18	σ (LISST)	Oblate	0.644	0.981	35.0	2.97
Sediment B	0.5–18	σ (LISST)	Oblate	0.581	0.902	167.1	3.89
CCZ sediment	0.5–32	D_{50}, σ (Malvern)	Oblate	1.221	0.988	48.2	3.81
CCZ sediment	0.5–18	D_{50}, σ (Malvern)	Oblate	1.128	0.982	59.0	1.30
Sediment B	0.5–18	D_{50}, σ (Malvern)	Oblate	0.782	0.864	259.0	2.55
Method 4.4 - Φ-function							
CCZ sediment	0.5–32	–	Oblate	0.901	0.956	29.0	2.47
CCZ sediment	0.5–18	–	Oblate	1.046	0.952	34.5	1.20
Sediment B	0.5–18	–	Oblate	0.721	0.573	189.4	3.91
CCZ sediment	0.5–32	D_{50}	Oblate	1.192	0.983	49.9	3.49
CCZ sediment	0.5–18	D_{50}	Oblate	1.098	0.944	62.6	1.50
Sediment B	0.5–18	D_{50}	Oblate	0.845	0.867	272.3	2.20
Method 4.4 - Γ-function							
CCZ sediment	0.5–32	–	Oblate	0.844	0.963	27.1	3.06
CCZ sediment	0.5–18	–	Oblate	0.780	0.868	31.5	2.40
Sediment B	0.5–18	–	Oblate	0.549	0.855	168.9	4.22
CCZ sediment	0.5–32	D_{50}	Oblate	1.169	0.984	44.2	3.13
CCZ sediment	0.5–18	D_{50}	Oblate	1.058	0.956	55.2	1.19
Sediment B	0.5–18	D_{50}	Oblate	0.783	0.842	261.5	2.66

G

Test Matrix

The following table summarizes the corresponding suspended sediment concentration (SSC) values obtained using each measurement method employed in this study, including the acoustically determined SSC from Method 3.1 (unconstrained case), the optically determined SSC, and the gravimetrically determined SSC.

Test_#	Sediment	ABS_Method3_SSC_g/L	Gravimetric_SSC_g/L	OBS_SSC_g/L
1	Sediment B	2.448		0.120
1	Sediment B	4.757		0.119
1	Sediment B	6.392		0.120
2	Sediment B	2.274		0.165
2	Sediment B	1.170		0.166
2	Sediment B	1.214	0.160	0.165
3	Sediment B	1.856		0.291
3	Sediment B	2.999		0.289
3	Sediment B	0.737	0.248	0.286
4	Sediment B	0.519		0.582
4	Sediment B	0.549		0.570
4	Sediment B	0.482	0.499	0.565
5	Sediment B	0.973		0.841
5	Sediment B	0.539		0.833
5	Sediment B	0.937	0.626	0.815
6	Sediment B	1.087	0.864	1.026
6	Sediment B	0.648		1.033
6	Sediment B	1.236	0.837	1.031
7	Sediment B	2.582		1.464
7	Sediment B	2.448		1.439
7	Sediment B	2.274		1.412
8	Sediment B	2.944		2.118
8	Sediment B	2.785		2.072
8	Sediment B	3.112		2.041
9	Sediment B	4.029		2.855
9	Sediment B	3.812		2.815
9	Sediment B	3.412	3.331	2.759
10	Sediment B	7.547		4.488
10	Sediment B	7.976		4.229
10	Sediment B	7.547		4.189
11	Sediment B	9.593	7.135	5.527
11	Sediment B	7.547		5.369
11	Sediment B	9.246	6.859	5.392
12	Sediment B	8.125		7.081
12	Sediment B	8.125		7.071
12	Sediment B	8.910		7.129
13	Sediment B	12.653		9.318
13	Sediment B	17.000		9.248
13	Sediment B	10.916	9.514	9.185
14	Sediment B	13.623	12.361	10.751

14	Sediment B	10.916		10.783
14	Sediment B	19.345	12.544	10.705
15	Sediment B	15.791		12.317
15	Sediment B	17.000		12.293
15	Sediment B	16.690		12.432
16	Sediment B	15.218	17.187	14.894
16	Sediment B	15.791		14.874
16	Sediment B	16.690	17.567	14.927
17	CCZ sediment	1.331	0.628	0.601
17	CCZ sediment	1.460		0.599
17	CCZ sediment	1.283	0.524	0.596
18	CCZ sediment	2.274	1.367	1.239
18	CCZ sediment	1.926		1.247
18	CCZ sediment	1.856	1.132	1.240
19	CCZ sediment	6.756	3.205	2.367
19	CCZ sediment	5.514		2.396
19	CCZ sediment	4.501		2.398
20	CCZ sediment	17.000		5.081
20	CCZ sediment	16.085		5.160
20	CCZ sediment	13.374	7.835	5.169
21	CCZ sediment	19.706	8.437	6.293
21	CCZ sediment	20.828		6.322
21	CCZ sediment	16.085	9.310	6.326
22	CCZ sediment	18.303	15.077	9.747
22	CCZ sediment	19.345		9.950
22	CCZ sediment	21.216	14.756	9.927
23	CCZ sediment	23.267	21.053	12.491
23	CCZ sediment	23.700		12.205
23	CCZ sediment	23.267	20.378	12.248
24	CCZ sediment	39.737	32.374	15.556
24	CCZ sediment	42.000	31.590	15.640

H

ABS Acquisition Information

The following table includes information of the acoustic acquisition settings of each measurement.

Test_#	Measur._#	Sediment	File_name	Temperature_C	ABS_Method3_SSC_g/L	Ping_rate_Hz	Bin_size_mm	Pulse_length_us	Number_of_bins	Range_mm
1	1	Sediment B	20260317161846.aqa	15	2.448	4	20	26.67	80	1600
1	2	Sediment B	20260317163252.aqa	15	4.757	4	20	26.67	80	1600
1	3	Sediment B	20260317164520.aqa	15	6.392	4	20	26.67	80	1600
2	1	Sediment B	20260317180642.aqa	15.5	2.274	4	20	26.67	80	1600
2	2	Sediment B	20260317181833.aqa	15.5	1.170	4	20	26.67	80	1600
2	3	Sediment B	20260317182751.aqa	15.5	1.214	4	20	26.67	80	1600
3	1	Sediment B	20260318101623.aqa	14.8	1.856	4	20	26.67	80	1600
3	2	Sediment B	20260318102637.aqa	14.8	2.999	4	20	26.67	80	1600
3	3	Sediment B	20260318103720.aqa	14.8	0.737	4	20	26.67	80	1600
4	1	Sediment B	20260319142012.aqa	8.9	0.519	4	20	26.67	80	1600
4	2	Sediment B	20260319142835.aqa	8.9	0.549	4	20	26.67	80	1600
4	3	Sediment B	20260319143601.aqa	8.9	0.482	4	20	26.67	80	1600
5	1	Sediment B	20260319152359.aqa	10.5	0.973	4	20	26.67	80	1600
5	2	Sediment B	20260319153328.aqa	10.5	0.539	4	20	26.67	80	1600
5	3	Sediment B	20260319154420.aqa	10.5	0.937	4	20	26.67	80	1600
6	1	Sediment B	20260319163102.aqa	10.9	1.087	4	20	26.67	80	1600
6	2	Sediment B	20260319163938.aqa	10.9	0.648	4	20	26.67	80	1600
6	3	Sediment B	20260319164735.aqa	10.9	1.236	4	20	26.67	80	1600
7	1	Sediment B	20260320120537.aqa	8.5	2.582	4	20	26.67	80	1600
7	2	Sediment B	20260320121320.aqa	8.5	2.448	4	20	26.67	80	1600
7	3	Sediment B	20260320122636.aqa	8.5	2.274	4	20	26.67	80	1600
8	1	Sediment B	20260320141405.aqa	9	2.944	4	20	26.67	80	1600
8	2	Sediment B	20260320142205.aqa	9	2.785	4	20	26.67	80	1600
8	3	Sediment B	20260320143015.aqa	9	3.112	4	20	26.67	80	1600
9	1	Sediment B	20260320220002.aqa	12.9	4.029	4	20	26.67	80	1600
9	2	Sediment B	20260320220823.aqa	12.9	3.812	4	20	26.67	80	1600
9	3	Sediment B	20260320221634.aqa	12.9	3.412	4	20	26.67	80	1600
10	1	Sediment B	20260322112143.aqa	16.1	7.547	4	20	26.67	80	1600
10	2	Sediment B	20260322113027.aqa	16.1	7.976	4	20	26.67	80	1600
10	3	Sediment B	20260322113805.aqa	16.1	7.547	4	20	26.67	80	1600

11	1	Sediment B	20260323114526.aqa	16.5	9.593	4	20	26.67	80	1600
11	2	Sediment B	20260323115318.aqa	16.5	7.547	4	20	26.67	80	1600
11	3	Sediment B	20260323120300.aqa	16.5	9.246	4	20	26.67	80	1600
12	1	Sediment B	20260323140404.aqa	16.6	8.125	4	20	26.67	80	1600
12	2	Sediment B	20260323141238.aqa	16.6	8.125	4	20	26.67	80	1600
12	3	Sediment B	20260323142315.aqa	16.6	8.910	4	20	26.67	80	1600
13	1	Sediment B	20260323150157.aqa	16.7	12.653	4	20	26.67	80	1600
13	2	Sediment B	20260323150940.aqa	16.7	17.000	4	20	26.67	80	1600
13	3	Sediment B	20260323151805.aqa	16.7	10.916	4	20	26.67	80	1600
14	1	Sediment B	20260323160608.aqa	16.9	13.623	4	20	26.67	80	1600
14	2	Sediment B	20260323161352.aqa	16.9	10.916	4	20	26.67	80	1600
14	3	Sediment B	20260323162146.aqa	16.9	19.345	4	20	26.67	80	1600
15	1	Sediment B	20260323171238.aqa	17.1	15.791	4	20	26.67	80	1600
15	2	Sediment B	20260323173423.aqa	17.1	17.000	4	20	26.67	80	1600
15	3	Sediment B	20260323174353.aqa	17.1	16.690	4	20	26.67	80	1600
16	1	Sediment B	20260323185501.aqa	17	15.218	4	20	26.67	40	800
16	2	Sediment B	20260323190303.aqa	17	15.791	4	20	26.67	40	800
16	3	Sediment B	20260323191123.aqa	17	16.690	4	20	26.67	40	800
17	1	CCZ sedimen	20260330103542.aqa	4.8	1.331	4	20	26.67	80	1600
17	2	CCZ sedimen	20260330104531.aqa	4.8	1.460	4	20	26.67	80	1600
17	3	CCZ sedimen	20260330105410.aqa	4.8	1.283	4	20	26.67	80	1600
18	1	CCZ sedimen	20260330122934.aqa	7.5	2.274	4	20	26.67	80	1600
18	2	CCZ sedimen	20260330123832.aqa	7.5	1.926	4	20	26.67	80	1600
18	3	CCZ sedimen	20260330124755.aqa	7.5	1.856	4	20	26.67	80	1600
19	1	CCZ sedimen	20260331101523.aqa	6.7	6.756	4	20	26.67	55	1100
19	2	CCZ sedimen	20260331102308.aqa	6.7	5.514	4	20	26.67	55	1100
19	3	CCZ sedimen	20260331103044.aqa	6.7	4.501	4	20	26.67	55	1100
20	1	CCZ sedimen	20260331160851.aqa	8.9	17.000	4	20	26.67	55	1100
20	2	CCZ sedimen	20260331161630.aqa	8.9	16.085	4	20	26.67	55	1100
20	3	CCZ sedimen	20260331162349.aqa	8.9	13.374	4	20	26.67	55	1100
21	1	CCZ sedimen	20260401100719.aqa	8.1	19.706	4	20	26.67	55	1100
21	2	CCZ sedimen	20260401101516.aqa	8.1	20.828	4	20	26.67	55	1100
21	3	CCZ sedimen	20260401102239.aqa	8.1	16.085	4	20	26.67	55	1100

22	1	CCZ sedimen 20260401123555.aqa	9.3	18.303	4	20	26.67	55	1100
22	2	CCZ sedimen 20260401124353.aqa	9.3	19.345	4	20	26.67	55	1100
22	3	CCZ sedimen 20260401125202.aqa	9.3	21.216	4	20	26.67	55	1100
23	1	CCZ sedimen 20260401140643.aqa	9.6	23.267	4	20	26.67	55	1100
23	2	CCZ sedimen 20260401141431.aqa	9.6	23.700	4	20	26.67	55	1100
23	3	CCZ sedimen 20260401142222.aqa	9.6	23.267	4	20	26.67	55	1100
24	1	CCZ sedimen 20260401150407.aqa	9.8	39.737	4	20	26.67	55	1100
24	2	CCZ sedimen 20260401151121.aqa	9.8	42.000	4	20	26.67	55	1100

I

Python Workflow

Example Code Used to Determine the Viscous Attenuation and Backscatter Terms

In [24]:
```
import numpy as np
import pandas as pd
import pickle
import copy
from math import pi, sqrt
import scipy.stats as stats
import matplotlib.pyplot as plt
import matplotlib.lines as mlines
from AquascatDataLoader import RawAquascatData, MeanAquascatProfile
from scipy.ndimage import median_filter, gaussian_filter1d
from matplotlib.lines import Line2D
from matplotlib.ticker import NullFormatter
```

In [25]:
```
# Load in ABS information from the CSV file
df = pd.read_csv('Continuousflow_ABS_table_CCZ.csv')
```

In [26]:
```
# Cutoff values for the range of the backscatter data to be used in the mean
profile calculation
Rmin = 0.04
Rmax = 0.8
YEAR = 2026

BS_list_quadra = []
BS_list_simple = []
missing_files = []
range_skipped_files = []
bad_time_rows = []

path = r"C:\Users\User\Desktop\Master ODE\02. Year 2\Blok 3 & 4\00. Thesis\01.
Allseas\02. Thesis\03. Post-processing\Vergne et al. 2021\5094304 - Julian modified
for own data CCZ gravimetric\acoustic_data"

for i in range(len(df.index)):
    date_str = str(df.loc[i, 'measurement date']).strip()
    time_value = df.loc[i, 'Time']
    time_str = str(time_value).strip()
    datetime_temp = pd.to_datetime(f"{date_str}-{YEAR} {time_str}", format="%d-%b-
%Y %H:%M:%S")

    file_name = (
        f"{path}\\"
        f"{datetime_temp.year}"
        f"{str(datetime_temp.month).zfill(2)}"
        f"{str(datetime_temp.day).zfill(2)}"
        f"{str(datetime_temp.hour).zfill(2)}"
        f"{str(datetime_temp.minute).zfill(2)}"
        f"{str(datetime_temp.second).zfill(2)}"
        f".aqa"
    )

    BS_raw = RawAquascatData(file_name)
    max_range = float(np.nanmax(BS_raw.r))
    min_range = float(np.nanmin(BS_raw.r))
    BS_quadra = MeanAquascatProfile()
    BS_quadra.compute_mean(BS_raw, Rmin, Rmax, mean='quadratic')
    BS_quadra.Test_number = df.loc[i, 'Test number']
    BS_quadra.Sediment = df.loc[i, 'Sediment']
    BS_quadra.Concentration = df.loc[i, 'Concentration gravimetric']
    BS_quadra.Temperature = df.loc[i, 'Temperature']
    BS_quadra.Measurement_number = df.loc[i, 'Measurement #']
    BS_quadra.Measurement_time = df.loc[i, 'Time']
    BS_list_quadra.append(BS_quadra)
```

In [27]:
```
# Load the background noise file
file_backnoise1 = (r"C:\Users\User\Desktop\Master ODE\02. Year 2\Blok 3 & 4\00.
Thesis\01. Allseas\02. Thesis\02. Sweden Tests\Organized
data\Background_measurments\20260316102630.aqa")
BS_noise_raw = RawAquascatData(file_backnoise1)
BS_noise = MeanAquascatProfile()
BS_noise.compute_mean(BS_noise_raw, Rmin, Rmax, mean="quadratic")
```

In [28]:

```
# Function to plot the backscatter and noise data
def plot_backscatter_and_noise(BS, noise, title=""):
    fig, ax = plt.subplots(2, 2, figsize=(11, 8), dpi=125)
    fig.suptitle(title, fontsize="x-large")
    r_bs = np.asarray(BS.r).ravel()
    r_noise = np.asarray(noise.r).ravel()

    for i in range(2):
        for j in range(2):
            f = 2 * i + j

            ax[i, j].plot(r_bs, BS.V[:, f], label="Raw backscatter")
            ax[i, j].plot(r_noise, noise.V[:, f], color="red", label="Background
noise")

            ax[i, j].set_title(BS.freqText[f])
            ax[i, j].set_yscale("log")

            if j == 0:
                ax[i, j].set_ylabel("V")
            if i == 1:
                ax[i, j].set_xlabel("Range (m)")

            ax[i, j].legend(loc="best")
            ax[i, j].grid(True)
    fig.tight_layout()
    return fig

k = 3

title = (f"Index {k} | " f"{BS_list_quadra[k].Sediment} | " f"
{BS_list_quadra[k].Concentration} g/L | " f"{BS_list_quadra[k].file_name}")

fig = plot_backscatter_and_noise(BS_list_quadra[k], BS_noise, title)
plt.show()
```

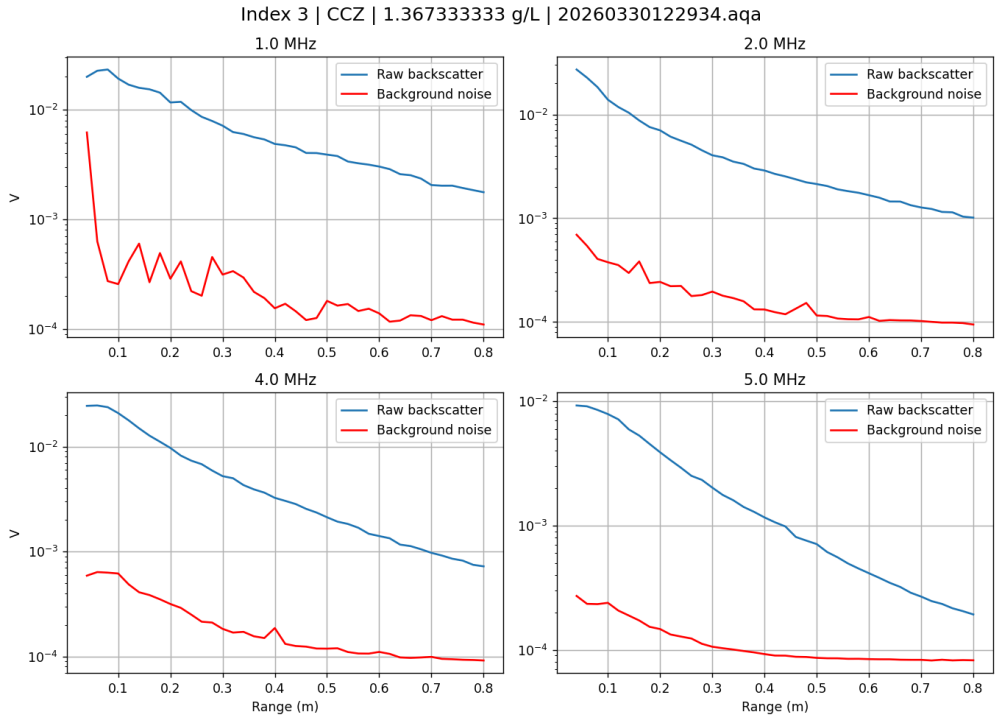

In [29]:

```
# de-spike and smooth background file
BS_noise_fit = copy.deepcopy(BS_noise)

filter_settings = {
    "1.0 MHz": {"median_size": 7, "sigma": 3},
    "2.0 MHz": {"median_size": 4, "sigma": 1},
    "4.0 MHz": {"median_size": 3, "sigma": 1},
    "5.0 MHz": {"median_size": 3, "sigma": 1},
}

for f in range(4):
    freq = BS_noise.freqText[f]
    median_size = filter_settings[freq]["median_size"]
    sigma = filter_settings[freq]["sigma"]
    V_noise = BS_noise.V[:, f].copy()
    V_med = median_filter(V_noise, size=median_size)
    BS_noise_fit.V[:, f] = gaussian_filter1d(V_med, sigma=sigma)

fig, ax = plt.subplots(1, 4, figsize=(15, 6), dpi=125)
r_noise = np.asarray(BS_noise.r).ravel()

for f in range(4):

    freq = BS_noise.freqText[f]
    ax[f].plot(BS_noise.V[:, f], r_noise, color="grey", alpha=0.5, linewidth=1.5)
    ax[f].plot(BS_noise_fit.V[:, f], r_noise, color="black", linewidth=2)
    ax[f].invert_yaxis()
    ax[f].set_xscale("log")
    ax[f].xaxis.tick_top()
    ax[f].xaxis.set_label_position("top")
    ax[f].set_xlabel(freq, fontsize=16, weight="bold", labelpad=12)
    ax[f].tick_params(axis="both", which="major", labelsize=16)


    if f == 0:
        ax[f].set_ylabel("Range (m)", fontsize=15)
    else:
        ax[f].tick_params(axis="y", left=False, labelleft=False)

fig.supxlabel("Signal amplitude (V)", fontsize=15, y=0.12)

legend_lines = [Line2D([0], [0], color="grey", lw=2, alpha=0.6), Line2D([0], [0],
color="black", lw=2)]
fig.legend(legend_lines, ["Original background", "Smoothed background"], loc="lower
center", bbox_to_anchor=(0.5, -0.02), ncol=2, fontsize=16, frameon=False)
fig.tight_layout(rect=[0, 0.10, 1, 1])
plt.show()

BS_noise = copy.deepcopy(BS_noise_fit)
```

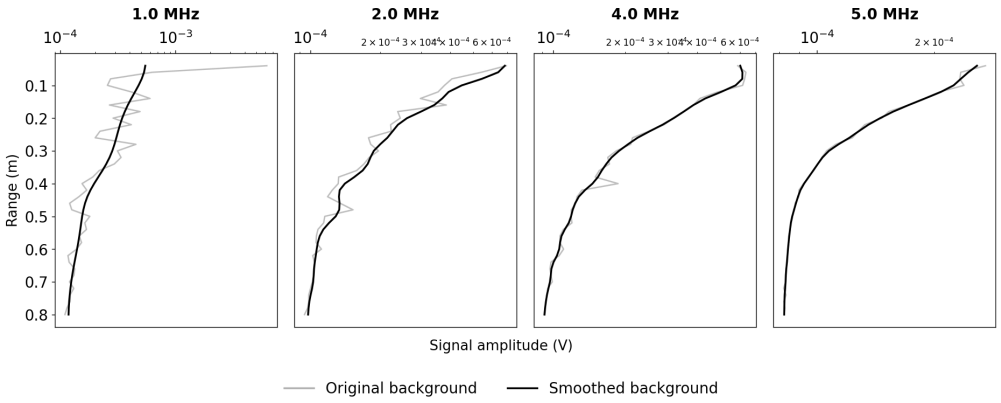

In [30]:

```
# Determine near-field region
c = 1500  # m/s

# Transducer radius obtained from Vergne et al. 2021
radius = np.array([0.00899999961256981, 0.00499999988824129, 0.00485000014305115,
0.00520000001415610])
frequency_MHz = np.array([1, 2, 4, 5])
freq_Hz = frequency_MHz * 1e6
wavelength = c / freq_Hz
nearfield_range = np.pi * radius**2 / wavelength

for f, r, nf in zip(frequency_MHz, radius, nearfield_range):
    print(f"Frequency: {f:.1f} MHz | " f"Radius: {r*1000:.2f} mm | " f"Near-field
range: {nf:.4f} m")
```

```
Frequency: 1.0 MHz | Radius: 9.00 mm | Near-field range: 0.1696 m
Frequency: 2.0 MHz | Radius: 5.00 mm | Near-field range: 0.1047 m
Frequency: 4.0 MHz | Radius: 4.85 mm | Near-field range: 0.1971 m
Frequency: 5.0 MHz | Radius: 5.20 mm | Near-field range: 0.2832 m
```

In [31]:

```
# Compute signal to noise ratio
SNR_list = []
SNR_dB_list = []

eps = 1e-12 # small value to avoid crashing when dividing by zero or taking log of
zero

for k in range(len(BS_list_quadra)):
    SNR = (BS_list_quadra[k].V**2) / (BS_noise.V**2 + eps)
    # SNR in dB
    SNR_dB = 6 * np.log10(SNR + eps)
    SNR_list.append(SNR)
    SNR_dB_list.append(SNR_dB)
    BS_list_quadra[k].SNR = SNR
    BS_list_quadra[k].SNR_dB = SNR_dB

print("Computed SNR for", len(SNR_list), "profiles")

def plot_snr_profile(BS, title=""):
    fig, ax = plt.subplots(2, 2, figsize=(11, 8), dpi=125)
    fig.suptitle(title, fontsize="x-large")

    r_bs = np.asarray(BS.r).ravel()

    for i in range(2):
        for j in range(2):
            f = 2 * i + j
            ax[i, j].plot(r_bs, BS.SNR_dB[:, f])
            ax[i, j].axhline(0, color="black", linestyle="--", linewidth=1)
            ax[i, j].set_title(BS.freqText[f])
            ax[i, j].set_ylabel("SNR [dB]")
            ax[i, j].set_xlabel("Range [m]")
            ax[i, j].set_xlim(0, Rmax)
    fig.tight_layout()
    return fig

# Selecting profile index to plot SNR profile
k = 12

fig = plot_snr_profile(BS_list_quadra[k], title=(f"SNR profile | " f"
{BS_list_quadra[k].Sediment} | " f"{BS_list_quadra[k].Concentration} g/L"))
plt.show(fig)
```

```
Computed SNR for 23 profiles
```

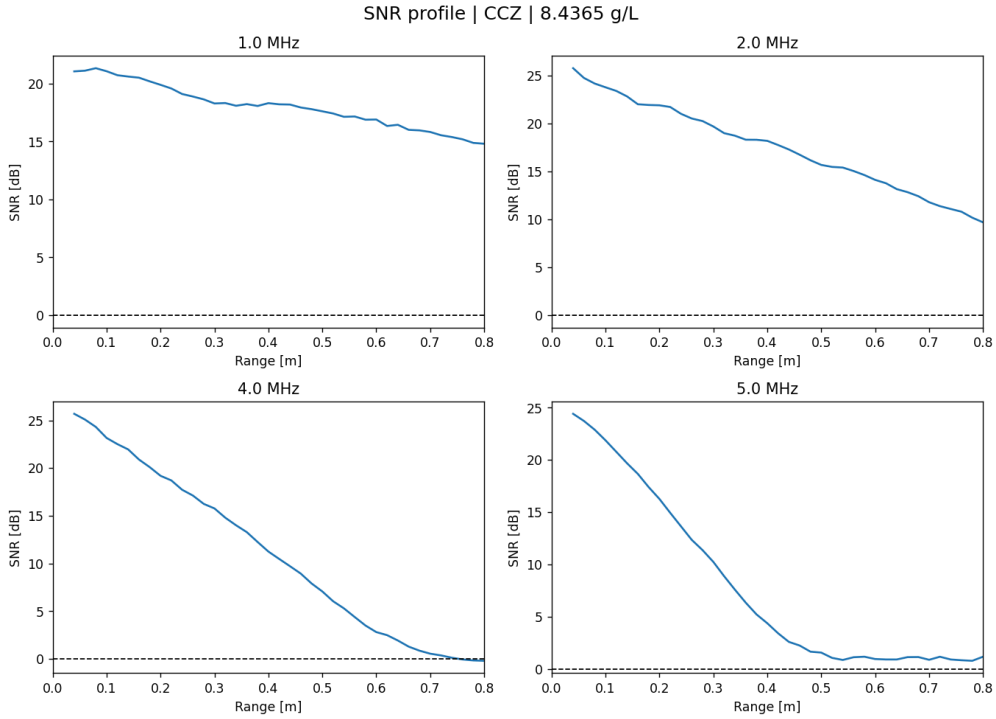
SNR profile | CCZ | 8.4365 g/L
1.0 MHz
2.0 MHz
4.0 MHz
5.0 MHz
SNR [dB]
Range [m]

In [54]:

```
# Set validrange for SNR > threshold and outside near field
SNR_threshold = 5
SNR_limit_range_list = []
SNR_valid_window_list = []
ind_min_raw_list = []
ind_max_raw_list = []

for k in range(len(BS_list_quadra)):
    r = np.asarray(BS_list_quadra[k].r).ravel()
    SNR = np.asarray(BS_list_quadra[k].SNR)
    threshold_ranges = {}
    valid_windows = {}
    min_temp = []
    max_temp = []

    for f in range(4):
        freq = BS_list_quadra[k].freqText[f]
        nf = nearfield_range[f]
        # Only consider region outside near field
        valid_mask = np.isfinite(r) & np.isfinite(SNR[:, f]) & (r > nf) & (SNR[:,
f] > SNR_threshold)
        valid_idx = np.where(valid_mask)[0]

        if len(valid_idx) == 0:
            threshold_ranges[freq] = np.nan
            valid_windows[freq] = np.nan
            min_temp.append(None)
            max_temp.append(None)

        else:
            ind_min = valid_idx[0]
            ind_max = valid_idx[-1]
            threshold_ranges[freq] = r[ind_max]
            valid_windows[freq] = (r[ind_min], r[ind_max])
            min_temp.append(ind_min)
            max_temp.append(ind_max)

    SNR_limit_range_list.append(threshold_ranges)
    SNR_valid_window_list.append(valid_windows)
    ind_min_raw_list.append(min_temp)
    ind_max_raw_list.append(max_temp)

for k in range(len(BS_list_quadra)):
    for f in range(4):
        ind_min = ind_min_raw_list[k][f]
        ind_max = ind_max_raw_list[k][f]
        if ind_min is not None and ind_max is not None:
            r = np.asarray(BS_list_quadra[k].r).ravel()
            # print(f"Profile {k}, Frequency {BS_list_quadra[k].freqText[f]}: Valid
fitted SNR > {SNR_threshold} range: {r[ind_min]:.2f} m to {r[ind_max]:.2f} m")
        # else:
            # print(f"Profile {k}, Frequency {BS_list_quadra[k].freqText[f]}: No
valid fitted SNR > {SNR_threshold} window")
```

In [46]:

```
# Helper functions
# Function for computing water attenuation
def alpha_w_function(freq, T=15):
    "Computing water attenuation in m^-1 from François and Garrison, 1982"
    if T > 20:
        alpha = (3.964*1e-4 - 1.146*1e-5*T + 1.45*1e-7 * T ** 2 - 6.5*1e-10 * T **
3) * 1e-3 * (np.log(10)/20) * (freq*1e-3) ** 2
    else:
        alpha = (4.937*1e-4 - 2.59*1e-5*T + 9.11*1e-7 * T ** 2 - 1.5*1e-8 * T ** 3)
* 1e-3 * (np.log(10)/20) * (freq*1e-3) ** 2
    return alpha

# Function for computing sound speed
def water_velocity(T=15):
    "Computing sound speed in m/s from Bilaniuk and Wong 1993"
    C = 1.40238744*1e3 + 5.03836171*T - 5.81172916*1e-2 * T**2 + 3.34638117*1e-4 *
T**3 - \
    1.48259672*1e-6 * T**4 + 3.16585020*1e-9*T**5
    return(C)

# Function for computing cell size (range correction)
def range_cells_function(BS, T=15):
    r = np.asarray(BS.r).ravel()
    # Default Aquascat cell size
    aquascat_cell_size = r[1] - r[0]
    # Pulse duration
    tau = aquascat_cell_size * 2 / 1500
    cel = water_velocity(T)
    real_cell_size = cel * tau / 2
    real_r = r / aquascat_cell_size * real_cell_size
    R_real = np.tile(real_r[:, np.newaxis], (1, len(BS.Freq)))
    return R_real
```

In [47]:

```
# Compute FCB linear regression
# Minor corrections to a few selected fitting bounds manually from Excel
manual_bounds_path = (r"C:\Users\User\Desktop\Master ODE\02. Year 2\Blok 3 & 4\00.
Thesis\01. Allseas\02. Thesis\03. Post-processing\Vergne et al. 2021\5094304 -
Julian modified for own data CCZ
gravimetric\FCB_manual_regression_Bounds_CCZ_new.xlsx")
manual_bounds = pd.read_excel(manual_bounds_path)

# Convert frequencies from Excel (MHz) to Python indices
freq_map = {1: 0, 2: 1, 4: 2, 5: 3}

for _, row in manual_bounds.iterrows():
    k = int(row["Index"])
    f_raw = int(row["Frequency"])
    f = freq_map[f_raw]
    r = np.asarray(BS_list_quadra[k].r).ravel()

    if pd.notna(row["Min"]):
        ind_min_raw_list[k][f] = np.argmin(np.abs(r - float(row["Min"])))

    if pd.notna(row["Max"]):
        ind_max_raw_list[k][f] = np.argmin(np.abs(r - float(row["Max"])))
```

In [50]:

```
# Compute fluid-corrected backscatter (FCB) and acoustic attenuation
FCB_list = []
R_list = []
intercept_list = []
alpha_list = []

# Background noise values for each frequency (in V), determined in seperate script
background_noise = np.array([
    9.61320e-05,
    8.98206e-05,
    8.56449e-05,
    8.16460e-05
])

for k in range(len(BS_list_quadra)):
    T = BS_list_quadra[k].Temperature
    alpha_w = alpha_w_function(BS_list_quadra[k].Freq, T)
    alpha_w_matrix = np.repeat([alpha_w], BS_list_quadra[k].r.size, axis=0)
    R_real = range_cells_function(BS_list_quadra[k], T=T)
    R_list.append(R_real)

    V_corrected = BS_list_quadra[k].V**2 - background_noise**2
    V_corrected[V_corrected <= 0] = np.nan
    V_corrected = np.sqrt(V_corrected)

    FCB = np.log(V_corrected) + np.log(R_real) + 2 * alpha_w_matrix * R_real
    FCB_list.append(FCB)

    alpha_temp = []
    intercept_temp = []

    for f in range(4):
        ind_min = ind_min_raw_list[k][f]
        ind_max = ind_max_raw_list[k][f]

        if ind_max is None:
            alpha_temp.append(None)
            intercept_temp.append(None)
            continue

        x = R_real[ind_min:ind_max, f]
        y = FCB[ind_min:ind_max, f]

        mask = np.isfinite(x) & np.isfinite(y)

        if np.sum(mask) < 2:
            alpha_temp.append(None)
            intercept_temp.append(None)
            continue

        linreg = stats.linregress(x[mask], y[mask])
        alpha_temp.append(-0.5 * linreg.slope)
        intercept_temp.append(linreg.intercept)

    alpha_list.append(alpha_temp)
    intercept_list.append(intercept_temp)


# Print alpha_s values
for k in range(len(alpha_list)):
    # print(f"\n Profile {k}")
    for f in range(4):
        alpha = alpha_list[k][f]
```

```
        # print(f"{BS_list_quadra[k].freqText[f]:>8} : {alpha if alpha is not None
else 'None'}")

# select a profile
k = 5

r = np.asarray(BS_list_quadra[k].r).ravel()
fig, ax = plt.subplots(1, 4, figsize=(14, 4), dpi=125)

for f in range(4):

    V_raw = BS_list_quadra[k].V[:, f]
    V_corr = np.sqrt(V_raw**2 - background_noise[f]**2)
    V_corr[V_raw**2 <= background_noise[f]**2] = np.nan
    ax[f].plot(r, V_raw, color="black", label="Raw signal")
    ax[f].plot(r, V_corr, color="red", label="Background corrected")
    ax[f].axhline(background_noise[f], color="blue", linestyle="--", linewidth=1.5,
label="Static background")
    ax[f].set_title(BS_list_quadra[k].freqText[f])
    ax[f].set_yscale("log")
    ax[f].set_xlabel("Range (m)")

    if f == 0:
        ax[f].set_ylabel("V")

    ax[f].grid(alpha=0.3)
    ax[f].legend(fontsize=7)

fig.suptitle(f"Signal cutoff check | Profile {k}", fontsize=14)

fig.tight_layout()
plt.show()
```

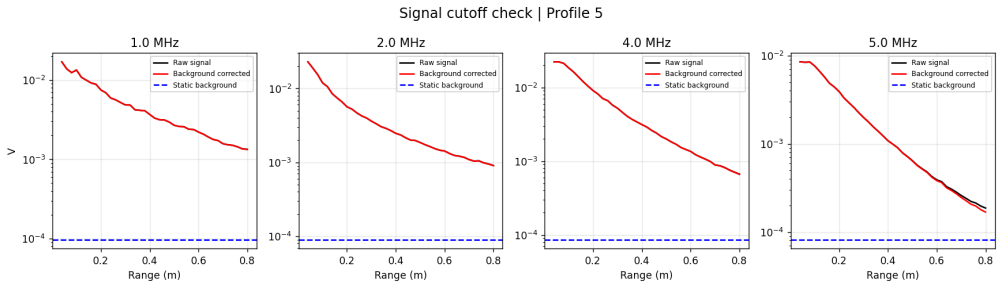

In [36]:

```
# Plot FCB with linear regression
def plot_FCB(FCB, R, BS, alpha, intercept, ind_min, ind_max, title=""):

    fig, ax = plt.subplots(2, 2, figsize=(11, 8), dpi=125)
    fig.suptitle(title, fontsize="x-large")
    r_bs = np.asarray(BS.r).ravel()

    for i in range(2):
        for j in range(2):
            f = 2 * i + j
            ax[i, j].plot(R[:, f], FCB[:, f], label="FCB")

            if ind_max[f] is not None and alpha[f] is not None:
                ax[i, j].plot(R[:, f], -2 * alpha[f] * R[:, f] + intercept[f],
color="red", label="FCB regression")
                ax[i, j].axvline(r_bs[ind_min[f]], color="black", linestyle=":",
label="Regression bounds")
                ax[i, j].axvline(r_bs[ind_max[f]], color="black", linestyle=":")

            ax[i, j].set_title(BS.freqText[f])

            if j == 0:
                ax[i, j].set_ylabel("FCB")
            if i == 1:
                ax[i, j].set_xlabel("Range (m)")

            ax[i, j].legend(loc="best", fontsize=7)
            ax[i, j].grid(alpha=0.3)

    fig.tight_layout()
    return fig

k = 12

title = f"FCB | {BS_list_quadra[k].Sediment} | {BS_list_quadra[k].Concentration}
g/L | Index {k}"
fig = plot_FCB(FCB_list[k], R_list[k], BS_list_quadra[k], alpha_list[k],
intercept_list[k], ind_min_raw_list[k], ind_max_raw_list[k], title)
plt.show()
```

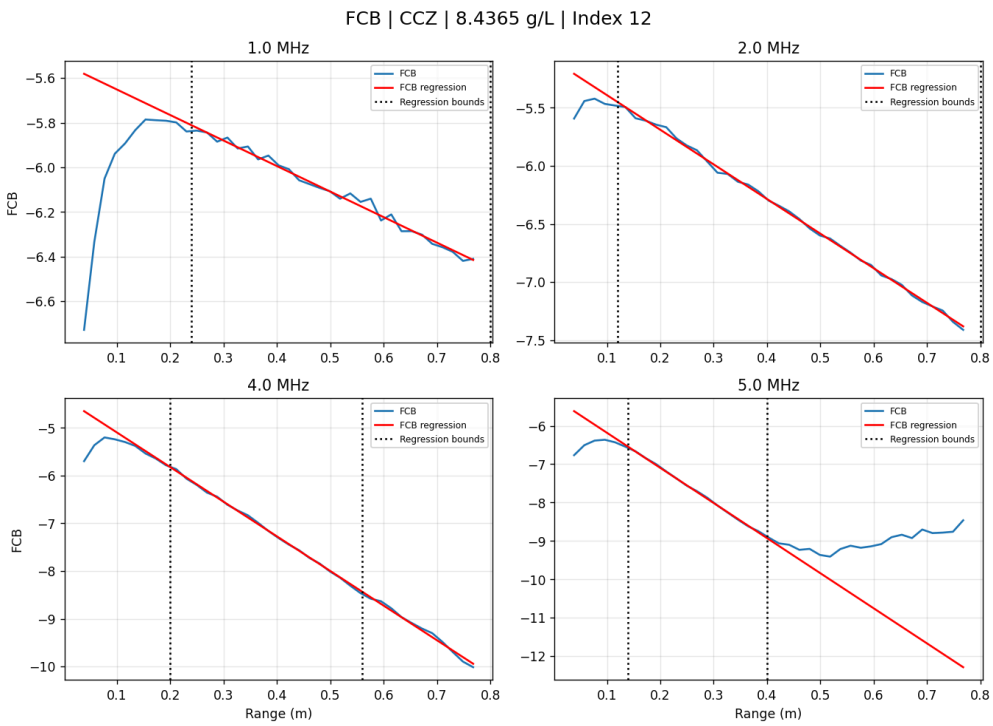

In [51]:

```
# Build alpha_s dictionary
freq_keys = list(BS_list_quadra[0].freqText)
alpha_dic = {freq: [] for freq in freq_keys}

for k in range(len(BS_list_quadra)):
    concentration = BS_list_quadra[k].Concentration
    for f in range(len(BS_list_quadra[k].Freq)):
        freq = BS_list_quadra[k].freqText[f]

        if alpha_list[k][f] is None:
            alpha_dic[freq].append([np.nan, np.nan])
        else:
            alpha_dic[freq].append([alpha_list[k][f], concentration])

# Regression alpha_s = a * SSC
a_list = []
r2_dic = {}

for freq in freq_keys:
    data = np.array(alpha_dic[freq], dtype=float)
    alpha_vals = data[:, 0]
    conc_vals = data[:, 1]
    mask = np.isfinite(alpha_vals) & np.isfinite(conc_vals)

    if np.sum(mask) < 2:
        a_list.append(np.nan)
        r2_dic[freq] = np.nan
        continue

    x = conc_vals[mask]
    y = alpha_vals[mask]
    a = np.sum(x * y) / np.sum(x**2)
    y_pred = a * x
    SSE = np.sum((y - y_pred)**2)
    SST = np.sum((y - np.mean(y))**2)
    r2 = 1 - SSE / SST if SST > 0 else np.nan
    a_list.append(a)
    r2_dic[freq] = r2


THESIS_PALETTE = [
    "#1fa040", "#1b8a5a", "#177482", "#125eab",
    "#0e48d3", "#0072ce", "#ffc372", "#f4a95e",
    "#ea8f49", "#df7535", "#d55b20", "#d14124",
    "#b07aa1", "#9b6aa5", "#865ba8", "#6a51a3"
]

freq_colors = {
    freq_keys[0]: THESIS_PALETTE[0],
    freq_keys[1]: THESIS_PALETTE[2],
    freq_keys[2]: THESIS_PALETTE[5],
    freq_keys[3]: THESIS_PALETTE[8],
}

marker_dic = {
    freq_keys[0]: "o",
    freq_keys[1]: "s",
    freq_keys[2]: "^",
    freq_keys[3]: "D",
}


def plot_attenuation_concentration(alpha_dic, freq_keys, a_list, r2_dic):
```

```
    fig, ax = plt.subplots(1, 1, figsize=(6, 4), dpi=125)
    fig.suptitle(r"Measured acoustic attenuation coefficient $\alpha_s$",
fontsize="x-large")

    max_conc = 0

    for i, freq in enumerate(freq_keys):
        data = np.array(alpha_dic[freq], dtype=float)
        alpha_vals = data[:, 0]
        conc_vals = data[:, 1]
        mask = np.isfinite(alpha_vals) & np.isfinite(conc_vals)

        if np.sum(mask) == 0:
            continue

        x = conc_vals[mask]
        y = alpha_vals[mask]
        max_conc = max(max_conc, np.nanmax(x))
        ax.plot(x, y, linestyle=" ", marker=marker_dic[freq],
color=freq_colors[freq], markersize=5,markeredgewidth=0.8, label=freq)

        if np.isfinite(a_list[i]):

            x_points = np.linspace(0, max_conc * 1.05, 100)
            ax.plot(x_points, a_list[i] * x_points,
                    color=freq_colors[freq], linestyle=":",
                    linewidth=2)

    ax.set_xlabel("SSC measured (g/L)", weight="bold", fontsize=14)
    ax.set_ylabel(r"$\alpha_s$ measured (m$^{-1}$)", weight="bold", fontsize=14)
    ax.set_xlim(0, max_conc * 1.1)
    ax.set_ylim(bottom=0)
    ax.grid(alpha=0.3)
    ax.legend(loc="best", fontsize=10)
    fig.tight_layout()
    return fig


fig = plot_attenuation_concentration(alpha_dic, freq_keys, a_list, r2_dic)
plt.show()

for i, freq in enumerate(freq_keys):
    r2 = round(r2_dic[freq], 3) if np.isfinite(r2_dic[freq]) else np.nan
    a = round(a_list[i], 4) if np.isfinite(a_list[i]) else np.nan
    # print(f"{freq}: R² = {r2}, a = {a}")
```

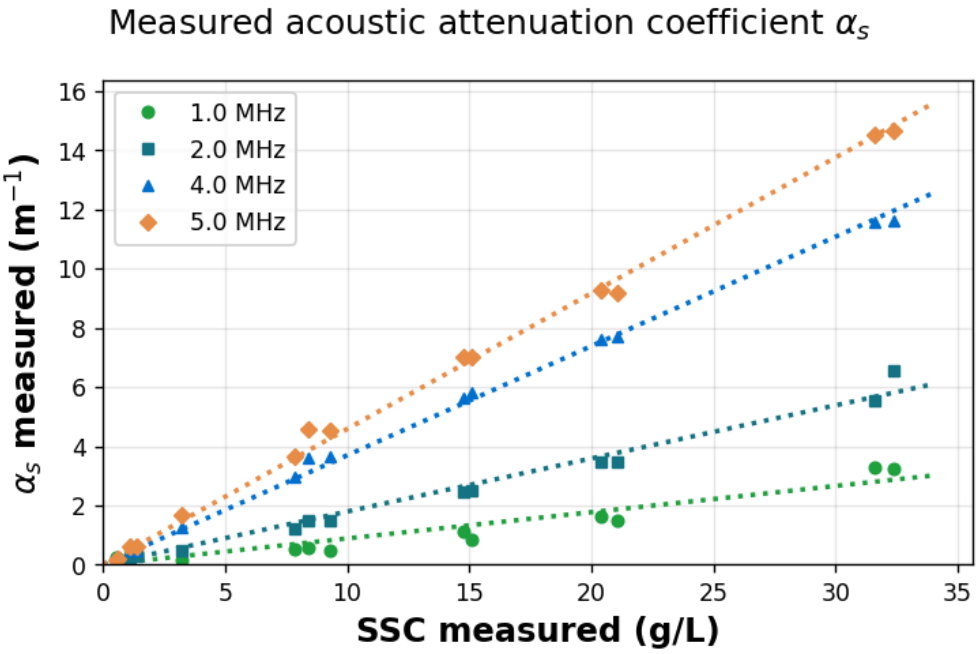

In [38]:

```
# Save alpha_s data
freq_list = []

for BS in BS_list_quadra:
    freq_list.append(BS.freqText)

data_attenuation = {"alpha_s": alpha_list, "freq": freq_list}
save_path = r"processed data sweden\alpha_s_data"

with open(save_path, "wb") as ff:
    pickle.dump(data_attenuation, ff)
```

In [52]:

```
# The backscatter term s_v is computed using the k_t calibration constant provided
by the instrument manufacturer and the previously measured attenuation \alpha_s
# First the proper value of k_t requires to be determined, taking into account the
cell size and the gain applied.
# Compute Kt values
kt_ref = {
    "1.0 MHz": 0.02756,
    "2.0 MHz": 0.01281,
    "4.0 MHz": 0.01067,
    "5.0 MHz": 0.00441
}

kt_list = []
tau_ref = 2.666666659933981e-05
c_ref = 1475

for k in range(len(BS_list_quadra)):
    kt_temp_list = []
    T = BS_list_quadra[k].Temperature
    r = np.asarray(BS_list_quadra[k].r).ravel()
    delta_r = r[1] - r[0]
    tau = 2 * delta_r / 1500
    cel = water_velocity(T=T)

    for f in range(len(BS_list_quadra[k].Freq)):
        freq = BS_list_quadra[k].freqText[f]
        Rx = BS_list_quadra[k].Rx[f]
        Tx = BS_list_quadra[k].Tx[f]
        gain = 10 ** ((Rx + Tx) / 20)
        kt = kt_ref[freq] * gain * np.sqrt((tau * cel) / (tau_ref * c_ref))
        kt_temp_list.append(kt)
    kt_list.append(kt_temp_list)
```

__Computing Sv__

$ s_v = \frac{3}{16 \pi} \frac{V_{rms}^2 r^2}{k_t^2} e^{4r(\alpha_s + \alpha_w)}$

In [40]:

```
# Update a few selected sv fitting bounds manually from Excel
sv_bounds_path = (r"C:\Users\User\Desktop\Master ODE\02. Year 2\Blok 3 & 4\00.
Thesis\01. Allseas\02. Thesis\03. Post-processing\Vergne et al. 2021\5094304 -
Julian modified for own data CCZ
gravimetric\Sv_manual_regression_Bounds_CCZ_backgr70min.xlsx")
sv_bounds = pd.read_excel(sv_bounds_path)

ind_min_sv_list = [x.copy() for x in ind_min_raw_list]
ind_max_sv_list = [x.copy() for x in ind_max_raw_list]
freq_map = {1: 0, 2: 1, 4: 2, 5: 3}

for _, row in sv_bounds.iterrows():
    k = int(row["Index"])
    f_raw = int(row["Frequency"])
    if f_raw not in freq_map:
        print(f"Skipping row: frequency {f_raw} not recognized")
        continue

    f = freq_map[f_raw]
    if k < 0 or k >= len(ind_min_sv_list):
        print(f"Skipping row: index {k} out of range")
        continue

    r = np.asarray(BS_list_quadra[k].r).ravel()
    if pd.notna(row["Min"]):
        ind_min_sv_list[k][f] = np.argmin(np.abs(r - float(row["Min"])))

    if pd.notna(row["Max"]):
        ind_max_sv_list[k][f] = np.argmin(np.abs(r - float(row["Max"])))
```

In [53]:

```
# Compute volume backscatter coefficient sv
R_mean_max = 0.8  # m

sv_list = []
sv_mean_list = []
sv_delta_list = []

for k in range(len(BS_list_quadra)):
    r_temp = R_list[k]
    n_range = BS_list_quadra[k].V.shape[0]
    kt_array = np.asarray(kt_list[k], dtype=float)
    kt_quadra = np.tile(kt_array, (n_range, 1)) * np.sqrt(4 / pi)
    T = BS_list_quadra[k].Temperature
    alpha_w = alpha_w_function(BS_list_quadra[k].Freq, T)
    alpha_w_matrix = np.tile(alpha_w, (n_range, 1))
    alpha_s_array = np.array([np.nan if a is None else a for a in alpha_list[k]],
dtype=float)
    alpha_s_array[alpha_s_array < 0] = 0
    alpha_s_matrix = np.tile(alpha_s_array, (n_range, 1))
    noise_matrix = BS_noise.V

    if noise_matrix.shape[0] != n_range:
        noise_matrix = noise_matrix[:n_range, :]

    V2_corrected = BS_list_quadra[k].V**2 - noise_matrix**2
    V2_corrected[V2_corrected <= 0] = np.nan
    sv_temp = ((3 / (16 * pi)) * V2_corrected * r_temp**2 *
               np.exp(4 * r_temp * (alpha_w_matrix + alpha_s_matrix)) /
               kt_quadra**2)

    sv_list.append(sv_temp)
    sv_mean_temp = []
    sv_delta_temp = []

    for f in range(4):
        ind_min = ind_min_sv_list[k][f]
        ind_max = ind_max_sv_list[k][f]
        if ind_max is None:
            sv_mean_temp.append(None)
            sv_delta_temp.append(None)
            continue

        r_f = np.asarray(R_list[k][:, f]).ravel()
        ind_max_range = np.where(r_f <= R_mean_max)[0]

        if len(ind_max_range) == 0:
            sv_mean_temp.append(None)
            sv_delta_temp.append(None)
            continue

        ind_max_limited = min(ind_max, ind_max_range[-1])

        if ind_min >= ind_max_limited:
            sv_mean_temp.append(None)
            sv_delta_temp.append(None)
            continue

        sv_window = sv_temp[ind_min:ind_max_limited + 1, f]
        mask = np.isfinite(sv_window)

        if np.sum(mask) == 0:
            sv_mean_temp.append(None)
            sv_delta_temp.append(None)
```

```
            continue

        sv_mean_temp.append(np.nanmean(sv_window[mask]))
        sv_delta_temp.append(np.nanmax(sv_window[mask]) -
np.nanmin(sv_window[mask]))

    sv_mean_list.append(sv_mean_temp)
    sv_delta_list.append(sv_delta_temp)

print(f"Computed sv for {len(sv_list)} profiles")
```

```
Computed sv for 23 profiles
```

In [42]:

```
k = 3

sv_start = sv_list[k]
sv_mean_start = sv_mean_list[k]
R = np.asarray(R_list[k][:, 0]).ravel()
R_start = R[0]
R_end = R[-1]
leg_list = BS_list_quadra[k].freqText

def plot_sv_article(sv, sv_mean, leg_list, R, R_start, R_end):
    fig, ax = plt.subplots(1, 1, figsize=(6, 4), dpi=125)

    for f in range(sv.shape[1]):
        if sv_mean[f] is None:
            continue

        color = freq_colors[freq_keys[f]]
        ax.axhline(sv_mean[f], color=color, linewidth=2)
        ax.plot(R, sv[:, f], linestyle=" ", marker="+", color=color, markersize=6)
        ax.text(R[-1], sv_mean[f] * 1.18, leg_list[f], color=color, weight="bold",
fontsize="large")

    ax.set_xlim(0.1, 0.8)
    ax.set_ylim(1e-4, 6)
    ax.set_xlabel("Range (m)", weight="bold", fontsize=14)
    ax.set_ylabel(r"$s_v$ (m$^2$/m$^3$)", weight="bold", fontsize=14)
    ax.set_yscale("log")
    ax.grid(alpha=0.3)
    fig.tight_layout()
    return fig

fig = plot_sv_article(sv_start, sv_mean_start, leg_list, R, R_start, R_end)
plt.show()
```

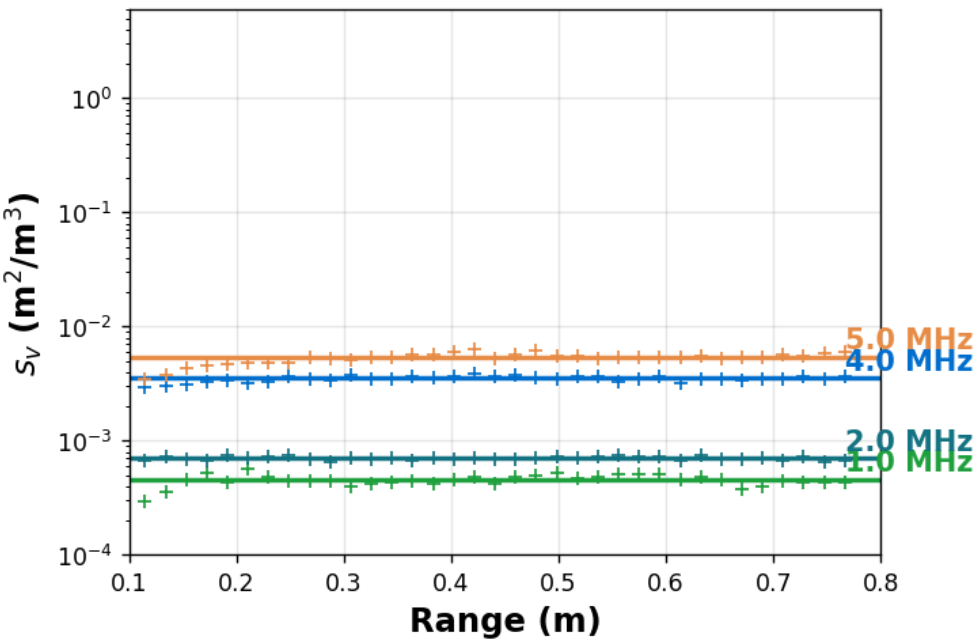

In [43]:

```
# Plots S_v relation to gravimetrically determined SSC
# Builds sv dictionary
freq_keys = list(BS_list_quadra[0].freqText)
sv_dic = {freq: [] for freq in freq_keys}

for k in range(len(BS_list_quadra)):
    concentration = BS_list_quadra[k].Concentration
    for f in range(len(BS_list_quadra[k].Freq)):
        freq = BS_list_quadra[k].freqText[f]

        if sv_mean_list[k][f] is None:
            sv_dic[freq].append([np.nan, np.nan])
        else:
            sv_dic[freq].append([sv_mean_list[k][f], concentration])

# Regression sv = a * SSC
asv_list = []
r2sv_dic = {}

for freq in freq_keys:
    data = np.array(sv_dic[freq], dtype=float)
    sv_vals = data[:, 0]
    conc_vals = data[:, 1]
    mask = np.isfinite(sv_vals) & np.isfinite(conc_vals)

    if np.sum(mask) < 2:
        asv_list.append(np.nan)
        r2sv_dic[freq] = np.nan
        continue

    x = conc_vals[mask]
    y = sv_vals[mask]
    a = np.sum(x * y) / np.sum(x**2)
    y_pred = a * x
    SSE = np.sum((y - y_pred)**2)
    SST = np.sum((y - np.mean(y))**2)
    r2 = 1 - SSE / SST if SST > 0 else np.nan
    asv_list.append(a)
    r2sv_dic[freq] = r2


def plot_sv_concentration(sv_dic, freq_keys, asv_list, r2sv_dic):
    fig, ax = plt.subplots(1, 1, figsize=(6, 4), dpi=125)
    max_conc = 0
    max_sv = 0

    for i, freq in enumerate(freq_keys):
        data = np.array(sv_dic[freq], dtype=float)
        sv_vals = data[:, 0]
        conc_vals = data[:, 1]
        mask = np.isfinite(sv_vals) & np.isfinite(conc_vals)

        if np.sum(mask) == 0:
            continue

        x = conc_vals[mask]
        y = sv_vals[mask]
        max_conc = max(max_conc, np.nanmax(x))
        max_sv = max(max_sv, np.nanmax(y))

        ax.plot(x, y, linestyle=" ", marker=marker_dic[freq],
color=freq_colors[freq], markersize=5, markeredgewidth=0.8, label=freq)
        if np.isfinite(asv_list[i]):
```

```
            x_points = np.linspace(0, max_conc * 1.05, 100)
            ax.plot(x_points, asv_list[i] * x_points, color=freq_colors[freq],
linestyle=":", linewidth=2)

    ax.set_xlabel("SSC measured (g/L)", weight="bold", fontsize=14)
    ax.set_ylabel(r"$s_v$ measured (m$^2$/m$^3$)", weight="bold", fontsize=14)
    ax.set_xlim(0, max_conc * 1.1)
    ax.set_ylim(0, max_sv * 1.4)
    ax.grid(alpha=0.3)
    ax.legend(loc="best", fontsize=10)
    fig.tight_layout()
    return fig

fig = plot_sv_concentration(sv_dic, freq_keys, asv_list, r2sv_dic)
plt.show()

for i, freq in enumerate(freq_keys):
    r2 = round(r2sv_dic[freq], 3) if np.isfinite(r2sv_dic[freq]) else np.nan
    a = round(asv_list[i], 6) if np.isfinite(asv_list[i]) else np.nan
    # print(f"{freq}: R² = {r2}, a = {a}, a×10³ = {round(a*1e3, 3) if
np.isfinite(a) else np.nan}")
```

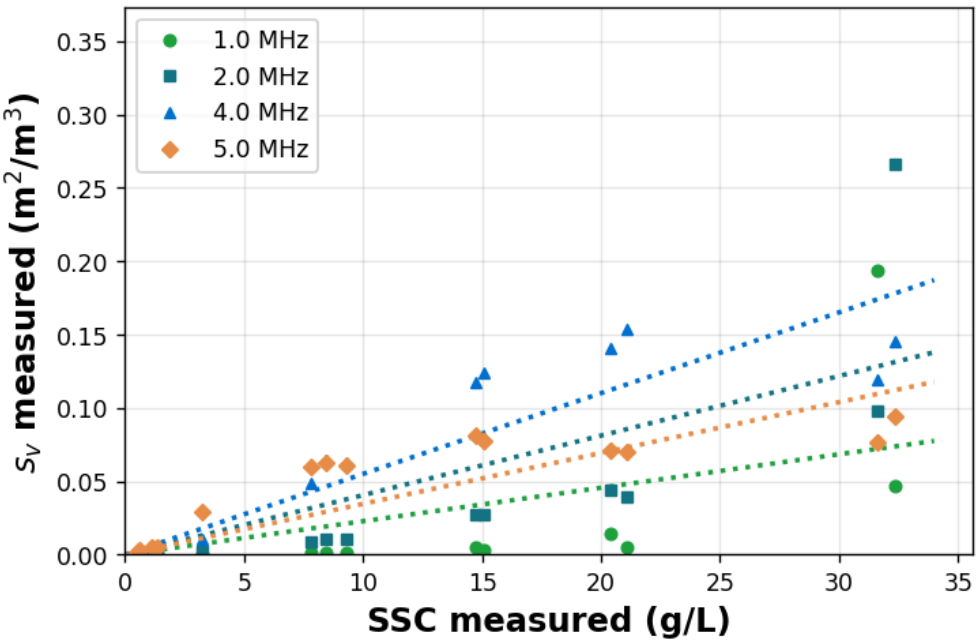

In [44]:
```
# Save sv data
freq_list = []

for BS in BS_list_quadra:
    freq_list.append(BS.freqText)

data_sv = {"s_v": sv_mean_list, "freq": freq_list}
save_path = r"processed data sweden\sv_data"

with open(save_path, "wb") as ff:
    pickle.dump(data_sv, ff)
```

In [ ]:
```
```

Exported with runcell — convert notebooks to HTML or PDF anytime at runcell.dev.

Example Code Used for Method 3.1 Inversion

In [2]:
```
import numpy as np
import pandas as pd
import pickle
import copy
from math import pi, sqrt, asin, atan
import matplotlib.pyplot as plt
import matplotlib.lines as mlines
from matplotlib.legend import Legend
import time # measuring time
from tqdm import tqdm
from AquascatDataLoader import RawAquascatData, MeanAquascatProfile
from matplotlib.colors import ListedColormap, BoundaryNorm
import matplotlib.patches as mpatches
from matplotlib.ticker import LogLocator, FuncFormatter
```

In [3]:
```
# Load in ABS information from the CSV file
df = pd.read_csv('Continuousflow_ABS_table_CCZ.csv')
```

In [4]:
```
# Loading measured alpha_s data
file = r'processed data sweden\alpha_s_data'
ff=open(file,'rb')
alpha_exp = pickle.load(ff)
ff.close()

# Loading measured s_v data
file = r'processed data sweden\sv_data'
ff=open(file,'rb')
sv_exp = pickle.load(ff)
ff.close()
```

In [5]:

```
# Density, water kinematic viscosity, oblate spheroids aspect ratio "h"
# Water viscosity (Sharqawy et al., 2010)
def seawater_viscosity(T, S, rho=1025):
    S_frac = S / 1000
    mu_w = 4.2844e-5 + 1 / (0.157 * (T + 64.993)**2 - 91.296)
    A = 1.541 + 1.998e-2 * T - 9.52e-5 * T**2
    B = 7.974 - 7.561e-2 * T + 4.724e-4 * T**2
    mu_sw = mu_w * (1 + A * S_frac + B * S_frac**2)
    nu_sw = mu_sw / rho

    return mu_sw, nu_sw


# Water density (UNESCO, 1983)
def seawater_density(S, T, p=0):
    S = np.asarray(S, dtype=float)
    T = np.asarray(T, dtype=float)
    p = np.asarray(p, dtype=float)

    rhow = (999.842594 + 6.793952e-2 * T - 9.095290e-3 * T**2 + 1.001685e-4 * T**3
- 1.120083e-6 * T**4 + 6.536332e-9 * T**5)
    rhost0 = (rhow + S * (0.824493 - 4.0899e-3 * T + 7.6438e-5 * T**2 - 8.2467e-7 *
T**3 + 5.3875e-9 * T**4)
        + S**1.5 * (-5.72466e-3 + 1.0227e-4 * T - 1.6546e-6 * T**2) + 4.8314e-4 *
S**2)

    kw = (19652.21 + 148.4206 * T - 2.327105 * T**2 + 1.360477e-2 * T**3 -
5.155288e-5 * T**4)

    kst0 = (kw + S * (54.6746 - 0.603459 * T + 1.09987e-2 * T**2 - 6.1670e-5 *
T**3)
        + S**1.5 * (7.944e-2 + 1.6483e-2 * T - 5.3009e-4 * T**2))

    kstp = (kst0 + p * (3.239908 + 1.43713e-3 * T + 1.16092e-4 * T**2 - 5.77905e-7
* T**3)
        + p * S * (2.2838e-3 - 1.0981e-5 * T - 1.6078e-6 * T**2)
        + 1.91075e-4 * p * S**1.5 + p**2 * (8.50935e-5 - 6.12293e-6 * T + 5.2787e-8
* T**2)
        + p**2 * S * (-9.9348e-7 + 2.0816e-8 * T + 9.1697e-10 * T**2))

    rho = rhost0 / (1 - p / kstp)
    rhodif = rho - 1000
    return rho, rhodif


T = 5
S = 34.7
p = 0

rho_w, rhodif = seawater_density(S, T, p)
mu, nu = seawater_viscosity(T, S, rho=rho_w)

print(f"Seawater density ρ = {rho_w:.2f} kg/m³")
print(f"Dynamic viscosity μ = {mu:.4e} Pa·s")
print(f"Kinematic viscosity ν = {nu:.4e} m²/s")
```

```
Seawater density ρ = 1027.44 kg/m³
Dynamic viscosity μ = 1.6183e-03 Pa·s
Kinematic viscosity ν = 1.5751e-06 m²/s
```

In [6]:

```
# Sediment density
rho_s = 2650

# Water kinematic viscosity
nu_0 = nu

# Aspect ratio for oblate spheroids
h_oblate = 1/40

# fine particles (h=h_oblate) radius lower limit
h_inf_radius = 1e-6

# Upper limit (h=1, spherical particles)
h_sup_radius = 30e-6
```

In [7]:

```
# Attenuation and backscatter model functions
# Form factor (Moate & Thorne, 2012)
def form_factor_function_MoateThorne2012(a_s, freq, C=1500, mica="false",
rho_s=2650):
    k = 2 * pi * freq / C
    x = k * a_s

    if mica == "false":
        f = (x**2 * (1 - 0.25 * np.exp(-((x - 1.5) / 0.35)**2))
             * (1 + 0.6 * np.exp(-((x - 2.9) / 1.15)**2))) / (42 + 28 * x**2)

    elif mica == "true":
        d1 = 0.2
        d2 = 1.7
        d3 = 0.15
        d4 = 0.2
        d5 = 3.5
        d6 = 0.9
        d7 = 0
        d8 = 0
        d9 = 1
        d10 = 1.4
        d11 = 0.3

        f = (x**2 * (1 - d1 * np.exp(-((x - d2) / d3)**2))
             * (1 + d4 * np.exp(-((x - d5) / d6)**2))
             * (1 + d7 * np.exp(-((x - d8) / d9)**2))) / (d10 + d11 * x**2) /
sqrt(rho_s)
    return f


# Sediment scattering (Moate & Thorne, 2012)
def xi_s_function_MoateThorne2012(a_s, freq, C=1500, mica="false", rho_s=2650):
    k = 2 * pi * freq / C
    x = k * a_s

    if mica == "false":
        Xi_s = 0.09 * x**4 / (1380 + 560 * x**2 + 150 * x**4)

    elif mica == "true":
        c1 = 0.3
        c2 = 1.46
        c3 = 0.95
        c4 = 0.19
        Xi_s = c1 * x**4 / (c2 + c3 * x**2 + c4 * x**4) / rho_s
    return Xi_s


# Viscous absorption for spherical particles (Urick, 1948)
def xi_v_function_Urick(a_s, freq, rho_s=2650, rho_0=1000, nu_0=1.2e-6, C=1500):
    omega = 2 * pi * freq
    k = omega / C
    b = np.sqrt(omega / (2 * nu_0))
    g = rho_s / rho_0
    delta = 0.5 * (1 + 9 / (2 * b * a_s))
    s = (9 / (4 * b * a_s)) * (1 + 1 / (b * a_s))
    Xi_v = (2 / 3) * k * a_s * (g - 1)**2 * (s / (s**2 + (g + delta)**2))
    return Xi_v


# Viscous absorption for oblate spheroids (Richards et al., 2003)
def xi_v_function_richards(a_s, h, freq, rho_s=2650, rho_0=1000, nu_0=1.2e-6,
C=1500):
```

```
    omega = 2 * pi * freq
    k = omega / C

    if h == 1:
        b = np.sqrt(omega / (2 * nu_0))
        g = rho_s / rho_0
        delta = 0.5 * (1 + 9 / (2 * b * a_s))
        s = (9 / (4 * b * a_s)) * (1 + 1 / (b * a_s))
        Xi_v = (2 / 3) * k * a_s * (g - 1)**2 * (s / (s**2 + (g + delta)**2))

    else:
        beta = np.sqrt(omega / (2 * nu_0))
        g = rho_s / rho_0
        epsilon = sqrt(1 - h**2)

        # Particles parallel to the acoustic wave
        alpha0 = (2 / epsilon**2) * (1 - sqrt(1 - epsilon**2) * asin(epsilon) /
epsilon)
        Li_pa = alpha0 / (2 - alpha0)
        K_pa = (8 / 3) * (2 * h / (1 - h**2) + 2 * (1 - 2 * h**2) / (1 - h**2)**(3
/ 2) * atan(sqrt(1 - h**2) / h))**(-1)
        s_pa = 9 / (4 * h * a_s * beta) * K_pa**2 * (1 + 1 / (K_pa * beta * a_s))
        delta_pa = Li_pa + 9 / (4 * h * a_s * beta) * K_pa**2
        Xi_v_pa = (2 / 3) * k * a_s * (g - 1)**2 * (s_pa / (s_pa**2 + (g +
delta_pa)**2))

        # Particles perpendicular to the acoustic wave
        gamma0 = sqrt(1 - epsilon**2) / epsilon**3 * asin(epsilon) - (1 -
epsilon**2) / epsilon**2
        Li_ort = gamma0 / (2 - gamma0)
        K_ort = (8 / 3) * (-h / (1 - h**2) - (2 * h**2 - 3) / (1 - h**2)**(3 / 2) *
asin(sqrt(1 - h**2)))**(-1)
        s_ort = 9 / (4 * h * a_s * beta) * K_ort**2 * (1 + 1 / (K_ort * beta *
a_s))
        delta_ort = Li_ort + 9 / (4 * h * a_s * beta) * K_ort**2
        Xi_v_ort = (2 / 3) * k * a_s * (g - 1)**2 * (s_ort / (s_ort**2 + (g +
delta_ort)**2))
        Xi_v = (1 / 3) * Xi_v_pa + (2 / 3) * Xi_v_ort
    return Xi_v
```

In [8]:

```
# Functions to compute h values depending on particle radius a
def h_var_func(a, h_fine=1/40, amin=1e-6, amax=30e-6):
    #This function returns h values depending on particle radius a:
    #h = 1 for a > amax
    #h = h_fine for a < amin
    #h varies linearly between h_fine and 1 for a in [amin, amax]
    h = np.zeros(len(a))
    h[a >= amax] = 1
    h[a <= amin] = h_fine
    test = (a < amax) * (a > amin)
    h[test] = a[test] * (1 - h_fine)  / (amax - amin) + (1 - amax * (1 - h_fine)  /
(amax - amin))
    return h

# Plotting h variations
def plot_h(a0_range, h_fine, amin, amax):
    fig, ax = plt.subplots(1, 2, figsize=(6, 3), dpi=100)
    ax[0].plot(a0_range, h_var_func(a0_range, h_fine, amin, amax))
    ax[0].set_xlabel('a (m)')
    ax[0].set_xscale('log')
    ax[0].set_ylabel('h')
    ax[0].set_ylim((0,1.1))
    ax[0].set_xlim((amin * 0.1, amax * 10))

    ax[1].plot(a0_range, h_var_func(a0_range, h_fine, amin, amax))
    ax[1].set_xlabel('a (m)')
    ax[1].set_ylabel('h')
    ax[1].set_ylim((0,1.1))
    ax[1].set_xlim((amin * 0.01, amax * 1.2))

plot_h(np.logspace(-7, -3, 200), h_oblate, h_inf_radius, h_sup_radius)
```

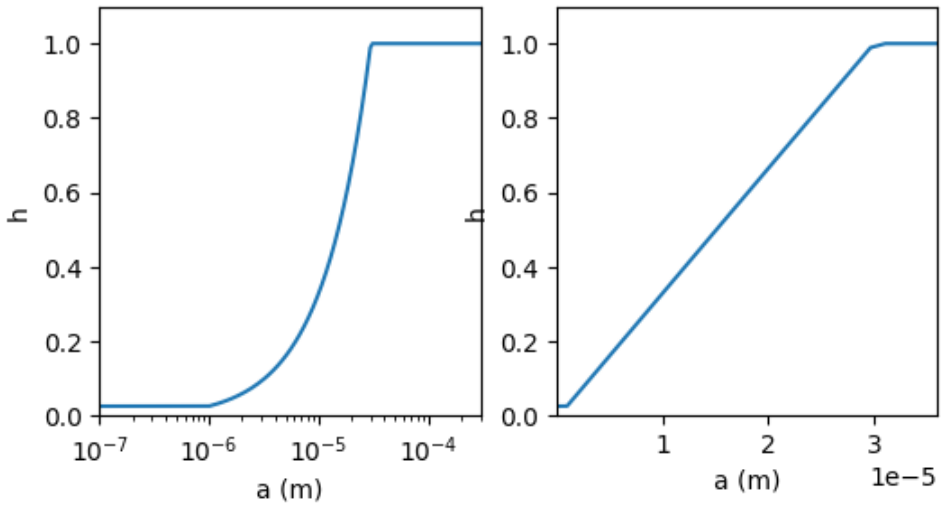

The class below allows to compute ζ and k_s^2 using:
- Richards et al. (2003) oblate spheroid model for χ_{sv} ;
- Moate and Thorne (2012) __mica__ model for f and χ_{ss}

In [9]:

```
class ComputeModelLognormOblate:
    def __init__(self, a50, sigma, freq, rho_s, nu_0, h_fine, h_inf, h_sup):
        # Position parameter
        self.a50 = a50
        # Scale parameter
        self.sigma = sigma
        # Frequencies
        self.freq = freq
        # Density
        self.rho_s = rho_s
        # kinematic viscosity
        self.nu_0 = nu_0
        # aspect ratio
        self.h_fine_value = h_fine
        self.h_inf_radius = h_inf
        self.h_sup_radius = h_sup
        self.zeta = np.zeros((len(self.freq)))
        self.ks2 = np.zeros((len(self.freq)))
        # Computing zeta and ks2
        self.compute()

    def simple_gaussian(self, x, m, s):
        """ This function returns a gaussian distribution """
        res = (1/ sqrt(2 * pi * s**2) * np.exp(-(x - m)**2 / (2 * s**2)))
        return res

    def compute(self) :
        """ This function computes zeta and ks2 by integration over a log-normal
distribution. The
        integral is computed as a sum"""
        # center of the sampling array
        F = round(np.log10(self.a50))
        # creating a sampling array
        a_sample = np.logspace(F - 6, F + 6, 3000)
        # Generating the aspect ratio h corresponding to each size
        h_sample = h_var_func(a_sample, h_fine=self.h_fine_value,
amin=self.h_inf_radius, amax=self.h_sup_radius)
        # computing the probability over the sampling array
        gaussian = self.simple_gaussian(np.log(a_sample), np.log(self.a50),
self.sigma)
        proba_vol = gaussian / sum(gaussian)

        # Computing number probability
        ss = np.sum(proba_vol / a_sample**3)
        proba_num = proba_vol/a_sample**3 / ss

        # Integrating zeta and ks2 over the distribution
        # Initializing
        temp_a2Xis = np.zeros((len(self.freq,)))
        temp_a2f2 = np.zeros((len(self.freq,)))
        temp_a3 = np.zeros((len(self.freq,)))
        temp_a2Xiv = np.zeros((len(self.freq,)))

        # Summing the integrals
        for i in range(len(a_sample)):
            a = a_sample[i]
            h = h_sample[i]
            temp_a2Xiv += a**2 * xi_v_function_richards(a, h, self.freq,
rho_s=self.rho_s, nu_0=self.nu_0) * proba_num[i]
            temp_a2Xis += a**2 * xi_s_function_MoateThorne2012(a, self.freq, mica =
'true') * proba_num[i]
            temp_a2f2 += a**2 * form_factor_function_MoateThorne2012(a, self.freq,
mica='true')**2 * proba_num[i]
```

```
            temp_a3 += a**3 * proba_num[i]


        self.zeta = 3 * (temp_a2Xiv / self.rho_s + temp_a2Xis) / (4 * temp_a3)
        self.ks2 = temp_a2f2 / temp_a3
```

Computation of ζ et k_s^2 for various values of a_0 and σ.

In [10]:
```
# a0 simulation parameters
d_min_um = 1      # 1 um
d_max_um = 40    # 40 um
a0_min_log = d_min_um / 2 * 1e-6
a0_max_log = d_max_um / 2 * 1e-6
a0_num_cases = 60 # in 60 steps in logarithmic steps

# sigma simulation parameters
sigma_min = 0.1
sigma_max = 2.0
sigma_steps = 0.05

# Setting the frequencies to compute
freq_list = np.array([1.0, 2.0, 4.0, 5.0]) * 1e6
freq_key_list = ['1.0 MHz', '2.0 MHz', '4.0 MHz', '5.0 MHz']
```

The following code block generates a large lookup table of modeled acoustic scattering properties for many combinations of:

- particle size
- particle size distribution width
- frequency

In [11]:
```
# Compute lookup tables
run_computing = "no"

if run_computing == "yes":
    a0_range = np.logspace(np.log10(a0_min_log), np.log10(a0_max_log),
a0_num_cases)
    sigma_range = np.arange(sigma_min, sigma_max, sigma_steps)
    int_base_zeta = np.zeros((a0_range.size, sigma_range.size, freq_list.size))
    int_base_ks2 = np.zeros((a0_range.size, sigma_range.size, freq_list.size))

    for j in tqdm(range(len(sigma_range))):
        for i in range(len(a0_range)):
            temp_ob = ComputeModelLognormOblate(a0_range[i], sigma_range[j],
freq_list, rho_s, nu_0, h_oblate, h_inf_radius, h_sup_radius)
            int_base_zeta[i, j, :] = temp_ob.zeta
            int_base_ks2[i, j, :] = temp_ob.ks2

    save_path = r"processed data sweden\tabul_zeta_ks2_lognorm_oblate"

    with open(save_path, "wb") as ff:
        pickle.dump({"zeta": int_base_zeta,
                     "ks2": int_base_ks2,
                     "sigma": sigma_range,
                     "a0": a0_range,
                     "freq": freq_list,
                     "freq_keys": freq_key_list}, ff)
```

In [12]:
```
# Opening the values
path = r'processed data sweden\tabul_zeta_ks2_lognorm_oblate'
ff = open(path,'rb')
dic_temp = pickle.load(ff)
int_base_zeta_lognorm_oblate = dic_temp['zeta']
int_base_ks2_lognorm_oblate = dic_temp['ks2']
sigma_range_lognorm_oblate = dic_temp['sigma']
a0_range_lognorm_oblate = dic_temp['a0']
freq_list_lognorm_oblate = dic_temp['freq']
freq_key_list_lognorm_oblate = dic_temp['freq_keys']
ff.close()
```

In [13]:
```
Mrange_lognorm_oblate = np.logspace(-2, 2, 500)

# Limit SSC to 80 g/l
Mrange_lognorm_oblate = Mrange_lognorm_oblate[Mrange_lognorm_oblate < 80]

# Creating an array with proper dimension to make the multiplication with zeta and
ks2 arrays
temp_M_range1 = np.zeros(np.shape(int_base_zeta_lognorm_oblate))
temp_M_range2 = np.repeat([temp_M_range1], Mrange_lognorm_oblate.size, axis=0)
for i in range(len(Mrange_lognorm_oblate)):
    temp_M_range2[i, :, :, :] = Mrange_lognorm_oblate[i]

# Final arrays of moddelled alpha_s and sv
alpha_th_lognorm_oblate = np.repeat([int_base_zeta_lognorm_oblate],
Mrange_lognorm_oblate.size, axis=0) * temp_M_range2
sv_th_lognorm_oblate = (3 / (16 * pi)) * np.repeat([int_base_ks2_lognorm_oblate],
Mrange_lognorm_oblate.size, axis=0)* temp_M_range2
```

Finding the best parameter set through the following objective function

$\rm{E(\boldsymbol{\theta})} = \sum_{j=1}^N \Bigg(A_j^2 \Bigg| \frac{\widehat{\alpha}_{s, j} - \alpha_{s, j}}{\alpha_{s, j}}\Bigg|^2 + A_j \Bigg| \frac{\widehat{s}_{v, j} - s_{v, j}}{s_{v, j}}\Bigg|^2\Bigg)$

$A_j = \left\{
\begin{array}{ll}
(f_j / f_0)^3 \quad \mbox{if } \alpha_{s, j}>0.1~\rm{m}^{-1} \\
0 \quad \mbox{if } \alpha_{s, j} \leq 0.1~\rm{m}^{-1}
\end{array}
\right.$

In [14]:
```
# Remove skipped files from dataframe
YEAR = 2026

skipped_file_names = [
    # "20260323185501.aqa",
    # "20260323190303.aqa",
    # "20260323191123.aqa",
]

df = df.copy()
df.columns = df.columns.str.strip()

df["datetime_temp"] = pd.to_datetime(df["measurement date"].astype(str).str.strip()
+ f"-{YEAR} " + df["Time"].astype(str).str.strip(),
                                     format="%d-%b-%Y %H:%M:%S", errors="coerce")

df["aqa_filename"] = df["datetime_temp"].dt.strftime("%Y%m%d%H%M%S") + ".aqa"
df_processed = df[~df["aqa_filename"].isin(skipped_file_names)].copy()
df_processed.reset_index(drop=True, inplace=True)

print(f"Original df length: {len(df)}")
print(f"Processed df length: {len(df_processed)}")
print(f"alpha_exp length: {len(alpha_exp['freq'])}")
print(f"sv_exp length: {len(sv_exp['freq'])}")
```

```
Original df length: 23
Processed df length: 23
alpha_exp length: 23
sv_exp length: 23
```

Reduce the lookup table for particle size and distribution width constraints

In [15]:

```
# Reduce sigma and particle size range
sigma_min_reduced = 0.1
sigma_max_reduced = 2.0

sigma_mask = (sigma_range_lognorm_oblate >= sigma_min_reduced) &
(sigma_range_lognorm_oblate <= sigma_max_reduced)

particle_min_um = 1
particle_max_um = 40

radius_min = particle_min_um * 0.5e-6
radius_max = particle_max_um * 0.5e-6

particle_mask = (a0_range_lognorm_oblate >= radius_min) & (a0_range_lognorm_oblate
<= radius_max)

sigma_range_reduced = sigma_range_lognorm_oblate[sigma_mask]
a0_range_reduced = a0_range_lognorm_oblate[particle_mask]
alpha_th_reduced = alpha_th_lognorm_oblate[:, particle_mask, :, :][:, :,
sigma_mask, :]
sv_th_reduced = sv_th_lognorm_oblate[:, particle_mask, :, :][:, :, sigma_mask, :]

print(f"Original alpha shape: {alpha_th_lognorm_oblate.shape}")
print(f"Reduced alpha shape : {alpha_th_reduced.shape}")
print(f"Original sv shape   : {sv_th_lognorm_oblate.shape}")
print(f"Reduced sv shape    : {sv_th_reduced.shape}")
```

```
Original alpha shape: (487, 60, 38, 4)
Reduced alpha shape : (487, 59, 38, 4)
Original sv shape   : (487, 60, 38, 4)
Reduced sv shape    : (487, 59, 38, 4)
```

In [21]:

```
def compute_error_function(df, freq_list, freq_key_list, Mrange, a0_range,
sigma_range, alpha_exp, alpha_model, sv_exp, sv_model):
    M_res_list = []
    a0_res_list = []
    sigma_res_list = []
    err_sv_total_list = []
    err_alpha_total_list = []
    err_tot_list = []

    freq_key_list = list(freq_key_list)

    res_DataFrame = pd.DataFrame(index=df.index)

    for freq in freq_key_list:
        res_DataFrame[f"Err s_v {freq}"] = np.nan
        res_DataFrame[f"Err alpha {freq}"] = np.nan

    res_DataFrame["Err s_v tot"] = np.nan
    res_DataFrame["Err alpha tot"] = np.nan
    res_DataFrame["Err total"] = np.nan
    res_DataFrame["Rel. SSC. err."] = np.nan
    res_DataFrame["SSC inv."] = np.nan
    res_DataFrame["SSC measured"] = df["Concentration gravimetric"].values
    res_DataFrame["SSC measured original"] = df["Concentration gravimetric
interpolated"].values

    for k in range(len(df)):
        err_sum_array_alpha = np.zeros((Mrange.size, a0_range.size,
sigma_range.size))
        err_sum_array_sv = np.zeros((Mrange.size, a0_range.size, sigma_range.size))
        valid_alpha_count = 0
        valid_sv_count = 0

        for f in range(len(alpha_exp["freq"][k])):
            key_freq = alpha_exp["freq"][k][f]
            a_exp = alpha_exp["alpha_s"][k][f]

            if key_freq not in freq_key_list:
                continue

            if a_exp is None or not np.isfinite(a_exp) or a_exp <= 0:
                continue

            if a_exp < 0.1:
                continue

            ind_freq = freq_key_list.index(key_freq)
            values_alpha = alpha_model[:, :, :, ind_freq]
            err_alpha = ((np.abs(values_alpha - a_exp) / a_exp) ** 2 *
(freq_list[ind_freq] * 1e-6) ** 6)
            err_sum_array_alpha += err_alpha
            valid_alpha_count += 1

        for f in range(len(sv_exp["freq"][k])):
            key_freq = sv_exp["freq"][k][f]
            sv_meas = sv_exp["s_v"][k][f]

            if key_freq not in freq_key_list:
                continue

            if sv_meas is None or not np.isfinite(sv_meas) or sv_meas <= 0:
                continue
```

```
            a_exp = alpha_exp["alpha_s"][k][f]

            if a_exp is None or not np.isfinite(a_exp) or a_exp < 0.1:
                continue

            ind_freq = freq_key_list.index(key_freq)
            values_sv = sv_model[:, :, :, ind_freq]
            err_sv = ((np.abs(values_sv - sv_meas) / sv_meas) ** 2 *
(freq_list[ind_freq] * 1e-6) ** 3)
            err_sum_array_sv += err_sv
            valid_sv_count += 1

        if valid_alpha_count == 0 and valid_sv_count == 0:
            M_res_list.append(np.nan)
            a0_res_list.append(np.nan)
            sigma_res_list.append(np.nan)
            err_sv_total_list.append(np.nan)
            err_alpha_total_list.append(np.nan)
            err_tot_list.append(np.nan)

            continue

        err_sum_array = err_sum_array_alpha + err_sum_array_sv
        min_error = np.nanmin(err_sum_array)
        ind_min = np.unravel_index(np.nanargmin(err_sum_array),
err_sum_array.shape)
        i_M, i_a0, i_sigma = ind_min
        M_inv = Mrange[i_M]
        a0_inv = a0_range[i_a0]
        sigma_inv = sigma_range[i_sigma]
        M_res_list.append(M_inv)
        a0_res_list.append(a0_inv)
        sigma_res_list.append(sigma_inv)
        err_sv_total = err_sum_array_sv[ind_min]
        err_alpha_total = err_sum_array_alpha[ind_min]
        err_sv_total_list.append(err_sv_total)
        err_alpha_total_list.append(err_alpha_total)
        err_tot_list.append(min_error)
        res_DataFrame.loc[k, "Err total"] = min_error
        res_DataFrame.loc[k, "Err s_v tot"] = err_sv_total
        res_DataFrame.loc[k, "Err alpha tot"] = err_alpha_total
        res_DataFrame.loc[k, "SSC inv."] = M_inv
        measured_ssc = df.loc[k, "Concentration gravimetric"]

        if measured_ssc != 0:
            res_DataFrame.loc[k, "Rel. SSC. err."] = abs(M_inv - measured_ssc) /
measured_ssc * 100

        for f in range(len(alpha_exp["freq"][k])):
            key_freq = alpha_exp["freq"][k][f]
            a_exp = alpha_exp["alpha_s"][k][f]

            if key_freq not in freq_key_list:
                continue

            if a_exp is None or not np.isfinite(a_exp) or a_exp <= 0 or a_exp <
0.1:
                continue

            ind_freq = freq_key_list.index(key_freq)
            values_alpha = alpha_model[:, :, :, ind_freq]
            err_alpha = ((np.abs(values_alpha - a_exp) / a_exp) ** 2 *
(freq_list[ind_freq] * 1e-6) ** 6)
            res_DataFrame.loc[k, f"Err alpha {key_freq}"] = err_alpha[ind_min]
```

```
        for f in range(len(sv_exp["freq"][k])):
            key_freq = sv_exp["freq"][k][f]
            sv_meas = sv_exp["s_v"][k][f]

            if key_freq not in freq_key_list:
                continue

            if sv_meas is None or not np.isfinite(sv_meas) or sv_meas <= 0:
                continue

            a_exp = alpha_exp["alpha_s"][k][f]

            if a_exp is None or not np.isfinite(a_exp) or a_exp < 0.1:
                continue

            ind_freq = freq_key_list.index(key_freq)
            values_sv = sv_model[:, :, :, ind_freq]
            err_sv = ((np.abs(values_sv - sv_meas) / sv_meas) ** 2 *
(freq_list[ind_freq] * 1e-6) ** 3)
            res_DataFrame.loc[k, f"Err s_v {key_freq}"] = err_sv[ind_min]

    return (M_res_list, a0_res_list, sigma_res_list, err_sv_total_list,
err_alpha_total_list, err_tot_list, res_DataFrame)

# Run inversion with reduced sigma range
(
    M_res_list_lognorm_oblate,
    a0_res_list_lognorm_oblate,
    sigma_res_list_lognorm_oblate,
    err_sv_list_lognorm_oblate,
    err_alpha_list_lognorm_oblate,
    err_tot_list_lognorm_oblate,
    res_lognorm_oblate_DataFrame
) = compute_error_function(
    df_processed,
    freq_list_lognorm_oblate,
    freq_key_list_lognorm_oblate,
    Mrange_lognorm_oblate,
    a0_range_reduced,
    sigma_range_reduced,
    alpha_exp,
    alpha_th_reduced,
    sv_exp,
    sv_th_reduced
)

# display(res_lognorm_oblate_DataFrame)
```

In [17]:

```
def plot_SSC_invers_vs_measured(measured_SSC, inv_SSC, fit_min=1.0, fit_max=18.0):
    measured_SSC = np.asarray(measured_SSC, dtype=float)
    inv_SSC = np.asarray(inv_SSC, dtype=float)

    # Remove invalid values
    mask = np.isfinite(measured_SSC) & np.isfinite(inv_SSC) & (measured_SSC > 0) &
(inv_SSC > 0)
    measured = measured_SSC[mask]
    inverted = inv_SSC[mask]

    # Select fitting range
    fit_mask = (measured >= fit_min) & (measured <= fit_max)
    measured_fit = measured[fit_mask]
    inverted_fit = inverted[fit_mask]

    if len(measured_fit) < 2:
        raise ValueError(f"Not enough points between {fit_min} and {fit_max} g/L to
calculate the fit.")

    fig, ax = plt.subplots(figsize=(7, 6), dpi=100)

    axis_min = 0.1
    axis_max = 100
    purple = "#6a51a3"

    x_ref = np.logspace(np.log10(axis_min), np.log10(axis_max), 300)
    x_fit_all = np.logspace(np.log10(measured_fit.min()),
np.log10(measured_fit.max()), 300)
    x_fit_range = np.logspace(np.log10(measured_fit.min()),
np.log10(measured_fit.max()), 200)

    ax.scatter(measured_fit, inverted_fit, s=55, facecolor=purple,
edgecolor=purple, alpha=0.6, label="Data used for fit", zorder=5)
    excluded_mask = ~fit_mask
    ax.scatter(measured[excluded_mask], inverted[excluded_mask], s=55,
facecolor=purple, edgecolor=purple, alpha=0.6, zorder=6)

    # Linear fit
    slope = np.sum(measured_fit * inverted_fit) / np.sum(measured_fit**2)
    yfit_all = slope * x_fit_all
    yfit_range = slope * x_fit_range
    yfit_data_fit = slope * measured_fit

    # Log-space uncertainty
    log_residuals = np.log(inverted_fit / yfit_data_fit)
    n = len(measured_fit)

    sigma_log = np.sqrt(np.sum(log_residuals**2) / (n - 1))
    upper_2std = yfit_range * np.exp(2 * sigma_log)
    lower_2std = yfit_range * np.exp(-2 * sigma_log)

    ax.plot(x_ref, 1.5 * x_ref, color="0.55", linestyle="--",lw=1.4, zorder=1,
label="±50% bounds")
    ax.plot(x_ref, 0.5 * x_ref, color="0.55", linestyle="--", lw=1.4, zorder=1)
    ax.fill_between(x_fit_range, lower_2std, upper_2std, color=purple, alpha=0.18,
zorder=2, label=r"Fit $\pm2\sigma_{\log}$")
    ax.plot(x_fit_all, yfit_all, color=purple, lw=2.5, linestyle="-", zorder=3,
label="Linear fit")
    ax.plot(x_ref, x_ref, color="black", lw=2.2, linestyle="-", zorder=4,
label="1:1 line")

    # Performance metrics
    yfit_data_all = slope * measured
```

```
    SSE_all = np.sum((inverted - yfit_data_all)**2)
    SST_all = np.sum((inverted - np.mean(inverted))**2)
    R2_all = np.nan if SST_all == 0 else 1 - SSE_all / SST_all
    RMSE_all = np.sqrt(np.mean((inverted - measured)**2))
    MARE_all = np.mean(np.abs((inverted - measured) / measured)) * 100
    SSE_fit = np.sum((inverted_fit - yfit_data_fit)**2)
    SST_fit = np.sum((inverted_fit - np.mean(inverted_fit))**2)
    R2_fit = np.nan if SST_fit == 0 else 1 - SSE_fit / SST_fit
    RMSE_fit = np.sqrt(np.mean((inverted_fit - measured_fit)**2))
    MARE_fit = np.mean(np.abs((inverted_fit - measured_fit) / measured_fit)) * 100

    metrics_df = pd.DataFrame({
        "Metric": [
            "Lower fitting threshold (g/L)",
            "Upper fitting threshold (g/L)",
            "Slope used for fit",
            r"$R^2$ all data",
            rf"$R^2$ {fit_min:g}--{fit_max:g} g/L",
            "MARE all data (%)",
            f"MARE {fit_min:g}--{fit_max:g} g/L (%)",
            "RMSE all data (g/L)",
            f"RMSE {fit_min:g}--{fit_max:g} g/L",
            rf"$\sigma_{{\log}}$ {fit_min:g}--{fit_max:g} g/L",
            r"$+2\sigma_{\log}$ factor",
            r"$-2\sigma_{\log}$ factor",
            "Number of points all data",
            "Number of points used for fit"
        ],
        "Value": [
            fit_min,
            fit_max,
            round(slope, 3),
            round(R2_all, 3),
            round(R2_fit, 3),
            round(MARE_all, 1),
            round(MARE_fit, 1),
            round(RMSE_all, 2),
            round(RMSE_fit, 2),
            round(sigma_log, 3),
            round(np.exp(2 * sigma_log), 2),
            round(np.exp(-2 * sigma_log), 2),
            len(measured),
            len(measured_fit)
        ]
    })

    ax.set_xlabel(r"Gravimetric SSC (g/L)", fontsize=17)
    ax.set_ylabel(r"ABS SSC (g/L)", fontsize=17)
    ax.set_title("CCZ Sediment", fontsize=17)
    ax.set_xscale("log")
    ax.set_yscale("log")
    ax.set_xlim(axis_min, axis_max)
    ax.set_ylim(axis_min, axis_max)
    ax.xaxis.set_major_locator(LogLocator(base=10.0))
    ax.yaxis.set_major_locator(LogLocator(base=10.0))
    formatter = FuncFormatter(lambda x, pos: f"{x:g}")
    ax.xaxis.set_major_formatter(formatter)
    ax.yaxis.set_major_formatter(formatter)
    ax.tick_params(axis="both", which="major", labelsize=16)
    ax.grid(True, which="both", alpha=0.3)

    handles, labels = ax.get_legend_handles_labels()
    legend_order = ["1:1 line", "±50% bounds", "Data points", "Linear fit", r"Fit
$\pm2\sigma_{\log}$"]
```

```
    ordered_handles = []
    ordered_labels = []

    for label in legend_order:
        if label in labels:
            idx = labels.index(label)
            ordered_handles.append(handles[idx])
            ordered_labels.append(labels[idx])

    ax.legend(ordered_handles, ordered_labels, fontsize=16)
    fig.tight_layout()
    return fig, metrics_df


fig, metrics_df = plot_SSC_invers_vs_measured(
    res_lognorm_oblate_DataFrame["SSC measured"].values,
    res_lognorm_oblate_DataFrame["SSC inv."].values,
    fit_min=0.499,
    fit_max=18
)

plt.show()
# display(metrics_df)
```

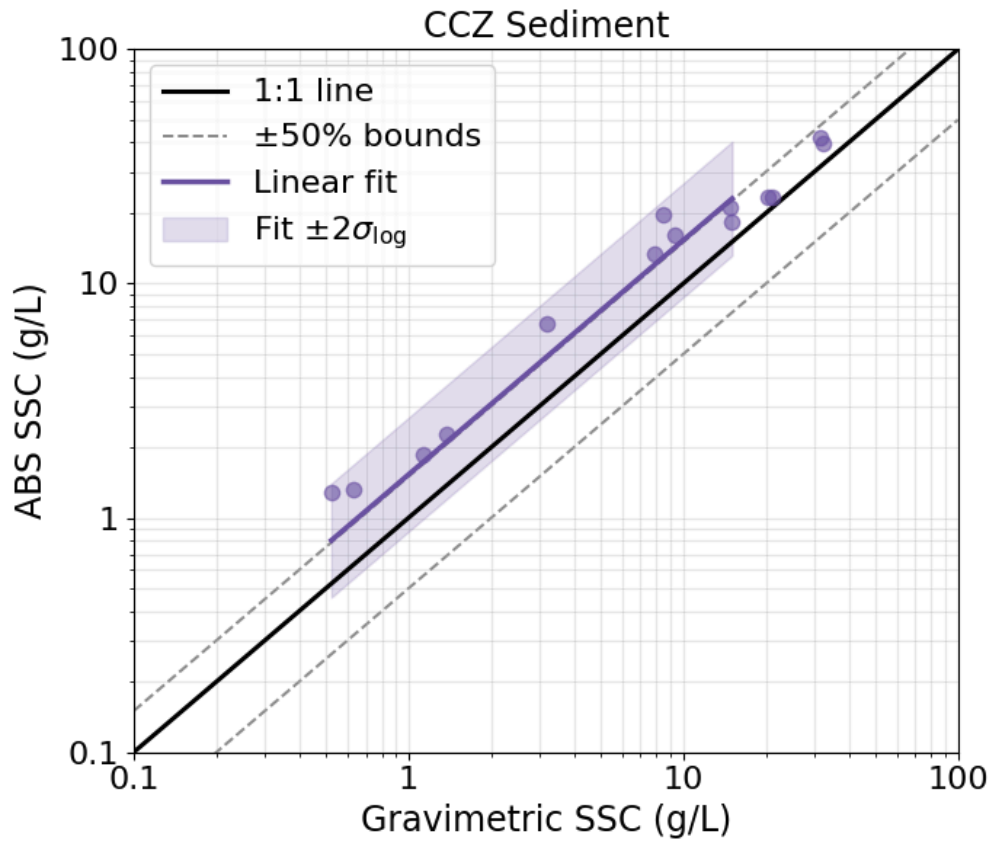

In [18]:

```
measured =res_lognorm_oblate_DataFrame["SSC measured"].values
inverted =res_lognorm_oblate_DataFrame["SSC inv."].values
ssc_df = pd.DataFrame({"Gravimetric SSC (g/L)": measured, "Inverted SSC (g/L)":
inverted})
```

In [19]:

```
def plot_inverse_a0_and_sigma(a0_res_list, sigma_res_list, df, particle_min_um,
particle_max_um, a0_max_log, sigma_min, sigma_max):
    fontsize = 17
    fig, ax = plt.subplots(1, 2, figsize=(13, 4), dpi=300)

    concentration = df["Concentration gravimetric"].to_numpy()

    # Convert radius to particle diameter [µm]
    a0_res = np.asarray(a0_res_list)
    diameter_um = 2 * a0_res * 1e6
    sigma_res = np.asarray(sigma_res_list)
    mean_diameter = np.nanmean(diameter_um)
    mean_sigma = np.nanmean(sigma_res)

    ax[0].plot(concentration, diameter_um, linestyle=" ", marker="d",
color="#865ba8", alpha=0.7)

    ax[0].set_xlabel("Gravimetric SSC (g/L)", fontsize=fontsize)
    ax[0].set_ylabel(r"$D_{50}$ [$\mu$m]", fontsize=fontsize)
    ax[0].set_xscale("log")
    ax[0].set_yscale("log")
    ax[0].set_xlim(0.1, 50)
    ax[0].set_ylim(0.5, 50)
    ax[0].set_xticks([1, 10])
    ax[0].set_xticklabels(["1", "10"])
    ax[0].set_yticks([0.1, 1, 10, 100])
    ax[0].set_yticklabels(["0.1", "1", "10", "100"])
    ax[0].axhline(particle_min_um, color="black", linestyle="--", label="Search
bounds")
    ax[0].axhline(particle_max_um, color="black", linestyle="--")
    ax[0].axhline(mean_diameter, color="black", linewidth=1, label=fr"Mean =
{mean_diameter:.2f} $\mu$m")

    ax[0].grid(which="both", alpha=0.3)
    ax[1].plot(concentration, sigma_res, linestyle=" ", marker="d",
color="#865ba8", alpha=0.7)
    ax[1].set_xlabel("Gravimetric SSC (g/L)", fontsize=fontsize)
    ax[1].set_ylabel(r"$\sigma$", fontsize=fontsize)
    ax[1].set_xscale("log")
    ax[1].set_xlim(0.1, 40)
    ax[1].set_xticks([1, 10])
    ax[1].set_xticklabels(["1", "10"])
    ax[1].set_ylim(0, 2.1)
    ax[1].axhline(sigma_min, color="black", linestyle="--", label="Search bounds")
    ax[1].axhline(sigma_max, color="black", linestyle="--")
    ax[1].axhline(mean_sigma, color="black", linewidth=1, label=fr"Mean =
{mean_sigma:.2f}")
    ax[1].grid(which="both", alpha=0.3)

    for a in ax:
        a.tick_params(axis="both", which="major", labelsize=fontsize)
        a.tick_params(axis="both", which="minor", labelsize=fontsize - 2)
        a.legend(frameon=True, fontsize=fontsize)

    fig.tight_layout()
    plt.show()

plot_inverse_a0_and_sigma(
    a0_res_list_lognorm_oblate,
    sigma_res_list_lognorm_oblate,
    df_processed,
    particle_min_um,
    particle_max_um,
```

```
    a0_max_log,
    sigma_min_reduced,
    sigma_max_reduced
)

mean_a0_lognorm_oblate = np.nanmean(np.asarray(a0_res_list_lognorm_oblate,
dtype=float))
mean_sigma_lognorm_oblate = np.nanmean(np.asarray(sigma_res_list_lognorm_oblate,
dtype=float))

print(f"Mean a0: {mean_a0_lognorm_oblate * 2e6:.2f} um")
print(f"Mean sigma: {mean_sigma_lognorm_oblate:.2f}")
```

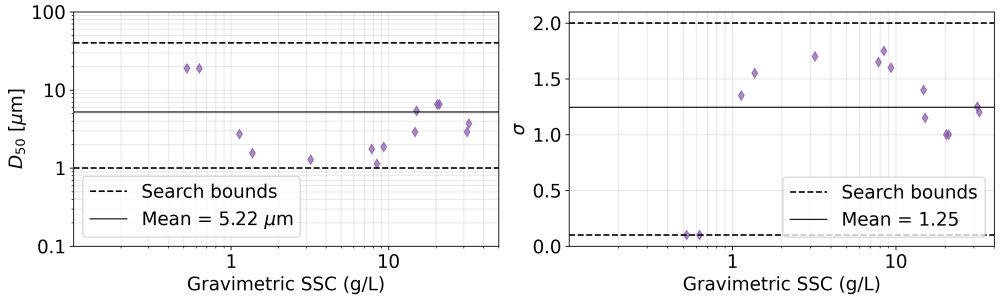


```
Mean a0: 5.22 um
Mean sigma: 1.25
```

In [20]:

```
# Ratio of measured/modelled alpha_s and s_v
dic_ratio_model_lognorm_oblate = {
    "alpha": {freq: [] for freq in freq_key_list_lognorm_oblate},
    "s_v": {freq: [] for freq in freq_key_list_lognorm_oblate}
}

num_exp = min(len(df_processed), len(alpha_exp["freq"]),
              len(sv_exp["freq"]), len(M_res_list_lognorm_oblate))

for k in range(num_exp):

    if (not np.isfinite(M_res_list_lognorm_oblate[k]) or
        not np.isfinite(a0_res_list_lognorm_oblate[k]) or
        not np.isfinite(sigma_res_list_lognorm_oblate[k])):
        continue

    concentration = df_processed["Concentration gravimetric"].iloc[k]

    if not np.isfinite(concentration):
        continue

    freq_list_temp = []
    freq_key_list_temp = []

    for freq in alpha_exp["freq"][k]:
        if freq not in freq_key_list_lognorm_oblate:
            continue


freq_list_temp.append(freq_list_lognorm_oblate[freq_key_list_lognorm_oblate.index(f
req)])
        freq_key_list_temp.append(freq)

    if len(freq_list_temp) == 0:
        continue

    model = ComputeModelLognormOblate(
        a0_res_list_lognorm_oblate[k],
        sigma_res_list_lognorm_oblate[k],
        np.array(freq_list_temp),
        rho_s,
        nu_0,
        h_oblate,
        h_inf_radius,
        h_sup_radius
    )

    alpha_model = model.zeta * M_res_list_lognorm_oblate[k]
    sv_model = 3 / (16 * pi) * model.ks2 * M_res_list_lognorm_oblate[k]

    for f, freq in enumerate(freq_key_list_temp):
        freq_alpha_ind = alpha_exp["freq"][k].index(freq)
        alpha_meas = alpha_exp["alpha_s"][k][freq_alpha_ind]
        if (alpha_meas is not None and np.isfinite(alpha_meas) and
            np.isfinite(alpha_model[f]) and alpha_meas > 0 and alpha_model[f] > 0):

            dic_ratio_model_lognorm_oblate["alpha"][freq].append(
                [concentration, alpha_meas / alpha_model[f]]
            )

        freq_sv_ind = sv_exp["freq"][k].index(freq)
        sv_meas = sv_exp["s_v"][k][freq_sv_ind]
```

```
        if (sv_meas is not None and np.isfinite(sv_meas) and
            np.isfinite(sv_model[f]) and sv_meas > 0 and sv_model[f] > 0):

            dic_ratio_model_lognorm_oblate["s_v"][freq].append([concentration,
sv_meas / sv_model[f]])


THESIS_PALETTE = [
    "#1fa040", "#1b8a5a", "#177482", "#125eab",
    "#0e48d3", "#0072ce", "#ffc372", "#f4a95e",
    "#ea8f49", "#df7535", "#d55b20", "#d14124",
    "#b07aa1", "#9b6aa5", "#865ba8", "#6a51a3"
]

freq_colors = {
    freq_key_list_lognorm_oblate[0]: THESIS_PALETTE[0],
    freq_key_list_lognorm_oblate[1]: THESIS_PALETTE[2],
    freq_key_list_lognorm_oblate[2]: THESIS_PALETTE[5],
    freq_key_list_lognorm_oblate[3]: THESIS_PALETTE[8],
}

marker_dic = {
    freq_key_list_lognorm_oblate[0]: "o",
    freq_key_list_lognorm_oblate[1]: "s",
    freq_key_list_lognorm_oblate[2]: "^",
    freq_key_list_lognorm_oblate[3]: "D",
}


fig, ax = plt.subplots(1, 2, figsize=(12, 5), dpi=200)

for freq in freq_key_list_lognorm_oblate:
    vals_alpha = np.asarray(dic_ratio_model_lognorm_oblate["alpha"][freq],
dtype=float)
    if vals_alpha.size > 0:
        ax[0].plot(vals_alpha[:, 0], vals_alpha[:, 1], linestyle=" ",
marker=marker_dic[freq], color=freq_colors[freq], alpha=0.75, label=freq)

    vals_sv = np.asarray(dic_ratio_model_lognorm_oblate["s_v"][freq], dtype=float)

    if vals_sv.size > 0:
        ax[1].plot(vals_sv[:, 0], vals_sv[:, 1], linestyle=" ",
marker=marker_dic[freq], color=freq_colors[freq], alpha=0.75, label=freq)

for a in ax:
    a.axhline(1, color="black", lw=0.9, label="Measured = modelled")
    a.axhline(1.5, color="gray", lw=0.8, linestyle=":")
    a.axhline(0.5, color="gray", lw=0.8, linestyle=":")
    a.set_xscale("log")
    a.set_yscale("log")
    a.set_xlim(0.1, 50)
    a.grid(alpha=0.3)
    a.legend(fontsize=9)

ax[0].set_ylim(0.1, 20)
ax[1].set_ylim(0.1, 1000)
ax[0].set_xlabel("Gravimetric SSC (g/L)", fontsize=13)
ax[0].set_ylabel(r"$\alpha_{s,\mathrm{measured}} / \alpha_{s,\mathrm{modelled}}$",
fontsize=13)
ax[0].set_title("Attenuation ratio", fontsize=14)
ax[1].set_xlabel("Gravimetric SSC (g/L)", fontsize=13)
ax[1].set_ylabel(r"$s_{v,\mathrm{measured}} / s_{v,\mathrm{modelled}}$",
fontsize=13)
ax[1].set_title("Backscatter ratio", fontsize=14)
```

```
fig.tight_layout()
plt.show()
```

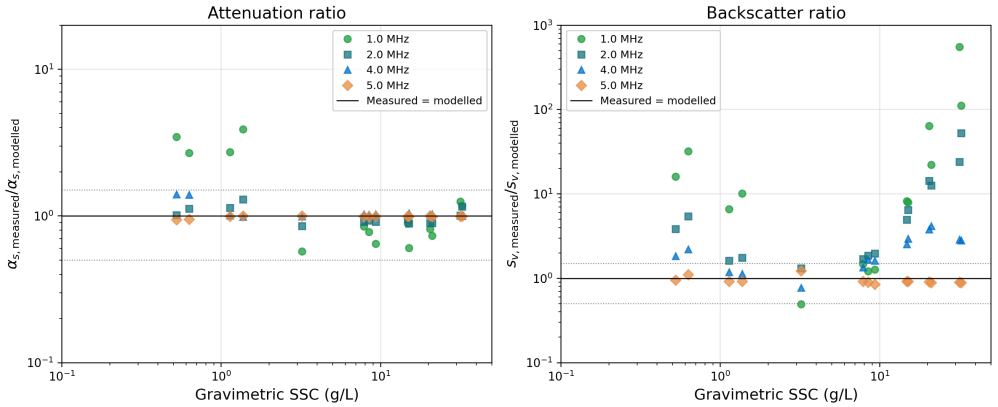

In [ ]:

Exported with runcell — convert notebooks to HTML or PDF anytime at runcell.dev.